ABSTRACT

Title of dissertation: MICROSCOPY OF
                          ELONGATED SUPERFLUIDS

                          Francisco Salces Cárcoba
                          Doctor of Philosophy, 2020

Dissertation directed by: Professor Ian Spielman
                            Joint Quantum Institute,
                            National Institute of Standards and Technology
                            and the University of Maryland College Park

This thesis covers three experiments with cold and ultracold (Bose–Einstein condensate based) alkali ^{87}Rb gases for quantum simulation. In the first experiment, we quantum simulate Abelian and non-Abelian gauge fields in the parameter space of a four-level quantum system. Then, we describe the experimental framework to perform optimal *in-situ* microscopy of elongated quantum gases. We then study the thermodynamics of individual one-dimensional Bose gases using *in-situ* resonant absorption imaging. Finally, we combine holographic microscopy and impulse correlations to digitally enhance our absorption images.

Microscopy of elongated superfluids

by

Francisco Salces-Carcoba

Dissertation submitted to the Faculty of the Graduate School of the
University of Maryland, College Park in partial fulfillment
of the requirements for the degree of
Doctor of Philosophy
2020

Advisory Committee:
Professor Luis A. Orozco, Chair
Professor Alicia Kollár,
Professor William D. Phillips,
Professor Mohammad Hafezi, Dean's representative
Professor Ian Spielman, Advisor

Foreword

Dear imaginary reader, if you are looking for a reference in one or more of the following topics: laser cooling and trapping of alkali gases, production of quantum degenerate Bose gases, measurement of first and second Chern numbers, *in-situ* resonant absorption imaging, digital processing tools for absorption imaging, trapped one-dimensional Bose gases, experimental determination of equations of state, or digital holography, you seem to be in the right place and I hope this document satisfies you.

Dedication

A mis abuelos, mi madre, y mi hermano

Acknowledgments

I wish to acknowledge those who have had a part in the making of this thesis.

On the one hand, there is scientific support. First, my advisor Ian Spielman deserves my deepest gratitude and admiration. It was great to share your wisdom and lack of it, and thank you for never saying no to silly questions or crazy ideas at your office's door. Second, I wish to thank Luis Orozco for answering my questions with other questions. After all, science is often about asking the right questions more than it is about finding the right answers. I want to specially thank Bill Phillips for an incredibly thorough revision of this document.

Special thanks to my local experts in coherent control (Ana), programming, linux, and numerical analysis (Chris), optics and "charged neutral atoms" (David), ^{87}Rb Rydberg atoms (Dalia), cavity and waveguide QED (Pablo), state of the art electronics (Alessandro), and many others who have shared something cool with me.

I want to highlight the influence of group postdocs during my PhD. Thanks to Seiji for making me realize that "everyday is Friday", and teaching me that I should "only do things when I need to to them" (a highly overseen lesson in the experimental life of a PhD student). Thanks to Chris for all the "covfefe" chatter times. Finally, thanks to Emine, Hsin-I Lu, Mingwu, Amilson, Qiyu, Hilary, Dim-

itris, and Ben for many bits of invaluable postdoc wisdom.

Just as important are my fellow graduate students. Thanks to Abby, Yuchen, and Andika for making the RbChip lab the best lab in the group. Thank you Dina, Lauren, Alina, and Graham for being there in RbK. Thank you Ana, Dan, Ryan, Mingshu, Junheng for making me feel at home in RbLi whenever I was around the JQI. Other students and postdocs at the JQI made my PhD experience special; thank you Varun, Roger, Elizabeth, Monica, Carlos, David, Pablo, Meng Chang, Prasoon, Ananya, Swarnav, Peter, Hector, Yang, Sarthak, Rory, Don, Nick, and all of you that ever wandered out of your labs just to hang out and share your piece of physics. Some lab interns have taken a piece of my PhD with them; Marcel, Pierre, Michael, Rob, Max, Martin, thank you for the good times.

On the other hand, there is a human component. Special gratitude goes to my mother Rosario, my grandparents Lilia and Felix, and my brother Ray for showing up Sunday after Sunday on my screen. I also thank my extended family; Luis Miguel, Dora, Felix, Ana, Arantxa, Maite, Lilia, Manuel, Julia, China, Esther, Raymundo, and others for always asking me how I was doing and ever more strongly supporting me. My memory holds a special place for Juan Carlos, Felix, and Paco, who despite having left are bound to these words of gratitude.

A highlight of my PhD experience was living in the international house of

Table of Contents

List of Tables

List of Figures

List of Abbreviations

1D	One dimensional
1DBG	One-dimensional Bose gas
3D	Three dimensional
μ-wave	Microwave
AOM	Acousto optic modulator
ARP	Adiabatic rapid passage
BEC	Bose–Einstein Condensate
CFF	Conflat flange
cMOT	Compressed MOT
DMD	Digital micromirror device
HWP	Half waveplate
IQHE	Integer quantum Hall effect
JQI	Joint Quantum Institute
LDA	Local density approximation
LIAD	Light induced atomic desorption
MOT	Magneto optical trap
NA	Numerical aperture
NIST	National Institute of Standards and Technology
PBS	Polarizing beam splitter
PFC	Photonic crystal fiber
PGC	Polarization gradient cooling
PSF	Point spread function
QWP	Quarter waveplate
RF	Radiofrequency
SLM	Spatial light modulator
SNR	Signal to noise ratio
SPP	Spiral phase plate
TEC	Thermo electric cooling
TOF	Time of flight
UHV	Ultra high vacuum
UV	Ultraviolet

Chapter 1:   Introduction

Quantum simulation is powerful. It probes aspects of quantum sytems that escape sophisticated theoretical tools with fully fledged experiments. The degree to which a quantum simulation realizes a physical system is left to the experiment. Ever challenging and exciting progress in quantum simulation feeds from novel experimental techniques and platforms. The RbChip laboratory at NIST, where the experiments described in this thesis take place, specializes in Bose–Einstein condensate (BEC) based quantum simulation. The choice of platform is well justified as BECs consitute a well-understood, fundamental form of quantum matter. In addition to hosting versatile control, they provide us with a rich experimental toolbox, of which a large section comes from optics. This is not surprising, as light-matter interaction is at the heart of the information throughput, or the exchange of information in measurement and control, in a majority of atomic systems.

A bosonic ensemble reaches quantum degeneracy when a significant number of particles occupy the same quantum state. While Bose enhancement leads to such a degenerate condensate, the Pauli exclusion principle dictates the occupation statistics of a degenerate fermionic ensemble. In either case, degenerate ensembles

may display macroscopic coherent behavior, making them remarkable platforms for the simulation of quantum matter. To date, quantum degeneracy has been experimentally attained for ensembles of light [1], bound light-matter quasiparticles [2], and dilute clouds of very cold atoms and molecules [3–5], showing the two kinds of bosonic and fermionic degeneracy. Similarly, a number of naturally ocurring degenerate Fermi gases include electrons in metals, liquid ^{3}He near the superfluid transition [6], and electrons in a superconductor [7]. In the case of cold atomic ensembles, a larger than unity phase-space density in the microscopic variables, position and momentum normalized by the appropriate power of $\hbar$, marks the classical to quantum degenerate transition. Macroscopically, high spatial density and low temperature maximize the phase-space density of the thermal ensemble. Since cold atomic gases are extremely dilute compared to air in practice, we find the quantum degenerate transition at ultra low temperatures.

The electronic level structure in our quantum degenerate gases (one of the internal atomic degrees of freedom) has a characteristic energy scale of a few eV. Under typical experimental conditions, the density of a BEC is 10^{14} atoms/cm^3. That is 10^5 to 10^8 times more dilute than the density of air under standard atmospheric conditions. Typically, these dilute gases are confined to regions in space of a few $1000\,\mu$m^3, and in the context of this thesis resemble white-blood cells in size, although not in shape. Their temperature can be of the order of a few tens of nK, which represents a part in 10^8 of the coldest naturally ocurring temperature ever

recorded of the cosmic microwave background [8], making them remarkably cold objects. Nevertheless, their phase-space density exceeds our everyday experience by ~ 10 orders of magnitude, starkly separating our lives from quantum degeneracy. For most of their ephemeral existence, these gases are suspended against gravity in an ultra high vacuum (UHV) environment, isolated from everything but for the presence of electromagnetic fields and our scientific curiosity.

We use a robust apparatus to produce BECs in our laboratory, usually referred to as the RbChip laboratory, allowing for relatively simple transitions in our setup when investigating different physics, and giving us new technical challenges every day. Nevertheless, this apparatus has some drawbacks, and we address them through a cycle of iterative design with a new, future apparatus. In Chapter 2, I describe the production of BECs in RbChip, touching on a few aspects of the current and future apparatus. In addition, I include a record of several procedural scripts representing the standardized hardware instructions. The description in Chapter 2 complements those found in previous dissertations emanating from our laboratory, giving a new perspective on the experiment and paving the way for upcoming experiments in the new apparatus.

I review in Chapter 3 a quantum simulation of Abelian and non-Abelian gauge fields with nontrivial topologies in single-particle state manifolds. This is an example of the BEC based quantum simulation possible in RbChip. Topologically

nontrivial physics is not exclusive to quantum systems, although topological classifications find extensive applications in condensed matter physics and high-energy physics. There, gauge field theories host topological observables quantifying the global properties of a system. We measure these observables in our simplified quantum simulation of the associated gauge fields, providing valuable physical insight for future experiments and applications.

A quantum simulator has two fronts; measurement and control. Chapter 3 describes our excellent control over the internal degrees of freedom of our BEC. Chapter 4 introduces our microscopy toolbox used as the basis for most of our measurements. Since high quality measurement is rooted in calibration and optimized signal processing, I give a technical overview of the different methods that we use every day. Eventually, the measurement quality directly impacts the extracted information, potentially limiting or broadening our physical understanding.

One of the unfulfilled milestones in quantum simulation is to reliably prepare, control, and probe arbitrarily entangled many-body quantum states. These highly-correlated states are a cornerstone in various fields of physics, from high-energy, condensed matter, nuclear, and plasma physics, regardless of the fundamental nature of the interaction (strong nuclear, weak nuclear, or electromagnetic). Examples abound showing how neither approximate theories nor powerful classical computers can reveal the intricate properties of these emergent forms of matter. A

path forward is studying strongly-correlated atomic systems through a controlled addition of strong effective interactions.

Various strategies exist to make cold and ultracold atoms interact strongly. The most notable example is using Feshbach resonances [9], where an external magnetic field is used to effectively tune the strength of interatomic interactions. Similarly, isolating a set of one or more modes of the electromagnetic field around an atomic ensemble can mediate long-range interactions between the atoms [10]. Some rare-earth atomic species have ground states with large magnetic moments giving strong dipole interactions [11]. Alternatively, engineering single-particle dispersion relations modifies interactions in trapped degenerate gases [12] and can significantly alter their impact. For instance, a deep periodic (lattice) potential can drive contact interacting Bose gases into a strongly correlated Mott insulating phase [13]. Promoting atoms to higher excited states gives a larger polarizability through which they can interact at long distances [14]. Finally, external potentials confine systems into effectively lower dimensions, where the modified density of states affects the role of interactions [15]. In Chapter 5, I introduce three models for one-dimensional Bose gases, highlighting the role of interactions.

We probe in Chapter 6 the strongly interacting regime by experimentally isolating dilute, individual one-dimensional Bose gases. These systems represent a first step towards the strongly correlated regime as their interactions become

more relevant when the linear density decreases. We probe these extremely dilute gases with the quantitative bright-field microscopy introduced in Chapter 4. In a first experiment, we recover their thermodynamic equations of state to identify the presence of strong interactions using the models from Chapter 5.

Finally, in Chapter 7 we expand the imaging toolbox for quantum gas based quantum simulation by importing the well-established methods of digital holographic microscopy. This form of microscopy translates a fraction of the hardware complexity to software, enhancing the signal to noise ratio with robust algorithmic tools. In a first experiment, we demonstrate the simultaneous absorptive and dispersive imaging of cold atom clouds. Then, we probe novel spatial field correlation functions revealing the aberrations of our microscope. Remarkably, we access optical transfer functions without sampling a localized point source in real space, but rather use point-correlations from atomic shot-noise. Inverting the transfer functions relieves our absorption images of most of the imperfections caused by aberrations. I end with a list of ideas for future experiments enabled by this powerful tool.

I present in Appendix A a simple transistor bank circuit for driving our high-current electromagnets in the future apparatus. The improvement with respect to the original design is a doubling of the density of transistor elements to reduce the power dissipation. Then, in Appendix B, I provide detailed documentation on the

computer-aided design (CAD) files comprising the design of the future apparatus. Departing from the main issues in our apparatus, I include all the proposed design features and extensive detail on the CAD subassemblies. In Appendix C, I describe the numerical implementation to solve the Yang–Yang thermodynamics system of coupled integral equations. I include a copy of the working code as a reference. Finally, in Appendix D, I summarize the design parameters of our homemade compound objective. We base our lens design the popular five-element design by Wolfgang Alt [16], and include a description of the ring spacers to achieve optimized performance.

This dissertation is a comprehensive compilation of methods for *in-situ* microscopy of elongated quantum gases, including calibrations and measurement techniques. Figure 1.1 shows the quantum simulator our laboratory at the end of the summer of 2019. This apparatus continues to thrive.
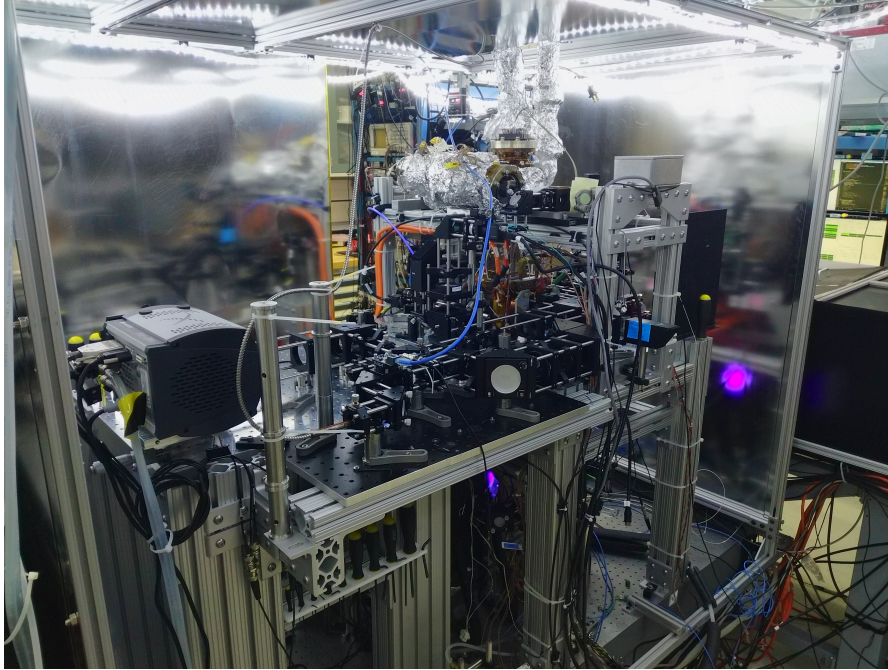
Figure 1.1: RbChip quantum simulator in the summer of 2019. The surrounding μ-metal enclosure is to shield atoms from external magnetic fields. Broadband UV/VIS light used to desorb ^{87}Rb reflects off the enclosure near bottom of the apparatus. The coordinate system indicates the frame of reference of our laboratory.

Chapter 2: Quantum degenerate gases

This chapter describes our scientific apparatus, from here on referred to as "RbChip", the experimental sequence used to produce ultracold degenerate Bose gases, and design features for an upgraded revision of the apparatus. RbChip is described in [17] and used throughout the experiments in this dissertation. A reliable and consistent daily operation motivated a "bugfix" release (to use a software metaphor) which we call "future apparatus", in which we copy the core RbChip design and revisit minor flaws. The future apparatus is being deployed at UMD during the writing of this thesis, and I briefly mention some design upgrades. Along the different stages of the sequence, we include Python scripts illustrating the procedures for the Labscript suite [18], our choice of versatile, open-source control software. Altogether, these elements provide enough information for the reader to understand how we experimentally produce quantum degenerate Bose gases.

This chapter is organized as follows. In Section 2.1 we briefly review the relevant electronic level structure of ^{87}Rb, how we introduce ^{87}Rb it into our vacuum system, and the methods that follow to cool it down using Doppler and sub-Doppler laser cooling. In Section 2.2, we introduce the optimized magnetic transport, and

describe the stages of radiofrequency (RF) evaporation, decompression, and evaporation in an optical dipole trap stages that precede the transition to BEC.

2.1 Making a cold atomic gas

The atomic species in this thesis is ^{87}Rb. This bosonic alkali is probably the most popular atom in cold and ultracold gas experiments. The combination of a single valence electron (shared by all alkali and singly ionized alkali-earth atoms), and addressable electronic transitions (with commercially available diode lasers), make it a friendly atom for experiments. Previous theses from the RbChip [17,19], RbK [20], and RbLi [21] teams, as well as from beyond the group [22], cover the details of the atomic structure of ^{87}Rb in fantastic detail. We leverage their content and adopt their common notation for this dissertation.

We show in Figure 2.1 the ground and first excited states of ^{87}Rb, along with the most relevant energy perturbations in leading order of magnitude in the presence of static magnetic fields of up to $20\,$G. Within the electronic ground $|5^2\mathrm{S}_{1/2}\rangle$ state of ^{87}Rb, the energy splittings arising from these perturbations obey $\hbar\Delta_F \gg \hbar\Delta_{HF} \gg \epsilon^{(1)} \geq \epsilon^{(2)}$, where $\hbar\Delta_F$ is the fine structure splitting, $\hbar\Delta_{HF}$ is the hyperfine splitting, and $\epsilon^{(1)}$ and $\epsilon^{(2)}$ represent the linear and quadratic contributions of the Zeeman shift respectively. The quadratic Zeeman shift becomes more obvious in the $|5^2\mathrm{P}_{3/2}\,F=1, m_F=-1\rangle$ state in Figure 2.1 in the range of $|\mathbf{B}|= 10\,$G field.
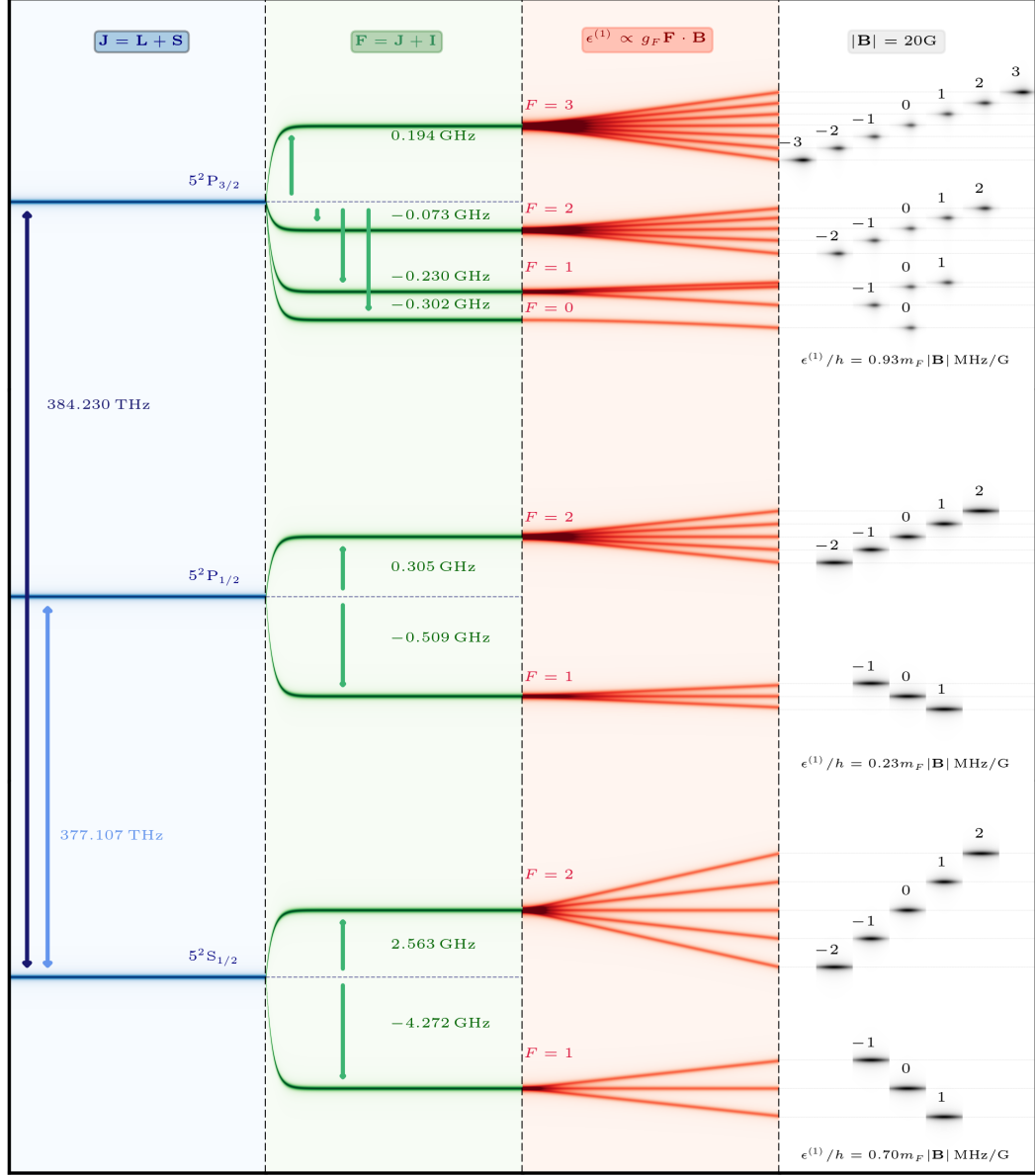
Figure 2.1: ^{87}Rb D-line. Schematic level structure (not to scale) of the D_1 and D_2 lines in ^{87}Rb. Exact numerical diagonalization in order of the leading perturbations yields the energy levels above. Starting after the fine structure (i.e. spin-orbit coupling) (blue), the hyperfine (green) and Zeeman split (red) manifolds appear on the right. The latter covers the range of experimentally attainable static magnetic fields $|\mathbf{B}| = [0, 20]$ G. Finally, the last panel to the right (gray) shows the magnetic m_F sublevel manifolds under a static magnetic field of $|\mathbf{B}| = 20$ G. Annotated frequency splitting factors indicate the magnitude of the perturbed energy scales.

2.1.1   Rb source

The source of ^{87}Rb in RbChip is a 1 g breakseal ampoule inside a mini ($\oslash = 1.33$ in) conflat-flange (CFF) short bellows placed under UHV. Near room temperature, and well bellow its melting point, the vapor pressure of metallic ^{87}Rb is high enough to diffuse into the nearby UHV regions, including a magneto-optical trap (MOT) glass cell. There, it reaches an equilibrium pressure determined by the conductance of the UHV manifold, active pumping elements, and alkali source temperature. We use a thermo-electric cooler (TEC) to maintain a constant temperature at the source. The TEC is in contact with the mini-CFF bellows through an aluminum collar, and sits on top of a $\oslash = 1.0$ in aluminum pedestal. Chilled ($T \sim 15\,^{\circ}$C) water runs through a straight $\oslash = 3/8$ in copper tube across the pedestal. The source subassembly is covered by a thermally insulating blanket inside of which we flow dry, gaseous N_2 to mitigate water vapor condensation. Figure 2.2 shows a schematic of the source in RbChip.

The ^{87}Rb source TEC is prone to failure. Figure 2.3 depicts a damaged source TEC still mounted on the pedestal (no bellows or collar shown) that failed when condensed water vapor short-circuited the TEC connections. We identify two risks leading to such potential failure. First is the risk of high humidity, which when combined with a large dewpoint can cause water vapor to condense near the TEC or thermocouple electric contacts. This is already mitigated by flowing the dry
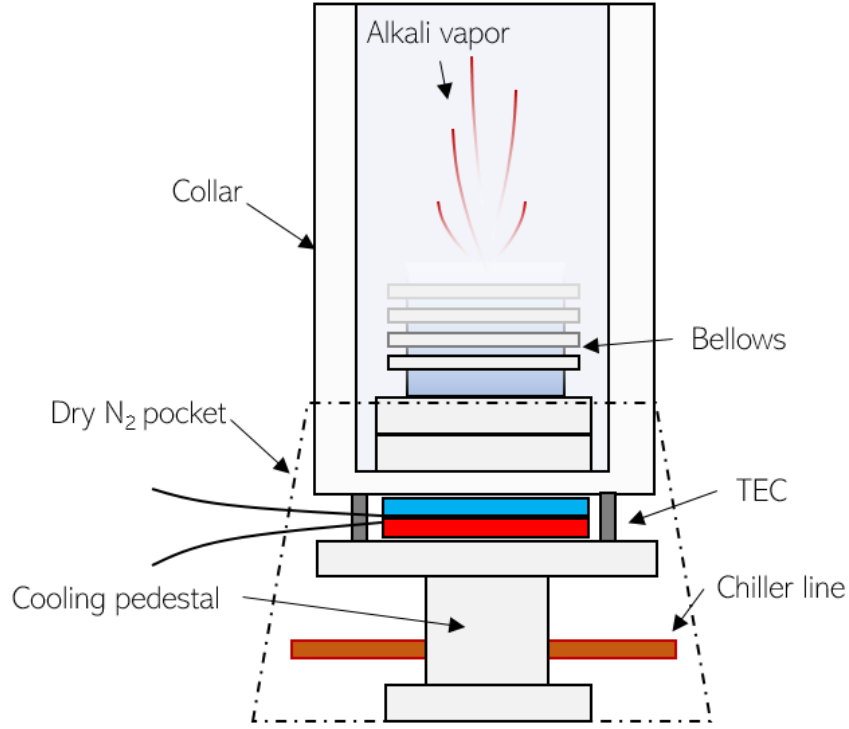
Figure 2.2: RbChip source. The TEC is mounted between a cooling pedestal and a collar surrounding the mini-CFF with the ^{87}Rb ampoule. The collar provides thermal contact to the TEC. The TEC heat is drained by the pedestal running cooling water. A dry air (N_2) pocket prevents water condensation around the TEC.

gaseous N_2. Second is the risk of poor thermal contact between the TEC, bellows, and water cooled pedestal depleting the TEC from a heat drain. The alkali source in the future apparatus has improved thermal conductance through an upgraded pedestal design [21]. To quantify the temperature stability of the ^{87}Rb source over a timescale comparable with the duration of a simple experiment, we command the TEC to $T = -0.500\,^\circ$C, and log the temperature for ~ 30 min. Figure 2.3 shows the histogram, with an approximate standard deviation of $\sigma_T \approx 0.03\,^\circ$C.

A reliably cold alkali source providing low background ^{87}Rb pressure is essen-
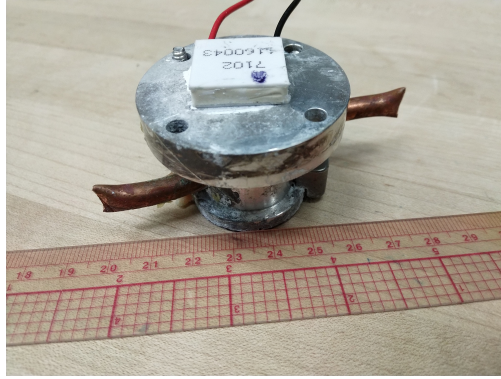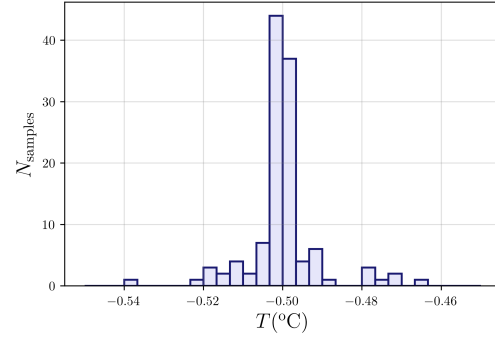
Figure 2.3: Damaged TEC and temperature log. (a) Damaged TEC unit. (b) Histogram of the logged temperature for 30 min. every 30 s under typical cycling experiment conditions (with the chilled water running and the regular heat load of the apparatus). The standard deviation of the histogram represents the temperature stability of the ^{87}Rb source.

tial for consistent experimental cycles. We may suddenly increase the equilibrium pressure inside the MOT glass cell by shining broadband ultraviolet (UV/VIS) light from an LED on the alkali atoms bound to the glass surface. This process is called light induced atomic desorption (LIAD), and was first investigated in experiments with paraffin coated vapor cells [23]. We use several ^{87}Rb "UV-soaking" cycles to make our experimental cycles more consistent. For instance, shining ~ 10 min of UV light at the beginning of the day gives enough ^{87}Rb vapor for a normal daily operation. Then, depending on the duration of a single experimental cycle, we may add a few additional seconds of UV light between consecutive repetitions. We sometimes soak the MOT glass cell with ^{87}Rb by commanding a controlled temperature rise of a couple of degrees, holding it constant over for up to a couple of days (e.g. the weekend), and then lowering it slowly.

2.1.2 Doppler cooling

At the start of an experiment, we load a MOT with $N = 5 \times 10^8$ atoms in $t \gtrsim 2.5\,\mathrm{s}$. We say we load a UV-MOT when we simultaneously shine $\approx 100\,\mathrm{mW}$ of broadband UV light as we load a MOT. A UV-MOT loads faster and ends up with slightly more atoms. To compare the MOT and UV-MOT, we collect the scattered $\lambda = 780\,\mathrm{nm}$ fluorescence and look at the loading traces of MOT and UV-MOT as in Figure 2.4. Furthermore, we investigate the effect of the daily 10 min UV-soaking described in the preceding section. For this, we load a MOT and UV-MOT and collect the scattered fluorescence (Figure 2.4) first in the absence of any preliminary UV-soaking, and then after a preliminary 10 min stage of UV-soaking. We find that the $1/e$ characteristic loading times from exponential rising fits (solid lines in Figure 2.4) to the fluorescence traces of a MOT and UV-MOT change from $\tau_{\mathrm{UV-MOT}} = 1.20(1)\,\mathrm{s}$, and $\tau_{\mathrm{MOT}} = 0.17(1)\,\mathrm{s}$ to $\tau_{\mathrm{UV-MOT}} = 2.01(1)\,\mathrm{s}$, and $\tau_{\mathrm{MOT}} = 0.50(1)\,\mathrm{s}$, depleting the loading efficiency, and final atom number as the background gas pressure changes. The UV-soaking impacts the background $^{87}\mathrm{Rb}$ pressure, and along with it, the associated collisional loss and final equilibrium atom number in a MOT. While further investigation is required to validate this picture, it is consistent with the observed changes in final atom number and loading rates in Figure 2.4.

Loading a UV-MOT is the first stage in our experimental sequence. Below is
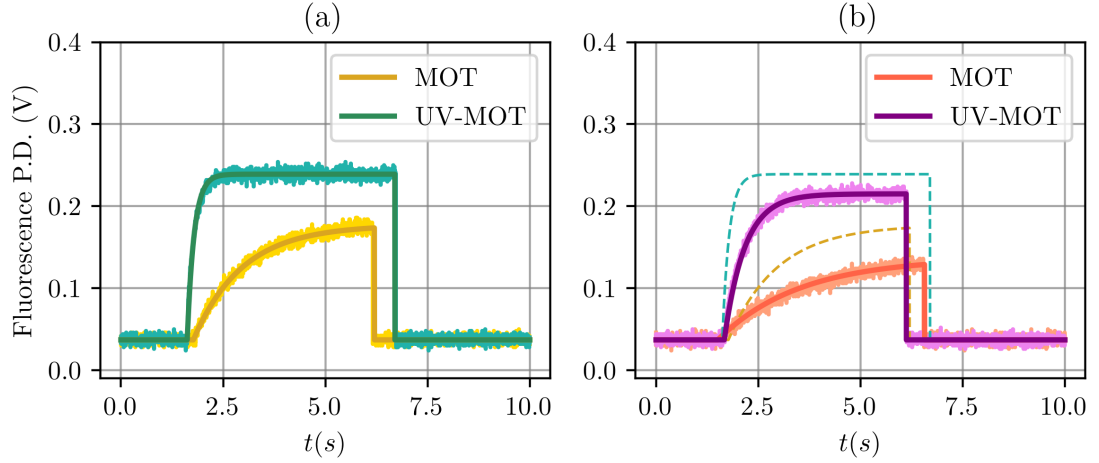
Figure 2.4: MOT and UV-MOT loading. Fluorescence photo-diode (P.D.) voltage traces during the loading of a MOT and UV-MOT for (a) no previous UV treatment and (b) after 10 min of UV-soaking the glass cell. Fits to the loading traces (solid lines) quantify the changes in loading rate and final atom number.

a set of scripted hardware instructions comprising "stage methods" for our Python-based control software to complement the description of our experimental sequence. Scripted instructions like the ones below qualitatively describe the minimum set of hardware instructions that implement various stages, and do not comprise working code.

```python
def prep(t):
    # Shine light
    UV_LED_digital_switch.go_high(t)
    for intensity, beam in zip(MOT_intensities, [cooling, repump]):
        set_beam(t, beam, intensity)

    # Set magnetic field coil currents
    for j, bias in enumerate([x_bias, y_bias, z_bias]):
        bias.constant(t, MOT_bias_field[j], units='A')
    MOT_quadrupole.constant(t, MOT_quad_current, units='A')

    # Frequency lock offsets
    MOT_lock.setfreq(t, zero_field_detuning, units='MHz')
    MOT_lock.setamp(t, amp=0, units='dBm')
    return 30*ms

def MOT(t):
    """ Load a UV-MOT; essentially wait for MOT_load_time """
    # Sample MOT fluorescence during MOT loading
    MOT_scope_trigger.go_high(t - 100 * ms)
```

16

```
    # Laser cooling
    open_shutters(t, [cooling, repump])
    return MOT_load_time
```

A first `prep` (preparation) stage sets all the laser intensities, frequency off-sets, and magnetic fields ready for the following `MOT` stage, where we cool atoms by resonantly scattering $\lambda_{D_2} = 780.24\,\mathrm{nm}$ photons off the closed cyclic transition (i.e. cooling transition [19]) going from $|5^2S_{1/2}, F = 2\rangle$ to $|5^2P_{3/2}, F = 3\rangle$ with $\approx 16\,\mathrm{MHz}$ of detuning from the zero-field resonance, and a quadrupole field strength of $\approx 10\,\mathrm{G/cm}$. In the presence of a quadrupole magnetic field, atoms localize near the field minimum, where three pairs of well balanced resonant laser beams intersect, effectively cooling atoms in three-dimensions (3D). An additional repump beam restores atoms that off-resonantly fall into $|5^2S_{1/2}, F = 1\rangle$, where they are no longer subject to laser cooling and trapping. The ultimate temperature achievable by ideal Doppler cooling (plane waves incident on two-level atoms) is the Doppler temperature

$$T_{\mathrm{D}} = \frac{\hbar\Gamma}{2k_B},$$

where $\hbar$ is the reduced Planck's constant, $\Gamma/2\pi = 6.067\,\mathrm{MHz}$ is the linewidth of the D_2 line [24], k_B is Boltzmann's constant, and which for ^{87}Rb is $T_{\mathrm{D}} \approx 146\,\mu\mathrm{K}$. We most likely never reach under $1\,\mathrm{mK}$ after the `MOT` stage due to several "real-life" limiting factors. First is the presence of multiple levels in the electronic level structure of ^{87}Rb (Figure 2.1), followed by suboptimal scattering rates from the intensity, and frequency detuning of cooling and repump light beams. Poorly balanced cooling beams typically result in warmer MOTs, and the final size and shape

of the cloud attenuate the cooling lasers as they propagate inside the MOT volume, further adding to the cooling inhomogeneities from imperfect polarizations and background stray magnetic fields. After reaching equilibrium at the end of the `MOT` stage, we turn off the cooling and repump light simultaneously. The atomic ensemble then ends up randomly distributed in the $|5^2\mathrm{S}_{1/2}, F = 1, 2\rangle$ ground hyperfine states, with an estimated normalized peak phase-space density (at the center of the cloud) of $\rho = 1 \times 10^{-6}$ [25].

The future apparatus includes various strategically placed holes with the goal of pre-aligning the MOT beams with the coil axis as it is assembled. Rectangular slots hold sliding golden mirrors that reflect beams along two of the three arms of the MOT (for more details see Appendix B). Finally, an imaging path along the main transport axis provides novel optical access for MOT diagnostics.

2.1.3 Sub-Doppler cooling

As noted, our atoms are not two-level atoms, allowing us to use polarization gradient cooling (PGC), a form of sub-Doppler cooling [26]. In preparation for PGC, we raise the quadrupole field to spatially compress the MOT, temporarily reducing the volume of the cloud by a factor of ~ 10 making it less susceptible to stray magnetic field gradients. We raise the quadrupole strength slowly to avoid heating the atoms during the execution of the `compressed_MOT` stage script below.

```python
def compressed_MOT(t):
    """Load compressed MOT in preparation for molasses."""
```

```python
    MOT_quadrupole.customramp(t, compressed_MOT_duration, CubicRamp,
        MOT_quad_current, compressed_MOT_quad_current,
        initial_deriv=0, final_deriv=compressed_MOT_quad_current_final_deriv,
        samplerate=1/compressed_MOT_step, units='A')
    for j, bias in enumerate([x_bias, y_bias, z_bias]):
        bias.customramp(t, compressed_MOT_duration, CubicRamp,
            MOT_bias_field[j], compressed_MOT_bias_field[j],
            samplerate=1/compressed_MOT_step, units='A')

    # Initial frequency ramp for optical molasses
    MOT_lock.frequency.customramp(t, compressed_MOT_duration, CubicRamp,
        compressed_MOT_frequency, molasses_start_frequency,
        samplerate=1/compressed_MOT_step, units='MHz')
    return compressed_MOT_duration
```

We implement PGC by suddenly zeroing the magnetic field to within a few $10\,\mathrm{mG}$ in $\sim 1\,\mathrm{ms}$, while simultaneously scanning the frequency detuning of the cooling laser from an initial $28.8\,\mathrm{MHz}$ to $192\,\mathrm{MHz}$ for $14.5\,\mathrm{ms}$. This cools the atoms down to a measured $575(75)\,\mu\mathrm{K}$, where it remains in excess of the Doppler temperature. We measure the temperature by allowing the cloud to freely expand and track its size after some time. The uncertainty in this thermometry comes from an uncertainty in the magnification due to reduced field of view, an effect which will be easier to mitigate in the future apparatus. The `optical_molasses` stage script below performs PGC.

```python
def optical_molasses(t):
    # Drop quadrupole and offset bias field currents
    MOT_quadrupole.constant(t, MOT_quad_current, units='A')
    for j, bias in enumerate([x_bias, y_bias, z_bias]):
        bias.constant(t, molasses_bias_field[j], units='A')

    # Shine optical molasses, scanning frequency detuning
    MOT_repump.constant(t, molasses_repump_intensity)
    MOT_lock.frequency.customramp(t, molasses_time, ExpRamp,
        molasses_start_frequency, molasses_end_frequency,
        molasses_detuning_ramp_width, samplerate=1/molasses_step,
        units='MHz')
    return molasses_time
```

A fundamental temperature "limit" is the recoil temperature given by

$$T_r = \frac{\hbar^2 k_r^2}{m k_B},$$

where $\hbar k_r = \hbar/\lambda_{\mathrm{D_2}}$ is the recoil momentum associated with a single photon of reduced wavelength ($\lambda = \lambda/2\pi$), and which for ^{87}Rb is $362\,\mathrm{nK}$. State of the art laser cooling experiments are able to reach a few T_r with highly optimized Doppler and sub-Doppler techniques [27]. Here, we are substantially hotter than most temperatures achieved by sub-Doppler cooling, suggesting that it might be possible to improve this by using different parameters than those used in our optimized stage. In addition to the usual polarization and stray gradient issues, some of our measurements suggest that we are limited by time as the cloud of atoms diffuse freely during this stage. Nevertheless, we find that achieving a higher spatial density seems more benefitial for the upcoming evaporative cooling where the cooling rates are dependent on the temperature and peak spatial density. It is not obvious that lower MOT temperatures are globally benefitial, and while the normalized phase-space density needs to increase, the optimal trajectory is hard to predict. The future apparatus is designed to be a better platform for optimizing and better diagnosing the PGC stage.

The current apparatus is vertically oriented, with gravity pointing along $\mathbf{e}_{\mathrm{y}}$, and the principal quantization axis along $\mathbf{e}_{\mathrm{z}}$, aligned to the axis of the quadruopole

coil pair (see Figure 1.1 for the reference coordinate system). Atoms are in either

of the two $|5^2S_{1/2}, F = 1\rangle$ and $|5^2S_{1/2}, F = 2\rangle$ states after the `optical_molasses`

stage. In order to prepare for the next stage of magnetic transport, we optically

pump atoms into the low-field seeking state $|5^2S_{1/2}, F = 2, m_F = 2\rangle$. We do this

by briefly pulsing a circularly polarized optical pumping beam propagating along

$-\mathbf{e}_x$ for $\tau = 605\,\mu s$ in the presence of a negative bias magnetic field along $\mathbf{e}_z$ during

the scripted `optical_pumping` stage.

```python
def optical_pump_2_2(t):
    """ Pulse optical pumping into 2,2 """
    MOT_lock.frequency.constant(t - 100*ms, optical_pumping_frequency,
        units='MHz')

    # Setup bias field (mostly along z)
    for j, bias in enumerate([x_bias, y_bias, z_bias]):
        bias.constant(t, optical_pumping_bias_field[j], units='A')

    pulse_beam(t, optical_pumping_beam,
        intensity=optical_pumping_intensity, pulse_time=optical_pumping_time)
    pulse_beam(t, MOT_repump,
        intensity=optical_pumping_repump_intensity,
        pulse_time=optical_pumping_time)
    return optical_pumping_time
```

Following the `optical_pumping` stage, we turn the quadrupole field back on to

trap the freely falling $|F = 2\rangle$ cloud, ramping the current up until it levitates the

$|F = 2, m_F = 2\rangle$ atoms against gravity. The vector field

$$\mathbf{B}(x, y, z) = Q \left[x\mathbf{e}_x + y\mathbf{e}_y - \left(2z + \frac{B_0}{Q} \right) \mathbf{e}_z \right] \tag{2.1}$$

formed by a quadrupole of strength $2Q$ centered at the origin and a nonzero bias

field B_0 along $\mathbf{e}_z$ provides hyperbolic confining potentials

$$U_q(x, y, z) = \mu_B g_F m_F Q \sqrt{x^2 + y^2 + \left(\frac{B_0}{Q} - 2z \right)^2}, \tag{2.2}$$

where the low-field seeking $m_F > 0$ states get trapped (if the atoms were in F=1, $m_F < 0$ will be trapped). Tipping the bias field along an arbitrary direction so that it points other than a principal axis produces conical section potentials (typically at this point we don't add shifting bias fields). The magnetic trapping stage script is below.

```python
def magnetic_trap(t):
    """ With all light off, load 2,2 atoms into a magnetic trap """
    # Ramp magnetic trap
    MOT_quadrupole.customramp(t, magnetic_trap_MOT_time, HalfGaussRamp,
        magnetic_trap_MOT_quad_current, initial_transport_current,
        magnetic_trap_MOT_ramp_width, samplerate=1 / magnetic_transport_step,
        units='A')

    for j, bias in enumerate([x_bias, y_bias, z_bias]):
        bias.customramp(t, magnetic_trap_MOT_time, HalfGaussRamp,
        magnetic_trap_MOT_bias_field[j], molasses_bias_field[j],
        magnetic_trap_MOT_ramp_width,samplerate=1/magnetic_trap_MOT_step,
        units='A')
    return magnetic_trap_MOT_time
```

The final quadrupole field ramp not only raises the field strength, but simultaneously ramps the bias field strength, shifting the center of the magnetic trap. There, the magnetic trap smoothly intersects the trajectory of the falling cloud without depleting its number by much or heating the cloud. We find that if we don't ramp the bias field then the magnetic transport doesn't work so well. We suspect one reason for this is the presence of magnetized objects around the atoms, and we believe that the bias field cancels such stray fields. The final quadrupole strength is made strong to provide an effectively deeper potential during magnetic transport. This stage marks the end of laser cooling in preparation for BEC in RbChip.

2.2 Making an ultracold atomic gas

Laser cooling alone is insufficient to reach quantum degeneracy, so we turn to forced evaporative cooling. Evaporative cooling combines a selective loss in atoms from the high energy tail of the thermal distribution with a collision driven thermalization which repopulates the high energy tail which results in an overall cooling of the gas. The estimated thermalization rates in a magnetic trap of $10 - 100\,\text{ms}$ (implied by collisional rates, which depend on temperature, and spatial density) are low enough that forced evaporation in the MOT cell region is impractical. In other words, the nonselective loss from the background gas pressure overwhelms the selective loss of forced evaporation. For instance, we may compare the vacuum-
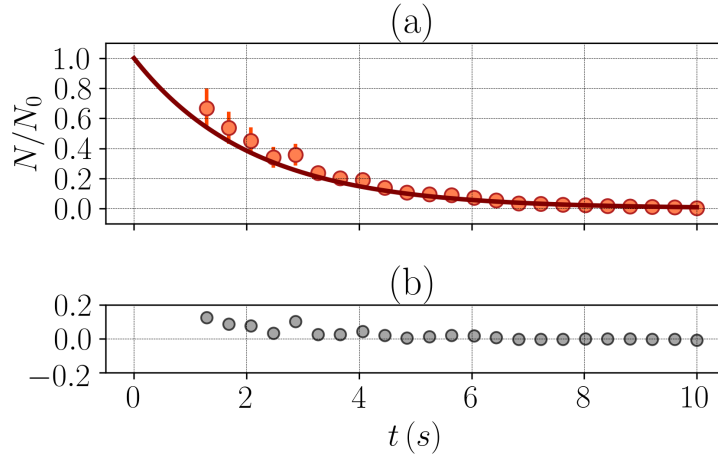
Figure 2.5: Lifetime of a magnetically trapped MOT. (a) Normalized atom number vs hold time (circles) in a magnetic trap measured right after the `optical_molasses` stage. A weighted least-squares fit accounts for lower uncertainty measurements in low atom number. Fitting to the simple exponential $N = N_0 \exp\left(-t/\tau\right)$ (solid line) gives a $1/e$ lifetime of $\tau = 2.14(22)\,\text{s}$. (b) Fit residuals. Larger atom number uncertainties near $t = 0$ come from counting errors in saturated cloud images.

limited lifetime of a magnetically trapped cloud in the MOT glass cell, measured to be 2.14(22) s in Figure 2.5, with the $t \geq 10$ s duration of evaporative cooling. The largely different timescales show just how unfeasible it is to evaporate atoms directly in the MOT cell. Both the current and future apparatus are designed to magnetically transport the laser cooled atoms to a second (science) glass cell with a desirable ~ 100 times lower pressure (and proportionally larger vacuum-limited trap lifetime). In the current apparatus, the lifetime is well in excess of 30 s, implying a modest UHV improvement factor, but giving enough time for evaporative cooling. Transport is the price to pay for using a LIAD ^{87}Rb source in our apparatus.

We keep the LIAD source and dual glass cell UHV system in the future apparatus. The glass cells, atomic source(s), and transport coils heavily constrain the UHV manifold. The future apparatus UHV system is indirectly pumped by two 25 L/s ion pumps through two $\oslash = 3/8$ in differential pumping tubes, in contrast with the single differential pumping tube and two ion pumps in RbChip. In addition, the glass cells are single ended with only one mini-CFF. This allows a clear line of sight along the magnetic transport axis. We provide further documentation for the future apparatus UHV manifold in Appendix B.

2.2.1 Magnetic transport

The thesis of Abigail Perry [17] describes our implementation of magnetic transport originally demonstrated in [28]. The transport sequence displaces the minimum of the quadrupole field gradient vertically along the transport axis, moving the cloud along the way. While a net displacement can be achieved by using two adjacent coil pairs, three adjacent coil pairs have the advantage of maintaining a nominal cloud aspect ratio. As shown in Figure 2.6, keeping the field gradient aspect ratio of three-coil pairs $\beta_3 = \partial_z B_z / \partial_y B_y$ constant locks the aspect-ratio of a cloud during transport. Only at the beginning and the end, where the cloud is accelerated/decelerated, does the aspect ratio change suddenly. During transport, we energize no more than three pairs of quadrupole coils at any given time.

Our apparatus has a "push" coil placed below the MOT to help launch the cloud into transport. The push coil is a single square-shaped coil aligned with the transport axis, but never used it in our sequence, and since removed in the future apparatus design. To retain the capability of assisting the beginning of transport with a displacement, we replace the push coil with an additional bias coil pair oriented along the principal quantization axis. Additionally, we design the a smaller transport coil pair spacing and optimize the coil shapes to cut down on heat dissipation and free optical access. Power dissipation causes thermally driven magnetic field drifts and hysteresis. To drive the transport currents with optimized power

dissipation, we put toghether an improved set of power transistor banks, described in Appendix A.

We use the `magnetic_transport` stage below to begin transport of magnetically trapped clouds.

```python
def magnetic_transport(t, **kwargs):
    """ Magnetic transport of 2,2 cloud """
    transport_oscilloscope_trigger.trigger(t, duration=0.1)

    # Compute switchover times and supply selection logic
    t_switch, flags = transport.t_switchover

    # Enable supply to feed coil pairs at switchover times
    for switch_time, flag in zip(t_switch[:7], flags[:7]):
        agilent_logic(t + switch_time, mode='transport', line=flag)

    # Switch bias field control to top servo near the end of transport
    kepco_logic(t + t_switch[7], enable=True, side='top')
    for j, bias in enumerate([x_bias, y_bias, z_bias]):
        bias.customramp(
            t + t_switch[7],
            t_switch[8] - t_switch[7],
            LineRamp,
            molasses_bias_field[j],
            transport_shim_field[j],
            samplerate=1/magnetic_transport_step,
            units='A',
        )

    # Carry on with final transport and deceleration
    for switch_time, flag in zip(t_switch[8:], flags[8:]):
        agilent_logic(t + switch_time, mode='transport', line=flag)

    # Smooth vertical decompression and shift to end
    y_bias.customramp(
        t + t_switch[9],
        transport_time - t_switch[9],
        LineRamp,
        transport_shim_bias[1],
        top_shim_bias[1],
        samplerate=1/magnetic_transport_step,
        units='A',
    )
    for j ,transport_current in enumerate([transport_current_1,
    transport_current_2, transport_current_3, transport_current_4]):
        transport_current.customramp(
            t,
            transport_time,
            transport.currents_for_channel,
            j + 1,
            samplerate=1/magnetic_transport_step,
            units='A',
        )
    return transport_time
```
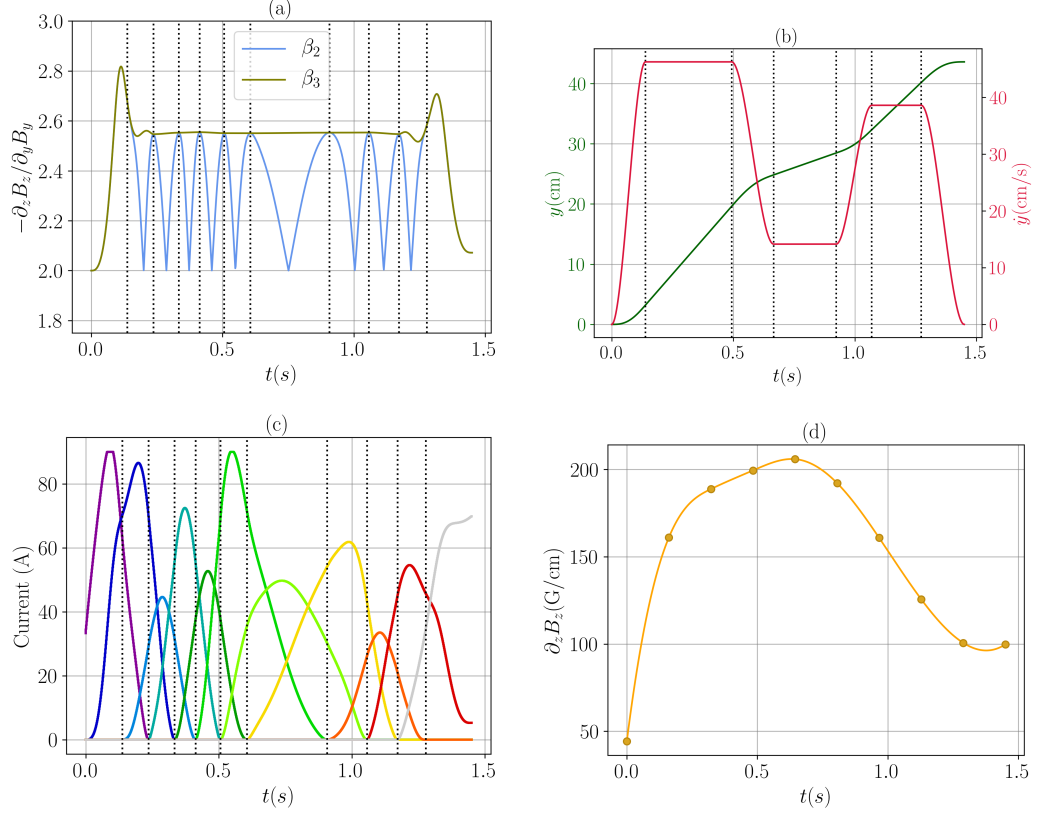
Figure 2.6: Optimized magnetic transport. (a) Calculated aspect ratio from two (β_2), and three (β_3) coil pairs. (b) Transport current traces per coil pair. (c) Vertical position and speed of the cloud. (d) Magnetic field z-gradient along $\mathbf{e}_z$.

A genetic optimization algorithm [17] found a local optimum in the ~ 40-dimensional parameter space spanned by the transport stage in the early days of RbChip. More recently, we implement a Gaussian process algorithm first used in [29] through the open-source package MLOOP, and maximize the final atom number at the end of transport, and after an inefficient stage of RF evaporation (see Section 2.2.2) as a proxy for phase space density. We find an improvement in the total transport time going from 2.2 s to 1.7 s, a reduction of $\approx 22\%$ with respect to the original value. While an improvement of 22% seems relatively low, it affects the long term stability of the apparatus and gives higher experimental reproducibility.

Figure 2.6 summarizes various features of the optimized transport, where we calculate the two and three-coil aspect ratio, the quadrupole coil currents, the position and speed of the cloud, and the quadrupole field gradient along $\mathbf{e}_z$ as a function of time. We are unable to reconstruct the transport trajectory in our apparatus as we lack imaging along the transport axis, a "bug" that will no longer be present in the future apparatus.

2.2.2 RF evaporation

We dress the $|F = 2, m_F = 2\rangle$ cloud with a $\sim 200\,\mathrm{mW}$ radiofrequency (RF) field produced by a single loop antenna located a few centimeters below the atoms to begin forced evaporation in the strong ($100\,\mathrm{G/cm}$ magnetic quadrupole trap. The RF field opens a fixed energy gap in the dressed state energy spectrum. We then chirp down the RF tone from $12\,\mathrm{MHz}$ to $3.5\,\mathrm{MHz}$ at a constant rate in an attempt to remain adiabatic with respect to the energy gap while addressing atoms with enough kinetic energy that approach resonance. As the changing RF tone addresses different sectors of the magnetically trapped cloud, adiabatic spin transitions flip the magnetically trapped $|m_F > 0\rangle$ atoms into antitrapped $|m_F \leq 0\rangle$ states. From the geometry of the magnetic trap, the ejected atoms belong to the high energy tail of the thermal distribution. After a $\sim 10 - 100\,\mathrm{ms}$ period of collisional thermalization, the temperature of the cloud drops. Nonadiabatic spin transitions near the quadrupole center limit RF evaporation at sufficiently low temperatures. These nonadiabatic Majorana losses remove atoms on the low

energy of the thermal distribution, causing effective heating [30]. This impedes the RF evaporation to continue cooling our gases. Below is the script describing RF evaporation in RbChip.

```python
def rf_evaporate(t, **kwargs):
    """ RF evaporation out of magnetic quadrupole """
    # Broadcast chirped RF tone
    RF_mixer.constant(t, rf_evaporation_mixer_voltage)
    RF_switch.go_high(t)
    RF_evap.frequency.ramp(t, rf_evaporation_time,
        rf_evaporation_initial_frequency,
        rf_evaporation_final_frequency,
        samplerate=1/rf_evaporation_step, units='MHz')
    return rf_evaporation_time
```

We seek to improve the RF evaporation in the future apparatus by incorporating a printed circuit board antenna with tunable RF polarization and nominally flat frequency response in the band $[0.1, 30]$ MHz. The independent control of the RF field, bias magnetic fields, and gradient cancellation coil pairs in planes parallel to the quadrupole coil plane gives us more control over the spin degree of freedom of the atoms without compromising optical access.

2.2.3   Decompression

Following the hybrid approach described in [25], while we begin evaporation in a magnetic trap, we then load into a spin-independent optical dipole trap and finish evaporating there. For this, we relax the quadrupole field strength to the point where gravity assists the cloud transfer into the dipole potential. The `decompress` stage below implements magnetic decompression.

```python
def decompress(t, **kwargs):
    """ Decompress from magnetic trap to dipole trap"""
    decompress_time = 0
```

```python
# Stop rf evaporation
RF_evap.setamp(t, -80*dBm)
RF_switch.go_low(t)
RF_mixer.constant(t, 0)

# Initial decompression
y_bias.customramp(t, initial_decompress_time, LineRamp,
    y_rf_shim_bias, y_decompress_initial_bias,
    samplerate=1/decompress_step, units='A')
science_quadrupole.customramp(t, initial_decompress_time, LineRamp,
    move_final_current, intermediate_decompress_current,
    samplerate=1 / decompress_step, units='A')
decompress_time += initial_decompress_time

# Intermediate decompression
t += initial_decompress_time
science_quadrupole.customramp(t, intermediate_decompress_time, LineRamp,
    intermediate_decompress_current, final_decompress_current,
    samplerate=1/decompress_step, units='A')
y_bias.customramp(t, intermediate_decompress_time, LineRamp,
    y_decompress_initial_bias, y_decompress_intermediate_bias,
    samplerate=1 / decompress_step, units='A')
decompress_time += intermediate_decompress_time

# Final decompression, ramp dipole on
t += intermediate_decompress_time
dipole_intensity.customramp(t, final_decompress_time, ExpRamp,
    initial_dipole_intensity, intermediate_dipole_intensity,
    initial_dipole_tau, samplerate=1/(2*decompress_step))
dipole_split.customramp(t, final_decompress_time, ExpRamp,
    initial_dipole_split, intermediate_dipole_split,
    initial_dipole_tau, samplerate=1/(2*decompress_step))
science_quadrupole.customramp(t, final_decompress_time, ExpRamp,
    final_decompress_current, 0.0,
    initial_dipole_tau, samplerate=1/(2*decompress_step), units='A')
y_bias.customramp(t, final_decompress_time, LineRamp,
    y_decompress_intermediate_bias, y_decompress_final_bias,
    samplerate=1 / (2*decompress_step), units='A')
decompress_time += final_decompress_time
t += final_decompress_time
return decompress_time
```

The are three substages of decompression; initial, intermediate and final, where we sometimes include a microwave (μ-wave), and then an RF adiabatic rapid passage (ARP) stage to transfer from $|F = 2, m_F = 2\rangle$ to $|F = 1, m_F = 1\rangle$ states. A reason to insert the μ-wave ARP stage between the first and second substages of decompression is that dipole evaporation is more efficient outside of $|F = 2, m_F = 2\rangle$ at low temperatures and higher density where three-body recombination begins to drive rapid nonvelocity selective loss. The reason to insert the RF ARP stage near the end of decompression is for state preparation purposes, as the spin-independent

dipole potential is able to hold atoms with $m_F \leq 0$. As the ARP stages are not needed for making a BEC, we omit their hardware instructions above.

2.2.4 Evaporation from a dipole trap

The ground state of a two-level atom will shift in energy due to the AC stark shift in the presence of an off-resonant optical field with frequency $\omega/2\pi$ and a detuning $\Delta = \omega - \omega_0$, away from the resonant frequency $\omega_0/2\pi$. Furthermore, in the presence of intensity gradients, spatially local energy shifts give rise to an external potential

$$U(\vec{r}) = -\frac{3\pi c^2}{2\omega_0^3} \left(\frac{\Gamma}{\omega_0 - \omega} + \frac{\Gamma}{\omega_0 + \omega} \right) I(\vec{r}) \tag{2.3}$$

known as optical dipole potential [31], where Γ is the linewidth, c is the speed of light, and $I(\vec{r})$ is the intensity distribution of light. The induced dipole scatters light in proportion to the intensity with a scattering rate

$$\Gamma_d(\vec{r}) = \frac{3\pi c^2}{2\hbar\omega_0^3} \left(\frac{\omega}{\omega_0} \right)^3 \left(\frac{\Gamma}{\omega_0 - \omega} + \frac{\Gamma}{\omega_0 + \omega} \right)^2 I(\vec{r}) \tag{2.4}$$

as long as the intensity is low enough that coherent scattering dominates. For multilevel alkali atoms such as ^{87}Rb we employ far detuned optical dipole traps such that $\hbar\Delta \gg \hbar\Delta_F \gg \hbar\Delta_{HF}$. For ^{87}Rb atoms in the hyperfine manifold of their electronic ground state $|5^2\text{S}_{1/2}, F, m_F\rangle$, an optical dipole trap realizes the spin-

dependent potential

$$U(\vec{r}) = \frac{\pi c^2}{2} \left(\frac{\Gamma_{\mathrm{D_2}}}{\omega_{\mathrm{D_2}}^3} \frac{2 + \mathcal{P} g_F m_F}{\Delta_{\mathrm{D_2},F}} + \frac{\Gamma_{\mathrm{D_1}}}{\omega_{\mathrm{D_1}}^3} \frac{1 - \mathcal{P} g_F m_F}{\Delta_{\mathrm{D_1},F}} \right) I(\vec{r}) \qquad (2.5)$$

where $\omega_{\mathrm{D_{1,2}}}$ represents the resonant D-line transition frequency, and $\Delta_{\mathrm{D_{1,2},F}} = \omega - \omega_{\mathrm{D_{1,2}}}$ is the detuning away from resonance including the specific hyperfine state F. Taking the possibility that Δ_{HF} matters resulting in differential m_F scalar shifts, the polarization of light enters through the factor $\mathcal{P} = \pm 1, 0$, accounting for $\sigma^{\pm}, \pi$ polarized light respectively, and where g_F is the Landé factor. Because the fine structure splitting exceeds the hyperfine structure splitting by seven orders of magnitude (see Figure 2.1), the perturbative form

$$U(\vec{r}) = \frac{3\pi c^2}{2\omega_0^3} \frac{\Gamma}{\Delta} \left(1 + \frac{\mathcal{P} g_F m_F}{3} \frac{\Delta_F}{\Delta} \right) I(\vec{r}) \qquad (2.6)$$

is appropriate for ^{87}Rb. Furthermore, the explicit choice of π polarized light makes $\mathcal{P} = 0$, giving the spin-independent potential

$$U(\vec{r}) = \frac{3\pi c^2}{2\omega_0^3} \frac{\Gamma}{\Delta} I(\vec{r}). \qquad (2.7)$$

A blue-detuned (red-detuned) $\Delta > 0$ ($\Delta < 0$) beam provides repulsive (attractive) potential energy to the atoms. We use a crossed optical dipole trap with two

red-detuned Gaussian beams of intensity

$$I(r,z) = \frac{4P}{\pi w_0^2(1 + z^2/z_R^2)} \exp\left[-\frac{2r^2}{w_0^2(1 + z^2/z_R^2)}\right] \tag{2.8}$$

of power P, minimum waist parameter w_0, and Rayleigh length $z_R = \pi w_0^2/\lambda$. The two beams have slightly different frequencies, so we get away with adding intensities (rather than fields) to estimate the total dipole potential. The two beams cross at near $90\,^\circ$ close to the center of the magnetic quadrupole trap. We separately control both the total power and the ratio of the individual powers so as to optimize both the initial aspect ratios of the trap, and the final desired trapping potential. Our setup is versatile, with a pair of different minimum waists of order $100\,\mu$m and total power $P \sim 5.0\,$W. The combined crossed dipole trap has an effective depth U_0 limiting the temperature of a thermal gas to $T \leq U_0/10k_B$ in equilibrium. The `dipole_evaporation` stage begins immediately after decompression, and lasts for $2\,$s, cooling the gas below the transition temperature $T_c \approx 250\,$nK. We image the clouds at different points during the final stages of `dipole_evaporation`, where a bimodal momentum distribution signals the appearance of a Bose–Einstein condensate. The temperature of our BEC can be decreased to $T \sim 25\,$nK before the optical dipole potential is overcome by gravity. The final temperature in RbChip is $T = 35(5)\,$nK with a normalized phase-space density well in excess of 1. This is the starting point of almost every experiment that we do.

```python
def dipole_evaporate(t, **kwargs):
    """ Dipole evaporation in cross dipole trap """
    dipole_intensity.customramp(t, dipole_evaporation_time, LineRamp,
        intermediate_dipole_intensity, final_dipole_intensity,
```
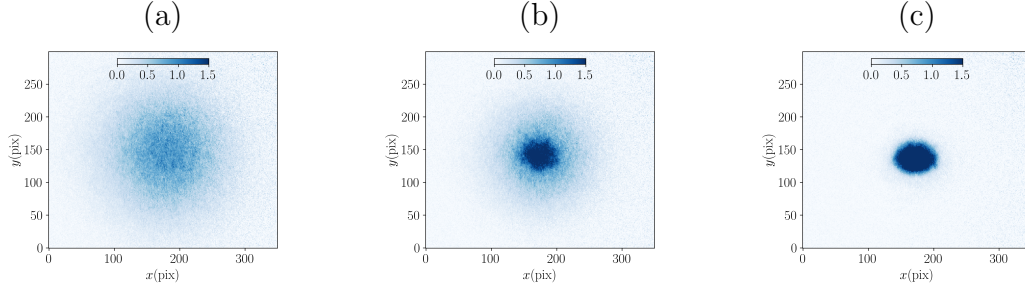
Figure 2.7: Thermal to BEC transition. Absorption images in time-of-flight giving the atomic momentum distributions after $t = 24\,\mathrm{ms}$ of free expansion. The BEC transition is marked by the change from (a) purely thermal (Maxwell–Boltzmann) to (b) bimodal, and (c) almost pure Thomas–Fermi (inverted potential shape) momentum distribution. BECs are optically denser than thermal clouds, as illustrated by the higher optical depths (colorbar). The scale of the pure BEC in (c) is $\sim 100\,\mu\mathrm{m}$.

```
        samplerate=1/dipole_evaporate_step)
    dipole_split.customramp(t, dipole_evaporation_time, LineRamp,
        intermediate_dipole_split, final_dipole_split,
        samplerate=1 / dipole_evaporate_step)
    return dipole_evaporation_time
```

Our Bose–Einstein condensates form in harmonic traps, where they would condense onto the ground state of the simple harmonic oscillator in the absence of interactions, but the otherwise weak interparticle interactions play a dominant role at sufficiently low temperatures where the kinetic energy can be neglected. There, the Thomas–Fermi approximation gives the correct energy eigenvalue related to the global chemical potential μ_0 in the mean-field approximation. The result is a difference in the equation of state of the system which affects the momentum distribution after a period of free expansion. The image sequence in Figure 2.7 shows the thermal to BEC transition. In the absence of interactions the density

distribution of a trapped thermal nondegenerate ensemble

$$n(\vec{r}) = n_0 e^{-U(\vec{r})/k_B T} \tag{2.9}$$

gives a Gaussian profile for a harmonic potential with a width that depends on temperature. Ultracold, mean-field interacting atoms in a BEC distribute according to the Thomas–Fermi distribution [32]

$$n(\vec{r}) = \begin{cases} n_0(1 - U(\vec{r})/\mu_0), & U(\vec{r}) \leq \mu_0. \\ \\ 0, & \text{otherwise.} \end{cases} \tag{2.10}$$

with the inverted shape of the potential $U(\vec{r})$ and in terms of a global chemical potential μ_0 in the approximation where we can ignore the kinetic energy of the atoms. The global chemical potential represents the mean-field energy of the center of the trap ... The signature of Bose–Einstein condensation in a harmonically trapped gas is the emergence of a bimodal momentum distribution combining a Gaussian (thermal) component and a quadratic (condensed) component. After putting together all the stages in this Chapter we compile a full sequence. The minimal BEC production script reads

```
start()
""" Begin experiment at t=0. Add returned durations from every stage """
t = 0
t += prep(t)
t += MOT(t)
# Add a 60 Hz trigger wait line
if wait_before_compressed_MOT:
    wait(label='compressed_MOT_wait', t=t, timeout=2)
t += compressed_MOT(t)
t += optical_molasses(t)
t += prep_optical_pumping(t)
```

```
t += optical_pump_2_2(t)
t += magnetic_transport(t)
t += rf_evaporate(t)
t += decompress(t)
t += dipole_evaporate(t)
t += off(t)
stop(t, target_cycle_time=40.0*s, cycle_time_delay_after_programming=True)
```

2.3   Conclusion

We described in this Chapter the production of ^{87}Rb BECs. We include different stages of the minimal experimental sequence required to make BECs while highlighting features of the current and future apparatus. Similarly, the descriptive Python scripts provide a reference for hardware instructions. The production of quantum degenerate ^{87}Rb detailed here precedes all the experiments detailed in later Chapters.

Chapter 3:   Topology of a spin 3/2 system

This chapter describes quantum simulated Abelian and non-Abelian gauge fields. We first dress the internal states of a BEC with radiofrequency (RF), and microwave (μ-wave) fields, encoding geometric phases in the dressed eigenstates as gauge degrees of freedom. Under this approach, the n-dimensional parameter space spanned by the parameters of the Hamiltonian host artificial gauge fields. When driven diabatically, but within the linear response regime, deflections in the states trajectories reveal the underlying gauge field curvatures. We measure these deflections using quantum state tomography, and after integrating the reconstructed curvatures around closed manifolds in parameter space, we measure the topological invariant known as Chern number. After benchmarking this method by measuring the first Chern number of a two-level system, we extend it to a four-level system with two pairs of twofold degenerate eigenstates, and measure the higher order topological invariant known as second Chern number for the first time. In general, the n-th Chern number is the topological invariant characterizing the topology of quantum systems with n-fold degenerate bands. Lastly, by parametrically inflating and displacing manifolds, we characterize the non-Abelian field strength, and drive a topological transition respectively.

This chapter is organized as follows. In Section 3.1, I review the role of geometry and topology in quantum systems using a spin 1/2 Hamiltonian as an example. Here, I introduce local and global quantities characterizing the abstract parameter spaces. Then, in Section 3.1.2 I review these quantities in the context of non-Abelian gauge fields. As a benchmarking experiment, I present the measurement of the first Chern number in Section 3.2. Later, I introduce the concept of generalized forces in the linear dynamical response of a driven quantum system in Section 3.2.1. Then, I present the measurement of the Abelian curvature component giving the first Chern number in Section 3.2.2. Finally, I extend the experiment to a spin 3/2 system comprised of doubly degenerate subspaces, where we characterize the gauge field curvatures, measure the first and second Chern numbers, and drive their topological transitions in Section 3.2.3. The results in this Chapter are published in [33].

3.1 Parameter space, geometry and topology

Hamiltonians are central to exploring, solving, and ultimately classifying a wide range of quantum mechanical systems. While in their different representations, mathematical properties like symmetries and transformations give insight to physical reality, topology emerges as a new and important tool for their high level classification [34, 35].

3.1.1 Topology of a spin 1/2 system

While geometry describes local properties of a surface embedded in a higher-dimensional space, or manifold, topology describes its global qualities. In quantum mechanics, geometry and topology describe manifolds in the abstract parameter space of a Hamiltonian. For instance, the general two-level Hamiltonian describing the physics of a spin-1/2 particle coupled to an external magnetic field

$$\hat{\mathcal{H}} = \alpha\hat{\sigma}_0 + \vec{\lambda}\cdot\vec{\sigma} = \begin{pmatrix} \alpha + \lambda_z & \lambda_x - i\lambda_y \\ \lambda_x + i\lambda_y & \alpha - \lambda_z \end{pmatrix}, \tag{3.1}$$

has a total of four independent parameters in the Pauli representation, where $\vec{\sigma} = (\hat{\sigma}_x, \hat{\sigma}_y, \hat{\sigma}_z)$ is the Pauli vector, $\hat{\sigma}_0$ denotes the identity operator, $\vec{\lambda} = (\lambda_x, \lambda_y, \lambda_z)$ is a coupling vector, and α is an arbitrary energy offset. Solving the Schrödinger equation gives a pair of (unnormalized) eigenstates

$$|\Psi_\pm\rangle = \begin{pmatrix} \lambda_z \mp |\vec{\lambda}| \\ \lambda_x + i\lambda_y \end{pmatrix}, \tag{3.2}$$

here in cartesian parametrization. Similarly, a spherical parametrization related to the cartesian parameters by the transformations $\lambda_x = \lambda_r \sin\lambda_\theta \cos\lambda_\phi$, $\lambda_y =$

$\lambda_r \sin \lambda_\theta \sin \lambda_\phi$, and $\lambda_z = \lambda_r \cos \lambda_\phi$ gives the eigenstates

$$|\Psi_\pm\rangle = \begin{pmatrix} \cos \lambda_\theta \mp 1 \\ e^{i\lambda_\phi} \sin \lambda_\theta \end{pmatrix}, \tag{3.3}$$

While the Hilbert space spanned by $|\Psi_\pm\rangle$ is always two-dimensional, the parameter space of all possible values $\{\alpha, \vec{\lambda}\}$, is four-dimensional. The two eigenstates and their corresponding eigenenergies in the two parametrizations

$$E_\pm = \alpha \mp |\vec{\lambda}| = \alpha \mp \lambda_r$$

are specific to a point $P_0 = \{\alpha_0, \vec{\lambda}_0\}$ in parameter space. Figure 3.1 is a visualization of a three-dimensional cartesian parameter space where $\alpha = 0$. In such a parameter space, a continous transformation of the Hamiltonian (through a continous variation of its parameters) defines a trajectory. Furthermore, closed trajectories bound surfaces, which may enclose volumes (e.g. Figure 3.1). Geometry and topology describe and classify quantum systems through the local and global properties of these constrained parametric manifolds. In an experiment, the ultimate constraint preventing full access to the parameter space is set by the tunability of the Hamiltonian.

While there is nothing quantum about geometry or topology (see [36–38] for beautiful examples of topological states in classical systems), their relevance
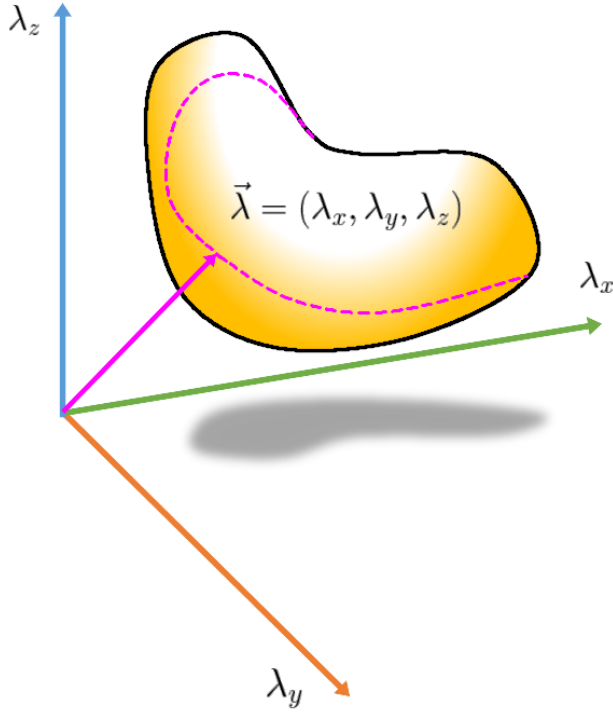
Figure 3.1: Parameter space. Visualization of a three-dimensional cartesian parameter space where a Hamiltonian, its eigenstates, and eigenenergies are specific to a point represented by the vector $\vec{\lambda}$ (solid magenta arrow). A continous variation of $\hat{\mathcal{H}}$ defines a trajectory (dashed magenta line), and a closed trajectory defines a surface (yellow). Closed surfaces enclose subspaces of the full parameter space.

was first highlighted in optics through the Pancharatnam phase [39], and later in electrodynamics through the Aharonov-Bohm effect [40]. Both of these instances match the Berry's phase [41] from the adiabatic evolution of quantum systems. Then, other instances such as the Zak phase [42] in discrete one-dimensional systems, and the Wilczek–Zee phase [43] in systems with degenerate subspaces, were highligthed for their relevance. Nowadays, topology plays a central role in understanding the quantized conductance of the integer quantum Hall effect (IQHE), a link first established in [44], where the parameter space is spanned by the quasi-momenta of the underlying the two-dimensional electron gas.

Following [41] closely, as the Hamiltonian 3.2 is adiabatically transformed, an eigenstate acquires a phase when evolving from $\{\alpha_0, \vec{\lambda}_A\}$ to $\{\alpha_0, \vec{\lambda}_B\}$. The final state

$$|\Psi_\pm\rangle_B = e^{i\Phi_d}\, e^{i\Phi_g} |\Psi_\pm\rangle_A, \tag{3.4}$$

has two separable phase contributions. The first contribution, Φ_d, is the dynamic phase associated with the unitary time evolution of $|\Psi_\pm\rangle$. The second contribution

$$\Phi_g = \int_{A \to B} i\langle \Psi_\pm | \hat{\nabla}_{\vec{\lambda}} | \Psi_\pm \rangle \cdot d\vec{\lambda}, \tag{3.5}$$

is the geometric phase associated with the trajectory traced when going from A to B, and $\hat{\nabla}_{\vec{\lambda}}$ is a parametric gradient operator along such trajectory. The vector-valued integrand

$$\vec{A}_\pm = i\langle \Psi_\pm | \hat{\nabla}_{\vec{\lambda}} | \Psi_\pm \rangle \tag{3.6}$$

is the Berry connection linking the initial and final states. Finally, the Berry curvature

$$\vec{B}_\pm = \nabla_{\vec{\lambda}} \times \vec{A}_\pm \tag{3.7}$$

appears when taking the curl of the Berry connection. The components of the curvature may be defined more generally through Stokes theorem using the eigenstate

in Equation 3.5 as

$$\vec{B}_k = \text{Im} \sum_{k \neq l} \frac{\langle \Psi_k | \hat{\nabla}_{\vec{\lambda}} \mathcal{H}(\vec{\lambda}) | \Psi_l \rangle \times \langle \Psi_l | \hat{\nabla}_{\vec{\lambda}} \mathcal{H}(\vec{\lambda}) | \Psi_k \rangle}{(E_k - E_l)^2}. \tag{3.8}$$

An interesting feature of Berry's curvature is the possible divergence in the denominator. Taking the definition in Equation 3.8, using the Hamiltonian in Equation 3.10, and its eigenstates in Equation 3.3, we evaluate the curvature

$$\vec{B}_{\pm} = \pm \frac{2 \sin^2(\lambda_\theta)}{\lambda_r^2} \hat{\mathbf{e}}_{\lambda_r} \propto \pm \frac{\vec{\lambda}_r}{\lambda_r^3} \tag{3.9}$$

in the spherical parametrization where

$$\hat{\nabla}_{\vec{\lambda}} = \partial_{\lambda_r} \hat{\mathbf{e}}_{\lambda_r} + \lambda_r^{-1} \partial_{\lambda_\theta} \hat{\mathbf{e}}_{\lambda_\theta} + (\lambda_r \sin \lambda_\theta)^{-1} \partial_{\lambda_\phi} \hat{\mathbf{e}}_{\lambda_\phi}.$$

We now draw the analogy with classical electromagnetism, letting the curvature take on the role of the gauge independent magnetic field strength, while the Berry connection acts as the gauge dependent vector potential. Then, the magnetic field in Equation 3.9 is sourced by a magnetic monopole centered in $(\lambda_r = 0)$. The analogy maps Gauss law to the definition of the first Chern number

$$C_1^{(\pm)} = \frac{1}{2\pi} \int_{\mathbf{S}} \vec{B}_{\pm} \cdot d\vec{\mathbf{S}}, \tag{3.10}$$

counting the number of monopoles enclosed by the spherical manifold. We cannot

use Stoke's theorem to directly evaluate the Chern number using Equation 3.10 due to the singular point in $\vec{B}_\pm$. We can nevertheless find $C_1^{(\pm)} = \pm 1$ by carrying out the appropriate path integrals around the singularity, as is done in [45].

The nonzero first Chern number as we evaluate it reveals that a spin 1/2 system described by the Hamiltonian in Equation 3.1 is singular in at least one point in the parameter space enclosed by the spherical manifold around $\lambda_r = 0$. The first Chern number is a topological invariant since its value does not depend on the local properties of the system or the choice of parametric representation of the manifold (we use spherical manifolds for their symmetry, leading to simple integrals). The gauge symmetry associated with the parametric transformations of the spin 1/2 eigenstates is the U(1) gauge, just like in electromagnetism. This means that under a gauge transformation $|\Psi\rangle \rightarrow e^{i\phi}|\Psi\rangle$, while the connection changes, the curvature remains the same, i.e. $\vec{B}_\pm$ is gauge independent.

3.1.2 Non-Abelian gauge fields

A non-Abelian gauge field is one where the different components of the connection fail to commute

$$[A_\mu, A_\nu] \neq 0, \tag{3.11}$$

where $\vec{A} = A_\mu$ is now expressed in tensor notation, adopting the Einstein summation convention for repeated indices. In the context of quantum systems, this is only possible in the presence of degenerate subspaces, where the connections

linking the states $|\psi_{i,j}\rangle$ within a degenerate space give rise to matrix-valued vector connection

$$A_\mu^{ij} = i\langle\psi_i|\partial_\mu\psi_j\rangle. \tag{3.12}$$

The matrix elements A_μ^{ij} encode the non-Abelian Wilczek–Zee phase [43]

$$\Phi^{ij} = \oint_C A_\mu^{ij} d\lambda_\mu, \tag{3.13}$$

the matrix-valued geometric phase acquired by the degenerate subspace eigenstates. Similarly, the matrix-valued, non-Abelian field curvature

$$F_{\mu\nu}^{ij}(\vec{\lambda}) = \frac{\partial A_\nu^{ij}}{\partial\lambda_\mu} - \frac{\partial A_\mu^{ij}}{\partial\lambda_\nu} + i[A_\mu^{ij}, A_\nu^{ij}], \tag{3.14}$$

is a generalization of the electromagnetic field tensor. In fact, under this notation, when the commutator vanishes (Abelian case), the first Chern number becomes

$$C_1 = \frac{1}{4\pi} \int_{S_2} \epsilon_{\eta\mu\nu} F_{\mu\nu} d^2 S_\eta, \tag{3.15}$$

where $\epsilon_{\eta\mu\nu}$ is the third-rank Levi–Civita symbol. The extension of the first Chern number for twofold degenerate non-Abelian gauge potentials is the second Chern number

$$C_2 = \frac{1}{32\pi^2} \int_{S_4} \epsilon_{\mu\nu\eta\xi} \text{Tr}(F_{\mu\nu}^{ij} F_{\eta\xi}^{ij})_{ij} d^4 S \tag{3.16}$$

46

evaluated in the four-dimensional manifold S_4, where ϵ_{ijkl} is the fourth-rank Levi–Civita symbol, taking into account only the antisymmetric components of the generalized curvature $\hat{F}_{\mu\nu}$. The trace on the integrand is over the ij matrix elements of the curvature $F_{\mu\nu}^{ij}$ in its final representation. For higher-dimensional systems with n-fold degeneracies, the n-th Chern number

$$C_n = \frac{1}{w_n} \int_{S_{2n}} \text{Tr} \underbrace{(\hat{F} \wedge \hat{F} \wedge ... \wedge \hat{F})}_{n} \, d^{2n}S \qquad (3.17)$$

involves an n-th order wedge product of the curvature acting as a generalized antisymmetric exterior product (e.g. generalized curl) [33]. The wedge product is traced out and integrated over the $2n$-dimensional manifold, with a normalizing factor w_n that depends on the dimensionality of the parameter space. Chern numbers count the number of singular points enclosed by a manifold in parameter space.

While a few interpretations for Chern numbers abound in different contexts (e.g. winding number for parallel transport, conductance quanta, etc...), we adopt the interpretation that Chern numbers count the number of monopole sources for the gauge fields in parameter space. Under this analogy, a nonzero first Chern number may count the number of Dirac monopoles sourcing a U(1) Abelian gauge field in three-dimensional parameter space. Similarly, a nonzero second Chern number may count the number of Yang monopoles sourcing an SU(2) non-Abelian gauge field in five-dimensional parameter space.

A spin-3/2 system may host degenerate submanifolds as either two pairs of doubly degenerate states or a triad of degenerate states and single state (a tetradegenerate manifold does not comprise a submanifold as it involves all eigenstates). We study a four-level system described by the Hamiltonian

$$\hat{\mathcal{H}} = -\frac{\hbar}{2}\vec{q}\cdot\vec{\Gamma}, \tag{3.18}$$

comprised by a pair of twofold degenerate subspaces, where $\vec{q} = (q_1, q_2, ..., q_5)$ is the five-dimensional coupling vector, $\vec{\Gamma} = (\hat{\Gamma}_1, \hat{\Gamma}_2, ..., \hat{\Gamma}_5)$ are the five gamma matrices, and $\hat{\Gamma}_0$ the identity operator. We use a representation in terms of the Pauli

operators in the degenerate submanifolds, where

$$\hat{\Gamma}_0 = \hat{\sigma}_0 \otimes \hat{\sigma}_0 = \begin{pmatrix} 1 & 0 & 0 & 0 \\ 0 & 1 & 0 & 0 \\ 0 & 0 & 1 & 0 \\ 0 & 0 & 0 & 1 \end{pmatrix}, \qquad \hat{\Gamma}_1 = \hat{\sigma}_y \otimes \hat{\sigma}_y = \begin{pmatrix} 0 & 0 & 0 & -1 \\ 0 & 0 & 1 & 0 \\ 0 & 1 & 0 & 0 \\ -1 & 0 & 0 & 0 \end{pmatrix},$$

$$\hat{\Gamma}_2 = \hat{\sigma}_0 \otimes \hat{\sigma}_x = \begin{pmatrix} 0 & 1 & 0 & 0 \\ 1 & 0 & 0 & 0 \\ 0 & 0 & 0 & 1 \\ 0 & 0 & 1 & 0 \end{pmatrix}, \qquad \hat{\Gamma}_3 = -\hat{\sigma}_z \otimes \hat{\sigma}_y = \begin{pmatrix} 0 & i & 0 & 0 \\ -i & 0 & 0 & 0 \\ 0 & 0 & 0 & -i \\ 0 & 0 & i & 0 \end{pmatrix},$$

$$\hat{\Gamma}_4 = \hat{\sigma}_0 \otimes \hat{\sigma}_z = \begin{pmatrix} 1 & 0 & 0 & 0 \\ 0 & -1 & 0 & 0 \\ 0 & 0 & 1 & 0 \\ 0 & 0 & 0 & -1 \end{pmatrix}, \qquad \hat{\Gamma}_5 = \hat{\sigma}_x \otimes \hat{\sigma}_y = \begin{pmatrix} 0 & 0 & 0 & -i \\ 0 & 0 & i & 0 \\ 0 & -i & 0 & 0 \\ i & 0 & 0 & 0 \end{pmatrix}.$$

3.2 Measuring topological invariants

3.2.1 Generalized forces in parameter space

It is not a simple task to extract topological invariants in the adiabatic limit (i.e. by directly measuring geometric curvatures and integrating them), although a few precedents have been set in [46,47]. The reason is twofold; on one hand dynamical phases tend to overwhelm geometric phases, making their practical detection

challenging. On the other hand experiments in high-dimensional parameter spaces quickly become impractical for the number of measurements required to sample enough closed trajectories. In order to detect the gauge field curvatures, and ultimately measure the associated topological invariants, we employ generalized forces in parameter space, first introduced in this context by [48]. The expectation is that systems following diabatic trajectories with a constant velocity $\dot{\lambda}_\nu$ deflect away from the driving direction with relative strength

$$f_\mu = \dot{\lambda}_\nu F_{\mu\nu}, \tag{3.19}$$

proportional to the curvature component along λ_μ. In the case of systems with degenerate subspaces, the linear response gives a state dependent deflection

$$f_\mu = \dot{\lambda}_\nu \mathrm{Tr}(\hat{\rho}\,\hat{F}_{\mu\nu}) = \dot{\lambda}_\nu \sum_{i,j} \rho_{ij} F_{\mu\nu}^{ij}, \tag{3.20}$$

where $\rho_{ij} = |\psi_i\rangle\langle\psi_j|$ are the density matrix elements in the degenerate subspace.

Generalized forces are analogous to the Lorentz force in electromagnetism, deflecting a system from its trajectory in proportion to the component of the curvature perpedincular to the driving speed. In contrast with the Abelian case, the non-Abelian field curvatures give state-dependent Lorentz-like deflections, a difference depicted in figure 3.2. The emergence of the gauge field curvature in the linear dynamical response of a driven system yields a scheme to probe the
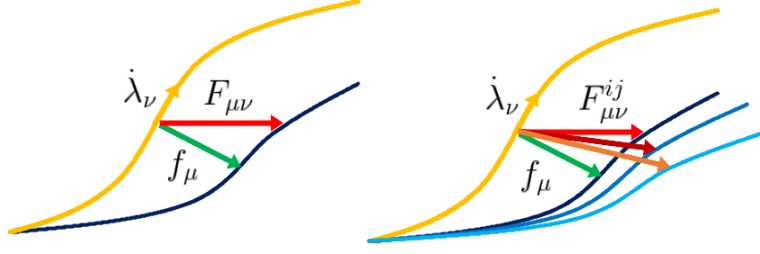
Figure 3.2: Generalized forces. Schematic effect from generalized forces under the influence of Abelian (left) and non-Abelian (right) field curvatures. As the system is driven along its trajectory (yellow), a Lorentz-like force (green) arises in the parameter space proportional to the magnitude of the curvature component orthogonal to the driving speed (red). The differences in the trajectory from the drive encode the magnitude of the curvature. A state-dependent force arises in the non-Abelian case, leading to multiple deflections (red, orange, and crimson arrows) and trajectories (dark blue, blue, and light blue curves) under a single drive.

topology of Abelian and non-Abelian gauge fields beyond the adiabatic limit. In fact, generalized forces are behind the recent realizations of atomic charge pumps in ultracold gases [49,50], and find an application in topological materials beyond the IQHE paradigm [51].

3.2.2 First Chern number

As an experimental benchmark, we dress a spin $1/2$ system comprised by the two hyperfine states $|F = 1, m_F = -1\rangle$, and $|F = 2, m_F = 0\rangle$ with a single μ-wave control field. The dressed state Hamiltonian in the rotating frame of the μ-wave field

$$\mathcal{H} = \frac{\hbar}{2} \begin{pmatrix} \Delta & \Omega e^{i\phi} \\ \Omega e^{-i\phi} & 0 \end{pmatrix} \tag{3.21}$$
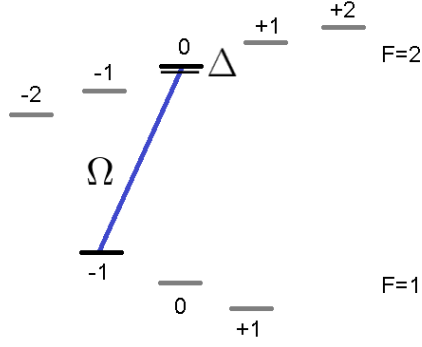
Figure 3.3: Two-level scheme. Bare states used to measure first Chern number with the generalized force deflections and a single control field.

has three independent parameters spanning a three-dimensional space given by the coupling strength Ω, phase ϕ, and detuning Δ. We constrain the parameters of the system to lie on a two-dimensional spherical surface described by the set of points $\vec{\lambda} = \Omega(\sin\theta\cos\phi, \sin\theta\sin\phi, \cos\theta)$ in a three-dimensional parameter space. By sheer coincidence, this space resembles the Bloch sphere used to represent quantum states, but the radius Ω is not restricted to 1, and θ represents the relative phase between simultaneously ramping detuning and external drive. We keep the ratio between the coupling strength and detuning to be $\Omega/\Delta \sim 10^{-2}$. As we require a robust two-level system, we actively control the bias magnetic field of $B_0 = 18\,\mathrm{G}$ to $\delta B_0/B_0 \approx 1\,\mathrm{ppm}$, or in terms of the residual fluctuations in the linear Zeeman splitting, $\delta\epsilon^{(1)} \sim h \times 10\,\mathrm{Hz}$.

The experiment to detect the field curvature happens in three stages; state preparation, diabatic drive, and state tomography to measure the deflected state trajectory (Figure 3.4). During the state preparation, we adiabatically dress the

52
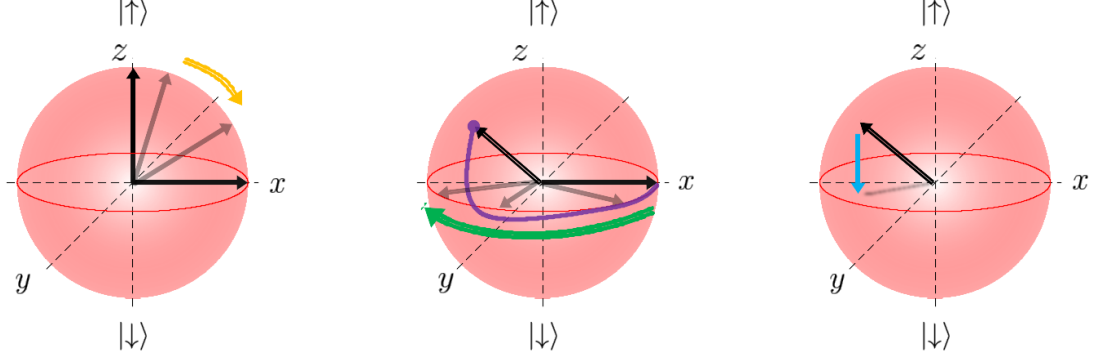
Figure 3.4: Experimental sequence to measure state deflection. We prepare a state superposition from an initial $|{\uparrow}\rangle$ state, and then drive the system at constant speed along ϕ (green). Finally, we perform projective state tomography (blue) in different points along the trajectory (purple) to reconstruct the expectation value of the magnetization $\langle \vec{\sigma} \rangle$.

bare $|F, m_F\rangle$ states with a single μ-wave tone into the Hamiltonian in 3.21, ramping Ω (and Δ) from 0 to $12\,\text{kHz}$ with variable phase θ. Then, the Hamiltonian and its local eigenstates traverse parameter space with velocity $\dot{\phi}$ as we ramp the phase of the coupling field. Finally, we perform state tomography at different times during the parametric evolution to reconstruct the trajectory from the generalized force

$$f_\theta = -\frac{\Omega \sin \phi}{2} \langle \hat{\sigma}_z \rangle \tag{3.22}$$

along θ. Using the definition in Equation 3.19, the Abelian curvature component

$$F_{\phi\theta} = -\frac{\Omega \sin \phi}{2\dot{\phi}} \langle \hat{\sigma}_z \rangle \tag{3.23}$$

is directly proportional to the expectation value of $\hat{\sigma}_z$ and inversely proportional to the driving speed $\dot{\phi}$. The reconstructed state evolution in Figure 3.5 is for an
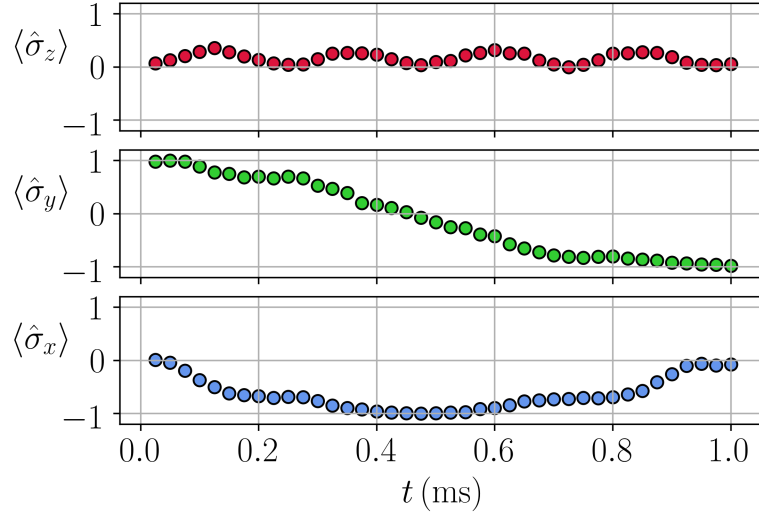
Figure 3.5: Two-level state tomography. Magnetization $\langle \vec{\sigma} \rangle(t)$ for an initial equal superposition state at different times during the driven evolution along ϕ.

equal superposition initial state ($\theta = \pi/2$). While the adiabatic limit predicts Larmor precession ($\langle \hat{\sigma}_z(t) \rangle = 0$) about the equator for an equal superposition of $|\uparrow\downarrow\rangle$, the linear dynamical response clearly shows a deflected trajectory during the diabatic evolution along ϕ. The Bloch vector trajectory in Figure 3.6 is reminiscent of the cycloids observed in [52]. The spherical symmetry of the constrained spherical manifold, and the calibrated linear drive along ϕ allow a straightforward computation of the first Chern number through the numerically evaluated integral

$$C_1 = \int_0^\pi F_{\theta\phi} \, d\phi = -\frac{2\dot{\phi}}{\Omega} \int_0^{t_\pi} \langle \hat{\sigma}_z \rangle \sin(\dot{\phi}t) \, dt = 1.07, \tag{3.24}$$

counting a singular point enclosed by the spherical manifold of the spin $1/2$ system.

Following this measurement, we add a second, parallel control field such that, if we insist on keeping the spherical radius constant, it acts to offset the location
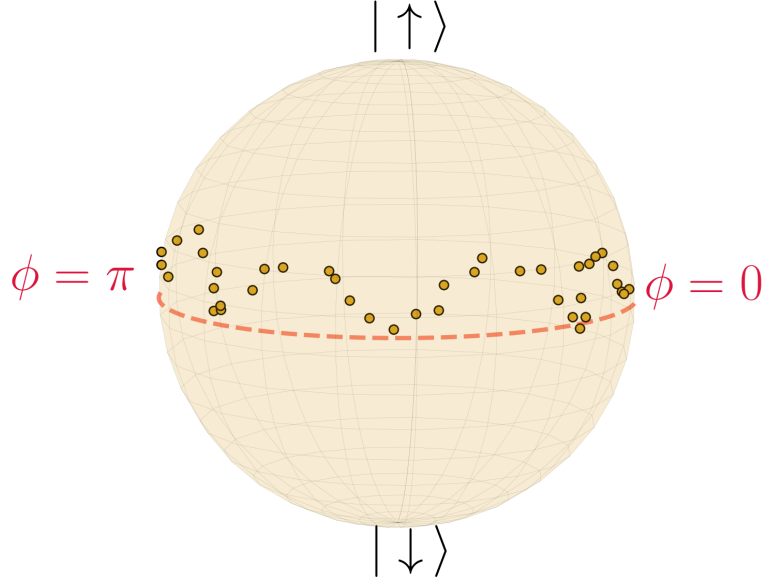
Figure 3.6: Projected Bloch trajectory. Projected spin $1/2$ magnetization $\langle\vec{\sigma}\rangle(\phi(t))$ in the Bloch sphere during the diabatic drive along ϕ. Even if the Bloch space is not parameter space, the Bloch vector shows the deflected trajectories due to the proportional relation in Equation 3.23.

of the sphere with respect to the singular point (monopole source) by an amount

$r_0 \propto \Omega/\Omega'$ proportional to the ratio of the two coupling strengths. We then repeat

the measurement of C_1 as a function of r_0 to observe the topological transition,

going from a sphere surrounding the monopole to a sphere enclosing no source

(Figure 3.7).
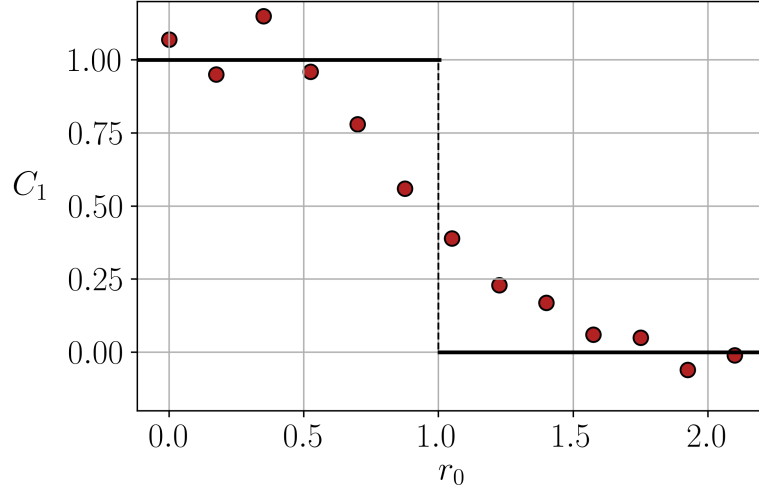
Figure 3.7: Topological transition of a spin $1/2$ system. Two control fields shift the enclosing manifold in parameter space from a region with a (monopole) singularity in the left where $r_0 < 1$, to a region without one. The topologically trivial region for $r_0 > 1$ has $C_1 = 0$. The black lines show the sharp topological transition expected to occur only in the true adiabatic limit, in the absence of any high-order dynamical response.

3.2.3 Second Chern number

Armed with the generalized force measurement scheme, we turn to the Hamiltonian in Equation 3.18. We use the bare hyperfine states shown in Figure 3.8, close to $m_F = 0$ for optimized robustness against magnetic field fluctuations. We relabel the bare hyperfine states as $|1, 0\rangle = |1\rangle$, $|1, -1\rangle = |2\rangle$, $|2, 0\rangle = |3\rangle$, and $|2, 1\rangle = |4\rangle$. Additionally, we constrain the parametric manifold to a four-dimensional hypersphere with points represented by the set of points

$$\vec{q} = (\Omega_B \cos \phi_B, -\Omega_A \cos \phi_A, -\Omega_A \sin \phi_A, \delta, -\Omega_B \sin \phi_B),$$

56
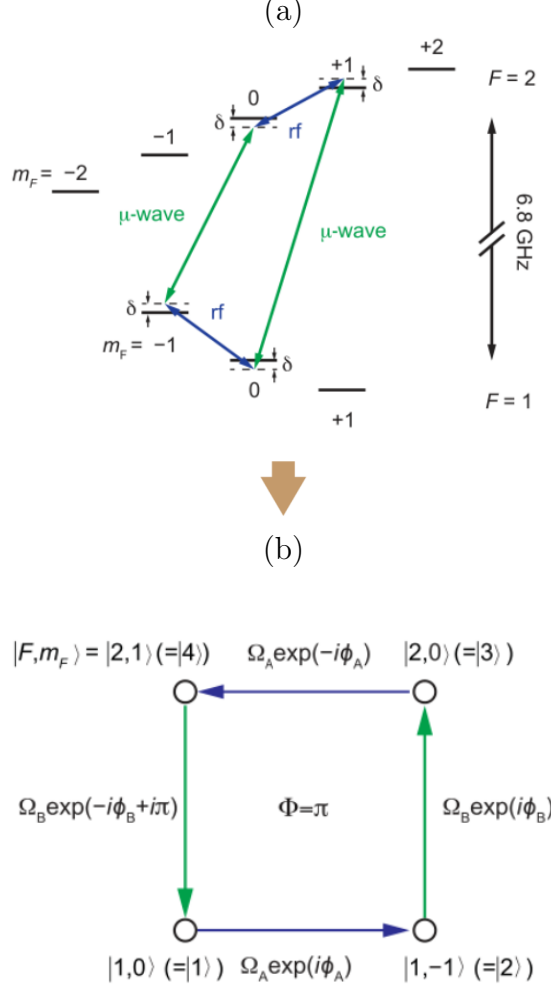
Figure 3.8: Second Chern number level scheme. Four levels realize the spin $3/2$ system from Equation 3.18. (a) Different initial superpositions of the bare hyperfine states are coupled with two pairs of RF (blue) and μ-wave (green) fields. (b) In the dressed state basis, cyclically coupled states wrap a total phase of $\Phi = \pi$ around the plaquette to guarantee the pair of twofold degenerate subspaces.

defined by four independent parameters and a fixed relative phase (the two phases are driven together $\phi_A = \phi_A(\phi_B)$), where Ω_A, Ω_B are the μ-wave and RF coupling strengths respectively, δ is a common single photon detuning, and ϕ_A, ϕ_B are the phases of the μ-wave and RF fields respectively.
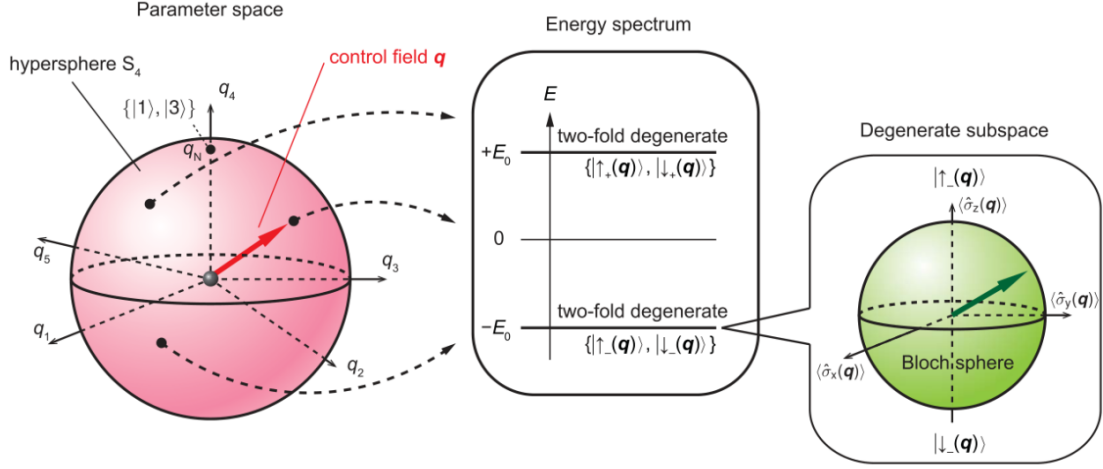
Figure 3.9: Second Chern space schematics. Four-dimensional hypersphere S_4 embedded in the five-dimensional parameter space. In some points $\mathbf{q} = \vec{q}$, the dressed state Hamiltonian 3.18 may turn into a pair two-fold degenerate bands (middle) with eigenstates $|\uparrow_\pm\downarrow_\pm\rangle$. Each degenerate subspace has a two-level Bloch sphere representing the degenerate state.

We repeat the protocol from the measurement of the first Chern number. This time, even with the hyper-spherical symmetry present, the higher dimensional parameter space demands more measurements. The protocol is equally split into three stages; state preparation, linear drive, and projective state tomography. In figure 3.9, I show a representation of the manifold, a four-dimensional hyperspherical surface in five-dimensional parameter space. In a given point in parameter space, the energy spectrum has two, twofold degenerate subspaces, where the non-Abelian geometric phases arise, given that the phase accumulated around the four level plaquette adds up to π. Since the degenerate subspaces are twofold degenerate, Bloch spheres represent the two states within a subspace, along with the expectation value of the magnetization $\langle\vec{\sigma}\rangle$. We perform all measurements in the degenerate subspaces, later constructing the generalized magnetization $\langle\vec{\Gamma}\rangle$

with the above representation. For instance, in Figure 3.10 I show a measure-
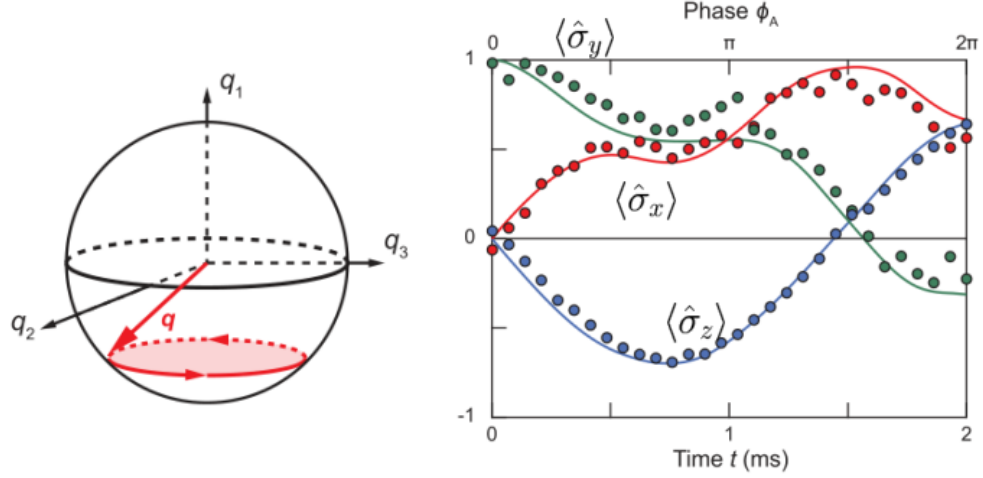
Figure 3.10: Subspace trajectory and tomography. In the left, a representation of the parameter space trajectory. On the right, the reconstructed state evolution during the trajectory inside a degenerate submanifold. For a given band, the two-level state trajectory may be used to construct the expectation value of $\hat{\Gamma}_i$. The straight lines are numerical solutions to the time dependent Schrodinger equation with Equation 3.18.

ment of the degenerate subspace magnetization $\langle \vec{\sigma} \rangle$. We first prepare the system at $\vec{q}_0 = (q_0/\sqrt{2})(-1, -1, 0, 0, 0)$, where $q_0/2\pi = 2\,\mathrm{kHz}$, and the initial magneti-zation $\langle \vec{\Gamma} \rangle = (1/\sqrt{2})(-1, -1, 0, 0, 0)$. We then drive the system around a "two-dimensional" circular trajectory $\vec{q}(t) = -(q_0/\sqrt{2})(1, \cos \dot{\phi}_A t, \sin \dot{\phi}_A t, 0, 0)$ (3.10) in the range $\phi_A = [0, 2\pi]$. From the local subspace magnetization $\langle \hat{\sigma} \rangle$, we construct for example

$$\langle \hat{\Gamma}_4 \rangle = \langle \hat{\sigma}_0 \otimes \hat{\sigma}_z \rangle = \frac{N_{|1\rangle} + N_{|3\rangle} - N_{|2\rangle} - N_{|4\rangle}}{N_{|1\rangle} + N_{|3\rangle} + N_{|2\rangle} + N_{|4\rangle}}, \qquad (3.25)$$

ultimately in terms of the atomic bare state populations $N_{|1,2,3,4\rangle}$. For a full, four-

dimensional circular trajectory

$$\vec{q}(t) = (q_0/\sqrt{2})(-\cos\dot\phi_A t, -\cos\dot\phi_A t, -\sin\dot\phi_A t, 0, \sin\dot\phi_A t), \qquad (3.26)$$

along $\phi_A = -\phi_B$, the reconstructed spin 3/2 magnetization $\langle\vec{\Gamma}\rangle$ for the initial ground degenerate eigenstate $|\uparrow_-\rangle = (\sqrt{2}|1\rangle - |2\rangle + |4\rangle)/2$ is in figure 3.11. Small deflections in the different projections of $\langle\vec{\Gamma}\rangle$ for the near-parallel transport of $|\uparrow_-\rangle$ are a manifestation of the curvature components in the four-dimensional parameter space.

We continue by investigating the state-dependence of the non-Abelian force in Equation 3.23. For this, we prepare different initial states and drive them along the same trajectory in parameter space. Here, we adopt the explicit spherical coordinates $(q, \theta_1, \theta_2, \phi_1, \phi_2)$ related to our control parameters by the transformations

$$\Omega_A = q\sin\theta_1\cos\theta_2,$$

$$\Omega_B = q\sin\theta_1\sin\theta_2,$$

$$\delta = q\cos\theta_1,$$

$$\phi_1 = (\phi_A + \phi_B)/2,$$

$$\phi_2 = (\phi_A - \phi_B)/2.$$

After preparing different initial states, we drive them along
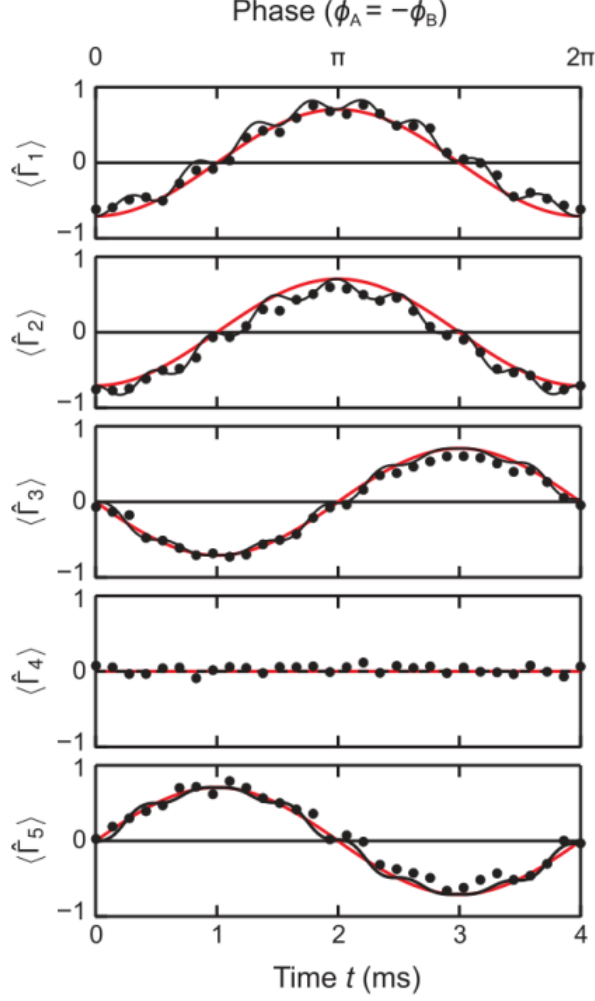
Figure 3.11: Four level state tomography. We reconstruct the generalized magnetization along a four-dimensional circular trajectory from the expectation value of the different $\hat{\Gamma}_i$ (black circles). Continous lines are the numerical solutions to the time dependent Schrodinger equation with Equation 3.18 in the adiabatic limit (red) and including the linear dynamical response (black).

$$\vec{q}_{\pm}(t) = (q_0/\sqrt{2})(-\cos\dot{\phi}_1 t, -\cos\dot{\phi}_1 t, \pm\sin\dot{\phi}_1 t, 0, \pm\sin\dot{\phi}_1 t), \tag{3.27}$$

at a rate $\dot{\phi}_1 = 2\pi \times 0.167\,\text{kHz}$, and measure the integrated deflections along θ_1, directly obtained by $\langle\hat{\Gamma}_4\rangle$. The left plot in Figure 3.12 shows how the magnitude
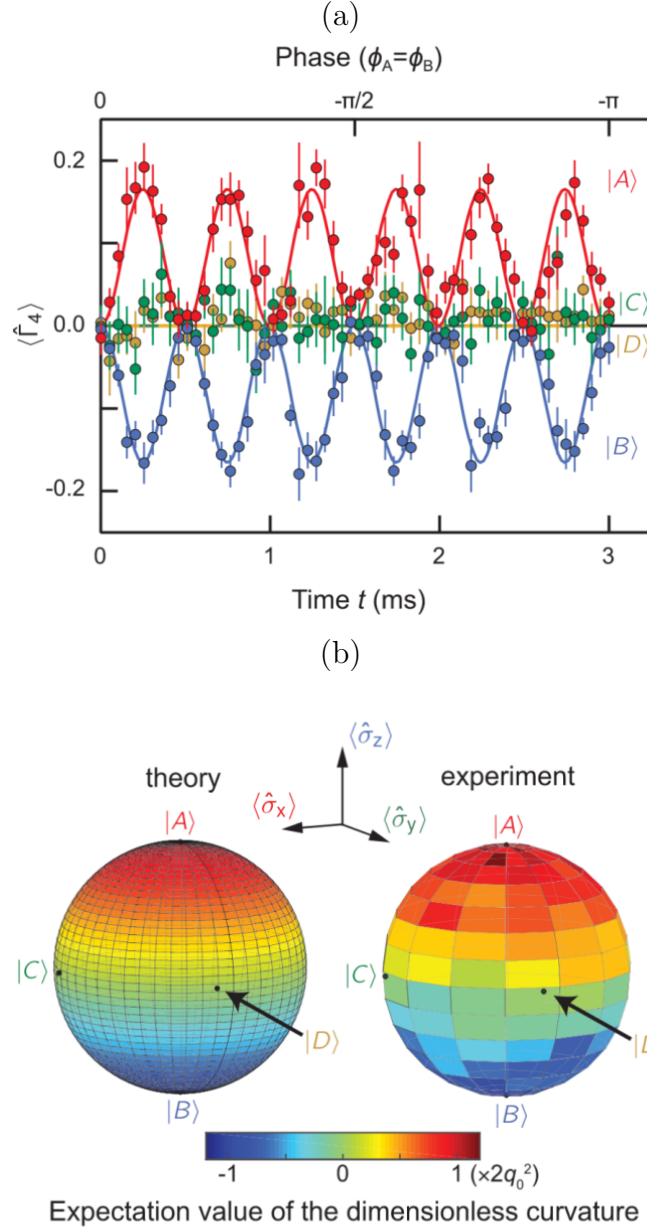
Figure 3.12: State dependent deflections. (a) Different initial states ($|A\rangle, |B\rangle, |C\rangle, |D\rangle$ in red, blue, green and yellow respectively) within the degenerate subspace deflect by different amounts under the same semi-circular trajectory $\vec{q}_-(t)$ along ϕ_1. The amplitude of the deflection is inferred from $\langle \hat{\Gamma}_4 \rangle$. (b) Comparison between theoretical and experimental survey of the dimensionless curvature component $2q_0^2 \hat{F}_{\theta_1\phi_1}$ for different initial states. The colors represent the magnitude of the curvature experienced by different states on the Bloch sphere. Black dots on the colored Bloch sphere show the four initial states $|A\rangle, |B\rangle, |C\rangle, |D\rangle$.

of the deflection changes with four initial states

$$|A\rangle = (\sqrt{2}|1\rangle - |2\rangle + |4\rangle)/2 = |\uparrow_-\rangle,$$

$$|B\rangle = (\sqrt{2}|3\rangle - |2\rangle - |4\rangle)/2 = |\downarrow_-\rangle,$$

$$|C\rangle = (|A\rangle + |B\rangle)/\sqrt{2},$$

and

$$|D\rangle = (|A\rangle + i|B\rangle)/\sqrt{2}$$

in the drive along $\vec{q}_-(t)$. These four independent measurements after a single, $T = 250\,\mu\text{s}$ ramp allow us to determine the four matrix elements of the dimensionless curvature component

$$2q_0^2 \hat{F}_{\theta_1\phi_1} = 0.01\hat{\sigma}_0 - 0.06\hat{\sigma}_x + 0.08\hat{\sigma}_y + 0.98\hat{\sigma}_z \tag{3.28}$$

$$= \begin{pmatrix} 0.99 & -0.06 - 0.08i \\ -0.06 + 0.08i & -0.97 \end{pmatrix} \tag{3.29}$$

in the Pauli matrix representation. The theoretical prediction is $2q_0^2 \hat{F}_{\theta_1\phi_1} = \hat{\sigma}_z$. Similarly, an additional set of four independent measurements give

$$2q_0^2 \hat{F}_{\theta_2\phi_2} = -0.08\hat{\sigma}_0 - 0.12\hat{\sigma}_x - 0.07\hat{\sigma}_y + 1.00\hat{\sigma}_z \tag{3.30}$$

$$= \begin{pmatrix} 0.92 & -0.12 + 0.07i \\ -0.12 - 0.07i & -1.08 \end{pmatrix}, \tag{3.31}$$

in agreement with the theoretical prediction $2q_0^2\hat{F}_{\theta_2\phi_2} = \hat{\sigma}_z$.

Finally, we record state deflections for 225 different initial states and represent the magnitudes of the same curvature component $\hat{F}_{\theta_1\phi_1}$ on the surface of the Bloch sphere (in Figure 3.12) to survey the state dependence, in good agreement with theory.

Prior to the measurement of the second Chern number, we probe how the strength of the non-Abelian gauge field depends with the distance away from the singular point (source). For this, we measure the magnitude of the curvature components with varying coupling strength q_0. Since the value of q_0 represents the hypershperical radius, increasing q_0 has the effect of increasing the distance from the hyperspherical surface S_4 to the monopole.

We perform similar experiments to reconstruct $\langle\hat{F}_{\phi_2\theta_2}\rangle$ for different values of q_0, keeping the linear response parameter $2\pi/q_0T = 0.25$ constant. We find that the non-Abelian Yang monopole is the source of a $1/q^2$ decaying field curvature, with the reconstructed matrix elements of the curvature component as a function of the radius q in Figure 3.13. Our measurement confirms the prediction made by C.N. Yang back in 1967 [53], that monopole fields of the SU(2) Yang–Mills field theory source $1/r^2$ decaying fields.
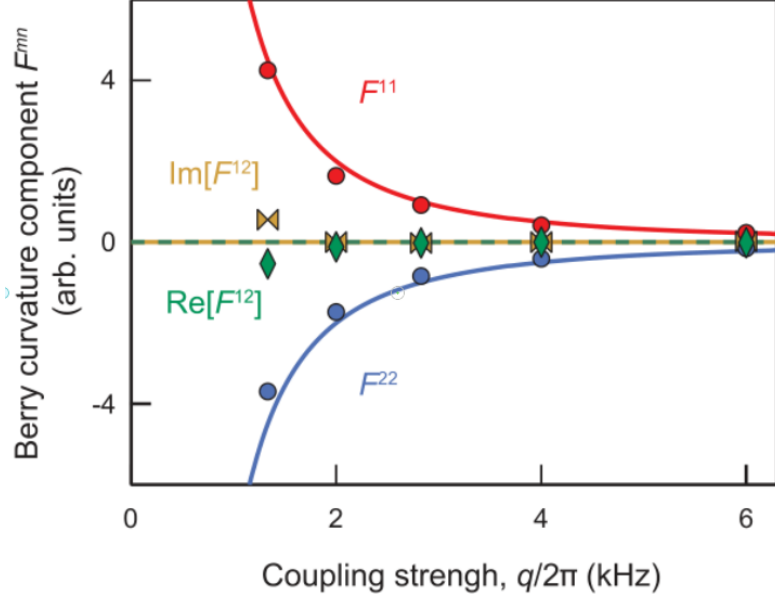
Figure 3.13: Non-Abelian field strength. Matrix elements of the field curvature component $\hat{F}_{\phi_2\theta_2}$ at increasing distances from the source. The curvature component $\hat{F}_{\phi_2\theta_2}$, expected to be proportional to $\hat{\sigma}_z$, shows a decaying magnitude in the nonzero diagonal elements $F^{11}_{\phi_2,\theta_2}$ (red), and $F^{22}_{\phi_2,\theta_2}$ (blue), and vanishing magnitude in the off-diagonal element $F^{12}_{\phi_2,\theta_2} = 0$ (yellow and green), with coupling strength $q = q_0$. The remaining element $F^{21}_{\phi_2,\theta_2}$ (complex conjugate of $F^{12}_{\phi_2,\theta_2}$) is not shown.

Finally, we exploit the hyperspherical symmetry of our parametric hyperspherical manifold S_4 to evaluate the second Chern number. It is sufficient to reconstruct the aforementioned components $\hat{F}_{\phi_1\theta_1}$, and $\hat{F}_{\phi_2\theta_2}$ and numerically integrate the reduced form of the second Chern number

$$C_2 = \frac{3q_0^4}{4\pi^2} \int_{S_4} \mathrm{Tr}(\hat{F}_{\phi_1\theta_1}\hat{F}_{\phi_2\theta_2})d^4S \tag{3.32}$$

where $d^4S = \sin^3\theta_1 \sin 2\theta_2 d\theta_1 d\theta_2 d\phi_1 d\phi_2$ is the hyperspherical surface element.

65

From the curvatures, we evaluate the second Chern number

$$C_2^{(-)} = 2q_0^4 \text{Tr}(\hat{F}_{\phi_1\theta_1}(\vec{q}_-(t))\hat{F}_{\phi_2\theta_2}(\vec{q}_-(t))) = 0.97(6)$$

for the degenerate ground band $|\uparrow\downarrow_-\rangle$, consistent with the theoretical expectation $C_2^{(-)} = 1$. The same measurement in the degenerate excited band $|\uparrow\downarrow_+\rangle$ gives

$$C_2^{(+)} = 2q_0^4 \text{Tr}(\hat{F}_{\phi_1\theta_2}(\vec{q}_+(t))\hat{F}_{\phi_2\theta_1}(\vec{q}_+(t))) = -0.93(6),$$

also in agreement with the theoretical expectation $C_2^{(+)} = -1$, and the sum of the Chern numbers across all bands is zero. We estimate the uncertainty in the measured topological invariants by propagating the uncertainty in atom number ratios (e.g. from Equation 3.25) as uncorrelated variables, since the absorption images in time-of-flight are dominated by photon shot noise and we separate bare state populations with a 3 ms Stern–Gerlach gradient pulse. The nonzero second Chern numbers indicate the manifold is topologically nontrivial, counting the number of SU(2) Yang monopoles enclosed by S_4.

Lastly, we drive a topological transition analogous to the one in the spin 1/2 system, by displacing the manifold away from the location of the singular point (Figure 3.14. We scan the radial offset q_{offset} in units of q_0, the original control field coupling strength, across the transition point $q_{\text{offset}} = 1$ until the hyperspherical manifold no longer encloses the Yang monopole. By simultaneously evaluating the
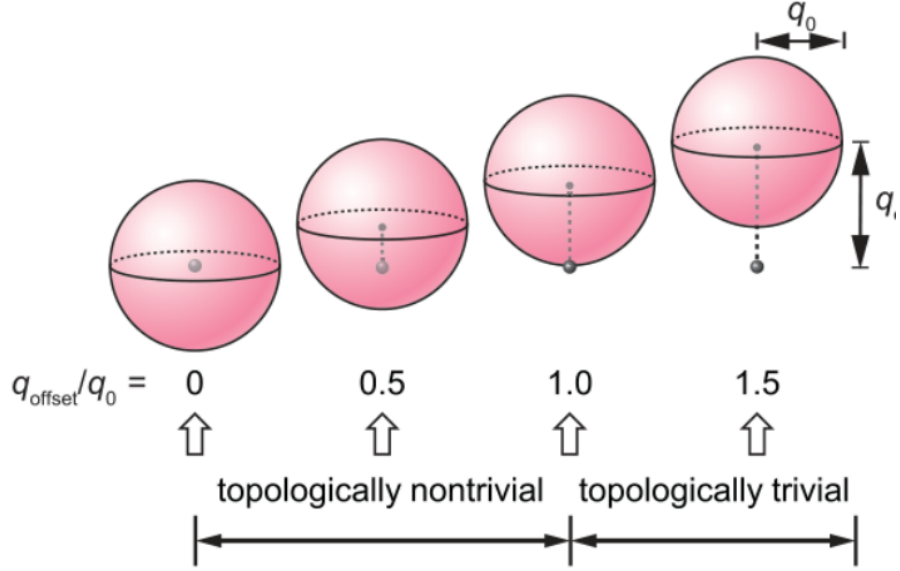
Figure 3.14: Schematic of a topological transition. A second control field displaces the enclosing manifold in parameter space away from the singular point by an amount q_{offset}/q_0. The critical point $q_{\text{offset}} = q_0$ marks the transition where the manifold no longer encloses the monopole.

first Chern number for the degenerate subspaces, we observe that the non-Abelian

topological transition is signaled only by the second Chern number (Figure 3.15)

in both bands. We conclude that the topology of the twofold degenerate spin 3/2

system is characterized by the second Chern number.
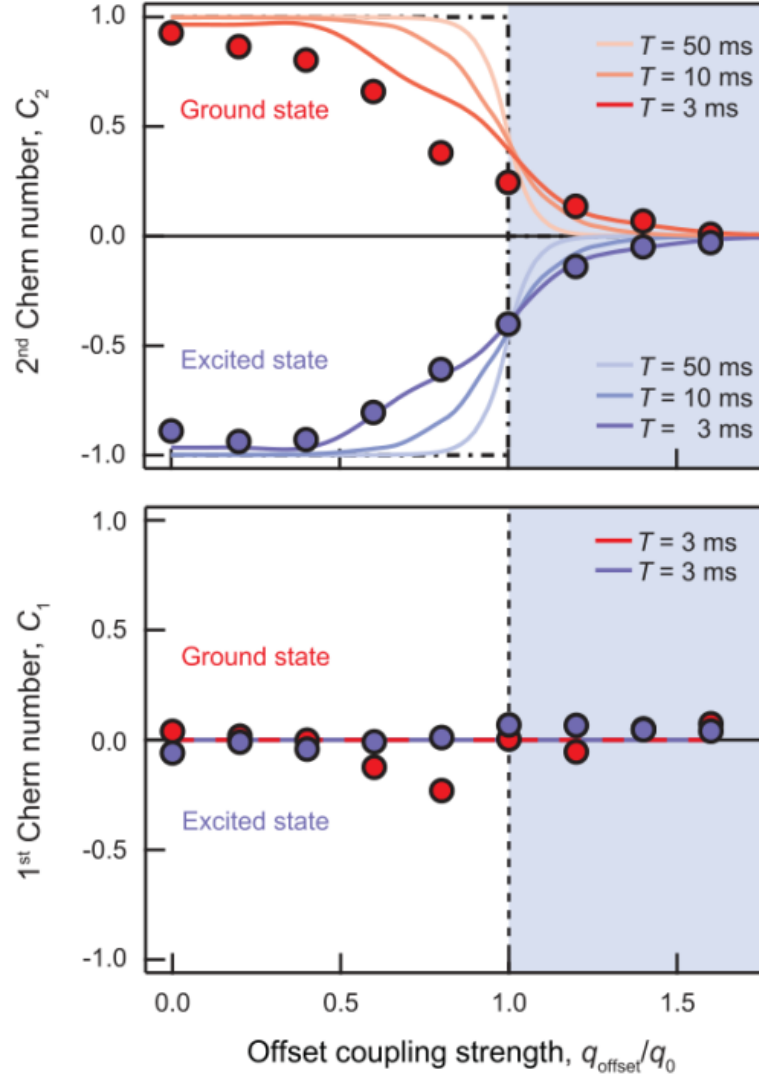
Figure 3.15: First and second Chern numbers across the topological transition. We evaluate both the first and second Chern numbers for the two degenerate submanifolds (ground in red and excited in blue) and observe the driven topological transition only in the second Chern number. As with the spin 1/2 topological transition, the transition sharpens near the true adiabatic limit, which we explicitly avoided. This is confirmed by the numerical predictions in the top, where increasing ramp rates (decreasing drive speed in parameter space) sharpen the topological transition. The first Chern number remains trivial across the transition.

3.3 Conclusion

We reviewed the topology of a spin 3/2 system with a pair of twofold degenerate subspaces. After defining the geometric and topological quantities that characterize gauge fields in the phase of the wavefunctions, we extracted the first Chern number in a spin 1/2 system. For this, we used the concept of generalized forces arising in the artificial parameter space of the Hamiltonian's parameters. We extended the measurement protocol to a higher dimensional quantum system, comprised of two pairs of twofold degenerate bands. Here, we measured the first and second Chern numbers characterizing the non-Abelian gauge field topology. The ideas from this experiment may be extended into other systems to establish new transport paradigms from higher order nontrivial topologies. The work comprising this Chapter is published in [54].

Chapter 4: Methods for *in-situ* microscopy

This chapter describes various methods for imaging quantum gases *in-situ* with modest spatial resolution and optimal signal-to-noise ratio (SNR). I describe basic imaging systems in the context of scalar diffraction, followed by the relevant aspects of light-matter interaction giving rise to the recorded intensity signals. I then present a number of practical calibration methods, and measurements including magnification, spatial resolution, and saturation intensity. I end with a detailed analysis of image processing methods, from estimating uncertainties to implementing linear reconstruction algorithms that improve our SNR.

This chapter is organized as follows. In the first section 4.1, I introduce basic considerations for imaging quantum gases, beginning with scalar diffraction theory and a survey of basic imaging systems in 4.1.1, followed by the semiclassical framework of light-matter interaction in 4.1.2. Later, in section 4.2, I present a few experimental techniques for optimized imaging. These techniques are important for high quality measurements of atomic density or density-density correlations. While some techniques are not specific to *in-situ* imaging, we focus on imaging trapped atomic systems. Beginning with magnification in 4.2.1, spatial resolution

in 4.2.2, and saturation intensity in 4.2.3, and finally, in section 4.3, describe image uncertainty estimation and propagation in 4.3.1, ideal and realistic signal-to-noise ratio from resonant absorption bright-field microscopy in 4.3.2, and a detailed account of image reconstruction algorithms in 4.3.3.

4.1 Microscopy of two-level atoms

In the context of imaging, we may treat a quantum gas as a collection of dipole antennas. Under this powerful abstraction, near-resonant optical fields couple with atomic ensembles, and relay information by absorbing, re-emitting, or shifting the phase of the incident light. The core task in the experiments presented in this thesis is microscopy, or the optimal retrieval of optical information emanating from microscopic systems.

4.1.1 Diffraction and the angular spectrum

A linearly polarized, monochromatic, and time-harmonic complex optical field satisfies the scalar Helmholtz equation

$$[\nabla^2 + k_0^2(1 + \chi(\vec{r}))]E(\vec{r}) = 0 \tag{4.1}$$

as it propagates through an inhomogeneous medium with complex electric susceptibility $\chi(\vec{r})$, and negligible magnetic susceptibility, and where $k_0 = \omega_0/c$, the free-space dispersion relation in terms of the angular frequency ω_0 and the speed

of light c. It is possible to separate the Helmholtz equation

$$[\nabla_\perp^2 + k_0^2]E(\vec{r}) + k_0^2\chi(\vec{r})E(\vec{r}) + \frac{\partial^2 E(\vec{r})}{\partial z^2} = 0, \qquad (4.2)$$

in the transverse and longitudinal differential operators. This equation can be formally integrated in z for a known field

$$E(\vec{r} \pm \delta z \mathbf{e}_z) = \exp\left[\pm i\delta z \sqrt{\nabla_\perp^2 + k_0^2(1 + \chi(\vec{r}))}\right] E(\vec{r}) \qquad (4.3)$$

propagating by $\pm\delta z$ along $\mathbf{e}_z$. A convenient representation of the transverse optical field is the angular spectrum

$$\tilde{E}(k_x, k_y; z) = \hat{\mathcal{F}}[E(\vec{r})] = \frac{1}{4\pi^2}\iint_{-\infty}^{\infty} E(x, y; z)e^{-i(k_x x + k_y y)}\,dx\,dy, \qquad (4.4)$$

in terms of a plane-wave decomposition. The angular spectrum $\tilde{E}(k_x, k_y; z)$ in the transverse spatial frequency space (k_x, k_y) forms a Fourier transform pair with the optical field $E(x, y; z)$ in the coordinate space (x, y), located at z. The angular spectrum transforms to

$$E(k_x, k_y; z \pm \delta z) = E(k_x, k_y, z)e^{\pm ik_z \delta z} \qquad (4.5)$$

under a displacement $\pm \delta z$ in free space propagation. Meanwhile, the longitudinal wavenumber

$$k_z^2 = k_0^2 (1 + \chi_0) - k_x^2 - k_y^2$$

sets a spatial frequency cutoff for evanescent ($k_z^2 < 0$), stationary ($k_z^2 = 0$), and propagating ($k_z^2 > 0$) modes in the homogeneous medium with susceptibility χ_0. In vacuum (or air), Equation 4.5 becomes the formal solution in Equation 4.3 for $\chi(\vec{r}) = 0$, as in Fourier space the transverse operator transforms to $\hat{\mathcal{F}}[\nabla_\perp] = i k_\perp$. When passing through an aperture described by the function $\mathcal{A}(x, y)$, the angular spectrum transforms according to

$$\tilde{E}_+(k_x, k_y; z \pm \delta z) = \hat{\mathcal{F}}[E_-(x, y, z) \mathcal{A}(x, y)]. \tag{4.6}$$

Similarly, upon propagating through a thin lens, the field giving rise to the angular spectrum

$$\tilde{E}_+(k_x, k_y; z) = \hat{\mathcal{F}}[E_-(x, y; z) e^{\frac{i k_0}{2f}(x^2 + y^2)}] \tag{4.7}$$

acquires a quadratic phase factor adding a constant curvature scaled by the focal length f to the wavefront. In the previous two situations, the different momentum components of the angular spectrum $\tilde{E}_+$ evolve according to 4.5 if propagating through free space. One of the key insights of the angular spectrum representation is that most imaging systems act as effective low pass filters for the incident angular

spectra. The high-frequency cutoff gives a diffraction-limited spatial resolution

$$\Delta \simeq \frac{0.61\lambda}{\text{NA}}, \tag{4.8}$$

derived from the Airy pattern an image would show, and related to the largest transverse wavenumber $k_{\text{NA}} = \pi/\Delta$ entering the numerical aperture $\text{NA} = \text{n}\sin\theta$, where θ_{NA} is the half angle of the aperture collecting the scattered field. This limit is valid for small apertures where the incident ray angles satisfy $\sin\theta_{\text{NA}} \approx \theta_{\text{NA}}$, an insight first provided by Abbe in 1867 [55]. We define the field of view using the Strehl ratio convention ... that a lateral translation degrading the spatial resolution by more than $\sim 20\%$ sets the field of view. Longitudinal translations preserve the spatial resolution limit within a depth of field

$$\zeta = \frac{\lambda}{\text{NA}^2}. \tag{4.9}$$

While maximizing the numerical aperture gives finer spatial resolution, the depth of field decreases more rapidly. The depth of field may be related to the Rayleigh range of a Gaussian beam matching the NA at $z >> z_R$ through the half angle described by the focusing/diverging waist away from focus. In this limit, the Rayleigh range $z_R = \zeta/\pi$ is approximately a third of the depth of field.

4.1.2   Imaging systems

An imaging system is the collection of optical elements that map optical fields into other planes along their propagation. Since detection is typically carried out in a two-dimensional plane, an imaging system transforms the transverse optical field from an object plane to the detection, or imaging plane. Different elements of an imaging system perform close to linear transformations on the propagating optical fields in the limit when the index of refraction experienced by the optical fields is independent of the intensity. The following examples of imaging systems are intended for the advanced undergraduate or graduate student starting the design of a simple imaging system.

A lensless imaging system (Figure 4.1) may contain flat mirrors, and apertures, but no lenses or other curved surfaces. Lensless imaging systems have no magnifying effect on the objects encoded by the optical field distributions. Since the intensity in the far field decays with the squared distance, for significantly distant objects the intensity becomes quite small, making recording more difficult in practice. Nevertheless, lensless microscopy does not compromise the image quality (i.e. reduced aberrations) at the detector.

A single lens imaging system may contain mirrors, apertures and one lens. Single lens microscopes are practical for either large or small values of the mag-
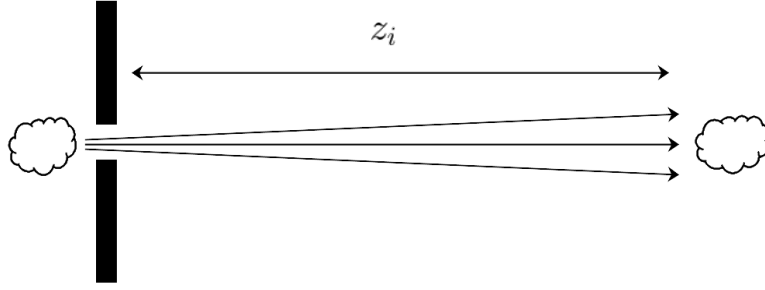
Figure 4.1: Lensless imaging system. The distance from the aperture to where an image is formed is z_i.

nification, especially in applications with constrained longitudinal space. A single (thin) lens imaging system produces images in different planes according to the lens-maker equation

$$\frac{1}{z_o} + \frac{1}{z_i} = \frac{1}{f}, \tag{4.10}$$

with magnification

$$M = -\frac{z_o}{z_i} \tag{4.11}$$

equal to the ratio of the distances from the lens to the object z_o and to the image z_i. The negative sign signifies a vertical inversion with respect to the orientation of the object. As an example, to demagnify an object by a factor of $1/3$, equation 4.11 relates the distances from object to image as $3z_o = z_i$. Then, picking an $f = 100\,\text{mm}$ singlet to realize this gives the values $z_o = 133\,\text{mm}$ and $z_i = 400\,\text{mm}$ through 4.10. In single lens imaging systems, when the object is placed at $z_o < f$ it forms a virtual image, i.e. with no projection.

A two lens imaging system may contain mirrors, apertures, and two lenses.
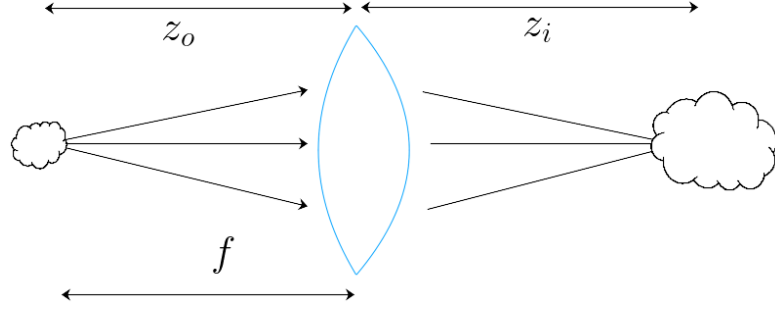
Figure 4.2: Single lens imaging system. The distance from the object to the lens is z_o, while the distance from the lens to the image is z_i. The lens has focal length f.

Two lens microscopes are a popular choice as they image optical fields in a more general way, and give access to Fourier planes. A Fourier plane is the plane where the angular spectrum of an optical field becomes diagonal in real space and the intensity represents a Fourier transform. This allows additional control on the angular spectrum (e.g. adding an aperture performs a spatial frequency filter). We can work out the effect of a two lens imaging system by chaining two single lens imaging systems. The distance from the object to the first (objective) lens with focal length f_1 is z_o, forming an image in

$$z_1^{-1} = f_1^{-1} - z_o^{-1} \tag{4.12}$$

with magnification $M_1 = -z_o/z_1$. Then, a second (eyepiece) lens with focal length f_2, at a distance z_2 behind z_1 forms an image in

$$z_i^{-1} = f_2^{-1} - z_2^{-1} \tag{4.13}$$

77

with additional magnification $M_2 = -z_2/z_i$. The total magnification becomes $M = M_1 M_2$. An interesting case arises when $z_o = f_1$, and $z_i = f_2$. There, the total magnification $M = -f_2/f_1$ given by the ratio of the focal lengths. As an
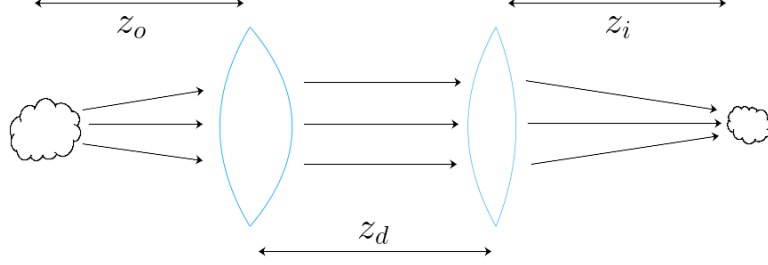
Figure 4.3: Two lens imaging system. The ray diagram corresponds to the path traveled by light. An image will form f_2 away from the second lens when the object is exactly at a distance f_1.

example, to magnify an object by $M = 8$ using a two lens imaging system, using an $f_1 = 40\,\text{mm}$ objective lens, we need to place an $f_2 = 320\,\text{mm}$ eyepiece a distance $z_d = 360\,\text{mm}$ behind the objective.

4.1.3 Light-matter interaction

The theory of scalar atom-light interaction describes how near-resonant light induces an electric dipole on the atom, which then scatters the light field. Several frameworks capture this interaction for a two-level system, including the minimal set of optical Bloch equations for the density matrix in the rotating frame of the

incident field [56]

$$\dot{\rho}_{ee} = i\frac{\Omega}{2}\left(\rho_{eg} - \rho_{ge}\right) - \Gamma\rho_{ee}$$

$$\dot{\rho}_{gg} = -i\frac{\Omega}{2}\left(\rho_{eg} - \rho_{ge}\right) + \Gamma\rho_{ee}$$

$$\dot{\rho}_{ge} = -\left(i\delta + \frac{\Gamma}{2}\right)\rho_{ge} - i\frac{\Omega}{2}(\rho_{ee} - \rho_{gg})$$

$$\dot{\rho}_{eg} = -\left(-i\delta + \frac{\Gamma}{2}\right)\rho_{eg} + i\frac{\Omega}{2}(\rho_{ee} - \rho_{gg})$$

describing the evolution of the driven system with coupling strength Ω, detuning $\delta = \omega - \omega_0$ from resonance, and damping Γ capturing the spontaneous emission from the excited state. The optical Bloch equations account for the evolution of ground $|g\rangle$, and excited $|e\rangle$ state populations through the matrix elements $\rho_{gg} + \rho_{ee} = 1$, as well as the atomic state coherences in $\rho_{eg} = \rho_{ge}^*$. The steady state solution obtained by setting $\dot{\rho} = 0$ in the optical Bloch system above gives the excited state population

$$\rho_{ee}^{ss} = \frac{\Omega^2}{\Gamma^2}\frac{1}{1 + \frac{2\delta^2}{\Gamma^2} + \frac{2\Omega^2}{\Gamma^2}} \tag{4.14}$$

from which the unitarity of $\hat{\rho}$ gives $\rho_{gg} = 1 - \rho_{ee}$. Similarly, the steady-state off-diagonal element related to the coherence is

$$\rho_{eg}^{ss} = -\frac{i\Omega}{\Gamma}\frac{1 + \frac{2i\delta}{\Gamma}}{1 + \frac{2\delta^2}{\Gamma^2} + \frac{2\Omega^2}{\Gamma^2}}, \tag{4.15}$$

from which the hermiticity of $\hat{\rho}$ gives $\rho_{eg} = \rho_{ge}^*$. The two-level atomic polarizability can be rewritten to give the macroscopic linear, electric susceptibility

$$\begin{aligned}
\chi(\vec{r}, \delta) &= \frac{\alpha(s_0, \delta)}{\epsilon_0} n(\vec{r}) \\
&= \frac{\sigma_0}{k_0} \frac{i - \bar{\delta}}{1 + s_0 + \bar{\delta}^2} n(\vec{r})
\end{aligned} \tag{4.16}$$

from the off-diagonal density matrix element solution. The steady state susceptibility governs light propagation inside the atomic medium, and gives its optical properties such as absorption, and phase shifts proportional to the atomic density distribution $n(\vec{r})$. The susceptibility in Equation 4.16 is in terms of the saturation parameter $s_0 = 2\Omega^2/\Gamma^2$, reduced detuning $\bar{\delta} = 2\delta/\Gamma$, driving field wavenumber $k_0 = 2\pi/\lambda$, and resonant atomic cross section $\sigma_0 = 3\lambda^2/2\pi$. Figure 4.4 illustrates the near-resonant absorption and phase-shift of a homogeneous cloud.
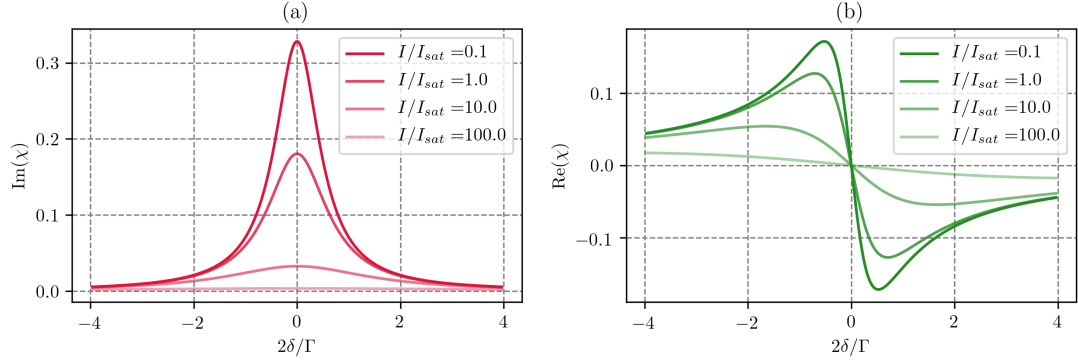
Figure 4.4: Two-level atomic susceptibility. Calculated (a) imaginary, and (b) real parts of the two-level atomic susceptibility from Equation 4.16. The power broadening is evident by the different saturation parameters. Other parameters used in this calculation are $\Gamma/2\pi = 6.06\,\mathrm{MHz}$, $\lambda = 780.24\,\mathrm{nm}$, $I_{\mathrm{sat}} = 1.67\,\mathrm{mW/cm^2}$, and a density of $n_0 = 10^{13}\,\mathrm{cm^{-3}}$ for $^{87}\mathrm{Rb}$.

The imaginary part of the susceptibility represents the absorption of a two-level atomic ensemble, where scattering of a near-resonant field causes intensity attenuation along the propagation of light

$$\frac{dI}{dz} = -n\sigma_0 I \frac{1}{1 + I/I_{\text{sat}}} \tag{4.17}$$

proportional to the density of the medium n [56]. The solution including saturation effects

$$n_{\text{col}}\sigma_0 = -\ln\left(\frac{I_a - I_d}{I_p - I_d}\right) + \frac{I_p - I_a}{I_{\text{sat}}}, \tag{4.18}$$

comprises the Beer–Lambert law giving the optical depth where n_{col} is the integrated column density of the cloud, I_a represents the intensity in the presence of atomic scatterers, I_p represents the intensity in the absence of scatterers, and the subtracted I_d represents the removal of the technical noise baseline.

4.2 Calibration methods for imaging systems

4.2.1 Magnification

We calibrate the magnification of imaging systems using two different methods. One method uses a testbench and the other uses the atoms.

We place in the first method a calibrated `USAF-1951` test target with sets of vertical and horizontal stripes sampling spatial frequencies down to $0.228\,\mu\text{m}^{-1}$

($\Delta x_{\min} = 4.38\,\mu$m). After setting up an imaging system, we first image the back illuminated `USAF-1951` test target in focus, shown in Figure 4.5. Then, we take the cross-sectional intensity across multiple line pairs, or elements labeled by e, belonging to a same group g. Finally, we find the line edges and compute the distances between them. The spatial frequencies (multiple line pairs = lp)

$$k_{lp} = 2^{g+(e-1)/6} \tag{4.19}$$

(in lp per mm) for group g and elements e, allow us to back out as many values of the magnification as the number of sampled group elements. The magnification may vary across the field-of-view due to resolution effects and/or uncertainty in line edge location, and we therefore take the mean magnification out of a single group when the variance is not too large. As an example, Figure 4.5 shows the measured magnification of $\langle M \rangle = 4.03(4)$ of a two-lens imaging system with $f_2 = 150\,$mm, and $f_1 = 34.3\,$mm, where the expected magnification is $M_{exp} = 4.37$, using group 6, and elements 2 through 6.

In the second method we scan the time-of-flight (TOF) of a falling cloud of atoms and measure its position as a function of time. The trajectory on the detector

$$y_d(t) = M\left(y_0 + v_0 t + \frac{1}{2}gt^2\right), \tag{4.20}$$

is magnified by a factor M. We fit the trajectory of the cloud to a scaled parabola and back out the magnification as a free parameter (assuming $g = 9.81\,$m/s^2). It
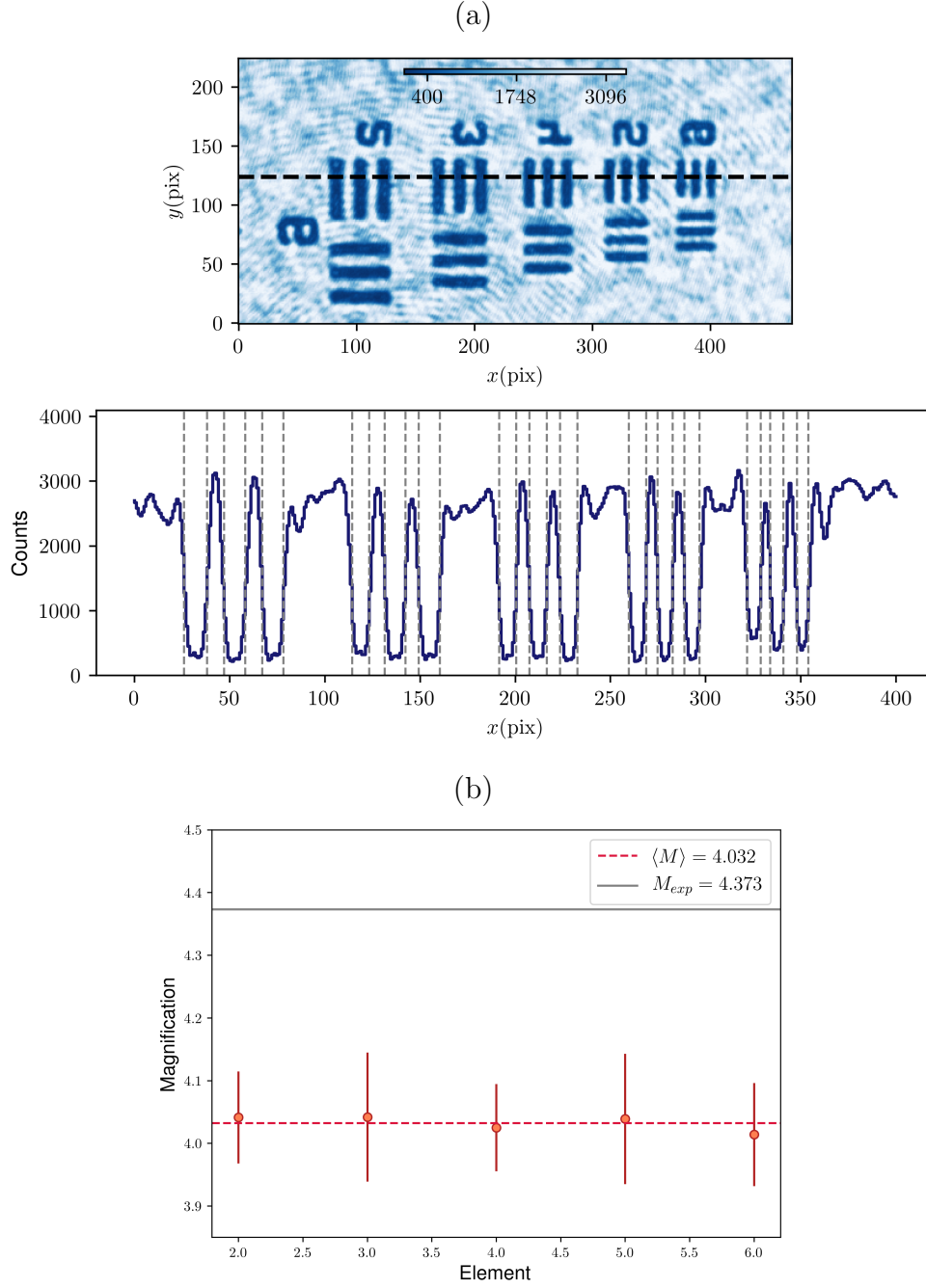
Figure 4.5: Measured magnification using a `USAF-1951` test target. (a) Image of test target pattern and horizontal cross-section giving distances in pixels between 5 different sets of lines (dashed gray). (b) Magnification from 5 different group 6 elements (red circles) and average (dashed red line). Errors in the two-lens locations and focal lengths propagate into the measured magnification $M = 4.03(11)$, different from the expected two-lens magnification (solid gray line) by $\approx 8\%$.

is desirable to do this experiment using an $|m_F = 0\rangle$ cloud as it is insensitive to stray magnetic field gradients that may change its trajectory. Figure 4.6 shows an example of this calibration method for a different imaging system,
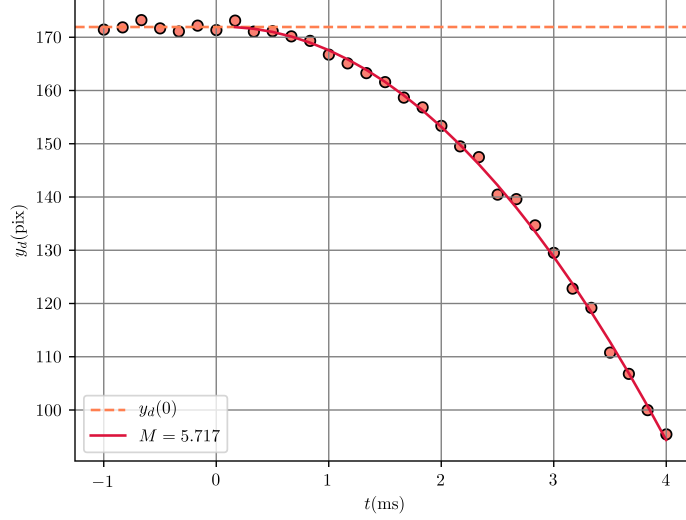
Figure 4.6: Measured magnification using free fall. By imaging a freely falling cloud of atoms, we reconstructh the unmagnified vertical trajectory from $t = -1\,\mathrm{ms}$, before the cloud is released in free fall, to $t = 4\,\mathrm{ms}$ after. The fit parabolic trajectory (solid red) spanning $t > 0$ gives the magnified trajectory, from which $M = 5.72(7)$.

4.2.2   Spatial resolution

We only calibrate the spatial resolution of an imaging system directly on a test bench setup. By using circular apertures with radius $a \ll \Delta$, much smaller than the expected diffraction-limited resolution of the imaging system, we produce images resembling Airy patterns on the image plane. For most $\lambda = 780\,\mathrm{nm}$ illumination microscopes, a $a = 1\,\mu\mathrm{m}$ pinhole is sufficient. Two example intensity patterns are in Figure 4.7, corresponding to a cut of the three-dimensional
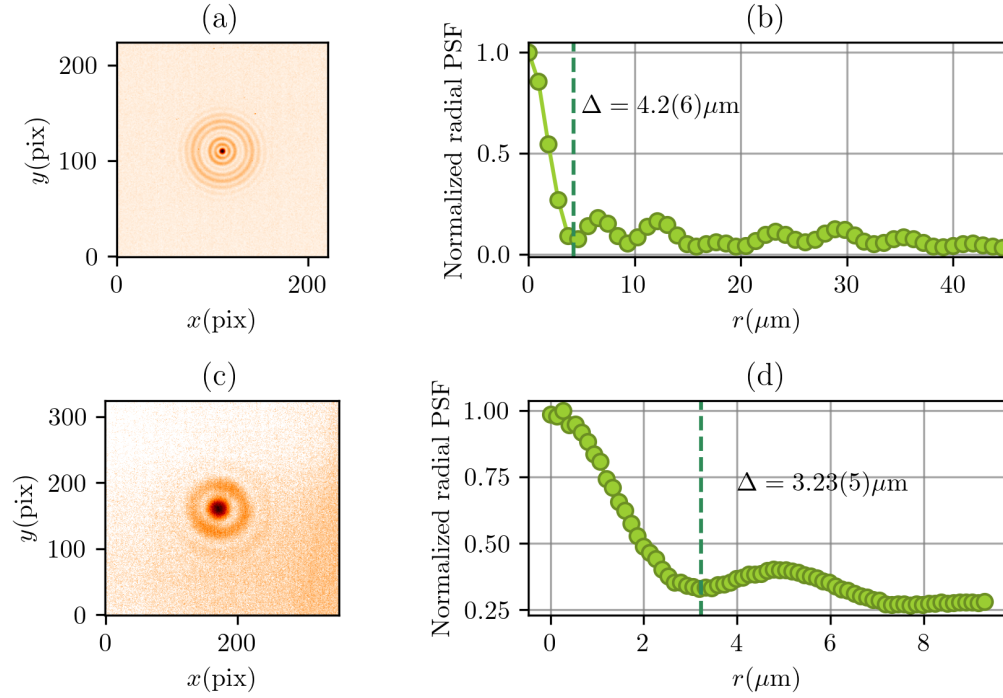
Figure 4.7: Measured point spread functions. (a) Point spread function (PSF) of a $1\,\mu$m pinhole imaged using an $M = 6$ imaging system dominated by spherical aberrations. (b) Azimuthally integrated PSF giving an effective spatial resolution of $\Delta = 4.2\,\mu$m. (c) PSF of a $1\,\mu$m pinhole using an $M = 42$ imaging system. (d) Azimuthally integrated PSF giving an effective spatial resolution of $\Delta = 3.2\,\mu$m.

point-spread-function (PSF) of two different imaging systems. In the absence of a perfect Airy intensity pattern, we take the effective spatial resolution as the distance from the peak to the first minimum of the intensity distribution. A practical consideration shown in Figure 4.7 is that while a larger magnification gives a larger number of pixels per diffraction ring in favor of a more precise calibration, the signal-to-noise ratio is worse under a similar exposure.

4.2.3 Saturation intensity

We probe our $|F = 2\rangle$ atomic ensembles with circularly polarized, resonant Gaussian beams. The choice of circular polarization in combination with nonzero bias magnetic fields addresses the effective two-level, stretched state ($|F = 2\rangle \rightarrow |F' = 3\rangle$) transition in the D_2 line of ^{87}Rb. Following [57], we typically pulse our resonant probe for $\tau = 20\,\mu$s, well within the recommended $\tau \leq 40\,\mu$s for ^{87}Rb to avoid changing the velocity enough so that the Doppler shift moves the cloud significantly away from resonance within the pulse time window. After the atoms scatter light, we image the scattered intensity I_a. Then, we pulse the probe a second time and image the intensity in the absence of scatterers I_p. A third image contains the dark field intensity I_d representing the technical noise baseline and stray background illumination. In the absence of saturation effects, we simply combine these images using the first term in Equation 4.18. Nevertheless, in spite of the inhomogeneous probe intensity over the cloud, an important calibration for the absorption profile of an atomic density distribution is I_{sat}, the saturation intensity at the cloud calibrated in counts per pixel at the image after a single exposure. Here, we present five different methods to calibrate the saturation intensity parameter. Since each I_{sat} calibration depends on the magnification of the imaging system, the examples below represent different instances of our *in-situ* imaging system and need not yield the same value.

First is the beam profiling method, combining the intensity of a probe beam and a measurement of its power, assuming that the uncalibrated count rate from the intensity profile match the measured power

$$P_0 = \sum_i I_i \Delta_p^2$$

where I_i is the intensity at pixel i and Δ_p is the square pixel size. As an ex-
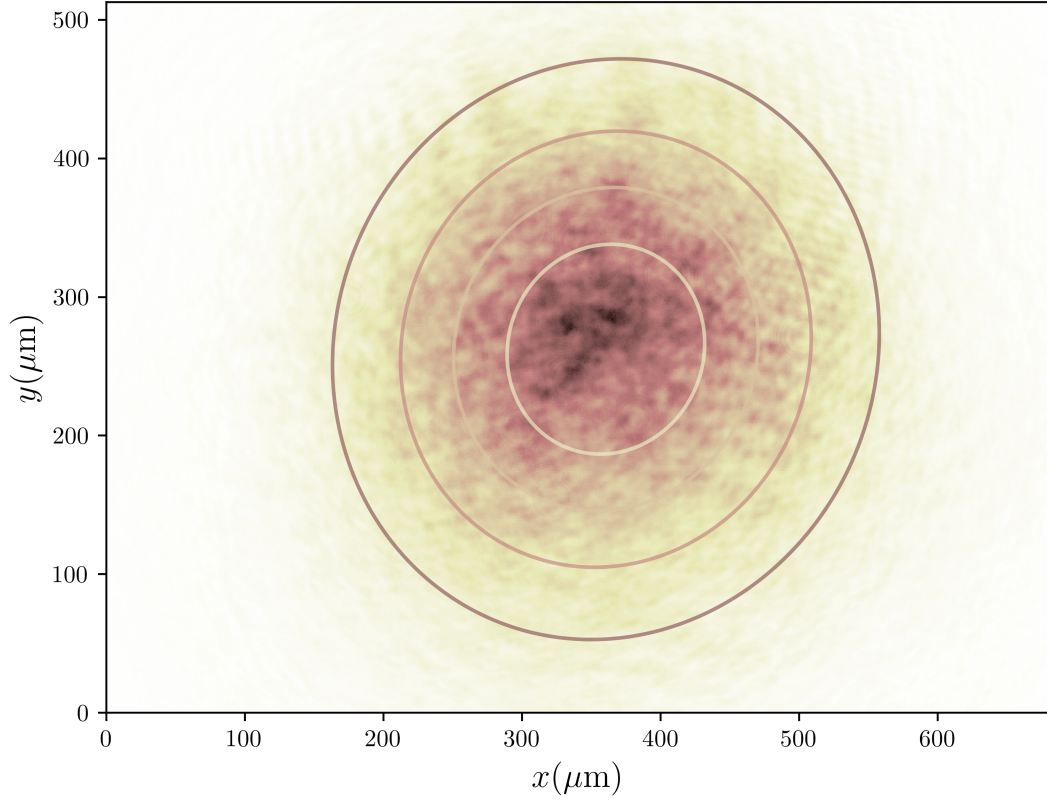
Figure 4.8: Beam profiling for I_{sat}. Raw probe intensity profile and Gaussian fit contours outlining σ, 2σ, 3σ, and 4σ away from the center.

ample of this method, we measure $P_0 = 23.3(7)\,\mu\text{W}$ with a calibrated 3% power meter in the probe from Figure 4.8 without taking into account any sensitivity

or gain variations right after the objective lens, but estimate $P_0 \approx 25.3(7)\,\mu\mathrm{W}$ at the location of the atoms after correcting for imperfect transmission factors (on the level of a few 0.1% per anti-reflection coated surface). Then, a two-dimensional Gaussian fit to the intensity profile gives a peak $I_m = 1966\,\mathrm{counts}$, and minor, and major waists $w_u = 103.6\,\mu\mathrm{m}$ and $w_v = 112.2\,\mu\mathrm{m}$. We then integrate to find the power $P_0 = 2\pi I_m w_u w_v$ from the two-dimensional Gaussian fit depicted in Figure 4.8 as the contours. The power from the beam profile $P_0 = 143.6 \times 10^6\,\mathrm{counts}$ gives a conversion factor of $5.76 \times 10^6\,\mathrm{counts}/\mu\mathrm{W}$. Taking the value for $I_{\mathrm{sat}} = 1.67\,\mathrm{mW/cm^2}$ for the stretched state imaging transition, the demagnified pixel area Δ_p^2/M^2, and the conversion factor (magnification $M = 5.33(10)$), we get a value $I_{\mathrm{sat}} = 104(15)\,\mathrm{counts/pixel}$. A drawback of this method is that the calibration compares an estimated intensity near the atoms with an intensity profile in the image plane, where the intensity is most certainly aberrated, magnified, and sometimes depleted by spurious scattering (e.g. dust, clipping apertures), causing this method to underestimate the saturation intensity value.

The second and third methods use the single photon recoil and power broadening effects respectively. The second method first demonstrated in [58], uses an orthogonal imaging system to look at the trajectory of the recoiling cloud in short time-of-flight following an imaging probe pulse. There, the displacement is limited

by the photon scattering rate

$$z(\delta, s_0) = z_0 + \eta \frac{\Gamma}{2} \frac{s_0}{1 + s_0 + \bar{\delta}^2} \tag{4.21}$$

where η is the conversion from scattering rate measured displacement for fixed scattering time. For this method and the third one, it is sufficient to take a set of data comprising the measured displacement of the cloud as a function of probe detuning and intensity. The second method measures the resonant peak displacement

$$\delta z = \delta z_{\text{max}} \frac{I/I_{\text{sat}}}{1 + I/I_{\text{sat}}}, \tag{4.22}$$

which reaches half of δz_{max} at exactly $I = I_{\text{sat}}$. We demonstrate this method in Figure 4.9, where an unweighted fit to the displacement gives $I_{sat} = 188(12)$counts. We then use the same dataset in Figure 4.9 (a) for the third method, where the effective linewidth

$$\Gamma_{\text{eff}} = \Gamma \sqrt{1 + I/I_{\text{sat}}} \tag{4.23}$$

broadens with increasing probe intensity [59]. Then, from a least squares fit to Equation 4.23, we find $I_{\text{sat}} = 225(19)$counts. In this case both numbers are in reasonable agreement, even though they come from slightly different physical effects.

The fourth method uses different approximations of the corrected Beer–Lambert law, writing the mean difference in counts between I_p, and I_a at the

(a)

(b)
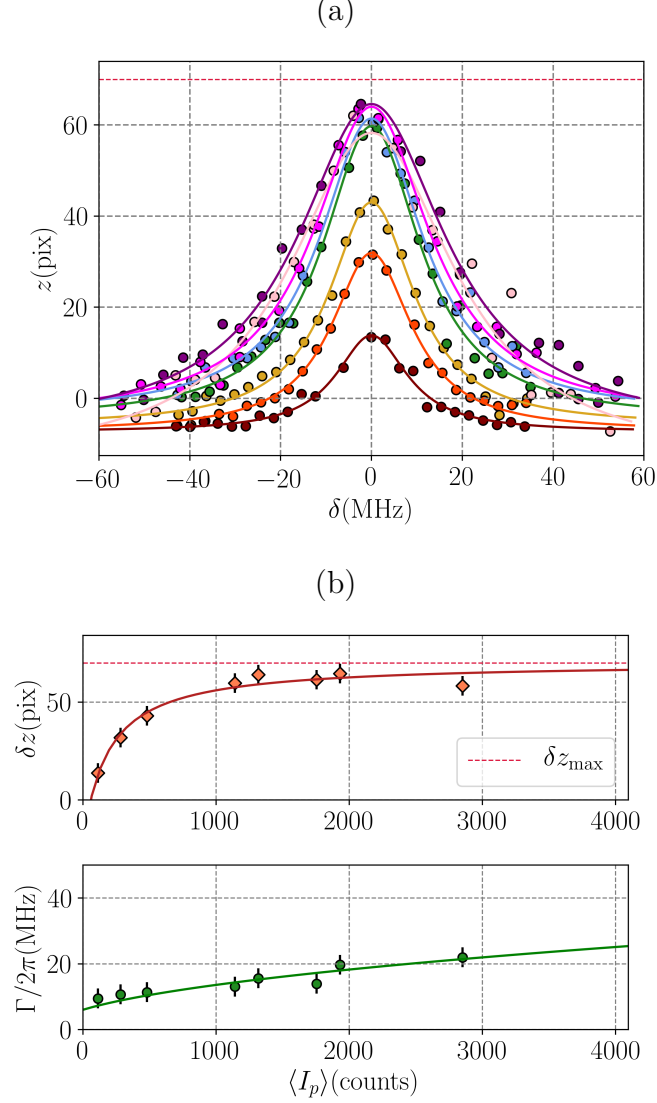
Figure 4.9: Displacement and power broadening for I_{sat}. (a) Measured cloud displacement across resonance for different probe intensities at fixed 20 μs of probe pulse time. (b) The measured peak displacement (diamonds) is proportional to the scattering rate (Equation 4.22), while the power broadened linewidth (circles) gives I_{sat} from Equation 4.23.

location of the cloud. While the exact Beer–Lambert solution and the approximations contain the same information, solving for I_{sat} using the difference in intensity rather than the nonlinear Equation 4.18 is more convenient if the approximations hold.

90

We start with the corrected optical depth in Equation 4.18. In the first limit, we assume a low probe intensity $I_p \ll I_{\mathrm{sat}}$, and low optical depth (low density) $n\sigma_0 \ll 1$, first allowing us to neglect the correction term so the absorbed fraction $I_a = I_p \exp(-n\sigma_0)$ from which we find a linear dependence $I_p - I_a = n\sigma_0 I_p$. We then linearize this relation to get $I_a \approx I_p(1 - n\sigma_0)$. On the other hand, in the opposite limit of large probe intensity $I_p \gg I_{\mathrm{sat}}$, we see that the saturation correction term is well in excess of the first term in Equation 4.18, allowing us to approximate $n\sigma_0 \approx (I_p - I_a)/I_{\mathrm{sat}}$. The transition from one approximation to the other at constant optical depth marks the value for I_{sat}. Finally we consider dilute clouds with negligible absorption such that $I_a \approx I_p$. There we may use the absorbed fraction $I_a/I_p = 1 - \eta$ to linearize the nonlinear term $\ln(1 - \eta) \approx -\eta$. In this approximation the optical depth reads $n\sigma_0 \approx (I_p - I_a)/I_p + (I_p - I_a)/I_{\mathrm{sat}}$, and the difference in counts is $I_p - I_a \approx n\sigma_0 I_p I_{\mathrm{sat}}/(I_p + I_{\mathrm{sat}})$. Table 4.1 summarizes the different approximations and the expected difference in intensities between I_p and I_a.

Low intensity, low density	High intensity, any density	Any intensity, low density
$I_p \ll I_{\mathrm{sat}}$, $n\sigma_0 \ll 1$	$I_p \gg I_{\mathrm{sat}}$	$I_a \approx I_p$
$I_p - I_a \approx n\sigma_0 I_p$	$I_p - I_a \approx n\sigma_0 I_{\mathrm{sat}}$	$I_p - I_a \approx n\sigma_0 \frac{I_p I_{\mathrm{sat}}}{I_p + I_{\mathrm{sat}}}$

Table 4.1: Beer–Lambert law approximations. Columns indicate the different regimes, approximations, and expected difference in counts between I_p and I_a.

Figure 4.10 illustrates a determination of I_{sat} using all three approximations.

We use a dilute cloud of atoms (where all three approximations hold) and measure the mean difference in counts per pixel between I_p and I_a at the location of the atoms. The dilute, elongated cloud of atoms has uncorrected (first term of Equation 4.18) optical depth of $n\sigma_0 = 0.15(5)$. Using both the crossover from linear to constant difference and the third approximation valid for all intensities, we fit the data and extract the optical depth $n_{\text{col}}\sigma_0 = 0.436(42)$ and the saturation intensity $I_{\text{sat}} = 226(34)$counts/pixel. The diagonal elements of the covariance matrix from the weigthed least-squares fit give the errors in the corrected optical depth and the saturation intensity, with a reduced chi-squared parameter $\chi^2 = 2.29$ suggesting that the photon shot noise uncertainty in the mean intensity difference is insufficient, especially at high probe intensity, where saturated absorption images cause large fluctuations in $I_p - I_a$.

The final method uses the sensor specifications, and is by far the simplest, requiring no atoms and a single set of measurements. In this method, we take a set of probe images at varying intensities and analyze the count statistics over a region with small structural probe fluctuations. Then, by fitting the variance with the power expansion model

$$\sigma_I^2 \approx \sigma_t^2 + \alpha \langle I_p \rangle + \beta \langle I_p \rangle^2 \tag{4.24}$$

where the first term σ_t^2 represents the technical noise variance independent of I_p,
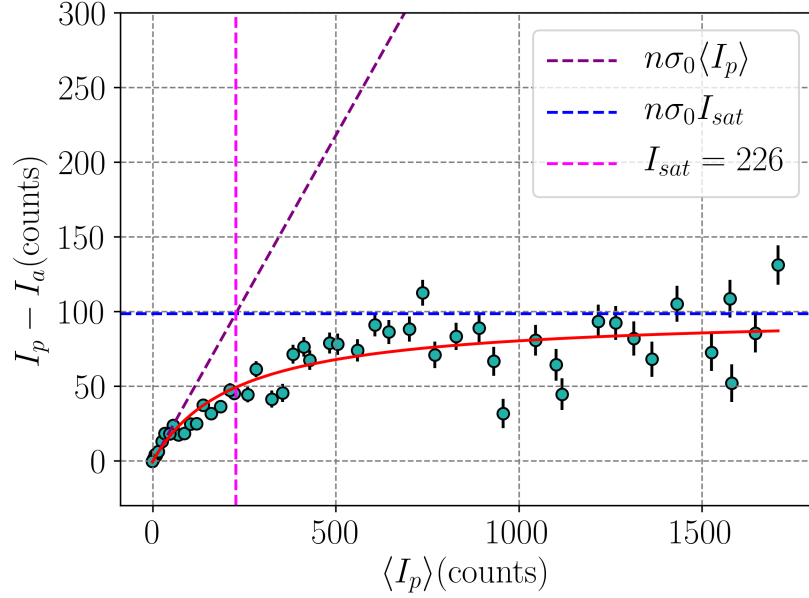
Figure 4.10: Linearized Beer–Lambert law measurement. The mean difference in atoms and probe images at the location of a dilute cloud of atoms $n\sigma_0 < 1$ as a function of incident probe intensity. The transition (dashed pink) point from the low intensity limit (dashed purple) to high intensity limit (dashed blue) gives I_{sat}. A weighted least squares fit (continous red curve) in the low density approximation gives a full model regardless of the probe intensity.

the second term represents photon shot noise with scaling factor α between counts and photoelectrons, and the third term captures the probe intensity fluctuations from spatial inhomogeneities over a region of interest. We are interested in isolating α from a single probe image to get a direct measurement of the linear conversion factor between counts and photoelectrons. Then, we may calibrate I_{sat} by combining the measurement of α with other sensor specifications. In practice, since our Gaussian probes are dominated by spatial inhomogeneities, we apply a set of spatial lowpass and highpass filters with different cutoff frequencies to systematically identify the mean (from the lowpass filtered intensity), and variance (from

the highpass filtered intensity). Figure 4.11 (a) shows the variance as a function of the mean detected counts in the absence of a lowpass filter along with a fit to the model in Equation 4.24, and Figure 4.11 (b) shows the linear fit coefficients for different lowpass cutoff frequencies, where the filtered fraction is the number of pixels within the spatial filter cutoff frequency divided by total number of pixels. We extrapolate the nominal values of the different coefficients from the linear intercept representing the unfiltered probe image to avoid low number statistics from small filter cutoffs. After extrapolating all coefficients for an unfiltered probe image, the background offset coefficient the technical noise gives $\sigma_t(0) \approx \sqrt{10}\,\mathrm{e}^-$, while $\alpha(0) = 0.239(11)\,\mathrm{counts/e}^-$. We proceed with a chain of unit conversions using sensor specifications and the characteristics of the probe pulse. First, a single $\lambda = 780\,\mathrm{nm}$ photon carries $\epsilon_\gamma = 2.53 \times 10^{-19}\,\mathrm{J}$ of energy, and the transition saturates at $I_{\mathrm{sat}} = 6.6 \times 10^{15}\,\mathrm{photons/s\,cm^2}$. Then, we use the object pixel area $(\Delta_p/M)^2$, where M is the magnification to convert into photons per second per pixel. Finally, we use the measured coefficient $\alpha(0)$, the manufacturer specified quantum efficiency of 0.35 to convert between photons and photoelectrons, a $20\,\mu\mathrm{s}$ pulse time, and the specified number of counts per photoelectron to get $I_{\mathrm{sat}} = 122(10)\,\mathrm{counts}$.

The different calibration methods do not overlap as we attempt them in alternating imaging systems, where the magnification, atomic clouds, and probe intensity all change. Nevertheless, Table 4.2 summarizes the different methods,
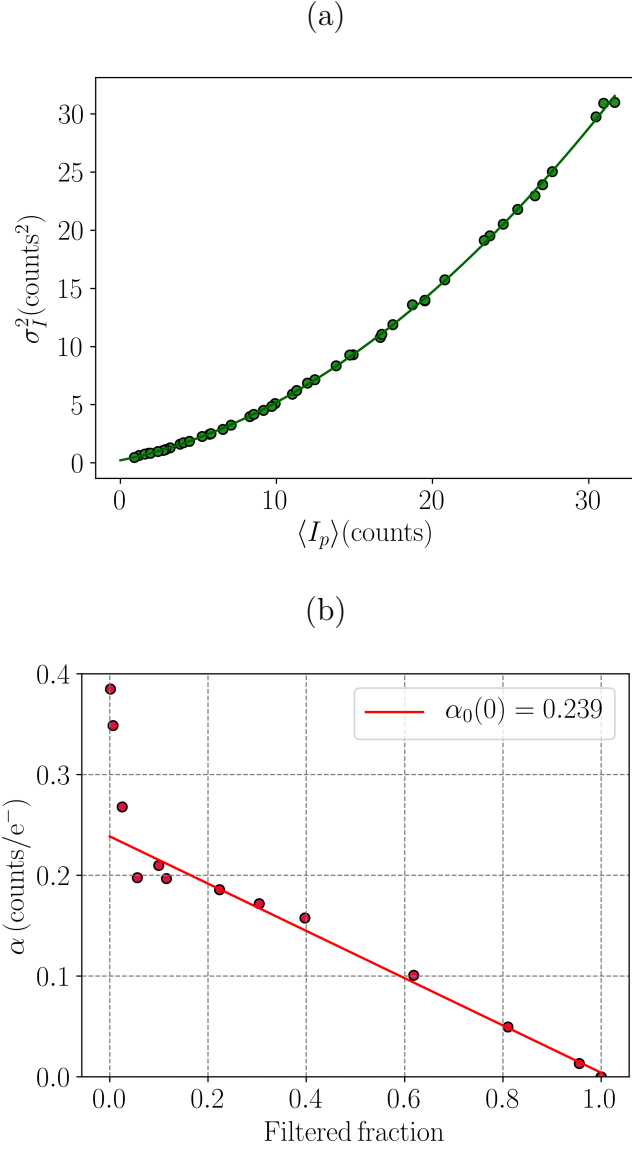
Figure 4.11: Probe intensity statistics. (a) Probe variance as a function of mean over a region of interest (circles) and fit to Equation 4.24 (solid line) for an unfiltered image where the dominant statistical coefficient is β. (b) Measured linear coefficient (circles) as a function of filtered fraction (see text). The linear extrapolation (solid line) gives the background linear coefficient α_0.

the calibrated values, and their biggest drawbacks.

Method	I_{sat} (counts/pixel)	Drawback(s)
Beam profile	104(15)	Typically underestimates calibration and assumes independent power measurement calibration
Recoiling cloud	188(12)	Needs two orthogonal imaging systems, and is subject to increasing Doppler shifts for long pulses [57]
Power broadening	225(19)	Requires power and frequency stabilization of the probe laser
Beer-Lambert approximations	226(34)	Needs good atom number stability and only meets two of the three approximations at low densities ($n\sigma_0 < 1$)
Counting statistics	122(10)	Needs careful analysis using spatial filtering on probes with structure and other artifacts

Table 4.2: I_{sat} calibrations. Summary of the different methods, example measured values, and drawbacks. The different values differ from each other because they represent systems with varying magnifications and pulse characteristics.

4.3   Image processing

This section summarizes a couple of image processing methods to obtain quantitative atomic density distributions with optimal signal-to-noise ratio. We hone these methods for the experiment in Chapter 6, but they are readily useful for absorption imaging of cold and ultracold atomic gases. The methods from the last subsection are published in [60] as a supplementary material.

We first estimate the uncertainty of the raw intensity signals in a photon shot noise limited measurement and compute the optimal signal-to-noise ratio in

a measurement of linear optical depth. We then give an overview of the image reconstruction algorithms used to remove the effects of spatial inhomogeneities in the images contaminating the signal of interest.

4.3.1 Estimating uncertainty

The uncertainty of a recorded intensity in a photon shot noise limited detection is described by the covariance matrix elements

$$\sigma_{ij} = \delta_{ij} \sqrt{I_i I_j}, \tag{4.25}$$

here in the pixel basis where the index i labels the i-th pixel. The uncertainty shows the uncorrelated pixel-to-pixel noise with magnitude $\sigma_{ii}^{1/2} = \sqrt{I_i}$ in counts at pixel i. We may propagate the uncertainty in quantities deriving from the measured intensity using the general linear covariance transformation

$$\hat{\Sigma} = \hat{\mathcal{U}} \hat{\sigma} \hat{\mathcal{U}}^T \tag{4.26}$$

where the diagonal elements of the propagated covariance matrix Σ approximate the propagated error if the transformation operator $\hat{\mathcal{U}}$ is band diagonal. In this way, we may propagate the correlated and uncorrelated uncertainty contributions when the linear operator $\hat{\mathcal{U}}$ is known in the same representation as the image covariance matrix σ. In the simpler case when the functional form of a quantity deriving from the intensity is known, we may use the normal uncorrelated error

propagation.

For example the photon shot noise limited uncertainties in the intensity from the resonant absorption images I_a, I_p, and I_d propagate using the corrected Beer–Lambert law from Equation 4.18. First, as I_d is a direct measurement of technical noise, it is not limited by photon shot noise, and for simplicity we subtract it directly from I_a and I_p. Then, the uncertainty in the corrected optical depth

$$\sigma_{od} = \sqrt{\left(\frac{1}{I_p} + \frac{1}{I_{\text{sat}}}\right)^2 I_p + \left(\frac{1}{I_a} + \frac{1}{I_{\text{sat}}}\right)^2 I_a}, \qquad (4.27)$$

in terms of the measured intensities and the calibrated I_{sat}.

4.3.2   Optimal signal-to-noise ratio

We now derive the general signal-to-noise ratio on the integrated optical depth from resonant absorption imaging. We provide a measurement using a dilute cloud of atoms to validate the qualitative features of this derivation.

We consider an imperfect detector (i.e. with technical noise sources) in a perfectly dark environment, where it remains insensitive to stray light, and omit any kind of post-detection amplification. We target detecting a column density n_{col} in focus using a microscope with magnification M and a detector with pixel

size Δ_p. We use the saturation intensity at the detector

$$N_{\text{sat}} = I_{\text{sat}} \times Q \times \left(\frac{\tau}{\varepsilon_\gamma}\right) \times \left(\frac{\Delta_p}{M}\right)^2 \tag{4.28}$$

expressed as the detected number of photons per pixel as the natural unit of intensity, where Q is the quantum efficiency, $I_{sat} = 1.67\,\text{mW/cm}^2$ is the saturation intensity, $\varepsilon_\gamma = h\nu$ is the energy of a single probe photon, and Δ_p/M is the effective pixel size at the object plane. Then, we cast Equation 4.18 into

$$y + \ln\left(\frac{x}{s}\right) - s\left(1 - x\right) = 0, \tag{4.29}$$

in terms of the absorbed $x = N_a/N_{\text{sat}}$, and unabsorbed $s = N_p/N_{\text{sat}}$ photon fractions. The optical depth is $y = \sigma_0 n$. Given an incident photon number $N_p = sN_{\text{sat}}$, and target column density $n_{\text{col}} = y/\sigma_0$, we numerically solve for the absorbed photon number $N_a = xN_{\text{sat}}$. Then, joining the uncorrelated photon shot noise and technical noise contributions, the uncertainties become $\sigma_a = \sqrt{N_a + \sigma_t^2}$, and $\sigma_p = \sqrt{N_p + \sigma_t^2}$. The technical noise is dominated by read noise σ_r and time integrated dark current background counts $\sigma_d = j_d\tau$, which add in quadrature. The propagated squared uncertainty in y is

$$\sigma_y^2 = \left(\frac{\partial y}{\partial N_a}\right)^2 \sigma_a^2 + \left(\frac{\partial y}{\partial N_p}\right)^2 \sigma_p^2 \tag{4.30}$$

$$= (1+x)^2 \left(1 + \frac{\sigma_r^2 + j_d^2\tau^2}{N_a^2}\right) + (1+s)^2 \left(1 + \frac{\sigma_r^2 + j_d^2\tau^2}{N_p^2}\right) \tag{4.31}$$

where j_d is the dark current sensor specification in photons per second. This is just the traditional result from independent error propagation. The "realistic" SNR becomes

$$
\begin{aligned}
\mathrm{SNR}_y^{(r)} &= y/\sigma_y \\
&= \frac{s\,(1-x) - \ln(x/s)}{(1+x)^2\left(1 + \frac{\sigma_r^2 + j_d^2\tau^2}{N_a^2}\right) + (1+s)^2\left(1 + \frac{\sigma_r^2 + j_d^2\tau^2}{N_p^2}\right)}
\end{aligned}
\tag{4.32}
$$

including technical noise, while the "ideal" SNR becomes

$$
\mathrm{SNR}_y^{(i)} = \frac{s\,(1-x) - \ln(x/s)}{(1+x)^2 + (1+s)^2}
\tag{4.33}
$$

without technical noise.

To compare the derived ideal and realistic SNR we numerically solve for the absorbed fraction as a function of incident probe intensity for two different commercially available sensors which we now call "typical" and "enhanced" CCDs. The main difference is a ~ 2 orders of magnitude price difference representing a factor of ~ 10 in technical noise suppression, and a factor of ~ 2 in quantum efficiency at $\lambda = 780\,\mathrm{nm}$ among other features. Figure 4.11 shows the side to side comparison, where each sensor displays the ideal and realistic SNR. At first glance, a factor of > 3 improvement even in the ideal SNR seems too expensive from one sensor to the other. This factor can be explained by a combination of larger quantum efficiency and pixel size in the enhanced CCD. Additionally, the realistic SNR shows that a reduced dark current and readout noise does not impact the
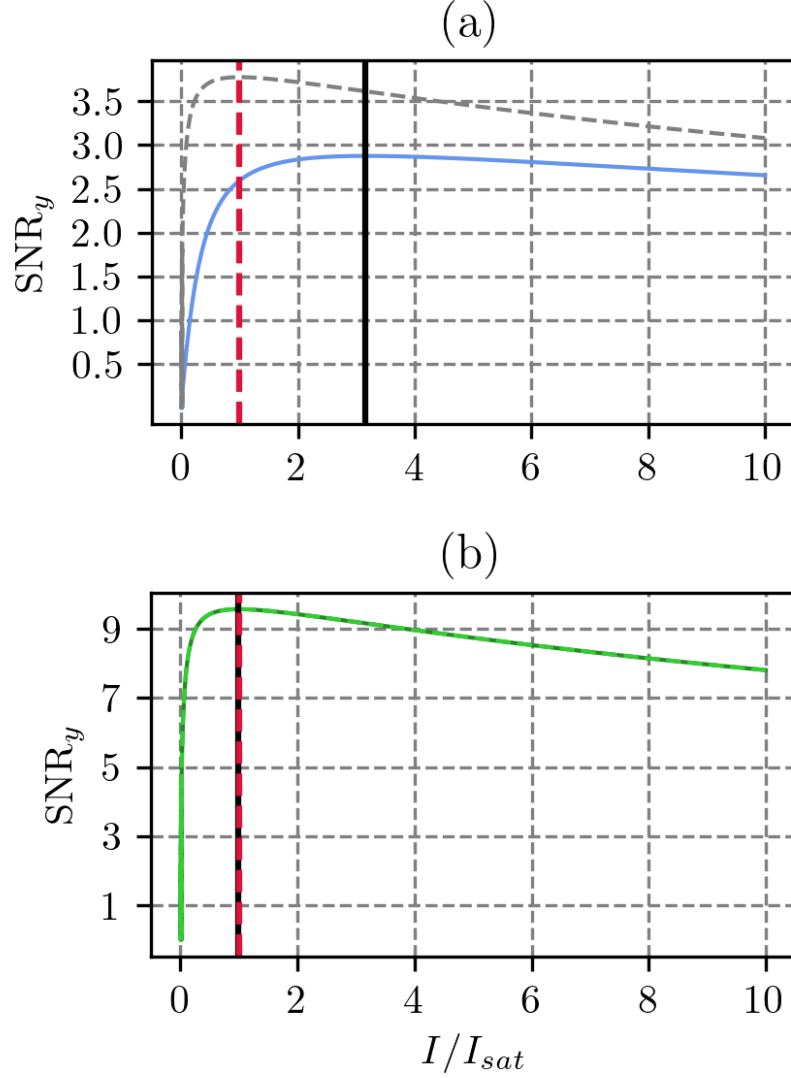
Figure 4.12: Comparison of SNR in optical depth. Modeled realistic (solid curve) and ideal (dashed curve) SNR for the optical depth for (a) a typical CCD, and (b) an enhanced CCD. The parameters used in the calculation above include a target optical depth of $n_{\mathrm{col}}\sigma_0 = 0.726$, a $\tau = 20\,\mu s$ resonant probe pulse, and an imaging magnification of 5.33. The straight red lines indicate the intensity for optimized SNR, while the dashed red lines indicate the $I_p/I_{\mathrm{sat}} = 1$ reference.

SNR for the short imaging pulses used in resonant absorption imaging. Simply put,

a typical CCD is close to optimal for absorption imaging, with the clear advantage

of costing less than an enhanced CCD. Another feature of the derived SNR is the

tunability using the incident probe intensity. In the ideal SNR case, the optimal probe intensity is $I_p/I_{\text{sat}} = 1$, while the increasingly important technical noise results in a shift away from saturation intensity depending on the target optical depth.
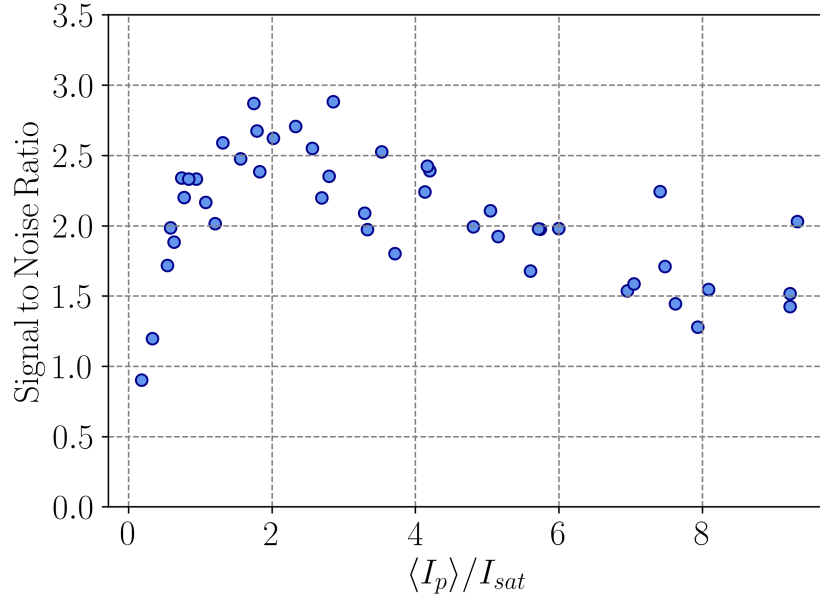
Figure 4.13: Measured SNR in optical depth. We validate the presence of an optimal probe intensity for the SNR in resonant absorption imaging.

We validate our derived model by measuring the tunable SNR as a function of probe intensity in Figure 4.13, where we image a dilute, elongated cloud of optical depth $n_{\text{col}}\sigma_0 = 0.75(5)$ using a $20\,\mu$s resonant probe pulse. We find a qualitative agreement in the features of Figure 4.11 with a typical CCD (SONY ICX618 Mono) with peak quantum efficiency of ~ 0.35 at $780\,$nm from Figure 4.12 (b).

4.3.3 Digital processing of intensity data

We process our raw probe intensity images to remove systematic noise contributions degrading the measurement of column and linear atomic densities. The process breaks down into several subprocesses, including linear probe reconstruction to optimally match a probe image to the atoms image I_a, dark field reconstruction to optimally match a dark image without residual spatial structure, and dimensionality reduction for statistical averaging, and a model of linear density in the case of spatiotemporal limited detection of atomic scatterers during the probe pulse.

During the resonant absorption imaging sequence described at the end of Section 4.1.3, mechanical vibrations between the consecutive I_p, and I_p images often shift spatial structure present in the probe resulting in fringe artifacts in the optical depth. We perform linear probe reconstruction to interpolate an optimal probe image I_p^{opt} using an ensemble of raw probe images to construct a linear basis. From here on, we adopt the notation where I represents a two-dimensional image, and $\mathbf{I}$ represents the same image as a rank-1 tensor (vector) in the pixel basis representation, where each element is the value of the intensity in a pixel. We seek to find the optimal probe intensity

$$\mathbf{I}_p^{opt} = \mathbb{R}\mathbf{c} \tag{4.34}$$

103

relating to a matrix $\mathbb{R}$ constructed from the ensemble of raw probe images as columns and a set of scalar coefficients $\mathbf{c}$ comprising the optimal linear combination. The optimal vector $\mathbf{c}$ satisfies the weighted linear regression

$$\mathbb{R}^\top \mathbb{W} \mathbb{R} \mathbf{c} = \mathbb{R}^\top \mathbb{W} \mathbf{I}_a, \tag{4.35}$$

with respect to the images containing atoms $\mathbf{I}_a$, and where $\mathbb{W}$ is a diagonal masking matrix of weights equal to zero for pixels containing atoms, and one elsewhere. We numerically investigate different shapes and sizes for the mask, and find that as long as the unmasked area is representative of the undesirable fringe artifacts, there is no significant difference between different masks (i.e. an elliptical mask is not different from a rectangular mask of similar dimensions). This way, we explicitly consider only spatial intensity fluctuations in the probe and exclude intensity fluctuations from the absorption of light by the atoms. We determine $\mathbf{c}$ by numerically solving the linear system represented by Equation 4.35, and construct the intensity image I_p^{opt} minimizing the sum squared error with I_a in the region outside of the mask set by $\mathbb{W}$. In addition, due to the dimensionality reduction in the abstract vector space formed by the basis from the linear regression, it reduces photon shot noise present in the reconstructed probes [61, 62]. Figure 4.14 shows the effect of probe reconstruction using 50 images as a basis. Even for a cloud with rich spatial features, the mask used in the linear probe reconstruction acts to only remove the fringe artifacts in the optical depth.

$$(a) \qquad\qquad\qquad\qquad (b)$$
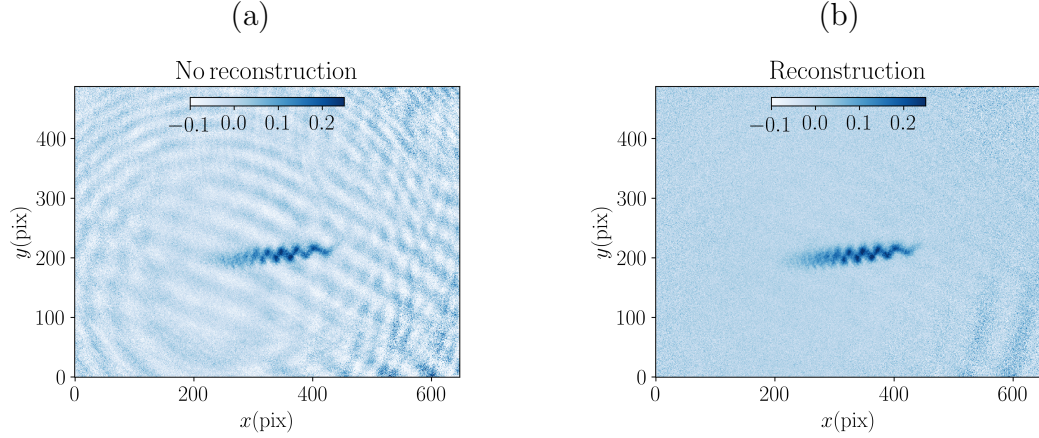
Figure 4.14: Linear probe reconstruction. Optical depth from absorption images of a cloud with rich spatial structure features (a) without reconstruction, and (b) after reconstruction using a 50 image basis.

Additionally to performing linear probe reconstruction, we correct for systematic effects in the raw dark field images (see Section 4.1.3). One of these effects arises from variations in ambient brightness over the line power cycle, an effect present when the CCD exposure intervals are not syncronized with the $\sim 60\,\mathrm{Hz}$ line. Another effect is stray light from imperfect extinction of laser beams (e.g. dipole trap beams, repump light). A last effect is structure arising from the readout pattern of the CCD. The net result is a spatially inhomogeneous difference in counts in the background light illumination. The difference in counts is small, contributing on the order of ≈ 1 count between I_a and I_p, but with an overall structure due to aperture, scattering, and readout effects. To correct for this effect, we fit a two-dimensional model to reconstruct the individual dark field images with a few contributions. The first one is the average dark field intensity $\bar{\mathbf{I}}_d$ vector representing the mean dark field common to the atoms and probe images. The second

105

contribution comes from feeding the raw dark field intensities into the probe reconstruction linear regression, giving a systematic dark field coefficient c_d^{sys} indicating how much is present in each probe image relative to the atoms image. Finally, we construct a principal component basis $\mathbf{P}_d^{(j)}$ from the set of all dark field images, and use the first few principal components representing other sources of correlated (structured) background illumination. The reconstructed dark field vectors

$$\mathbf{I}_d^{rec} = \bar{\mathbf{I}}_d + c_d^{sys}\mathbf{I}_d + \sum_l \mathbf{P}_d^{(l)} \tag{4.36}$$

account for the slight differences in the atoms and probe intensity dark fields.

After reconstructing the probe and dark field images, we compute the absorbed fraction

$$f = \frac{I_p^{opt} - I_a}{I_p^{opt} - I_d^{rec}} \tag{4.37}$$

in terms of the reconstructed images, as well as the calibrated saturation parameter

$$s = \frac{I_p^{opt} - I_d^{rec}}{I_{sat}} \tag{4.38}$$

in terms of the saturation intensity I_{sat} and the reconstructed images. These two quantities give rise to the naïve optical depth

$$\sigma_0^* n^* = -\alpha \log(1 - f) + sf \tag{4.39}$$

106

where n^* is a naïve column density, and $\alpha = \sigma_0^*/\sigma_0$ is the empirical ratio of the ideal two-level and effective scattering cross sections from an imperfect probe. Typically the value of α is close 1, and in the experiments relevant to this discussion, we use $\alpha = 0.92(4)$ to account for residual ellipticity in circularly polarized probe and/or magnetic field orientation along an axis different from the probe axis. In reality, the naïve optical depth is not exactly accurate for systems narrower than either the optical scattering length $\sqrt{\sigma_0/\pi} = \sqrt{3\lambda^2/2\pi^2}$, or the imaging resolution Δ in at least one direction. This is because either of these two conditions violates the assumptions behind the Beer's law. To improve this, we later present a model of linear densities useful in the context of thin, 1D systems violating both of these conditions.

We often improve our SNR by repeating an experiment N times, and then computing ensemble averages to get a $\sqrt{N}$ factor improvement. We find that when we compute the mean optical depth to statistically improve the SNR, it is better to first average the absorbed fraction and saturation terms before using Equation 4.18. Doing so avoids amplifying the noise baseline as the nonlinear logarithm amplifies small value fluctuations in the signal.

Similarly, we are often interested in one-dimensional "cuts" of the two-dimensional optical depth, especially when imaging elongated systems. There, we integrate column densities over a number of pixels to produce a single pixel

with a linear density distribution. While this operation incorporates the total absorbed fraction, a quantity conserved by scalar diffraction, integrating over a large number of pixels adds excess photon shot noise from pixels with no atoms. We apply dimensional reduction of the mean absorbed fraction to mitigate the effect of the integrated photon shot noise. This process suppresses the apparent integrated absorption due to photon shot noise in regions where we know the approximate limited response of our imaging system. We first crop our images to a region-of-interest containing the full extent of our imaging response function (e.g. point spread function). Then, for each position along the integration direction x_i, we extract the full linear slice of mean absorbed fraction $\langle f(x_i, y) \rangle$ from all members of the dataset at that pixel in the central and few nearest m pixels labeled by an index j. In the pixel basis representation, we obtain the set of vectors $\{ \langle \mathbf{f}(x_{i+j}, y) \rangle \}$. Using this large set, we perform uncentered principal component analysis [63] and extract only the first m normalized principal components to construct a dimensionally reduced absorbed fraction $\langle f_r(x_i) \rangle$. The improved naïve optical depth becomes

$$\sigma_0^* \langle n_r^* \rangle \approx -\alpha \log(1 - \langle f_r \rangle) + \langle s f_r \rangle, \qquad (4.40)$$

from which the average naïve linear density

$$\langle n_r^*(x) \rangle = \frac{\Delta y}{\sigma_0} \sum_y \sigma_0^* \langle n_r^*(x, y) \rangle \qquad (4.41)$$

108

is an improved estimate of the linear density distribution.

Finally, we derive a model of linear density from the column density including diffusion effects during the probe pulse. A problem for clouds with extremely narrow spatial extent in at least one dimension is that they do not just absorb light in one location of space. During the scattering process, many absorption and emission events take place, causing diffusion of the atomic wavepacket around its originally narrow confinement. This implies that we cannot infer the column density from the usual Beer's law, which assumes a stationary, extended absorber. Another consideration is the finite spatial resolution introduced by the diffraction of scattered light into our imaging system. The modified solution to Beer–Lambert law

$$\sigma_0 g(x, y, t) = -\alpha \log(1 - f(x, y, t)) + s(x, y) f(x, y, t), \tag{4.42}$$

for a column, time dependent absorbed fraction, and where $g(x, y, t)$ represents the column density convolved with the time-dependent atomic diffusion and spatially limited imaging resolution. The limitations imply that we have access to

$$f_m(x) = \frac{1}{\tau} \int_0^\tau \int f(x, y, t) dy \approx \Delta y \sum_y \langle f_r(x, y) \rangle, \tag{4.43}$$

in terms of the undiffracted absorbed fraction. We model the convolved column

density

$$g(x, y, t) \approx \frac{n(x)}{\sqrt{2\pi\sigma_y^2(x,t)}} e^{-y^2/2\sigma_y^2(x,t)} \tag{4.44}$$

as a horizontally diffusing, vertical gaussian function. The underlying assumption is that the atoms are only able to move along a weakly confined x direction. The Gaussian form approximates the vertical absorption profile with unit integral (preserving the absorbed fraction), and variance

$$\sigma_y^2(x, t) = \frac{\sigma_0}{\pi} + \frac{1}{3}\sigma_{v_y}^2 t^2 \tag{4.45}$$

equal to the optical scattering length $\sqrt{\sigma_0/\pi}$ at $t = 0$, representing the mean squared radius of a scatterer. The isotropic momentum diffusion gives a mean squared velocity

$$\sigma_{v_y}^2(x, t) = \frac{1}{3}(2\pi)^{-1}\Gamma_s(x)v_{rec}^2 t \tag{4.46}$$

in terms of the recoil velocity $v_{rec} = \hbar k_r/m$ and the spatially inhomogeneous resonant scattering rate

$$\Gamma_s(x) = \frac{\Gamma}{2}\frac{s(x)}{1 + s(x)}, \tag{4.47}$$

ignoring the Doppler shifts away from resonance. Put together, the y-variance of the absorption profile

$$\sigma_y^2(x, t) = \frac{\sigma_0}{\pi} + \frac{\Gamma}{6}\frac{\hbar^2}{m^2\sigma_0}\frac{s(x)}{1 + s(x)}t^2 \tag{4.48}$$

grows quadratically in time, approximating isotropic scattering where the change in velocity per scattering event is $v_{rec}^2/3$. This correction is important for higher absorbed fractions, where we find it systematically amplifies the atomic density by up to $\approx 30\%$.

4.4   Conclusion

This Chapter reviewed an important set of tools that enable quantitative and precise microscopy of cold atomic ensembles. We presented simple models for imaging systems and the light-matter interaction that nevertheless capture the essential aspects of imaging cold atoms. We reviewed the calibration, and measurement methods providing guidelines for improved image processing and data analysis. We covered the propagation of uncertainty, and analyzed the optimized signal-to-noise ratio in absorption imaging, which are essential in the absolute determination of atomic column densities. Lastly, the image processing algorithms remove systematic contributions from the environment and the detection process. Some of the methods in this Chapter, including the probe reconstruction, dark frame reconstruction, and the model for diffusive linear absorption are published in [60] as a supplementary material.

Chapter 5: Thermodynamic models for one-dimensional Bose gases

This chapter reviews three models describing the thermodynamics of homogeneous one-dimensional Bose gases (1DBG), highlighting the different regimes in which they are valid.

This Chapter is organized as follows. First, I introduce the general one-dimensional Bose gas in Section 5.1. Then I review the ideal (non-interacting) Bose gas in the grand canonical ensemble in Section 5.2. There, using a virial expansion I give the equations of state valid at low fugacity. Later, contact interactions of arbitrary strength enter in the Lieb–Liniger model, where exact solutions for the interacting ground state capture the zero temperature thermodynamics in Section 5.3. Finally, nonzero temperature effects enter with the Yang–Yang thermodynamics, building upon the Lieb–Liniger model in the presence of thermal excitations in Section 5.4. Remarkably, the Yang–Yang thermodynamics remains exact for arbitrarily strong contact repulsive interactions, and arbitrary temperatures. I finish this Chapter by commenting on the experimental distinctions between different one-dimensional regimes in Section 5.5.

5.1 One-dimensional, contact-repulsive bosons

The general, second quantized Hamiltonian that describes pairwise interacting bosons in one-dimension (1D) [64] is

$$
\mathcal{H} = \int dz dz' \left[\hat{\Psi}^\dagger(z) \left(\frac{\hat{p}^2}{2m} + U(z) \right) \hat{\Psi}(z) + \hat{\Psi}^\dagger(z) \hat{\Psi}^\dagger(z') V(z - z') \hat{\Psi}(z) \hat{\Psi}(z') \right]
$$
(5.1)

where $\hat{p} = i\hbar \partial_z$ is the momentum operator in the real space representation, m is the mass, $\hat{\Psi}^\dagger(z), \hat{\Psi}(z)$ are bosonic field creation and annihilation operators obeying the commutation relation $\left[\hat{\Psi}(z), \hat{\Psi}^\dagger(z') \right] = \delta(z - z')$, $U(z)$ is an external potential, and $V(z - z')$ is the pairwise interaction potential which depends only on the interparticle separation and whose functional form determines the character of the interaction. In what follows, I consider repulsive contact interactions between pairs of bosons, such that $V(z - z') = V_0 \delta(z - z')$, and $V_0 > 0$.

For vanishing interactions, and in the absence of an external potential (i.e. $V(z - z') = U(z) = 0$), the system is an ideal, homogeneous 1D Bose gas. In Section 5.2, I review the thermodynamics of such an ideal Bose gas using the grand canonical ensemble, giving exact thermodynamics at any temperature. As interactions become non-vanishing, a many-body treatment in Section 5.3 gives the exact ground state solutions of 5.1. These zero-temperature solutions comprise the Lieb–Liniger model [65], valid for any interaction strength. Finally, in Section 5.4,

I review the exact Yang–Yang thermodynamics [66] solutions for nonzero temperatures and arbitrary interaction strength. All the models describing homogeneous systems may be extended for inhomogeneous systems ($U \neq const.$) through the local density approximation (LDA) [67]. In the LDA, subsystems of approximately constant density behave like homogeneous systems and models apply locally.

5.2   Ideal Bose gas model

One-dimensional Bose gases follow an ideal behavior dominated by Bose statistics in the limit of vanishing interactions. The ideal Bose thermodynamics starts with the partition function in the grand canonical ensemble

$$\mathcal{Z} = \prod_k \sum_{n_k} e^{(\mu - \epsilon_k) n_k / k_B T} = \prod_k \frac{1}{1 - e^{(\mu - \epsilon_k)/k_B T}} \tag{5.2}$$

where k_B is Boltzmann's constant, T is the temperature, and $\epsilon_k \propto k^2$ is the non-interacting (free) particle energy, with $p = \hbar k$ the single particle momentum. Other quantities derive from it through the grand canonical potential $\Omega = -k_B T \ln \mathcal{Z}$. For instance, starting with the one-dimensional pressure

$$\mathcal{P} = -\frac{\Omega}{L} = \frac{k_B T}{L} \ln \left(\prod_k \frac{1}{1 - e^{(\mu - \epsilon_k)/k_B T}} \right)$$

$$= -\frac{k_B T}{L} \sum_k \ln \left(1 - e^{(\mu - \epsilon_k)/k_B T} \right)$$

in a (1D) volume of length L, we can extend it into the continuum, where $N, L \to \infty$, but the density remains constant, and sums turns into integrals weighted by the density of states. Then, the 1DBG pressure density becomes

$$\mathcal{P} = -k_B T \int_{-\infty}^{\infty} \ln\left(1 - e^{(\mu - \epsilon(k))/k_B T}\right) \rho(k) dk$$

$$= -\frac{k_B T}{2\pi} \int_{-\infty}^{\infty} \ln\left(1 - z e^{-\beta \epsilon(k)}\right) dk, \tag{5.3}$$

now in terms of the fugacity $z = e^{\beta\mu}$, and where $\beta = 1/k_B T$. Doing a power series expansion on the integrand in terms of small fugacity parameter $z \ll 1$ (valid for instance when $\mu/k_B T \ll 0$) gives the virial pressure equation of state

$$\mathcal{P} = -\frac{k_B T}{2\pi} \int_{-\infty}^{\infty} \sum_{n=1}^{\infty} \left[(-1)^{n+1} \frac{(-z e^{\beta \epsilon(k)})^n}{n}\right] dk$$

$$= \frac{k_B T}{2\pi} \sum_{n=1}^{\infty} \frac{z^n}{n} \int_{-\infty}^{\infty} e^{-n\beta \epsilon(k)} dk$$

$$= \frac{k_B T}{2\pi} \sum_{n=1}^{\infty} \frac{(-z)^n}{n^{3/2}} \sqrt{\frac{2m\pi}{\hbar^2 \beta}}$$

$$= \frac{k_B T}{\lambda_{dB}} \mathrm{Li}_{\frac{3}{2}}(z), \tag{5.4}$$

assuming a free particle dispersion in the continuum $\epsilon(k) = \hbar^2 k^2 / 2m$, and where $\lambda_{\mathrm{dB}} = (2\pi\hbar^2/mk_B T)^{1/2}$ is the thermal de–Broglie wavelength capturing the width of the momentum distribution. Here, $\mathrm{Li}_n(z)$ is the n-th order polylogarithm, convergent only for $|z| < 1$, well justified for the virial expansion. The direct relationship between intensive and extensive thermodynamic quantities comprises an

equation of state. Here, the virial equation of state relates pressure with temperature and chemical potential in the limit of small fugacity $z \ll 1$. Similarly, we can derive the virial entropy

$$
\begin{aligned}
\mathcal{S} &= -\left(\frac{\partial \Omega}{\partial T}\right)_{L,\mu} = -L\left(\frac{\partial \mathcal{P}}{\partial T}\right)_{\mu} \\
&= L\frac{\partial}{\partial T}\left[\frac{k_B T}{\lambda_{dB}}\mathrm{Li}_{\frac{3}{2}}(z)\right] \\
&= \frac{L}{\lambda_{dB}}\left(\frac{3}{2}k_B\mathrm{Li}_{\frac{3}{2}}(z) - \frac{\mu}{T}\mathrm{Li}_{\frac{1}{2}}(z)\right)
\end{aligned}
\tag{5.5}
$$

equation of state. Here, the linear entropy grows with subsystem size L/λ_{dB}, and decreases with temperature. To better visualize these virial equations of state, Figure 5.1 shows the virial pressure and entropy landscape in a μ, T region where the virial expansion is valid. Both the linear pressure and entropy increase with increasing temperature and chemical potential.

While the ideal Bose gas virial equations of state make quantitative predictions for 1D systems, they are highly constrained by the approximations that sustain them. Even outside the virial limit, the ideal Bose gas equations of state only correctly describe noninteracting bosons. At sufficiently high temperatures, Bose statistics stop weighing in and the classical ideal gas law recovers the correct equations of state. Clearly, the ideal Bose gas model and its approximations are insufficient for a full thermodynamic description of the system in Equation 5.1.
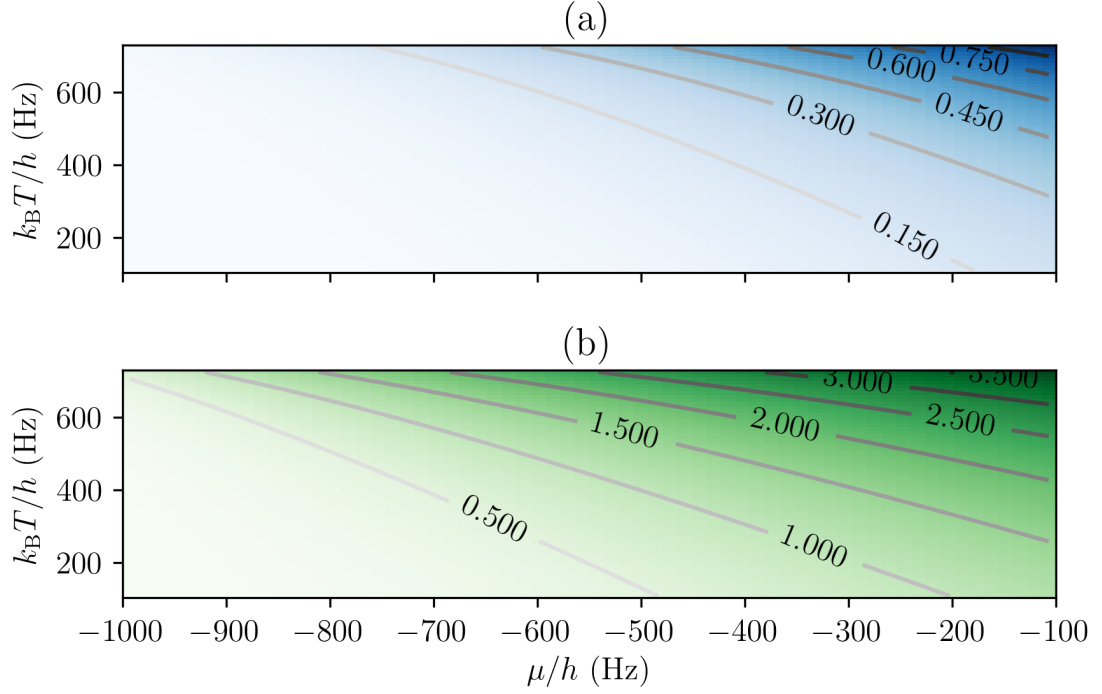
Figure 5.1: Virial equations of state of 1D Bose gas. (a) Peak normalized pressure $\mathcal{P}(\mu,T)/\mathcal{P}_0$, and (b) entropy $\mathcal{S}(\mu,T)$ in units of k_B in the virial expansion $z \ll 1$ for an ideal one-dimensional Bose gas of length $L = 10\,\mu\mathrm{m}$. The contours represent isochoric and adiabatic lines.

5.3 Lieb–Liniger model

Lieb and Liniger diagonalized the Hamiltonian in Equation 5.1 by using the now well known Bethe ansatz [68] which for N bosons is

$$|\Psi_N(k_1, k_2, ..., k_N)\rangle = \frac{1}{\sqrt{N!}} \int \Phi_N(z_i|k_j)\, \hat{\Psi}^\dagger_{z_1} \hat{\Psi}^\dagger_{z_2}...\hat{\Psi}^\dagger_{z_N}|\mathbf{0}\rangle d^N z \qquad (5.6)$$

where k_j label momenta, $\phi_N(z_i|k_j) = \phi(z_1, z_2, ..., z_N|k_1, k_2, ..., k_N)$ comprise the momentum wavefunctions, $\hat{\Psi}_z$ introduces a shorthand notation for $\hat{\Psi}(z)$ and $|\mathbf{0}\rangle$ denotes the vacuum state in the number (Fock) representation. The ansatz in Equa-

tion 5.6 is justified as $\mathcal{H}$ commutes with $\hat{N}$, the total number operator, reducing the problem to finding momentum eigenstates with the implication that the total number of atoms is conserved. To find such solutions, the first quantized Lieb–Liniger Hamiltonian

$$\hat{H} = -\frac{\hbar^2}{2m} \sum_{i=1}^{N} \frac{\partial^2}{\partial z^2} + g \sum_{i \neq j} \delta(z_i - z_j) \tag{5.7}$$

can be diagonalized by solving the time-independent Schrödinger equation $\hat{H}\phi_N = E_N\phi_N$.

We first consider a one-dimensional ring of length L with periodic boundary conditions where N bosons are placed along z. Then, we ensure that the average number of bosons in any given segment is ≈ 1 by dividing the ring into N equal length segments. In the absence of potential energy, plane wave solutions satisfy the local Schrödinger equation. In order to include the effect of δ-interactions, we impose inter-segment boundary conditions implying continuities $\phi_{z_i} = \phi_{z_{i+1}}$ and first derivative discontinuities in $\phi'_{z_i} - \phi'_{z_{i+1}} \propto g\phi_{z_i}$. This results in N phase shifted local plane waves. The Bethe-ansatz solution builds on the fact that every time a boson meets the boundary, it scatters off a delta barrier (neighboring boson) and acquires a phase shift proportional to the relative momenta. The many-body wavefunction

$$\phi_N(k_1, k_2, ..., k_N) = \prod_{j=1}^{N} e^{ik_j z_j} \prod_{j>n} \left(1 - \frac{ic}{k_j - k_n} \mathrm{sgn}(k_j - k_n)\right) \tag{5.8}$$

captures the build up of all the phase shifts by virtue of the interaction wavenumber $c \propto g$. The sgn function ensures a symmetrized (bosonic) wavefunction. Equation 5.8 comprises the exact, N-body solution together with the set of quantum numbers for k_i, and recovers the free particle solution in the non-interacting limit where $g \to 0$. The eigenenergies E_N are obtained by solving the closed system of coupled nonlinear equations arising from the periodic boundary conditions

$$e^{ik_j L} \prod_{j \neq n}^{N} \frac{k_j - k_n - ic}{k_j - k_n + ic} = 1 \qquad (5.9)$$

also known as the Bethe system. We take the logarithm on both sides to get the set of quantization conditions

$$i(k_j L - 2\pi \eta_j) + \ln \prod_{j \neq n}^{N} \frac{k_j - k_n - ic}{k_j - k_n + ic} = 0$$

$$i(k_j L - 2\pi \eta_j) + \sum_{j=1}^{N} \ln \left(e^{i\theta(k_j - k_n)} \right) = 0$$

$$k_j L + \sum_{j=1}^{N} \theta(k_j - k_n) = 2\pi \eta_j$$

where η_j are a set of 2π-phase winding integers and the angles $\theta(k) = 2 \arctan(k/c)$ encode the phase shifts. Following the derivation in [65], we focus on the ground state, where the momenta are evenly distributed about zero (i.e. minimizing their sum). By letting $\eta_j = j$, with the set of j running evenly around $j = 0$ (e.g.

$j = -N/2...N/2$ for even N), the system reads

$$k_j L + \sum_j \theta(k_j - k_n) = 2\pi j \qquad (5.10)$$

Subtracting any pair of consecutive equations yields

$$(k_{j+1} - k_j)L + \sum_j [\theta(k_{j+1} - k_n) - \theta(k_j - k_n)] = 2\pi$$

$$\Delta k_j L + \sum_j [\theta(k_j - k_n - \Delta k_j) - \theta(k_j - k_n)] = 2\pi$$

$$\Delta k_j L + \sum_j [\Delta k_j \theta'(k_j - k_n) + O(\Delta k_j^2)_n] = 2\pi,$$

where the backward difference approximation inside the sum incorporates every-thing in terms of the derivative $\theta'(k)$. In the continuum, the quasi-momentum distribution function $\rho(k) = \lim_{\Delta k \to dk} 1/\Delta k L$ enters so that $L\rho(k)dk$ corresponds to the number of states in an interval dk. Then, sums are replaced by integrals as prescribed by $\sum_k f_k \to L \int_{-q}^{q} f(k)\rho(k)dk$ and

$$1/\rho(k) + 1/\rho(k) \int_{-q}^{q} \theta'(k - k')\rho(k')dk' = 2\pi$$

$$1 + \int_{-q}^{q} \theta'(k - k')\rho(k')dk' = 2\pi\rho(k)$$

$$1 + \int_{-q}^{q} \frac{2c}{c^2 + (k - k')^2}\rho(k')dk' = 2\pi\rho(k), \qquad (5.11)$$

giving an integral equation for the ground state distribution $\rho(k)$, bounded by a

cutoff quasi-momentum q. Under these definitions, the particle density is

$$n = \frac{N}{L} = \int_{-q}^{q} \rho(k)dk. \tag{5.12}$$

From here on, I refer to $\theta'(k - k')$ as the Lieb–Liniger kernel. We rescale the problem following [65], letting $\tilde{k} = k/q$, and $\tilde{c} = c/q$, so that Equation 5.11 becomes

$$1 + \int_{-1}^{1} \frac{2\tilde{c}}{\tilde{c}^2 + (\tilde{k} - \tilde{k}')^2} \rho(\tilde{k}')d\tilde{k}' = 2\pi\rho(\tilde{k}). \tag{5.13}$$

Since the density n is kept constant in the thermodynamic limit ($N \to \infty, L \to \infty$ keeping $N/L = n$), the dimensionless interaction constant $\gamma = c/n$ fully characterizes the exact ground state solution. The density is bounded by

$$\tilde{c} = \gamma \int_{-1}^{1} \rho(\tilde{k})d\tilde{k}. \tag{5.14}$$

The solution to the coupled integral Equations 5.13–5.14 is exact and can be found numerically with iterative recursion. Figure 5.2 displays a set of numerically evaluated $\rho(k)$ and $\theta'(k)$, showing their qualitative features in different interaction regimes at constant density. The quasi-momentum distribution $\rho(k)$ broadens as the interactions become more relevant until finally $\rho(k) \to (2\pi)^{-1}$ as $\gamma \to \infty$. On the other hand, the Lieb–Liniger kernel (a normalized Lorentzian with a width poportional to the interaction wavenumber c) tends to become narrower as interactions become less relevant ($\gamma \to 0$). From the solution of the Lieb–Liniger
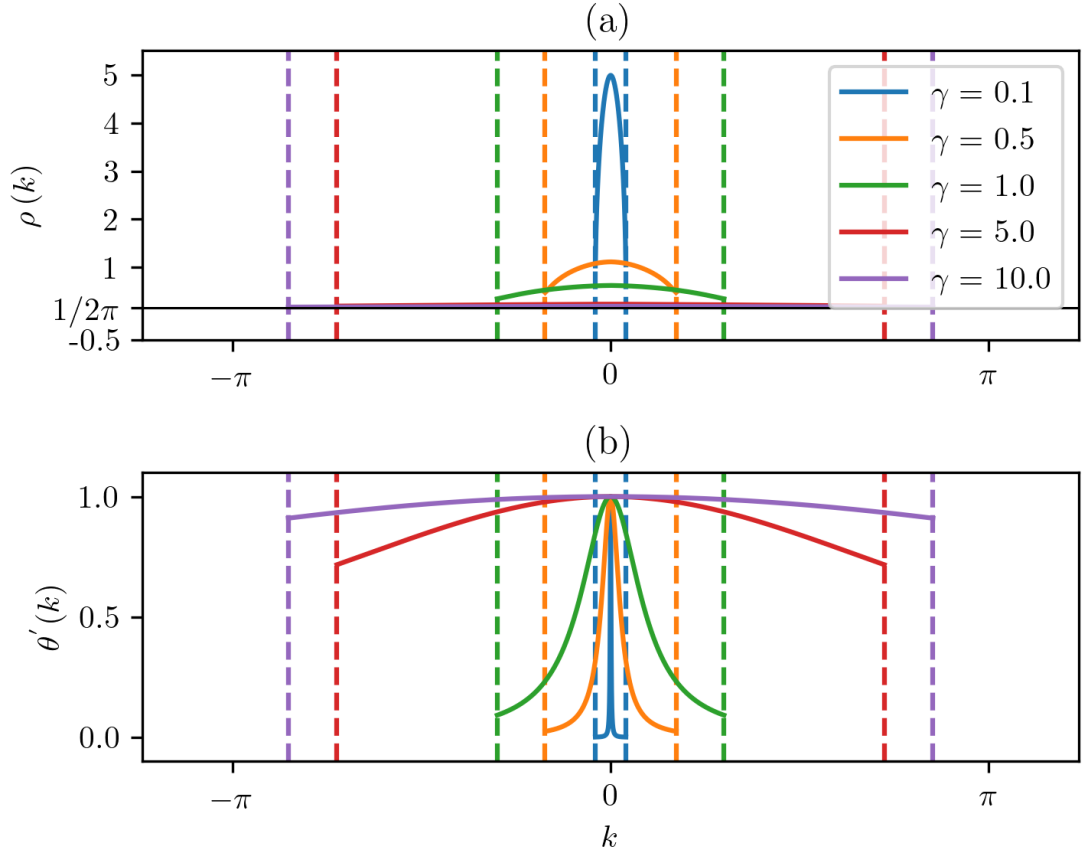
Figure 5.2: Lieb Liniger kernels and distributions. (a) Computed quasi-momentum distributions, and (b) Lieb–Liniger kernels for different values of γ. Dashed-vertical lines indicate the cutoff quasi-momenta q for which the density meets its constant value.

system, other quantites become accessible. An example is the exact ground state energy per particle

$$\frac{E_0}{N} = \frac{\hbar^2 n^2}{2m} e(\gamma),\tag{5.15}$$

where the dimensionless function

$$e(\gamma) = \frac{\gamma^3}{\tilde{c}^3} \int_{-1}^{1} \tilde{k}^2 \rho(\tilde{k}) d\tilde{k}\tag{5.16}$$

incorporates all interaction regimes. Then, from Equation 5.15 the chemical potential becomes

$$
\begin{aligned}
\mu &= \frac{\partial E_0}{\partial N} = \frac{\hbar^2}{2mL^2}\frac{\partial}{\partial N}\left(N^3 e(\gamma)\right) \\
&= \frac{\hbar^2}{2mL^2}\left(3N^2 e(\gamma) + N^3\frac{de}{d\gamma}\frac{d\gamma}{dN}\right) \\
&= \frac{\hbar^2 n^2}{2m}\left(3e(\gamma) - \frac{c}{n}\frac{de}{d\gamma}\right) \\
&= \frac{\hbar^2 n^2}{2m}\left(3e(\gamma) - \gamma\frac{de}{d\gamma}\right) \\
&= \frac{\hbar^2}{2m}\tilde{\mu}(\gamma),
\end{aligned}
\tag{5.17}
$$

representing the cost of adding one particle into the ground state. Figure 5.3 shows the numerically estimated $e(\gamma), \tilde{\mu}(\gamma)$, in agreement with the results in [65]. An interesting thing happens if we take the Fermi-energy of the spinless, one-dimensional free Fermi gas

$$
\varepsilon_F = \frac{\hbar^2 k_F^2}{2m} = \frac{\hbar^2\pi^2 n^2}{2m},
\tag{5.18}
$$

for which the associated Fermi momentum wavenumber is $k_F = \pi n$, and compare it against the energy per particle in Equation 5.15, but take the limit of infinitely relevant interactions

$$
\lim_{\gamma\to\infty}\frac{E_0}{N} = \frac{\hbar^2 n^2}{2m}\frac{\pi^2}{3} = \frac{\varepsilon_F}{3}.
\tag{5.19}
$$
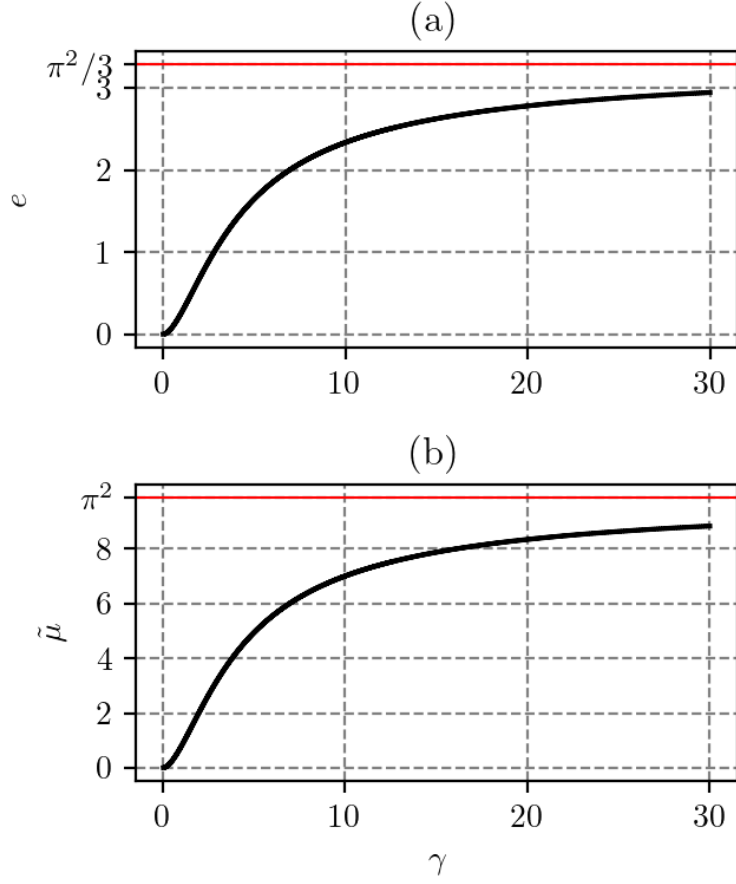
Figure 5.3: Lieb Liniger energy and chemical potential. (a) Dimensionless energy, and (b) chemical potential density as a function of γ. The horizontal lines indicate the infinitely strong interaction limits where $\gamma \to \infty$ and the gas fermionizes.

Remarkably, the chemical potential in this limit

$$\lim_{\gamma \to \infty} \mu = \frac{\hbar^2}{2m} \left(3n^2 \frac{\pi^2}{3} \right) = \frac{\hbar^2 k_F^2}{2m} = \varepsilon_F, \tag{5.20}$$

matches the Fermi-energy, and therefore in the limit of infinitely strong interactions, the gas behaves much like an ideal Fermi gas [69]. This phenomenon is called fermionization, emerging as hard-core bosons avoid each other to minimize their energy, in close resemblance to spinless Fermions following the Pauli exclusion

125

principle. Even though some thermodynamic properties map in the fermionized limit, others such as the momentum distribution and odd-order correlation functions do not. This is due to the inherently symmetrized bosonic wavefunctions.

The Lieb–Liniger model provides exact, ground state (zero-temperature) solutions for homogeneous 1D Bose gases in terms of a dimensionless interaction parameter γ. In the limit of infinitely strong interactions, the tendency of hard-core interacting bosons to avoid each other shapes the chemical potential to match a spinless Fermi gas. While the Lieb–Liniger thermodynamics provides such useful insight, it remains useful only in the zero-temperature limit. The most important consequence of the Lieb–Liniger interaction parameter is that the relevance of interactions γ scales inversely with the linear density n, so interactions become increasingly relevant as the number of bosons per unit length decreases.

5.4 Yang–Yang model

A few years after Lieb and Liniger developed their model, C. P. Yang and C. N. Yang studied the excitation spectrum, extending the thermodynamics beyond zero-temperature [66]. The Yang–Yang model describes the still exact solutions for an interacting, homogeneous gas at nonzero temperature, representing a remarkable case where the many-body problem is solvable at any temperature and interaction strength.

To see how the Lieb–Liniger model changes, we follow [66] closely, extending the definition in Equation 5.11 to include particle and hole densities

$$2\pi(\rho(k) + h(k)) = 1 + \int_{-\infty}^{\infty} \frac{2c}{c^2 + (k - k')^2}\rho(k')\,dk' \qquad (5.21)$$

as independent contributions to an excitation away from the ground state. In the presence of excitations, we look at the increase in entropy density of the distribution in the interval between k and $k + dk$

$$\ln\left[\frac{(p + \varrho)!}{p!\varrho!}\right] = L\left[(\rho(k) + h(k))\ln(\rho(k) + h(k)) - \rho(k)\ln\rho(k) - h(k)\ln h(k)\right]dk,$$

as the logarithm of the number of possible orderings of $p = L\rho(k)dk$ particles and $\varrho = Lh(k)dk$ holes, where we have used Stirling's formula $\ln(\zeta!) \approx \zeta(\ln\zeta - 1)$. From this, we arrive to the linear entropy

$$\mathcal{S} = L\int\left[(\rho(k) + h(k))\ln(\rho(k) + h(k)) - \rho(k)\ln\rho(k) - h(k)\ln h(k)\right]dk \qquad (5.22)$$

of the thermal ensemble. The free energy density $\mathcal{F} = e - T\mathcal{S}$ is minimized for constant density n, which together with $\mathcal{F}$ are functionals of $\rho(k)$ and $h(k)$. We determine $\rho(k)$ and $h(k)$ that minimize $\mathcal{F} - \mu n$, to ultimately solve for the μ that gives the right n, i.e. recovering the equation of state. We do this through the free

energy variation

$$
\delta \int \left[\left(\frac{\hbar^2 k^2}{2m} - \mu \right) \rho(k) dk - \frac{k_B T}{L} d\mathcal{S} \right] =
$$
$$
\int \left[\left(\frac{\hbar^2 k^2}{2m} - \mu - k_B T \ln \frac{\rho(k) + h(k)}{\rho(k)} \right) \delta\rho(k) - k_B T \ln \frac{\rho(k) + h(k)}{h(k)} \delta h(k) \right] dk,
$$

which, using the individual particle and hole density variations

$$
\delta\rho(k) = -\delta h(k) + \frac{1}{2\pi} \int \frac{2c}{c^2 + (k - k')^2} \delta\rho(k') dk', \tag{5.23}
$$

becomes

$$
\int \delta\rho(k) \left[\frac{\hbar^2 k^2}{2m} - \mu - k_B T \ln \frac{h(k)}{\rho(k)} - \frac{k_B T}{2\pi} \int \frac{2c}{c^2 + (k - q)^2} \ln \left(1 + \frac{\rho(k)}{h(k)} \right) dq \right] dk = 0,
$$
$$
\tag{5.24}
$$

and from this we derive the integral relation

$$
k_B T \ln \left(\frac{h(k)}{\rho(k)} \right) = \frac{\hbar^2 k^2}{2m} - \mu - \frac{k_B T}{2\pi} \int \frac{2c}{c^2 + (k - q)^2} \ln \left(1 + \frac{\rho(k)}{h(k)} \right) dq. \tag{5.25}
$$

We set the left hand side of this equation to define $\epsilon(k)$

$$
\epsilon(k) = \frac{\hbar^2 k^2}{2m} - \mu - \frac{k_B T}{2\pi} \int \frac{2c}{c^2 + (k - q)^2} \ln \left(1 + e^{-\epsilon(q)} \right) dq, \tag{5.26}
$$

corresponding to the energy of the excitation, or the energy dispersion for the thermal ensemble. This is the central addition of the Yang–Yang model to the

Lieb–Liniger model, extending the Lieb–Liniger equations to include thermal effects, with the modified Lieb–Liniger integral system

$$2\pi\rho(k)\left(1 + e^{\epsilon(k)/k_B T}\right) = 1 + \int_{-\infty}^{\infty} \frac{2c}{c^2 + (k-q)^2}\rho(q)\,dq, \qquad (5.27)$$

in downstream relationship from μ, T to n, and the rest of the equations of state derived before. As an example, the Yang–Yang linear pressure equation of state is

$$\mathcal{P} = \frac{k_B T}{2\pi} \int_{-\infty}^{\infty} \ln\left(1 + e^{-\epsilon(k)/k_B T}\right) dk, \qquad (5.28)$$

whith a virial expansion in the low fugacity limit carried in reference [70], and the Yang–Yang entropy equation of state

$$\mathcal{S} = \frac{k_B T}{2\pi} \int_{-\infty}^{\infty} \left[(\rho(k) + h(k)) \ln\left(1 + e^{-\epsilon(k)/k_B T}\right) + \rho(k)\frac{\epsilon(k)}{k_B T}\right] dk, \qquad (5.29)$$

from the pressure (e.g. in [64]) includes both the particle and hole densities. Finally, all the relations in the Yang–Yang thermodynamics reduce to the Lieb–Liniger thermodynamics for $T = 0$, and to the ideal Bose gas thermodynamics when $c = 0$. The Yang–Yang thermodynamics has no fundamental bounds in its validity across the parameter space of temperature and interaction strength. Appendix C describes practical considerations for numerically integrating the equations of state.

5.5 The one-dimensional regimes

We initially prepare degenerate Bose gases that live and interact in three dimensions using the sequence from Chapter 1 in RbChip. From Section 2.2, the frequency associated with the thermal energy of a degenerate 3D gas in equilibrium is $k_B T/h = 420\,\text{Hz}$, with a trap depth on the scale of $U_0 \sim 10 k_B T$. The motional dynamics follow the characteristic harmonic trapping frequency $\omega/2\pi \sim 100\,\text{Hz}$. Additionally, the mean-field energy scale gives a frequency of $4\pi\hbar^2 a n_0/mh \sim 100\,\text{Hz}$, directly related to the global chemical potential μ_0. The energy scale hierarchy in a 3D Bose gas follows $U_0 > k_B T > \mu_0 \gtrsim \hbar\omega$.

Different length scales define an equivalent hierarchy. For instance, the thermal de–Broglie wavelength $\lambda_{\text{dB}} = (2\pi\hbar^2/mk_B T)^{1/2} \sim 1\mu\text{m}$ gives the magnitude for the inverse momentum distribution width. The harmonic oscillator gives an oscillator length $l_\omega = \sqrt{h/m\omega} = 2.7\mu\text{m}$. Mean-field interactions provide a healing length from the global chemical potential $\xi = \hbar/\sqrt{2m\mu_0} \sim 0.75\mu\text{m}$ in a superfluid, and the mean interatomic spacing from the average (volumetric) density is $n_0^{-1/3} \sim 10\mu\text{m}$. In addition, the s-wave scattering length sets the lowest bound, which for ^{87}Rb is $a \sim 5\,\text{nm}$. In our case, the length scale hierarchy in a 3D Bose gas follows $n_0^{-1/3} > l_\omega > \lambda_{\text{dB}} > \xi > a$.

We acknowledge three different 1D regimes for harmonically trapped Bose

gases. We refer to the first one as the elongated gas regime, exclusively defined by the aspect ratio condition $\omega_\perp > \omega_\parallel$, where $\omega_\perp/2\pi$ represents the geometric mean of the transverse trapping frequencies, and $\omega_\parallel/2\pi$ is the longitudinal trapping frequency. Trapped gases in this regime look thin and elongated, and their properties at sufficiently low temperatures ($k_B T < \mu$) are modeled accurately by the Gross–Pitaevskii equation (GPE) [71, 72]. Elongated gases have reduced, but not completely frozen dynamics in two out of three dimensions. Atoms in one of the trapping quadratures are free to interact with atoms in other quadratures whenever $\hbar\omega_\perp < \mu$. Similarly, atoms may scatter into other trapping quadratures when enough kinetic energy is available and $k_B T > \hbar\omega_\perp$. Elongated gases are effectively still 3D, but remain interesting for their ability to host metastable topological defects such as solitons [73], solitonic vortices [74], and spin domain walls [75].

We refer to the second regime as the quasi-1D regime. Here, the conditions $\hbar\omega_\perp > \mu > \hbar\omega_\parallel$ further constrain the classification. In this case, even though transverse dynamics freeze completely, the unconstrained thermal energy may be in excess of the chemical potential $k_B T > \mu$ causing thermal fluctuations to overwhelm other quantum fluctuations present in the degenerate regime. The quasi-1D regime displays the phenomenon of quasi-condensation [76], where at sufficiently low temperatures the coherence length becomes smaller than the size of the system, but larger than the mean atomic separation, implying the absence of a global phase coherence present in our 3D BECs. Experimentally, this results in supressed

131

density fluctuations and enhanced phase fluctuations, which exchange roles after free expansion in time-of-flight (TOF) as shown in Figure 5.4. While the three images represent $\omega_\perp/\omega_\parallel > 1$, a cloud in the elongated regime need not even look elongated. A quasi-1D cloud shows enhanced phase fluctuations *in-situ* translate to density fluctuations as "self-interfering" sections of the cloud overlap. Finally, a gas in the full 1D regime is characterized by a transverse harmonic energy scale overwhelming the thermal energy and chemical potential energy scales.

Last, we refer to the third regime as the full 1D regime. In the full 1D regime, the energy required to excite transverse dynamics overwhelms the thermal energy, chemical potential, and longitudinal motion energy. A harmonically trapped Bose gas enters the full 1D regime when $\hbar\omega_\perp > k_B T > \mu \gg \hbar\omega_\parallel$. Such a deeply 1D Bose gas may reach quantum degeneracy only at ultra low temperatures, beyond the quasi-condensate phase [76]. Exotic 1D physics for a harmonically trapped Bose gas may occur near the threshold where the interparticle spacing becomes comparable to the scattering length, and the scattering problem cannot be regularized as originally done in [77], but these lie outside of the scope of this dissertation. Table 5.1 summarizes the different regimes and their characteristic energy and lengthscale hierarchies. Given the three models at the beginning of this Chapter, we draw a "phase" space in Figure 5.5 for a full 1D homogeneous Bose gas. The relevant parameters are temperature T in units of a 1D degeneracy temperature $T_d = \hbar^2 n^2/2mk_B$, and the relevance of interactions parametrized by the Lieb–Liniger parameter γ.
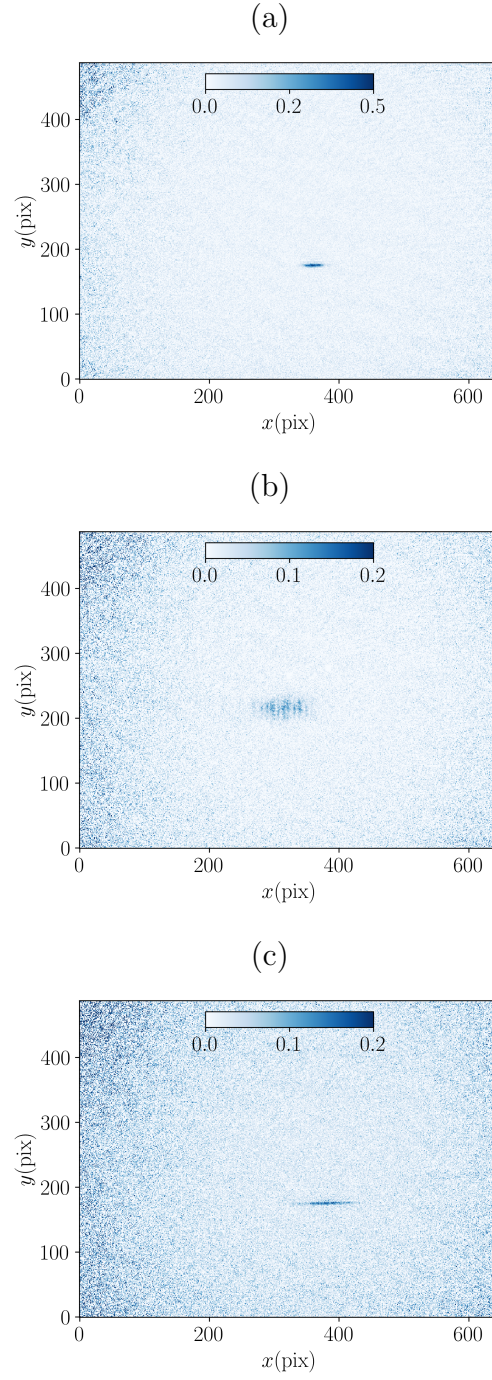
Figure 5.4: One dimensional regimes. Absorption images for (a) a cloud in the elongated gas regime, (b) in the quasi-1D regime after a short time-of-flight ($t = 3\,\mathrm{ms}$), and (c) in the full 1D regime.

Elongated	Quasi-1D	Full 1D
$\hbar\omega_\perp > \hbar\omega_\parallel$	$\hbar\omega_\perp > \mu > \hbar\omega_\parallel$	$\hbar\omega_\perp > k_B T > \mu > \hbar\omega_\parallel$
$l_\perp < l_\parallel$	$l_\perp < \xi < l_\parallel$	$l_\perp < \xi < \lambda_{\mathrm{dB}} < l_\parallel$
Topological defects	Quasi-condensation	Fermionization

Table 5.1: Summary of energy and lengthscale hierarchies defining 1D regimes. The bottom row shows examples of physics milestones accessed in each regime.

The ideal Bose gas lies at the left in this $T - \gamma$ parameter space, where $\gamma \approx 0$. The virial expansions further restrict the ideal Bose gas "phase" to the top left corner, where $T \gg T_d$. While Bose statistics weigh in at temperatures $T \sim T_d$, a homogeneous 1DBG may never condense, we refer to the green region as the classical 1D regime. After allowing weak interactions $\gamma < 1$, sufficiently low temperatures give a mean-field describable 1DBG, highlighted in blue in Figure 5.5. Finally, crossing the $\gamma = 1$ line into more relevant interactions tends to the fermionized Bose gas on the right side of Figure 5.5. At a high enough temperature, even in the presence of strong interactions, thermal fluctuations dominate over quantum fluctuations, leading to the "classical" hard core Bose gas. In the next Chapter 6 we find our 1DBGs scatter near the degeneracy $T/T_d = 1$, and strongly interacting regime $\gamma = 1$ boundary.
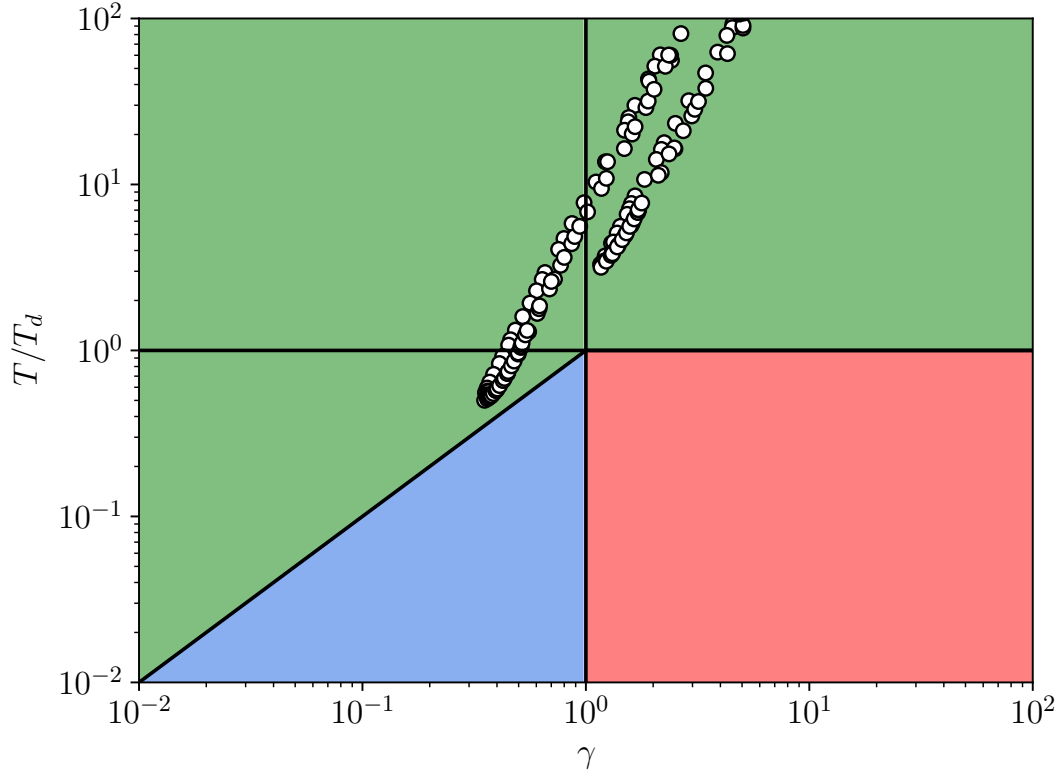
Figure 5.5: Temperature and interaction parameter space. Different colors highlight the continously connected classical (green), weakly interacting degenerate (blue), and strongly interacting degenerate (red) full 1D gas regimes. The scattered data is represents instances of experimentally sampled states from Chapter 6.

5.6 Conclusion

We reviewed three models describing the thermodynamics of homogeneous, one-dimensional Bose gases with contact repulsive interactions. The absence of interactions gives the ideal Bose gas thermodynamics, for which a virial expansion arises in the limit of low fugacity. In contrast, the Lieb–Liniger thermodynamics give exact solutions for arbitrary interactions at zero temperature. The Lieb–Liniger model implies that low densities increase the relevance of interactions $\gamma \propto n^{-1}$, thereby adding an important ingredient for strong correlations. The Yang–Yang thermodynamics extends the exact Lieb–Liniger thermodynamics for nonzero temperatures, making it the most versatile model for 1D Bose gases across a wide parameter space. Last, we introduced the experimental criteria to distinguish different trapped 1D Bose gas regimes.

Chapter 6: Equations of state of individual 1D Bose gases

This chapter studies the thermodynamics of isolated one-dimensional Bose gases (1DBGs) in the full 1D regime by using optical dipole traps. The long-term motivation for isolating 1DBGs in spin-independent traps is to depart the mean-field interaction regime using the inverse density dependence of the interaction parameter γ from Chapter 5, where the 1DBG tends to fermionize. There, a vastly unexplored range of experiments exists where spinor gases are no longer easily described by multi-component mean-field theories. Furthermore, the addition of Raman beams to engineer spin-dependent dispersions [78] opens the possibility of quantum simulating exotic magnetic phases in strongly correlated 1D systems [79]. For this, we envision the capability of cooling the trapped 1DBG to mitigate the heating from spontaneous emission associated with the Raman dressing.

Our first challenge experimentally is to confine an individual Bose gas into one-dimension, for which we design and implement a high aspect-ratio crossed optical dipole trap. The resulting shallow potential along 1D allows the most energetic particles to leave in a "spontaneous" form of evaporative cooling. Then, using the quantitative bright-field microscopy tools from Chapter 4, we measure the *in-situ*

linear density distributions using resonant absorption imaging. The local density approximation (LDA) links the known trapping potential to the chemical potential, and then to the observed local density. Finally, we retrieve the global chemical potentials and temperatures by fitting the density equations of state with the exact Yang–Yang thermodynamics from Chapter 5. We find that while our individual 1D Bose gases undergo evaporative cooling, they escape the degenerate regime.

This Chapter is organized as follows. In Section 6.1, I describe the design, and characterization of the combined blue and red-detuned crossed dipole trap giving an extreme aspect ratio to enter the full 1D regime. In Section 6.2, I describe measurements of the density equations of state using *in-situ* resonant absorption imaging, and the subsequent analysis using the Yang–Yang thermodynamics. Reference [60] reports most of the results from this Chapter.

6.1 Trap design and characterization

We design and characterize the dipole traps used to enter the full 1D regime, as defined in Chapter 5, Section 5.5. Most experiments creating 1DBGs in this regime opt for two-dimensional optical lattices [15,80,81], giving an inhomogeneous ensemble of 1DBGs. An alternative approach is tight magnetic confinement from atom chips [82,83], giving individual, single spin component 1DBGs. The inhomogeneous ensembles in 2D-optical lattice experiments prevents direct access to local observables, and individual 1DBGs are never truly isolated from each other, even

in deep lattices with suppressed tunneling. Atom chip experiments rule out experiments with multiple spin components, and are limited to bosons with nonzero magnetic moment. Our realization bridges the two approaches, entering the full 1D regime with individual and isolated ensembles in spin-independent potentials.

6.1.1   Transverse dipole trap

After introducing red-detuned Gaussian beam dipole traps in Chapter 2, we now introduce blue-detuned Laguerre–Gaussian (LG)beam dipole traps. LG beams comprise solutions to the scalar Helmholtz equation in cylindrical coordinates, with circlularly symmetric Gaussian beams representing the lowest eigenmode. We start with the full spectrum of electric field modes

$$E_m^l(r, \phi, z) \ = E_0 \frac{A_m^l}{w(z)} \left(\frac{\sqrt{2}r}{w(z)} \right)^l \mathcal{L}_m^l \left(\frac{2r}{w^2(z)} \right) e^{-r^2/w^2(z)} e^{ikr^2/2R(z)} e^{il\phi} e^{-i\zeta(z)}, \ (6.1)$$

with amplitude E_0, and where $\mathcal{L}_m^l$ is the generalized (or associated) Laguerre polynomial of order l and index m. The integers $m = 0, 1, ...$ and $l = -m, ...m$ count the number of $m + 1$ radial nodes and $2\pi l$ phase windings (i.e. topological vortex charge) around ϕ respectively [84]. Similarly, the normalization factor

$$A_m^l = m! \left(\frac{2}{\pi m!(|l|+m)!} \right)^{1/2}$$

depends on the mode indices. Here, we adopt the standard Gaussian waist $w(z) = w_0\sqrt{1 + (z/z_R)^2}$, Rayleigh length $z_R = \pi w_0^2/\lambda$, wavefront radius $R(z) = z[1 +$

$(z/z_R)^2]$, wavenumber $k = 2\pi/\lambda$, and Guoy phase $\zeta(z) = \arctan z/z_R$. The normalized $m = 1$, $l = 0$ field

$$
\begin{aligned}
E_0^1(r, \phi, z) = \sqrt{\frac{P}{\pi}} \frac{2r}{w_0^2(1 + z^2/z_R^2)} \times \\
\exp\left[-\frac{r^2}{w_0^2(1 + z^2/z_R^2)}\right] \times \\
\exp\left[-\frac{ikr^2}{2R(z)} - i\phi + i\zeta(z)\right],
\end{aligned}
\tag{6.2}
$$

now in terms of the total power P, and minimum waist w_0, has a linearly increasing amplitude with r modulated by a Gaussian envelope, therefore giving a quadratically increasing radial intensity

$$
I_0^1(r, z) = \frac{2P}{\pi w^2(z)} \frac{2r^2}{w^2(z)} e^{-2r^2/w^2(z)},
\tag{6.3}
$$

which has a fantastic harmonic expansion around $r = 0$. Since blue-detuned dipole beams repel atoms from the high intensity regions, the hollow core of LG beams trap atoms around $r = 0$, while simultaneously giving reduced scattering rates. This last fact has been suggested to enhance precision spectroscopy inside a blue-detuned hollow-core Bessel beam [85]. Similarly, [86] uses a LG_{01} hollow-core trap to guide the longitudinal expansion of magnetically trapped ultracold ^{87}Rb. To our knowledge, no other experiments use blue-detuned LG_{01} dipole traps to enter the full 1D regime with ultracold ^{87}Rb.

The far-detuned three-dimensional LG_{01} dipole potential in the limit of an

ideal linearly polarized mode becomes

$$U(r, z) = \frac{6P\Gamma c^2}{\Delta\omega_0^3} \frac{r^2}{w^4(z)} e^{-2r^2/w^2(z)}. \tag{6.4}$$

Figure 6.1 shows numerically evaluated transverse and longitudinal potential land-scapes. While the transverse potential provides isotropic radial confinement, the longitudinal landscape forms an antitrap. Physically, the antitrap comes from the longitudinal gradient of the transverse zero-point energy in the harmonic approximation. While the potential $U(r = 0, z) = 0$ vanishes exactly in a line, atoms still feel the repulsion away from $r = 0$. For a focusing LG_{01} mode, the transverse zero-point energy falls off away from the focus as a Lorentzian with a width parameter proportional to the Rayleigh length of the LG_{01} mode. While the transverse minimum of the LG_{01} beam traps, the longitudinal maximum antitraps. The numerically calculated longitudinal antitrap shows this effect in the bottom right panel of Figure 6.1. The transverse harmonic trapping frequency varies by $\sim 20\%$ at $z = z_R$.

We use a custom, $2\,\text{in.}$ diameter, 2π-spiral phase plate (SPP) from `RPC Photonics` to wind a $+1$ charge around a $\lambda = 532\,\text{nm}$ Gaussian beam. We choose this method to produce LG beams over holographic techniques based on digital micro-mirror devices (DMDs) or spatial light modulators (SLMs) for a superior mode conversion efficiency, and high quality anti-reflection coatings. For example,
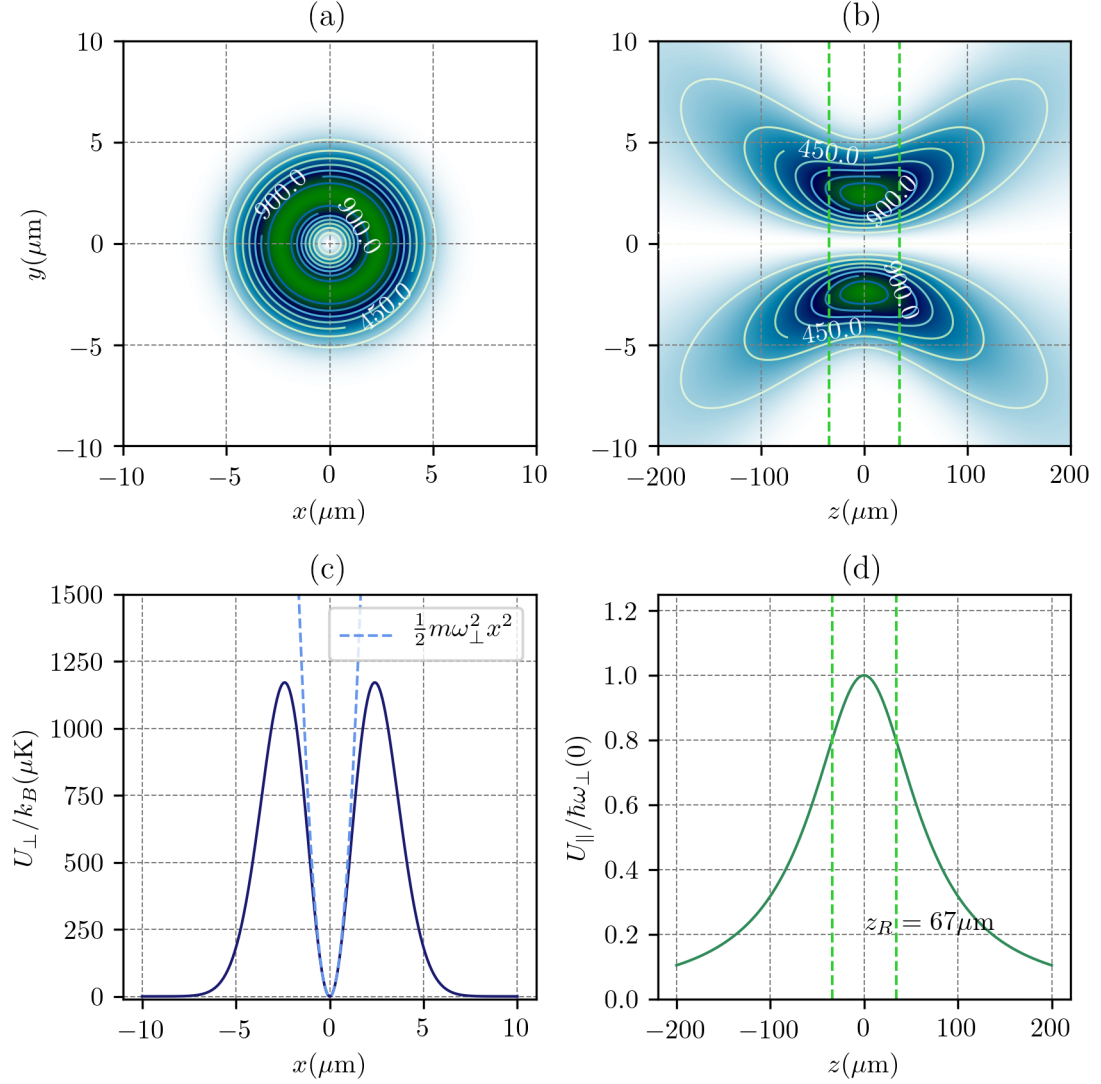
Figure 6.1: Potential landscapes from a blue-detuned LG_{01} dipole trap. The beam propagates along $\mathbf{e_z}$. (a) Two-dimensional transverse and (b) longitudinal potential landscapes for ^{87}Rb. The different contours indicate thermal isopotentials measured in mK. (c) Cross-sectional transverse, and (d) longitudinal potential landscapes for ^{87}Rb. Dashed vertical lines in (b), (d) indicate the Rayleigh length z_R, and the radial harmonic expansion with an estimated peak trapping frequency $\omega_\perp/2\pi = 51$ kHz at $z = 0$ in (c). The parameters used in this calculation are $w_0 = 3.40\,\mu$m, $P = 1.0$ W, $\lambda = 532$ nm.

we estimate that the minimum waist of an SPP mode exhibits a > 40dB extinction

ratio in the peak to vortex intensity level, only limited by the dynamic range of

our detector.

We start with a Gaussian beam with an $1/e^2$ beam diameter of $2.3(2)\,\mathrm{mm}$ coming out of a $25\,\mathrm{W}$ `Millennia-eV` laser. A large fraction of the power coming out of the laser pumps a Ti:Sapph cavity to produce $\lambda = 790\,\mathrm{nm}$ Raman beams as described in [19]. We pick off $\sim 3.0\,\mathrm{W}$ of power before the Ti:Sapp input and send them through a half-waveplate (HWP) followed by a polarizing beam splitter (PBS) to limit the maximum power entering our LG beam setup. A second HWP after the PBS matches the optimum input polarization for a custom `IntraAction` `ASM-802B47` fused-silica, high-power acousto-optic modulator (AOM) operating at $80\,\mathrm{MHz}$. We block the zero-th order and pick the first order out of the AOM, allowing us to tune the intensity through the input radiofrequency power of the AOM. We then inject the first order into a single mode, polarization mantaining photonic crystal fiber (PCF) `LMA-PM-15` with copper heat sinks at the tips to enable high-power injection. We align the linear polarization of the beam to the fast axis of the fiber with a HWP, and match the $1/e^2$ mode field diameter of $12.2(1)\,\mu\mathrm{m}$ at 532nm by focusing the beam with a `EO 84-339`, 0.42 numerical aperture (NA) aspheric lens. The combined AOM diffraction and fiber injection efficiency give a maximum $P_0 = 1.0\,\mathrm{W}$ at the fiber output.

After collimating the PCF output with a matching `EO 84-339` lens giving a $1/e^2$ beam diameter close to $2.3\,\mathrm{mm}$, we send the Gaussian beam through a

Glan-Laser polarizer and HWP to clean and match the desired linear polarization. We sample $\sim 2\%$ of the beam and send it to a fast photo-diode to monitor the intensity. Finally, we convert the beam into a LG mode with the SPP, after which it focuses down near the atoms with the help of a high-NA `EO 49-104` aspheric lens. The two aspheric lenses form an effective $M = 0.8$ telescope, conjugating the PCF mode diameter into a $w_0 \approx 5\,\mu$m focused LG beam at the location of the atoms. In principle, this beam could be magnified by an additional factor of 2 (limited by the 45° angled 1 in. mirror apertures) before focusing down to an NA-limited minimum waist $w_0 \approx 3\,\mu$m. While we test this on the bench by profiling such a beam in Figure 6.2, we avoid doing this in the final setup to prevent strong aberration effects in the tightly focused LG beam, such as radially imbalanced traps and local intensity minima capable of trapping small, spurious clouds of cold atoms. Using the largest available aperture leads to a tighter focus, as well as undesirable aberrations. We find that a $w_0 \approx 6\,\mu$m gives an estimated peak transverse trapping frequency well in excess of 10kHz with 1 W of power.

We characterize our transverse dipole trap by profiling the LG intensity on the testbench around its minimum waist. Figure 6.2 shows a sampled three-dimensional LG beam profile in the case where we maximally use the available optical aperture before the aspheric lens (giving the minimum possible w_0). We fit the individual profiles using Equation 6.3 and reveal a vertical angle and slightly imbalanced radial intensity, both undesirable features for dipole traps. Nevertheless, the fit reveals the location and size of w_0, which together with the power give
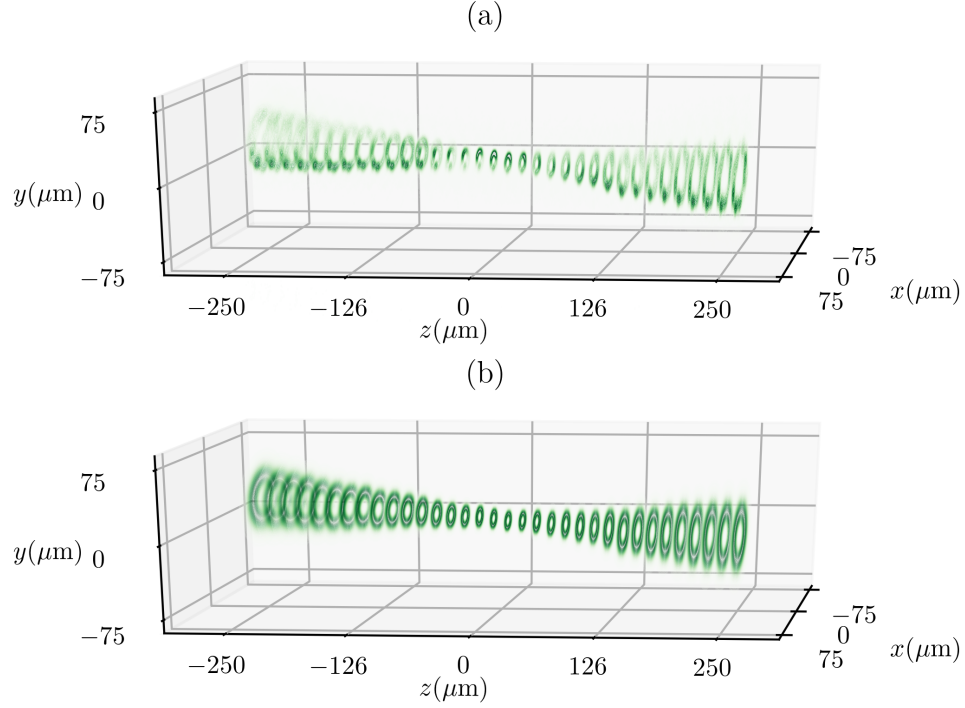
Figure 6.2: Three-dimensional beam profile of a tightly focused LG dipole beam. (a) LG_{01} profile, and (b) set of two-dimensional fits, givinga minimum waist $w_0 = 3.43(3)\,\mu\text{m}$, Rayleigh length $z_R = 69.5(8)\,\mu\text{m}$, and an estimated peak transverse trapping frequency of $\omega_\perp/2\pi = 51\,\text{kHz}$ with $1\,\text{W}$ of power.

an estimated peak trapping frequency in the transverse direction.

We align the minimum waist of the blue-detuned dipole trap with the *in-situ* BEC in two stages. In the first stage, we remove the SPP and coarsely adjust the blue-detuned Gaussian beam focus to hit the center of a large magnetically trapped cloud produced at the end of RF evaporation (see Chapter 2). We then pulse the beam to "pierce" a hole in the middle of a magnetically trapped cloud. We then maximize the density depletion caused by the repulsive Gaussian beam, and adjust its position in the xy plane. In the second stage, we put the SPP back on to pierce

145

a hole in the repulsive barrier, and optimize the number of atoms that we can adiabatically transfer into the LG_{01} hollow core. Then, we optimize the longitudinal alignment of the minimum waist by performing a differential measurement using the magnetically trapped atoms as a probe. Again, we pulse the LG_{01} intensity to maximum level for $t = 1\,\text{s}$ to deplete the density of a large magnetically trapped cloud, but we image perpendicular to the LG_{01} beam propagation axis. We form contrast images by subtracting the average optical depth of depleted clouds from the average optical depth without depletion. The contrast in Figure 6.3 outlines the focused LG_{01} beam profile. Finally, we are able to align the minimum waist of the LG beam to within $10\mu\text{m}$ of distance to the BEC along $\mathbf{e}_z$, and $2\mu\text{m}$ along $\mathbf{e}_\perp$.
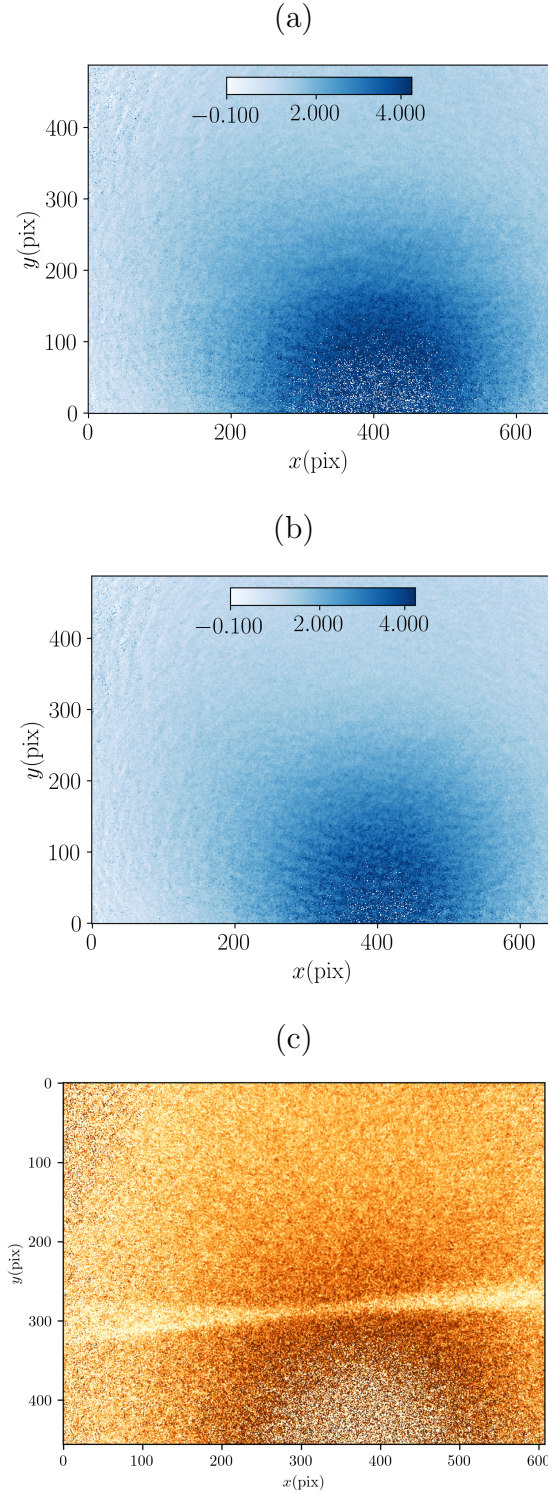
(a)

(b)

(c)

Figure 6.3: Contrast alignment method. We compare the images of two magnetically trapped clouds (a) in the presence, and (b) absence of a bright pulse of the LG_{01} beam. (c) Average optical depth contrast using 20 repetitions in the presence, and absence of the repulsive LG_{01} beam. A clear profile traverses the image from left to right, showing the minimum waist.

6.1.2   Longitudinal dipole trap

We add longitudinal confinement to cancel and overcome the antitrap in Figure 6.1 using a red-detuned Gaussian beam. The design is straightforward, using a $\lambda = 1064\,\text{nm}$ Gaussian beam similar to those forming the cross dipole trap from Chapter 2. In order to isolate elongated 1DBGs with lengths in excess of $100\,\mu\text{m}$, we overcome the LG_{01} Rayleigh length with the Gaussian waist of the red-detuned longitudinal trap. Because we have limited $\lambda = 1064\,\text{nm}$ power, we constrain the Gaussian beam aspect ratio to be elliptical rather than circular.
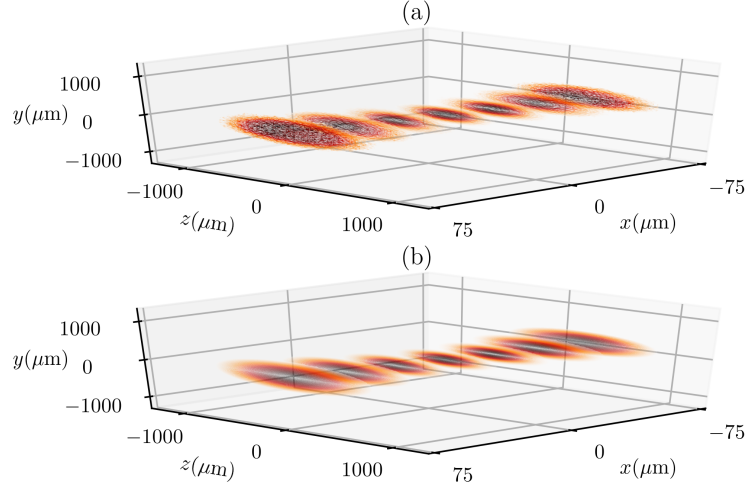

Figure 6.4: Three-dimensional beam profile of a focused, elliptical Gaussian beam. The beam propagates perpendicular both to gravity and the LG_{01} propagation axis.(a) Longitudinal beam profiles, and (b) set of fits giving a minimum horizontal waist $w_{0x} = 203(2)\,\mu\text{m}$, Rayleigh length $z_R \sim 10(0)\,\text{cm})$, and estimated peak longitudinal trapping frequency of $\omega_\parallel/2\pi = 35\,\text{Hz}$ using $750\,\text{mW}$ of power.

We prepare the red-detuned Gaussian beam with a similar launch as the

blue-detuned Gaussian beam, with an AOM tuning the final intensity level. After launching a peak power of $750\,$mW into a single-mode, polarization maintaining fiber, we collimate the fiber output and clean the outcoupled linear polarization with a high-power Glan-Laser polarizer. After aligning the linear polarization with a HWP, we use a rotatable anamorphic prism pair with anamorphic magnification of 2.0 to give the transversely round Gaussian an elliptical profile with aspect ratio $w_x \approx 2w_y$. Finally, we combine this elliptical beam with one of the two original Gaussian beams forming the evaporating cross-dipole trap along $\mathbf{e}_x$ using a PBS. The beams then focus down to a minimum waist near the atoms. We profile the beam in the testbench to validate our design, as shown in Figure 6.4.
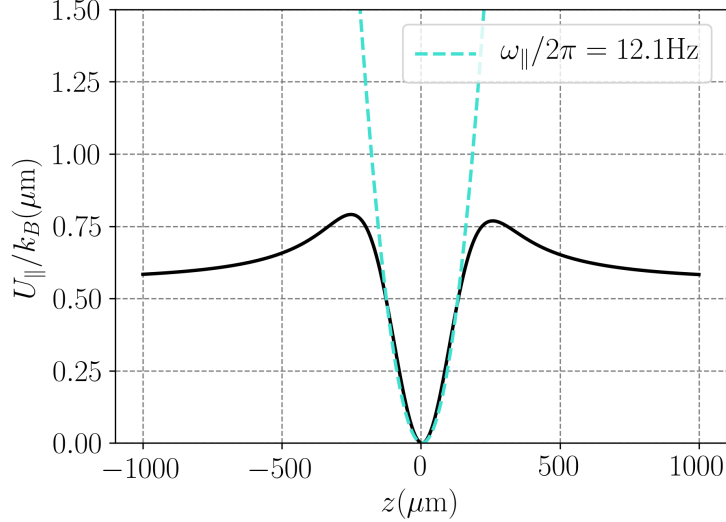

Figure 6.5: Calculated combined longitudinal potential. The combined longitudinal potential shows a barrier near the transition from Gaussian (exponentially decaying, attractive trap) to Lorentzian (algebraically decaying, repulsive antitrap). A harmonic expansion around the center (dashed) is only valid for displacements smaller than the final size of the 1DBGs, so we consider the full combined model.

The focused red-detuned Gaussian beam crosses the LG_{01} beam at $\sim 90\,°$ to provide longitudinal confinement with low harmonic curvature $\omega_\parallel \approx 2\pi \times 35\,\text{Hz}$. Additionally, we use the AOM to slightly control the depth for longitudinal evaporation. The longitudinal intersection of the two dipole traps forms a combined potential between the antitrap and longitudinal trap with an effective harmonic frequency of $\omega_\parallel/2\pi = 12.13(20)\,\text{Hz}$. While the combined longitudinal potential has a harmonic component, it is mostly anharmonic. Neglecting arbitrary energy offsets, the combined potential

$$U(z) = \frac{\hbar\omega_\perp^{(0)}}{1 + (z - z_a^2)/z_R^2} + U_t e^{-2z^2/w_x^2} \tag{6.5}$$

has two contributions from the antitrap, and the longitudinal Gaussian beam, assuming $\mathbf{e}_z$ is perpendicular to the direction of gravity. The peak transverse trapping energy $\hbar\omega_\perp^{(0)}$ represents the maximum of the antitrap, falling off as a Lorentzian centered about z_a with a width proportional to the Rayleigh length z_R of the LG_{01} beam. The contribution from the red-detuned longitudinal trap gives a depth U_t, growing like a Gaussian beam of waist w_G. Figure 6.5 shows the combined longitudinal potential with $U_0 = 0$ where the individual contributions show the decaying antitrap dominate at long distances.

6.2   Density equations of state

We load the 1D Bose gases by slowly transitioning from an initial 3D crossed dipole trap to our final combined blue and red-detuned trap. Figure 6.7 shows the intensity ramps that put the atoms into the full-1D regime. There are four loading stages, labeled by (i), (ii), (iii), and (iv). During stage (i), we raise the LG_{01} trap intensity above the threshold where it levitates atoms against gravity, while simultaneously keeping the original crossed dipole constant. Then, in stage (ii), we gently lower the intensity of the crossed dipole trap until it mostly provides longitudinal confinement, but is otherwise unable to levitate the atoms against gravity. During the third stage (iii), we ramp the longitudinal dipole trap intensity adiabatically to the point where it overcomes the longitudinal confinement of the remaining crossed dipole beams. Finally, in (iv) we simultaneously ramp the LG_{01} trap to its final intensity and extiniguish the crossed dipole beams. Eeach stage takes $t = 250\,\text{ms}$. We optimize the adiabaticity of the loading procedure by minimizing residual motion of the cloud after finishing the transfer. In Figure 6.6, we illustrate four steps in the systematic optimization, where we compare the amounts of residual motion, net displacement, and breathing dynamics of the cloud after loading it into the final 1D trap. Damped dipole oscillations and complicated breathing dynamics indicate anharmonic dephasing. As a result, the quality of the small amplitude dipole oscillations improves with smaller net displacements.
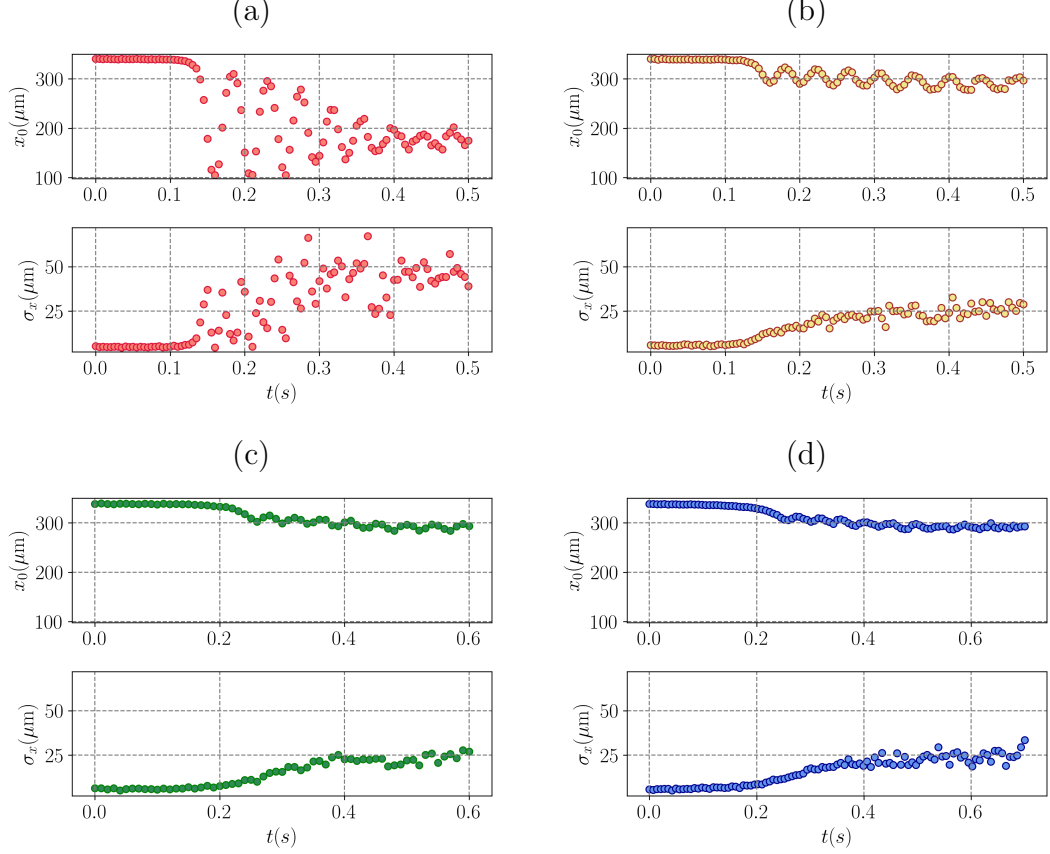
Figure 6.6: Optimization of the loading procedure. We track the center of mass (x_0) and width (σ_x) of the 1D clouds during the loading stages (i)-(iv). (a) Loading with three $t = 150$ ms linear ramps and a last $t = 50$ ms ramp giving large amplitude dipole oscillations. (b) Loading after fixing the alignment of the longitudinal trap relative to the center of the LG_{01}. (c) Loading after increasing the durations of all the ramps to $t = 150$ ms. (d) Loading after we simultaneously increase the stage durations to $t = 250$ ms, and use the sigmoid ramps shown in Figure 6.7 (b).

We image the 1D Bose gases with a sequence of repump and resonant probe $20\,\mu$s pulses, transferring atoms first from $|F = 1, mF = 0\rangle$ to $|F = 2\rangle$ in the hyperfine ground state manifold, and then absorbing light in the resonant $5S_{1/2}|F = 2\rangle$ to $5P_{3/2}|F = 3\rangle$ transition. The average intensity is $2.5\,I_{\text{sat}}$ (see Chapter 4). We first acquire an image of the absorbed light I_a, followed by an image of the probe I_p, and an image of the background light in the absence of any illumination I_d. We
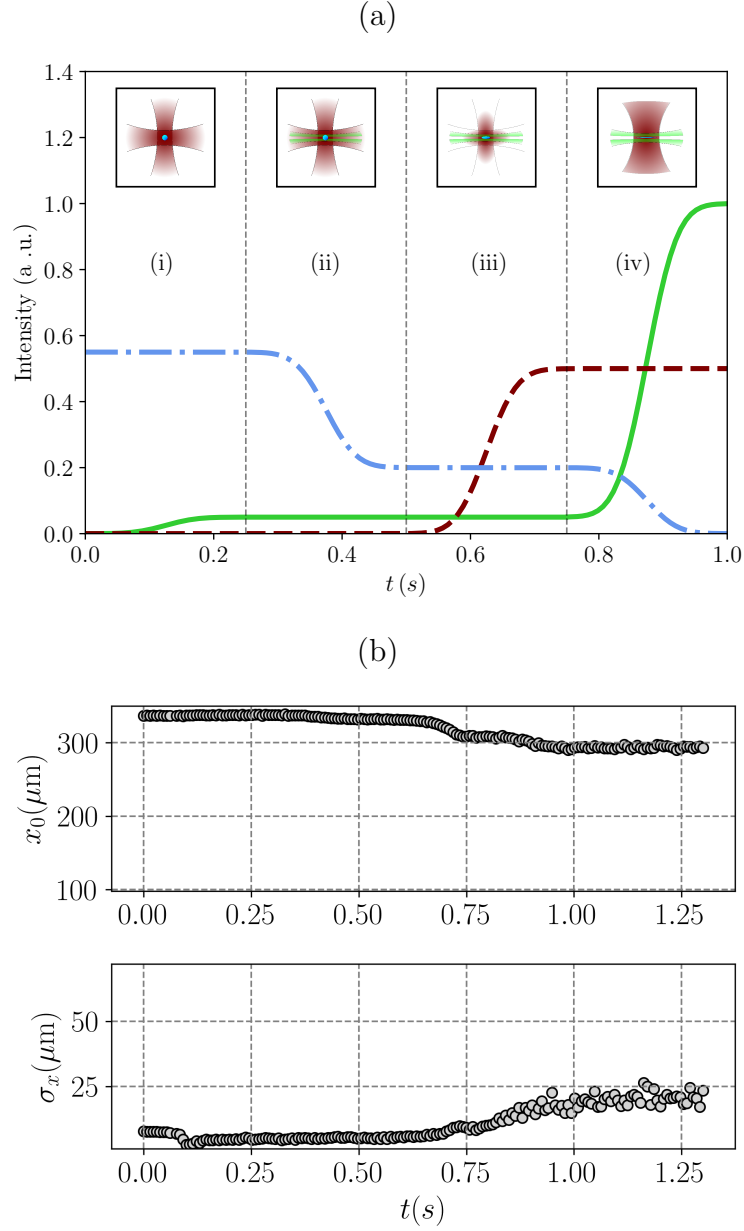
Figure 6.7: Loading procedure for 1D Bose gases. (a) Schematic directly reproduced from [60]. (b) Center of mass and width dynamics of the 1D cloud during, and slightly after the optimized transfer, where negligible residual dipole and breathing dynamics are present.

combine these images and process them using the methods in Chapter 4, Section 4.3.3 to obtain linear density profiles like the one in Figure 6.8. Furthermore, we build ensembles with $N \sim 100$ repetitions to improve the signal-to-noise ratio of
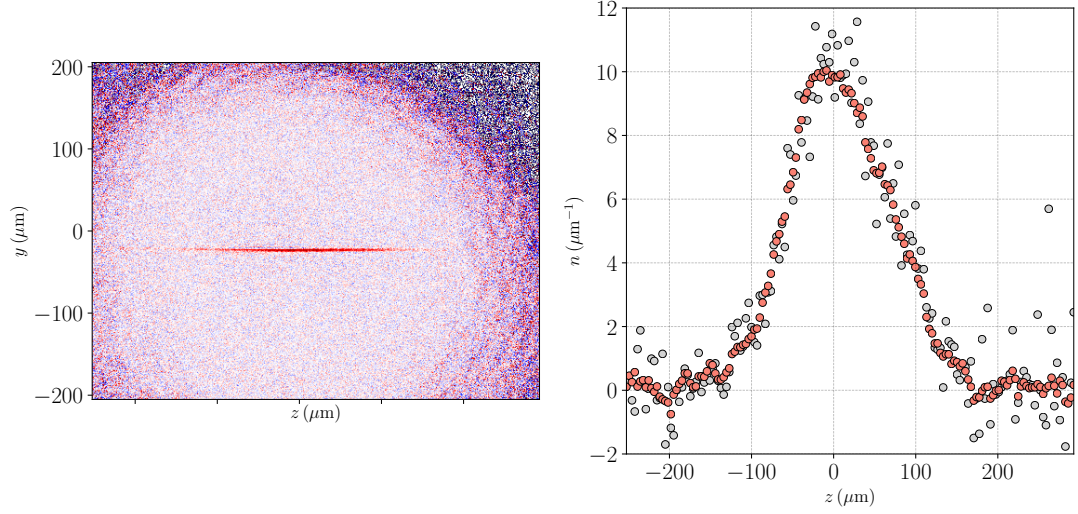
the density distributions.

Figure 6.8: 1D density profiles from *in-situ* images. Absorption image of an individual 1DBG after image processing described in Chapter 3. By integrating the optical depth, we obtain the linear density profile of an individual 1DBG (gray circles). We increase the signal-to-noise ratio by averaging of $N = 110$ individual such profiles into a single density profile (pink circles).

6.2.1 Global Yang–Yang fits

We acquire two datasets with 1D Bose gases similar to the example in Figure 6.8. In one dataset, we load the same 1D traps starting with different 3D clouds, including BECs and nondegenerate (thermal) clouds, and image the density distributions right at the end of the loading procedure. In a second dataset, we load a 1D trap from the most degenerate 3D BEC we can produce using dipole evaporation, and then hold it in time and image it at different times following the loading procedure. We then use the Yang–Yang (YY) thermodynamics from Chapter 5 and the local density approximation (LDA) to fit the observed density

distributions, and extract the global temperature T, and global chemical potential μ_0. The LDA

$$\mu(z) = \mu_0 - U_\parallel(z) \tag{6.6}$$

links the known longitudinal potential to local variations in the chemical potential. The YY equations of state then predict the local densities as if it were a homogeneous 1D Bose gas. The two datasets comprise 24 different realizations labeled by an index j, as depicted in Figure 6.9. We perform local (on a per-realization-basis) YY fits, and a global (across all realizations) YY fit to extract the thermodynamic states of our 1DBGs. The two give the same qualitative results, summarized in Figure 6.10.

We find our 1DBGs enter the strongly interacting regime at the lower achieved temperatures, with a record Lieb–Liniger parameter from Chapter 5 of $\gamma \approx 3$. Unfortunately, when we collapse our data into the $T/T_d, \gamma$ parameter space in Figure 5.5 from Chapter 4, we note that we fall short of entering the strongly-interacting, degenerate regime at the same time. While Table 6.1 summarizes the calibrated and fit parameters for the longitudinal potential (and chemical potential), the free parameters of global chemical potential μ_0, and temperature T reveal an interesting outcome. We vary the 3D cloud temperature T_{3D} in the first dataset, and find that the global chemical potential μ_0, and atom number N follow a similar trend, while the 1D temperature opposes the 3D trend. We then hold our 1DBGs in time, and observe the global chemical potential and number show decaying
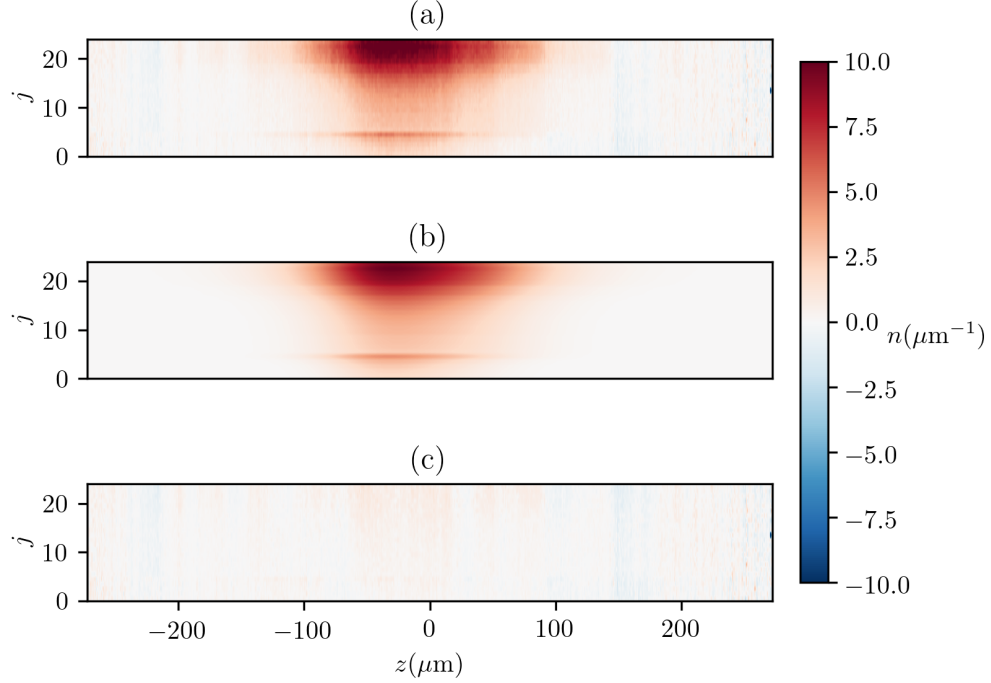
Figure 6.9: Global YY fit. *In-situ* density distributions (a) across all realizations labeled by j, the (b) evaluated global YY fit, and (c) global fit residuals. Local fits (on a per realization basis) leave the qualitative results unchanged.

trends, while the 1D temperature keeps decreasing. The 1D temperature tends to a value consistent with the longitudinal trap depth, from which we conclude the 1DBGs undergo evaporative cooling. We find that the global chemical potential decreases with increasing 3D temperature, an expected result from inefficient loading at higher temperatures since the spatial 3D density is lower. Nevertheless, we see an interesting trend in 1D temperature, where colder 3D gases result in warmer 1D clouds. This result is counterintuitive, and suggests a breakdown of adiabaticity in the loading at first glance. On further analysis, after normalizing
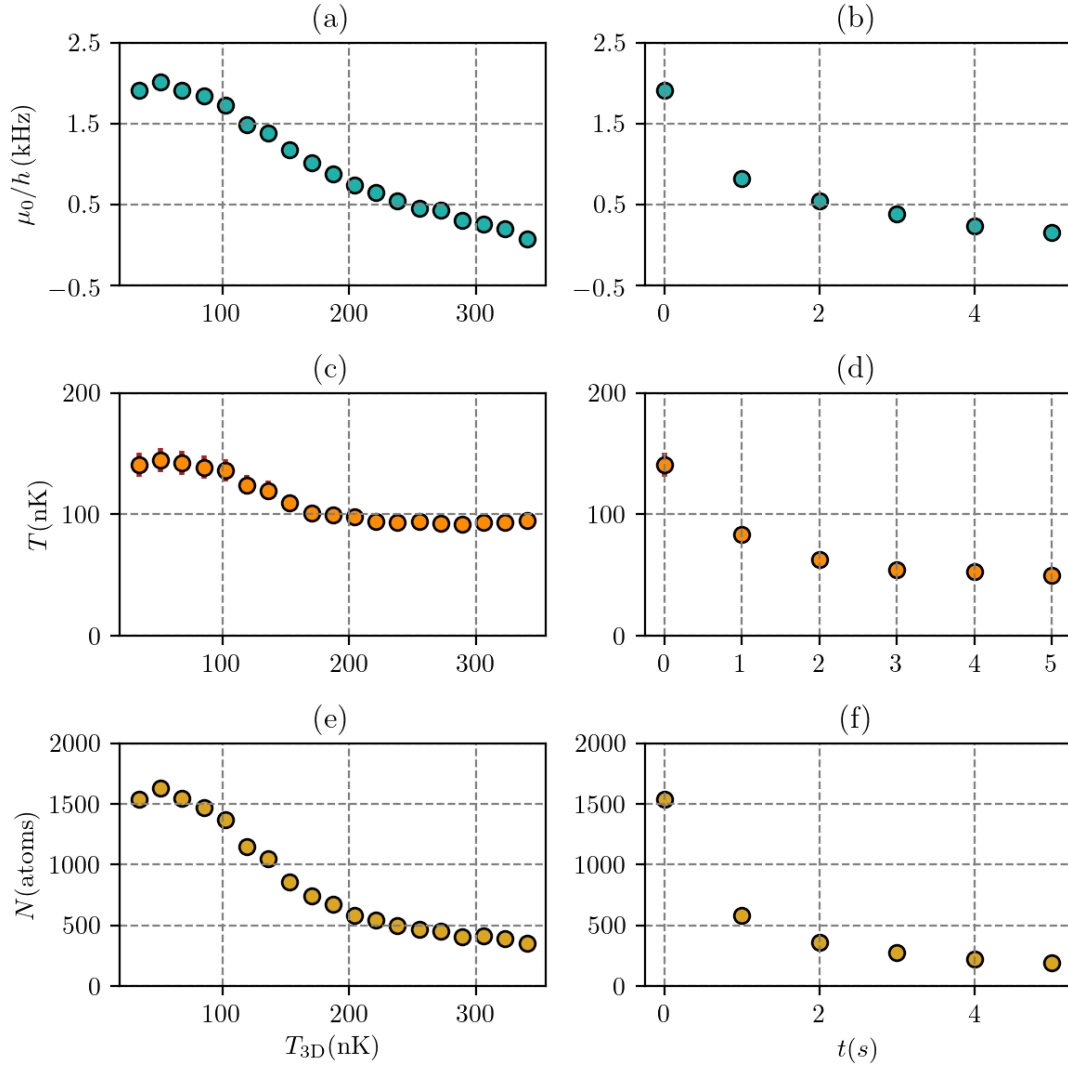
Figure 6.10: Temperature, global chemical potential, and number. Experimentally extracted global chemical potential as a function of 3D gas temperature (a), and time (b), 1DBG temperature as a function of the 3D gas temperature (c), and time (d), and atom number as a function of the 3D gas temperature (e), and time (f).

the 1D temperature by the peak one-dimensional degeneracy temperature

$$T_d^{(0)} = \frac{\hbar^2 n_0^2}{2mk_B} \tag{6.7}$$

at the center of the 1DBG, we reveal the peak degeneracy parameter $T/T_d^{(0)}$. Figure 6.11 shows the transformed fit parameters after this, allowing us to regain an intuitive interpretation in the first experiment where degenerate 3D gases result in degenerate 1DBGs. On the other hand, the 1DBG degeneracy parameter increases over time, into the classical regime. We conclude that the evaporative

Parameter	Calibrated value	Value from fit	Calibration method
$\omega_\perp/2\pi$	$17\,(4)\,\mathrm{kHz}$	$17\,(2)\,\mathrm{kHz}$	Transverse expansion in TOF
z_a	$0\,(10)\,\mu\mathrm{m}$	$-7.670\,(8)\,\mu\mathrm{m}$	Alignment precision
z_R	$185\,(29)\,\mu\mathrm{m}$	$185\,(5)\,\mu\mathrm{m}$	Intensity profile of LG beam
U_t/k_B	$-1.17\,(25)\,\mu\mathrm{K}$	$-1.37\,(6)\,\mu\mathrm{K}$	Intensity profile of Gaussian beam
w_G	$203\,(2)\,\mu\mathrm{m}$		Intensity profile of Gaussian beam
$\omega_z/2\pi$	$12.13\,(20)\,\mathrm{Hz}$		Small amplitude dipole oscillations
δz		$8.19\,(30)\,\mu\mathrm{m}$	

Table 6.1: Global YY fit parameters. We used calibrated values and their uncertainties as initial guesses and bounds for the global YY fit.

cooling along the longitudinal axis of the tube trap is unable to increase or even maintain degeneracy.

While we lack more experimental evidence to support the following argument, we believe that the observed inefficient evaporative cooling results from the slower relative decrease in 1D temperature with respect to the 1D degeneracy parameter proportional to the peak density. This is in stark contrast with 3D evaporative cooling, where although the condensation temperature T_c changes with the peak

density, it does so slowly compared to the global temperature, allowing the 3D Bose gas to condense. We can use the commonly used definition of degeneracy temperature T_d as the temperature for which the interparticle spacing equals the thermal de–Broglie wavelength. In D-dimensions, the degeneracy threshold $\lambda_{dB} = l_D$ gives the scaling relationships

$$n^{-1/D} = \left(\frac{2\pi\hbar^2}{mk_BT_d} \right)^{1/2} \tag{6.8}$$

$$T_d = \frac{2\pi\hbar^2 n^{2/D}}{mk_B} \tag{6.9}$$

between the D-dimensional particle density and the degeneracy temperature. The small, sublineal drop in T_d relative to a drop in n (i.e. from forced evaporative cooling) in 3D is far more forgiving than the large, superlinear drop in T_d relative to a drop in n in 1D. The degeneracy parameter gives an additional interpretation of the spontaneous evaporative cooling, where a slower decrease in the global 1DBG temperature relative to the decrease of T_d drives the system away from quantum degeneracy.
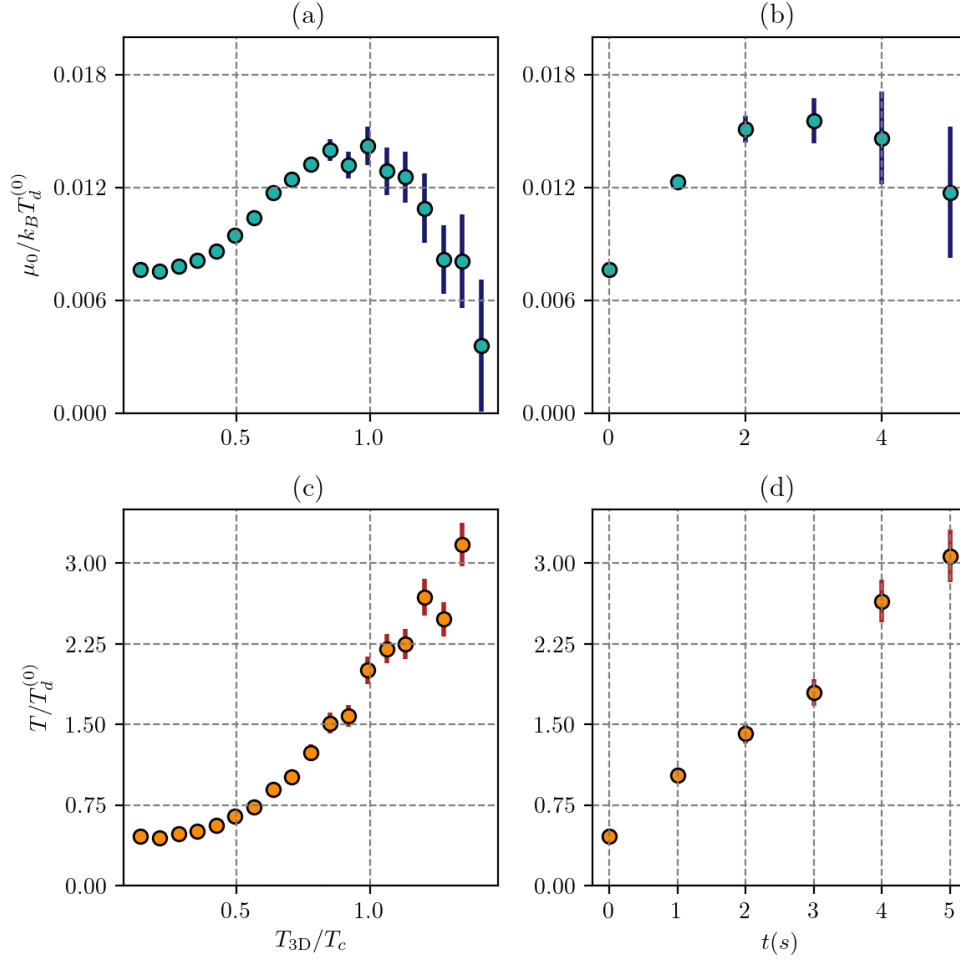
Figure 6.11: Degeneracy global fit parameters. Normalized global fit parameters (with Equation 6.7) showing the reduced global chemical potential as a function of (a) the 3D gas temperature, and (b) time, and the peak degeneracy parameter as a function of (a) the 3D gas temperature, and (b) time.

6.3 Conclusions

We obtained density equations of state from *in-situ* images of individual 1DBGs. We extracted their temperature and global chemical potential from global Yang–Yang thermodynamics fits in the local density approximation. By loading a degenerate 3D gas into 1D, and holding it in time, we observed a simultaneously decreasing temperature and number, suggesting evaporative cooling along the longitudinal direction. While future experiments need cooling to mitigate the spontaneous emission heating from Raman coupled dispersion relations in spin-orbit coupling (SOC), we observed that the 1DBG escapes degeneracy. We conclude that while our 1DBG loses atoms along the longitudinal direction, its temperature goes down slower than the dropping degenerate temperature, and therefore alternative cooling schemes need to be introduced for future experiments with SOC 1DBGs. Our 1DBG implementation remains appealing for experiments with 1D spinor gases beyond the mean-field regime.

Chapter 7:   Holography of cold and ultracold gases

This chapter implements off-axis holographic microscopy to digitally enhance imaging of cold and ultracold ^{87}Rb. We first study it on a test bench and establish the minimum requirements for both the off-axis reference beam, and the reconstruction algorithm. We then holographically image cold atoms in a MOT, reproducing the simultaneous absorptive and dispersive imaging demonstrated early in laser cooled metastable Xenon [87] using the unscattered probe as the local oscillator (i.e. spatial homodyne detection), and in laser cooled ^{87}Rb [88] using an external local oscillator (i.e. spatial heterodyne detection). Reference [89] is an excellent compilation on holographic imaging methods for cold atoms. In this dissertation we first extract the full optical transfer function encoded in the density-density correlations acting as the impulse of the linear, time-invariant microscope as we lack an appropriate *in-situ* point source. Then, we compensate higher order aberrations to enhance our absorption images through a Wiener deconvolution algorithm. This is to our knowledge, the first instance of such a digital aberration compensation for high-order aberrations in images of cold atoms.

This Chapter is organized as follows. In Section 7.1, we introduce holography

in the specific context where an off-axis reference beam acts as a local oscillator allowing the imaging of the determination of both the amplitude, and phase of the optical fields after digital reconstruction. We first experiment with test samples to establish the methods for a cold atom implementation. In Section 7.2, we use digital holographic microscopy to image MOTs. There, we demonstrate the simultaenous absorption and phase contrast imaging of cold atomic samples. In Section 7.3, we apply knowledge of the reconstructed optical fields to detect and compensate the effect of optical aberrations in our *in-situ* absorption images.

7.1 Holography

Holography finds its etymological root in "holos" or whole, and "graphos" meaning record. For a complex optical field, a "whole record" of information is the jointly measured amplitude and phase. Any measurement where the amplitude and phase enter as simultaneous observables may be considered a form of holography. Nevertheless, in optical microscopy we almost exclusively detect the intensity of a field. When the polarization of an optical field is homogeneous (scalar), and its spectrum monomodal (monochromatic), we may implement holography interferometrically to encode the phase as an amplitude modulation. Holography recovers the amplitude and phase of electromagnetics fields through an interferogram [90], extending beyond the visible region of the spectrum, from network communications microwave band [91], to X-ray imaging of biological samples [92]. We demonstrate the power of this imaging technique in the absorption images of ultracold ^{87}Rb,

163

where we detect and correct the effects of optical aberrations.

7.1.1   Field reconstruction

We form holograms by recording the interference pattern of a reference field R (local oscillator) with the object field E at the same temporal frequency (Figure 7.1). The local oscillator is off-axis when it reaches the image plane of the imaging system, giving an intensity

$$I_H = |E + R|^2 = I_E + I_R + 2\sqrt{I_E I_R}\Re[e^{i(\phi_E - \phi_R)}]$$

encoding the individual field intensities and relative phase profile. All phases and amplitudes are functions of the transverse spatial coordinates and may be represented as vectors in the pixel basis (e.g. $E = E_i$ and i is the pixel index, e.g. see Section 4.3.1 in Chapter 3). Then, a field reconstruction algorithm gives the field

$$E^* = \frac{1}{I_R}\mathcal{F}^{-1}\tilde{\mathcal{H}}\mathcal{F}R^* I_H \tag{7.1}$$

as a linearly transformed intensity. Here, $*$ denotes complex conjugation, $\mathcal{F}$ is the two-dimensional Fourier transform operator, $\mathcal{F}^{-1}$ its inverse, and $\tilde{\mathcal{H}}$ is a mask in conjugate (k) space acting as a lowpass filter.

We experimentally investigate recording and reconstructing fields from holograms. We use a $1\,\mu$m pinhole, $780\,$nm illumination, and a two-lens microscope
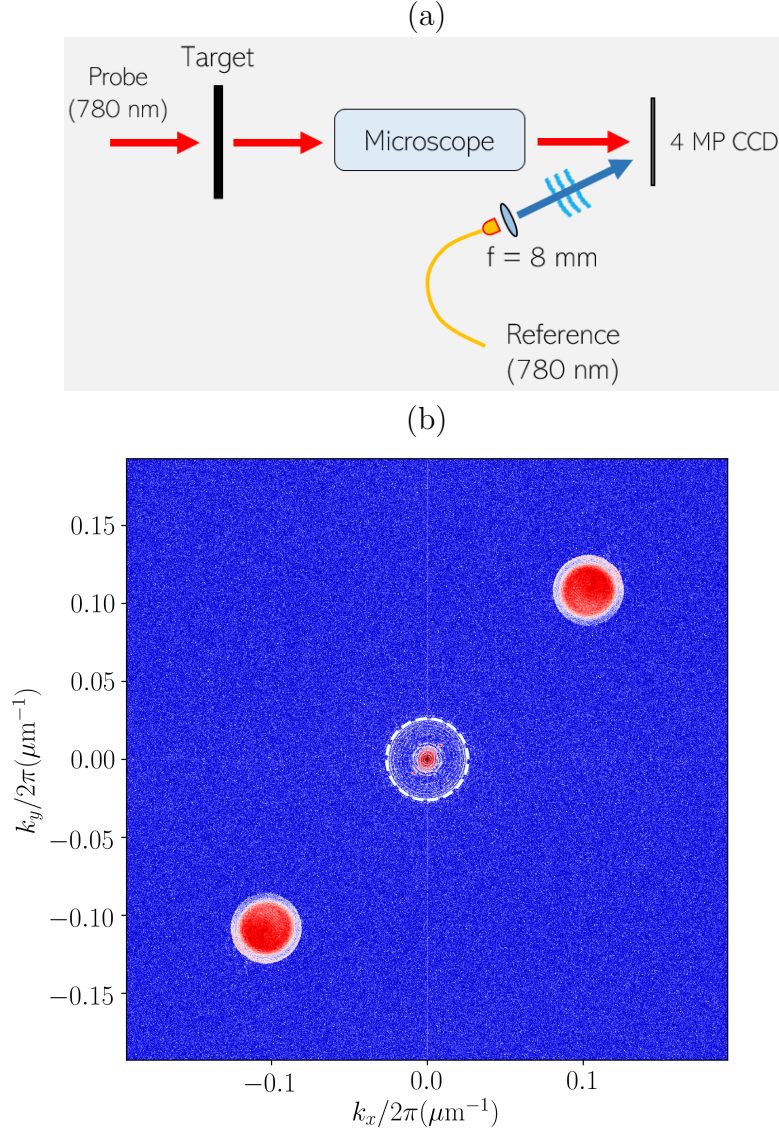
Figure 7.1: Hologram of pinhole and flat wavefront. (a) Schematic of the off-axis holographic microscope. (b) The magnitude of the power spectral density of the hologram shows a central spectrum cutting off sharply at k_{NA} (dashed white contour), and two twin images containing slightly magnified copies of the spectrum away from $k = 0$.

with $\mathrm{NA} = 0.12$. The reference is a phase coherent, collimated beam incident at $31\,°$ from the optical axis. The single collimated reference beam at the image plane approximates a plane reference wave. We begin by computing the power spectral

density of a hologram

$$\mathrm{PSD}_H = |\mathcal{F}(I_H)|^2. \tag{7.2}$$

The magnitude of the power spectral density of such a hologram shows two "side-bands" in the spatial frequency domain (k-space), known as twin images, and a "DC" spectrum around $|k| = 0$ as illustrated in Figure 7.1. While the center and orientation of the sidebands, or "twin images", depends on the angle of incidence and relative orientation of R with respect to E, their spectrum depends on the reference beam wavefront projection on the detector. The ultimate k-space cutoff is given by the numerical aperture of the microscope, so the optimal location and angle of incidence of R center the twin images spectra in the band $k_{\mathrm{pix}} > k > k_{\mathrm{NA}}$. The reason is that for a sensor with pixel size Δ_p and diffraction limited spatial resolution $\Delta_\perp$, the optimal placement in this band implies no loss of information either in the image space aperture where $k_{\mathrm{pix}} = \pi/\Delta_p$, or the object space aperture where $k_{\mathrm{NA}} = \pi/\Delta_\perp$. To increase the k-spectral dynamic range without sacrificing the spatial resolution of the object field, we would like to use large area sensors with small pixel size. Finally, since the reconstruction algorithm places no constraints in the model for R, the exact shape of the wavefront for R is irrelevant as long as there exists a good model for it.

We do a second experiment in the test bench using a single uncollimated reference beam at the image plane to approximate a spherical reference beam. We find that when R is far from flat (i.e. curved wavefront), for example in the
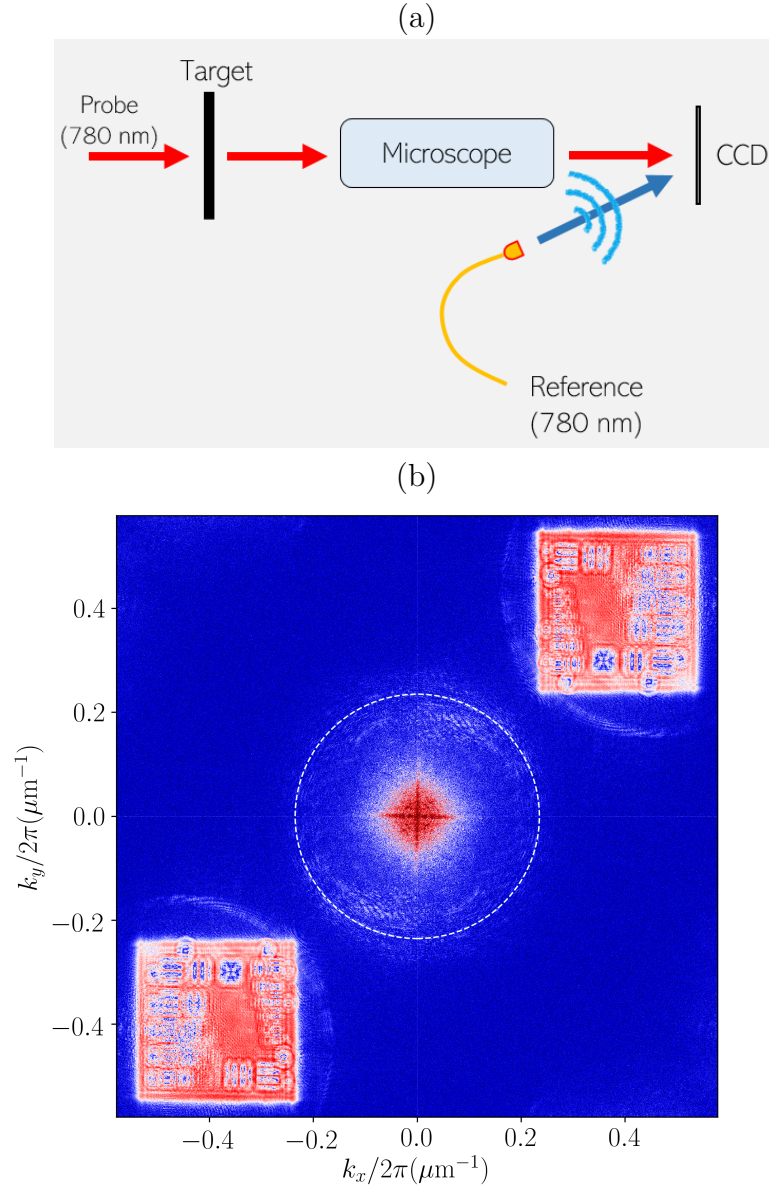
166

Figure 7.2: Hologram of USAF test target and curved wavefront. (a) Schematic of the off-axis holographic microscope. (b) The magnitude of the power spectral density of the hologram showing the DC spectrum cutting off sharply at k_{NA} (dashed white contour), and two twin images containing slightly magnified copies of the spectrum away from $k = 0$. The residual curvature of the curved reference wavefront acts as an additional "lens", undoing the Fourier transform and revealing the real space structure of the object in k-space.

`USAF-1951` test target hologram in Figure 7.2, an effective virtual lens further

Fourier transforms the power spectra of the twin images. This gives rise to an

167

image in k-space that corresponds to the real-space image. Because of this we might in principle flatten a reference beam's wavefront by changing its curvature in such a way as to make the twin image power spectrum congruent with the DC power spectrum.

After applying the linear reconstruction from Equation 7.1 onto the hologram in Figure 7.1 we determine the amplitude and phase of the optical field. These optical fields may be numerically manipulated with the transformations first introduced in Chapter 4, Section 4.1.1. For example, in Figure 7.3 we reconstruct the field of the point source hologram in Figure 7.1. The model reference wave uses a radius of curvature in addition to the angle of incidence, which we measure with respect to the optical axis to use as a first guess for our model. We optimize our models by varying the parameters (i.e. angles, and radii of curvature) in an attempt to flatten the relative wavefront of the hologram.

We then return to the first hologram (pinhole and plane-like reference wave), and apply the reconstruction operator in Equation 7.1. We focus on a circular region of interest where the interference pattern has good signal-to-noise ratio (SNR). Figure 7.3 shows the amplitude and phase of the reconstructed pinhole field. Using the region of interest does not affect the reconstruction (it is equivalent to an additional mask on I_H), and in this example helps to unwrap the phase in Figure 7.3. Reconstructed fields may then be manipulated around the image plane using

Equations 4.5, and 4.8, allowing us to remove the presence of spherical aberrations present in the pinhole images.
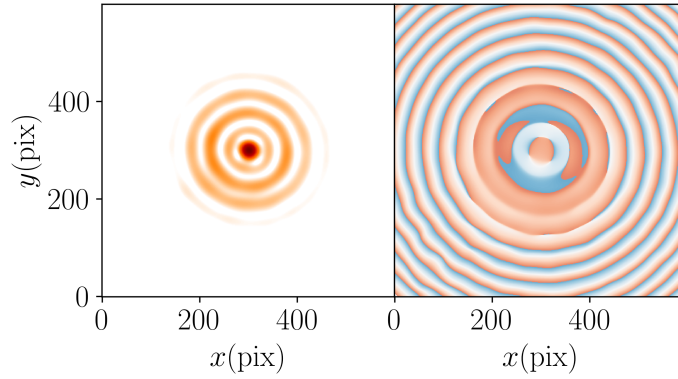
(a)
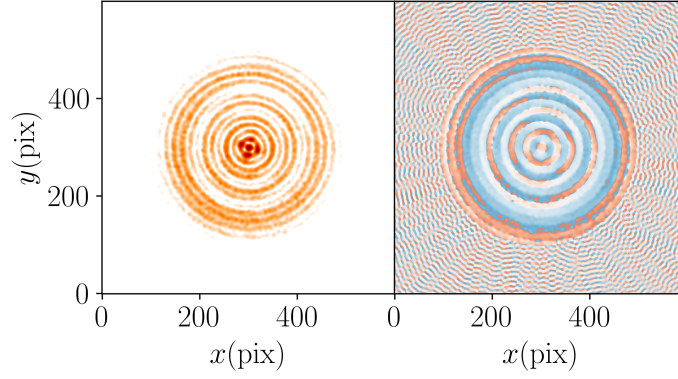
(b)

Figure 7.3: Reconstructed pinhole field. (a) Amplitude and phase of the reconstructed optical field scattered by a $1\,\mu$m pinhole. The reconstructed amplitude gives the intensity, and the unwrapped phase are consistent with the point spread function of a spherically aberrated microscope. (b) Amplitude and phase of the reconstructed optical field scattered by the same pinhole with a fourth order phase correction representing $\sim 4\lambda$ spherical aberration compensation.

Having developed the minimum set of holographic microscopy tools we upgrade our cold atom imaging to extract phase information. The addition of a single reference beam that can coherently interfere with the scattered optical fields of interest is the only requirement in existing experimental setups. In the following Section, we upgrade the MOT imaging to perform digital holography and implement our own simultaneous absorption and phase contrast imaging of cold atoms. Then, in the final Section, we implement high-order digital aberration compensation to enhance the quality of our absorption imaging.

7.2   Simultaneous absorption and phase contrast microscopy

We make holograms of the scattered probe fields in the presence and absence of atomic ensembles and distill information about the atomic clouds from a differential signal just as in resonant absorption imaging. Here, information is encoded in the scattered field ratio

$$\eta(x,y) = E_a(x,y)/E_p(x,y), \tag{7.3}$$

between the two reconstructed atoms field E_a and probe field E_p, and which all depend on the transverse spatial coordinates (x,y). The holographically reconstructed scattered field ratio maps the complex electric susceptibility of the imaging transition (e.g. from Section 4.1.3 in Chapter 4) after a near-resonant

interaction with the atomic ensemble. There, the scattered optical field incorporates the absorption and phase-shift in its magnitude and phase respectively. In the paraxial approximation the transmitted field in the presence of atoms $E_a(x, y) = e^{(\alpha(\delta, s_0) + i\beta(\delta, s_0))n_{\text{col}}(x,y)} E_p(x, y)$ is proportional to the transmitted field in the presence of atoms after traversing an object with a transverse column density distribution $n_{\text{col}}(x, y)$ where strong diffraction and other nonlinear effects can be neglected. Then, the scattered field ratio

$$\eta(\delta, s_0, x, y) = \exp\left[z(\delta, s_0)n_{\text{col}}(x, y)\right], \tag{7.4}$$

can be linearized in the limit of a dilute, and thin object, where light does not get deflected when traversing the atomic medium

$$\eta(\delta, s_0, x, y) \approx 1 + z(\delta, s_0)n_{\text{col}}(x, y), \tag{7.5}$$

effectively separating the effects of resonant absorption and dispersion in the real and imaginary parts respectively, and where $\alpha(\delta, s_0)$, and $\beta(\delta, s_0)$ depend on the detuning from resonance δ, and saturation parameter s_0, and $n_{\text{col}}(x, y)$ encodes the density distribution of the scatterers.

We demonstrate the spatial heterodyne imaging first implemented in [88], by simultaneously measuring the absorption, and phase shift from a holographically imaged MOT. The MOT has a peak optical depth of ~ 2, and fills a large por-

tion of the sensor aperture. We scan the probe frequency across resonance, and in Figure 7.4 show the two-level response from the holographically reconstructed field ratios. After computing the field ratios, the integrated squared magnitude $\propto I_a/I_p$ gives the imaginary part of the susceptibility, while the integrated angle $\propto \phi_a - \phi_p$ gives the real part proportional to absorbed fraction, and integrated phase shift respectively. This imaging method is advantageous in comparison with either resonant absorption or phase contrast imaging, since each reconstructed field ratio gives both the real and imaginary parts of the susceptibility. The hardware implementation of the dispersive digital holographic microscope is far simpler than a conventional Zernike phase contrast microscope, since it does not require a custom, microfabricated phase mask (see for example Reference [93]).

Holographic reconstruction together with digital propagation (e.g. through Equation 4.5) gives access to the "volumetric" optical field around the image plane, and it is tempting to propagate the reconstructed fields back to the object plane. Then, it would seem that by propagating these fields back to different points along the thickness of a cloud of atoms and measuring its transverse profile at each point, we may infer its three-dimensional density distribution with a "voxel" (three dimensional generalization of a pixel) limited resolution given by the transverse spatial resolution times the depth of field. As it turns out, this 3D imaging is unfeasible with just a single probe because the plane-to-plane scattered fields integrate the dielectric response along the propagation axis in a space-ordered fashion

giving the longitudinal field

$$E(z) = \mathcal{S}\left[\exp\left(-i\int_{z_0}^{z}(K_\perp + V(z'))dz'\right)\right], \qquad (7.6)$$

with the space-ordered product denoted by $\mathcal{S}[\cdot]$. Here, the scalar diffraction is split into a longitudinal, potential-like, refraction $V(z')$ term, and a transverse, kinetic-like, dispersion $K_\perp$ term, both of which are proportional to the atomic density. This implies that the missing information about the space ordering along z is required for a full 3D reconstruction. This intuition is consistent with the widely applied medical tomographic imaging techniques, where 3D imaging of extended objects employ multiple 2D projections of 3D objects in combination with algorithmic inversion of the signals. Then, in order to perform an equivalent 3D holographic imaging of cold and ultracold atomic clouds we would need multiple probes incident along different directions in addition to digital reconstruction algorithms to provide enough information for a 3D deconvolution.
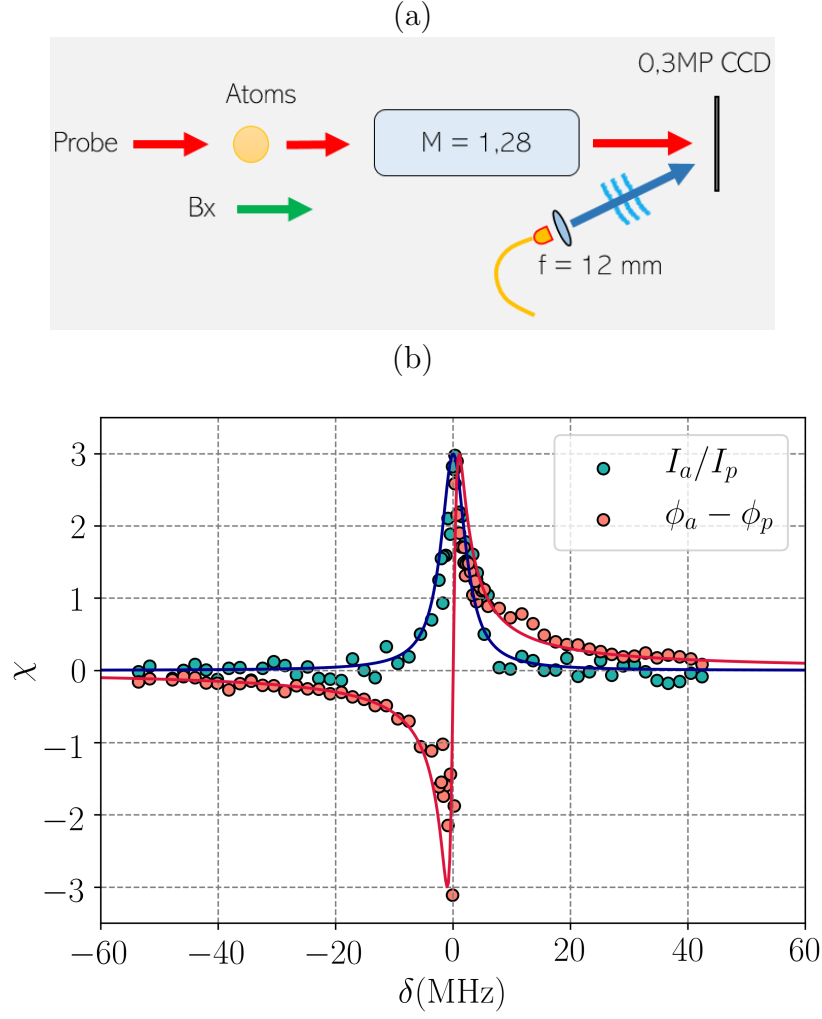
Figure 7.4: Simultaneous absorption and phase contrast microscopy. (a) Schematic of the upgraded MOT microscope using a plane reference wave. (b) Scan of the probe frequency detuning revealing the atomic susceptibility from the integrated holographically reconstructed field ratios. The fits (solid lines) have the natural linewidth as the single free parameter, giving $\Gamma/2\pi = 5.97(6)\,\mathrm{MHz}$.

7.3 Aberration compensation

All the optical fields propagating from the object plane, through the microscope, and to the image plane become aberrated. This is due to slight imperfections in the optical transfer function of the microscope. Our microscopes act as linear,

time-invariant systems whose response to an impulse, for example, in the real space representation (e.g. imaging a point scatterer) reveals the transfer function in that domain. There, the signal $\mathcal{S}$

$$\mathcal{S} = \mathcal{O} \star \mathcal{T} + \mathcal{N} \tag{7.7}$$

is the convolution of a linear, time-invariant transfer function $\mathcal{T}$, and the object $\mathcal{O}$ function representing the object plane scattering function. The measurement noise $\mathcal{N}$ represents the degradation of information by the act of measurement. While the noise is fundamentally impossible to avoid, a deconvolution operation may remove the effects of an imperfect transfer function.

The image formed by the optical fields scattered by a point object is the point spread function (PSF), and the optical theory of aberrations provides quantitative PSF models that capture the effects of different aberrations. For instance, the Zernike theory of aberrations relates the different symmetry-breaking terms around the optical axis of a microscope with circular apertures [94]. Recently, free-form optics provides a new paradigm which could be used to find a more general class of transformations [95]. Unfortunately, most cold and ultracold gas experiments lack the technical capabilities to characterize *in-situ* PSFs because extended clouds of atoms lack sharp spatial features to act as impulse sources. Here, because we effectively lack the appropriate $g^{(1)}(\vec{r}) \propto \delta(\vec{r})$ impulse source, we

develop a method to characterize the aberrations of our microscope using higher-order impulse correlation functions beyond the $g^{(1)}(\vec{r}) \propto \langle n(\vec{r}) \rangle$ average impulse. Specifically, we exploit the dominant atomic shot noise present in thin, elongated superfluids to act as a second order impulse correlation $g^{(2)}(\vec{r}_1, \vec{r}_2) \propto \delta(\vec{r}_1 - \vec{r}_2)$. We then combine digital holography with a calibration of our optical aberrations to digitally invert the optical transfer function and correct our absorption images.

We implement off-axis, digital holographic imaging for our ultracold elongated clouds, where the trapping frequencies after dipole evaporation are $\omega_\perp/2\pi = 190\,\mathrm{Hz}$ in the transverse direction and $\omega_\parallel/2\pi = 10\,\mathrm{Hz}$ in the longitudinal direction. We deploy a pair of consecutive two-lens imaging systems amounting to a total magnification of $M = 31.7(4)$. The last image plane concides with a charge-coupled device (CCD) sensor with pixel size $\Delta_p = 13\,\mu\mathrm{m}$). The diffraction-limited, transverse spatial resolution of the primary objective lens is $\Delta_\perp = 1.23\,\mu\mathrm{m}$ at the object, spanning an equivalent 3 pixels in the image plane. Both the field of view (FOV) and the depth of field (DOF) are estimated to be $\Delta_f = 40(2)\,\mu\mathrm{m}$, and $\zeta = 5.0(5)\,\mu\mathrm{m}$, respectively. We take images of our elongated superfluids from a single plane, with effective thickness $\delta z < \zeta$. Since our initial condensates have an *in-situ* thickness of $r \sim 16\,\mu\mathrm{m}$, we achieve thin slices by pulsing a resonant microwave pulse for $\tau = 15\mu\mathrm{s}$ from $|F = 1\rangle$ to $|F = 2\rangle$ while applying a strong quadrupole field gradient of $\delta_z B_z \sim 100\,\mathrm{G/cm}$. Then, we shine a resonant probe and reference beam resonant with the $|F = 2\rangle \rightarrow |F' = 3\rangle$ transition in the D_2 line

176

for 20μs to produce the desired non-holographic and holographic intensity records. Our combined gradient strength and microwave coupling strength give a bound for the thickness of the thinly sliced clouds of $\delta z \approx 1\,\mu$m, well below the DOF.

Off-axis holographic microscopy extends the regular absorption imaging acquisition series from a minimum of three to up to five images, where the image with atoms A is a hologram of the scattered probe intensity, and the image without atoms U is a hologram of the unscattered probe intensity. Then, we may still individually record the unscattered probe intensity P, the reference beam intensity R, and the dark field intensity D. As usual, we subtract D from all images to remove the noise baseline from background illumination prior to further processing.

7.3.1 Impulse density-density correlations

We gain access to the optical transfer function through calibrated scattered field correlation functions. To calibrate the aberrations present in our imaging system, we probe an effectively uncorrelated atomic ensemble. Once prepared, our thinly-sliced elongated BECs are incapable of developing long-range correlations (e.g. through interactions), because they are in the weakly interacting mean-field regime where interaction timescales are in excess of $10\,$ms. We attribute all long-range correlations present after short imaging exposures to our imaging system.

The effective absence of long-range correlations happens for example in a
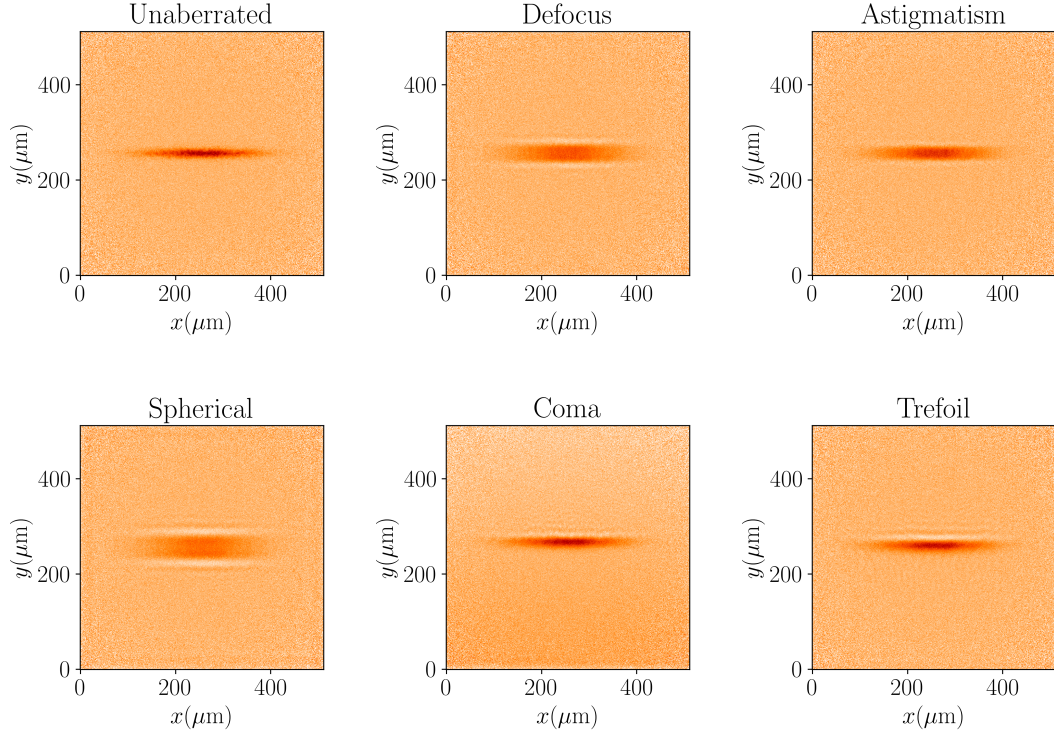
Figure 7.5: Aberrated absorption images. We simulate the qualitative effects from different aberrations in the optical depth. Similar features appear even for different types of aberrations, making it hard to differentiate defocusing from spherical aberrations, or vertical coma from oblique trefoil. For this simulation we consider a thin, elongated cloud ($150\,\mu$m) giving a peak optical depth ~ 0.5 in resonant absorption imaging. We add atomic shot noise by modulating the local density with randomly drawn Poisson distributed noise, and use a Gaussian $w_0 = 250\,\mu$m probe with peak intensity $I_p/I_{sat} = 5$. To simulate a realistic detector, we simulate photon shot noise limited measurements.

dilute, non-degenerate Bose gas, where the dominant correlation length is the unresolvable thermal de–Broglie wavelength $\lambda_{\mathrm{dB}} \ll \Delta x$. Another example is in a deeply degenerate, dilute Bose-gas where the long-range correlations develop from the superfluid healing length $l_\mu \ll \Delta x$. In both instances, atom shot noise

dominates the two-point density correlations

$$\langle n(\vec{r}; z) \, n(\vec{r}'; z') \rangle = n(\vec{r}, z) \, \delta(\vec{r} - \vec{r}')\delta(z - z'), \tag{7.8}$$

where from here on I adopt the notation $\vec{r} = (x, y)$ to denote transverse spatial coordinates, and $\vec{k} = (k_x, k_y)$ to denote transverse k-space coordinates. The Fourier transform of this density-density correlation function is

$$\langle n(\vec{k}; z) \, n(\vec{k}'; z') \rangle = \frac{n(\vec{k}, z)}{2\pi} \, \delta(\vec{k} - \vec{k}')\delta(z - z'), \tag{7.9}$$

where the density distribution in front of ensures vanishing correlations in the absence of atoms. The symbol $\langle ... \rangle$ indicates an expectation value, which we approximate by taking an ensemble average over a finite set of experimental realizations.

The complex susceptibility is proportional to the density n and maps any density-density correlations in the gas, which we assume to be of the form in Equation 7.3.1. Rather than looking at $\eta(\vec{k})$, the scattered field ratio, we study the scattered fraction

$$\begin{aligned}
\xi(\vec{r}) &= 1 - \eta(\vec{r}) \\
&= \delta E_p(\vec{r})/E_p(\vec{r}) \\
&\approx z(\delta, s_0)n(\vec{r}),
\end{aligned}$$

representing the relative fluctuations in the constant incident field. We are ultimately interested in the effect of an imaging transfer function $\mathcal{T}$ acting on the scattered fraction, therefore transforming the scattered fraction

$$\xi'(\vec{r}) = \mathcal{T}(\vec{r})\xi(\vec{r}). \tag{7.10}$$

Turning to the k-space representation, the scattered fraction obeys the paraxial approximation and has the exact diffraction integral solution [96]

$$\xi'(\vec{k}) = \mathcal{T}(\vec{k}) \left[\frac{ik_0}{2} \int_0^{\Delta z} e^{\frac{i|\vec{k}|^2 z}{2k_0}} \chi(\vec{k}, z) \, dz \right] \tag{7.11}$$

as the field propagates by Δz through a medium with susceptibility $\chi(\vec{k}, z) \propto n(\vec{k}, z)$. Since $\xi(\vec{k})$ is complex-valued, four different possible correlation functions

$$\mathcal{C}_{\pm}(\vec{k}, \vec{k}') = \langle \xi(\vec{k}) \, \xi(\pm\vec{k}') \rangle, \tag{7.12}$$

and

$$\mathcal{K}_{\pm}(\vec{k}, \vec{k}') = \langle \xi(\vec{k}) \, \xi^*(\pm\vec{k}') \rangle, \tag{7.13}$$

exist in the k-space representation, containing various projections of the same information. We note that the condition $f(\vec{k}) = f(-\vec{k})$ valid for a real-valued signal $f(\vec{k})$ (such as the intensity), no longer needs to hold for these complex-valued field correlations.

We now turn to evaluating these correlations. For this, we take a set of N realizations of ξ', labeled by index m

$$\{\xi'^{(m)}(k_i)\} = \{\mathcal{T}_{ij}\,\xi^{(m)}(k_j)\},\tag{7.14}$$

such that $\xi^{(m)}(\vec{k}) = \xi^{(m)}(k_i)$ represents a single realization of ξ over all of $k_\perp$-space, and $\mathcal{T}_{ij}$ is a matrix common to all realizations scrambling information and correlations around the angular spectrum. Using the $k_\perp$-space representation from above,

$$\begin{aligned}\mathcal{C}'_\pm(\vec{k},\vec{k}') &= \mathcal{T}(\vec{k})\mathcal{T}(\pm\vec{k}')\left(\frac{ik_0}{2}\right)^2 \times \\ &\int_0^{\Delta z}\int_0^{\Delta z} dzdz'e^{\frac{i|\vec{k}|^2z}{2k_0}}e^{\frac{i|\vec{k}'|^2z'}{2k_0}}\langle\chi^{(m)}(\vec{k},z)\chi^{(m)}(\pm\vec{k}',z')\rangle,\end{aligned}\tag{7.15}$$

eqnarraywhere the ensemble average only enters the different realizations of the scatterer distribution. Similarly,

$$\begin{aligned}\mathcal{K}'_\pm(\vec{k},\vec{k}') &= \mathcal{T}(\vec{k})\mathcal{T}^*(\pm\vec{k}')\left(\frac{k_0}{2}\right)^2 \times \\ &\int_0^{\Delta z}\int_0^{\Delta z} dzdz'e^{\frac{i|\vec{k}|^2z}{2k_0}}e^{-\frac{i|\vec{k}'|^2z'}{2k_0}}\langle\chi^{(m)}(\vec{k},z)\chi^{*,(m)}(\pm\vec{k}',z')\rangle,\end{aligned}\tag{7.16}$$

in their full, explicit forms. We use Equation 7.3.1 to reduce the correlators

$$\begin{aligned}\mathcal{C}'_\pm(\vec{k},\vec{k}') &= \mathcal{T}(\vec{k})\mathcal{T}(\pm\vec{k}')\langle\chi_\perp^{(m)}(\vec{k})\chi_\perp^{(m)}(\pm\vec{k}')\rangle \times \\ &\left(\frac{ik_0}{2}\right)^2\int_0^{\Delta z}e^{\frac{iz}{2k_0}(|\vec{k}|^2+|\vec{k}'|^2)}n(z)^2\,dz,\end{aligned}\tag{7.17}$$

and

$$\mathcal{K}'_{\pm}(\vec{k}, \vec{k}') = \mathcal{T}(\vec{k})\mathcal{T}^*(\pm\vec{k}')\langle\chi_{\perp}^{(m)}(\vec{k})\chi_{\perp}^{*,(m)}(\pm\vec{k}')\rangle \times \tag{7.18}$$

$$\left(\frac{k_0}{2}\right)^2 \int_0^{\Delta z} e^{\frac{iz}{2k_0}\left(|\vec{k}|^2 - |\vec{k}'|^2\right)} n(z)^2 \, dz,$$

first carrying out an integral in the longitudinal components, where in both cases the $k_{\perp}$-space density-density correlations move outside of the remaining z-integral, and then further integrating in the transverse component with $\langle\chi(\vec{k})\chi_{\perp}(\vec{k}')\rangle = \chi_0\delta(\vec{k} + \vec{k}')$,

$$c'_{\pm}(\vec{k}) = \int \mathcal{C}'_{\pm}(\vec{k}, \vec{k}')d\vec{k}' \tag{7.19}$$

$$= \mathcal{T}(\vec{k})\mathcal{T}(\mp\vec{k})\left(\frac{ik_0\chi_0}{2}\right)^2 \int_0^{\Delta z} e^{\frac{iz|\vec{k}|^2}{k_0}} n(z)^2 \, dz, \tag{7.20}$$

and $\langle\chi(\vec{k})\chi^*(\vec{k}')\rangle = \chi_0\delta(\vec{k} - \vec{k}')$,

$$\kappa'_{\pm}(\vec{k}) = \int \mathcal{K}'_{\pm}(\vec{k}, \vec{k}')d\vec{k}' \tag{7.21}$$

$$= \mathcal{T}(\vec{k})\mathcal{T}^*(\pm\vec{k})\left(\frac{k_0|\chi_0|}{2}\right)^2 \int_0^{\Delta z} e^{\frac{iz|\vec{k}|^2}{2k_0}} n(z)^2 \, dz. \tag{7.22}$$

As an example for a specific transfer function model we turn to a polar Zernike representation in the unit circle

$$\mathcal{T}(k_r, k_\theta) = \mathcal{A}(k_r, k_\theta)\exp\left(i\sum_{n=0}^{\infty}\sum_{m=0}^{n}\alpha_n^m Z_n^m(k_r, k_\theta)\right), \tag{7.23}$$

in terms of the normalized n-th Zernike polynomials $Z_n^m(k_r, k_\theta)$ of order m, and

the aperture function $\mathcal{A}$. As a toy example, we include only the lowest (second) order polynomial contributing to defocus

$$\mathcal{T}_{df}(k_r, k_\theta) = e^{i\alpha_2^0\sqrt{3}(2k_r^2-1)} \tag{7.24}$$

and find that while the correlators

$$\kappa_\pm^{df}(k_r, k_\theta) = \frac{k_0^2|\chi_0|^2}{4} \int_0^{\Delta z} e^{\frac{iz|\vec{k}|^2}{2k_0}} n(z)^2 \, dz \tag{7.25}$$

have no additional structure from the imaging transfer function, the correlators

$$c_\pm^{df}(k_r, k_\theta) = e^{2i\alpha_2^0\sqrt{3}(2k_r^2-1)}\frac{k_0^2\chi_0^2}{4} \int_0^{\Delta z} e^{\frac{iz|\vec{k}|^2}{2k_0}} n(z)^2 \, dz \tag{7.26}$$

gets periodically modulated with a quadratically growing frequency depending directly on the defocus coefficient α_2^0. This is the result observed in [96], using intensity correlations.

We study the effects of aberrated pupil functions from Equation 7.23 in numerically simulated absorption images and correlation functions. While the density-density correlations from intensity encode the correct imaging transfer function [97], digital inversion would lead to amplification of noise around certain spatial frequencies where the information is missing in the amplitude of the field, but present in the phase. Figure 7.6 shows the numerically simulated density-

density correlation function from intensity images, where there is only real-valued information. and the correlation function $c_-(\vec{k})$ from scattered field signals with phase information. Similarly, Figure 7.7 shows the numerically simulated density-
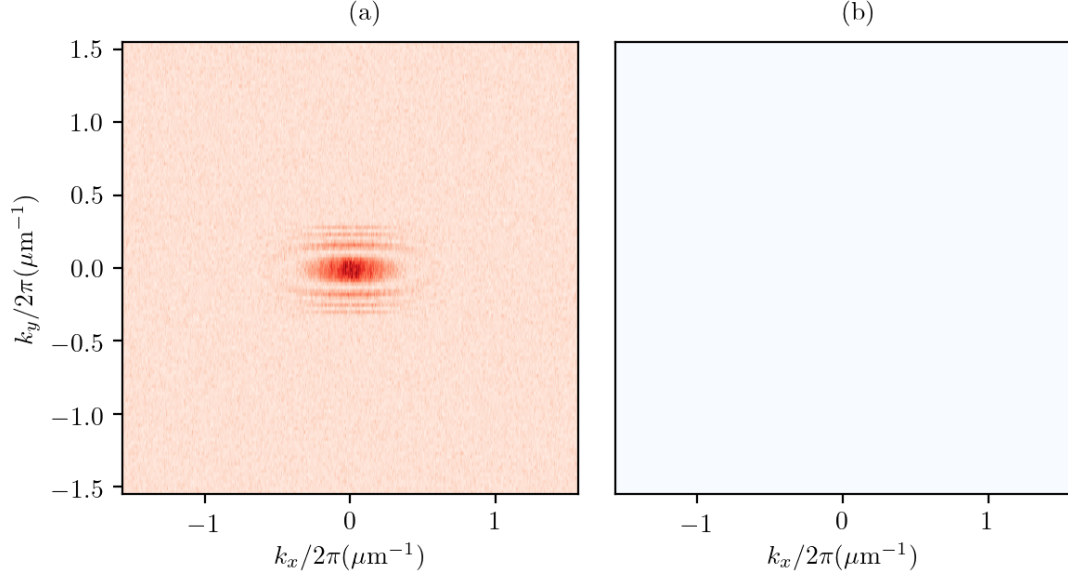
Figure 7.6: Simulated intensity correlations. (a) Real and (b) imaginary parts of the intensity-intensity correlation function encoding the density-density correlation function. We use closely balanced defocus and vertical astigmatism, as well as residual spherical aberrations. In the absence of aberrations, we expect a delta-like function centered around $k = 0$. The intensity correlations lack an imaginary component.

density correlation function from holographically reconstructed field images, where both real and imaginary parts contain long-range structure.

We proceed by measuring the atomic correlations deriving from intensity, and holographically reconstructed fields scattered by the same atomic ensemble. Figure
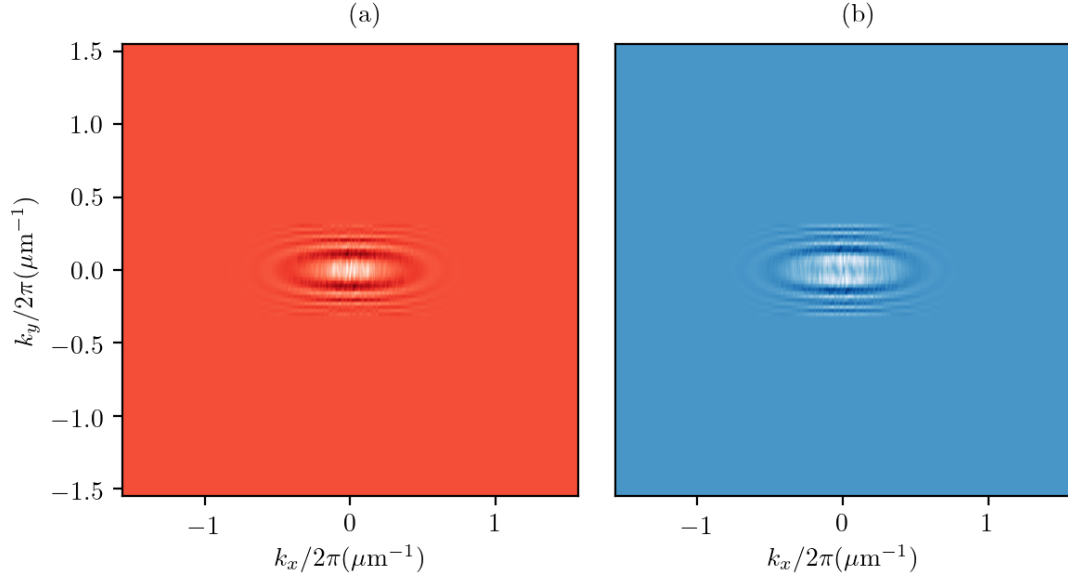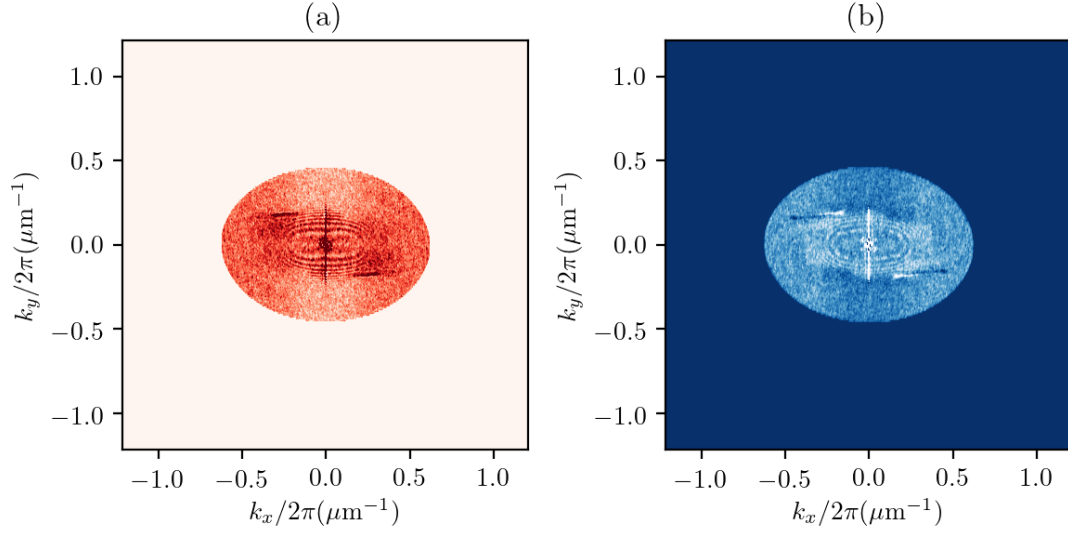
Figure 7.7: Simulated field correlations. (a) Real and (b) imaginary parts of the density-density correlation functions from holographically reconstructed fields. The c_- correlator shows structure in both its real and imaginary parts.

7.8 shows the real-valued density-density correlations from intensity, while Figure 7.9 shows the complex-valued field correlations. There are qualitative differences in these correlation functions. First, the intensity-based correlation functions have better signal-to-noise ratio because the information is maximally projected onto the pixel basis. This is in contrast with the holographic measurements, where the intensity is split into two parts encoding phase and amplitude information. Therefore, the intensity-based correlation functions have an enhancement of up to $\sqrt{2}$ in signal-to-noise ratio for a fixed number of measurements. Second, the field-based correlation function c_- from Figure 7.7 shows a phase shift feature

between the real and imaginary parts. This phase shift can be interpreted from the oscillation of information between phase and amplitude.
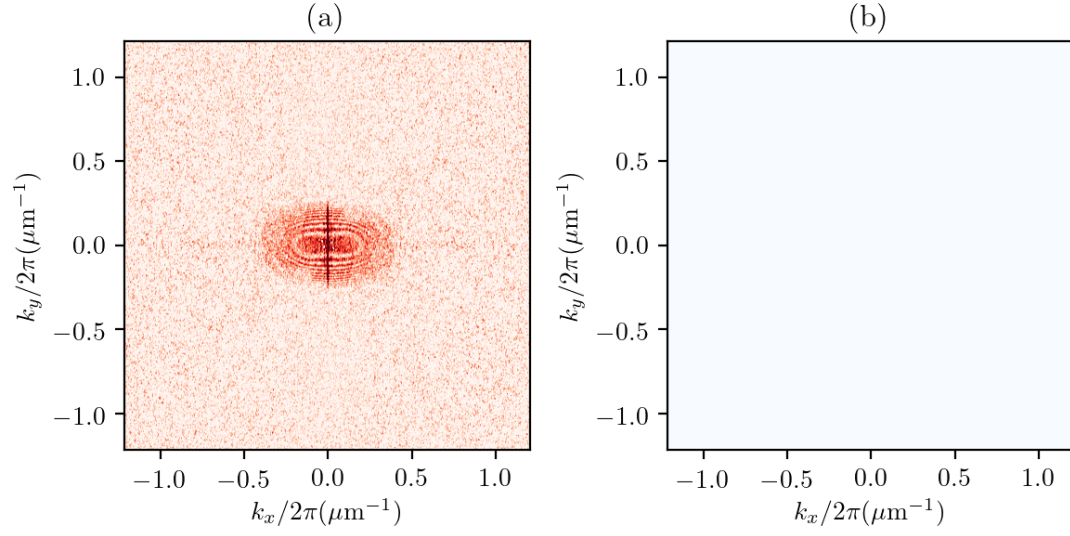
Figure 7.8: Measured intensity correlations. (a) Real and (b) imaginary parts of the density-density correlation functions from intensity images.

Figure 7.9: Measured field correlations. (a) Real and (b) imaginary parts of the density-density correlation function c_- from the holographically reconstructed fields. The additional, hard cutoff disk in the field-field correlation functions represents the holographic reconstruction filter $\tilde{\mathcal{H}}$ from Equation 7.1

.

7.3.2 Inversion of the imaging system

We restore some of the spatial resolution of our images using the transfer function from the scattered field correlations. When we have all the information from the complex field correlation functions, we apply Wiener deconvolution to approximately invert the imaging transfer function [98]. A Wiener filter in k-space has a transfer function

$$\mathcal{W}(\vec{k}) = \frac{\mathcal{T}^*(\vec{k})}{|\mathcal{T}^*(\vec{k})|^2 + \mathcal{N}(\vec{k})},$$

(7.27)

where $|\mathcal{T}|$ is the modulus of the linear transfer function, $\mathcal{T}^*$ its complex conjugate, and $\mathcal{N}$ is the noise power spectrum. The Wiener filter attenuates the amplification of high spatial frequencies during the inversion with a cutoff set by the noise power spectrum. Additionally, it prevents divergences outside the aperture where the Zernike pupil is defined. Figure 7.10 illustrates the computed optical depth from reconstructed intensities, and the corresponding image after applying a Wiener deconvolution.
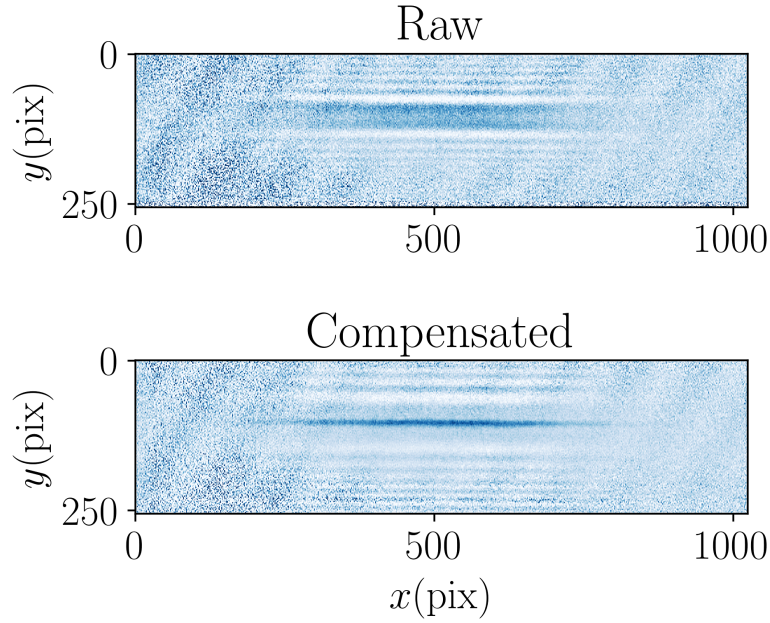
Figure 7.10: Raw and corrected optical depth. Here we use the extracted Zernike coefficients to model the pupil function acting as $\mathcal{T}$. Then, by applying the Wiener filter from Equation 7.27 we partially restore the quality of our absorption images.

7.4   Conclusions

We imported the tools from digital holography into experiments with cold and ultracold atoms. We demonstrated a straightforward implementation of phase-contrast microscopy in cold atoms using the holographically reconstructed phase difference from the scattered field ratio. This microscopy technique has the advantage of simultaneously accessing the amplitude and phase of the optical fields. We then showed the characterization and digital inversion of the optical transfer function using an extended, uncorrelated atomic source. Holographic imaging is promising for cold atom microscopy holding an unprecedented simple implementation, and utility of the methods developed in this Chapter. Once a transfer function is known, holographic imaging and reconstruction giving fields may be combined early in the image processing sequence to remove the effects of aberrations.

Appendix A: Transistor banks

We drive the quadrupole field currents with unipolar `Agilent 6672A` power supplies capable of driving up to 100 A. When passing through the coils, the current dissipates into heat depending on the resistive load, as well as transduces into magnetic fields depending on the inductive load. The magnetic fields are restricted to vary at a rate of a couple of kHz, set by the inductive time constant of the circuit. In order to precisely drive the transport sequence, we put all coil pairs under active current feedback using closed loop Hall effect current probes `CLSM-50LA`. The ability to switch on/off big currents robustly and precisely is critical, as is watching power dissipation requirements.

We drive a total of eleven pairs of quadrupole coils with four different power supplies. Only three pairs of coils may be powered simultaneously at any given time. It is common practice to build power circuits with banks of transistors controling the current via gate voltages. Having several MOSFETs connected in parallel (in a bank) makes it possible to drive larger current loads with distributed power dissipation. RbChip has a total of eight transistor banks comprised of two power MOSFETs (`IXFN520N075T2`) each. We mount the banks into aluminum

plates with water cooling lines (`Lytron CP10` series) and we apply `Dow-Corning 340` silicon compound at the aluminum MOSFET interface to optimize thermal contact and meet the desired power dissipation.

For increased safety, we include `5KP58ALFTR-ND` diodes between the source and the drain to prevent current backflow, even though the MOSFETs have an internal protection diode. We use thick $(1/4 \,\text{in})$ copper bars to improve electrical contact in the power circuit. Below is a circuit diagram for a single bank in RbChip.
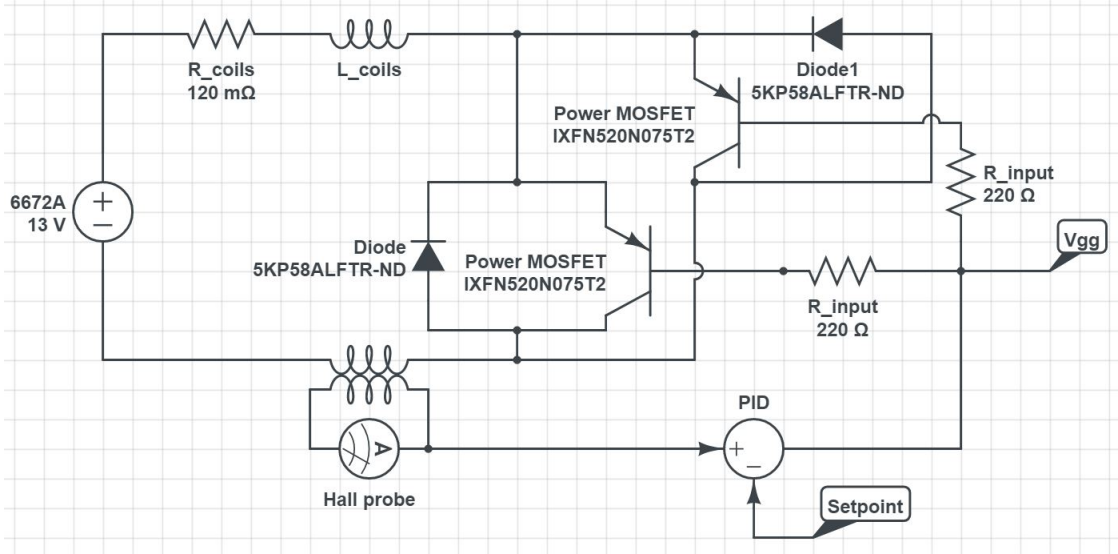
Figure A.1: A voltage power supply, typically set to $V_{aa} = 13\,\text{V}$, drives the two MOSFET transistors bank. The coil pair is represented by the series resistor and inductor, flowing current into the MOSFET drain terminal and back to the power supply through the source. The measured current feeds the error signal along with the current setpoint, which produce the precise gate voltage entering the MOSFET through a $R2 = 220\,\Omega$ resistor matching the gate input resistance.

Even with this design, we often experience excess heating potentially leading

MOSFETs to burn sequentially in a chain reaction (whenever an element malfunctions, the neighbors take on their load and risk failure). This prevents the transport sequence to work so we are faced with the need to upgrade the transistor banks to further optimize power dissipation. We double the density of transistors to have an extra factor of 2 in power dissipation rate. In addition, we upgrade the cooling plates to `Aavid Thermaloy 416501U00000G`, having twice as many water cooling line passes and better contact between the copper tubes and the aluminum.

Based on previous experience, MOSFETs from the same manufactured batch work best together (they seem more likely to have matching internal resistances and in consequence are able to drive closely matching loads). To assemble the banks, we drill a series of holes forming a grid to guide the MOSFETs into their final positions. Below is a picture of the bank plates as they were being populated A.2. Each plate holds exactly thirty two MOSFETs.

We fabricate the contact slabs from $\sim 1/4$ in thick silver-plated copper bars with rounded edges (`McMaster 88865K621`). We cut them to a length of ~ 3 in and drill enough holes to place the round contacts, which consist of tapered $\sim 3/8$ in copper fittings. We then solder these into the slabs using a blowtorch and thick unleaded solder wire. We mount the MOSFETs through the fittings with wide button-head screws, and nuts below. It is crucial that every hole is well aligned to provide gentle, yet robust tightening. Finally, we taped a few K-type thermocou-
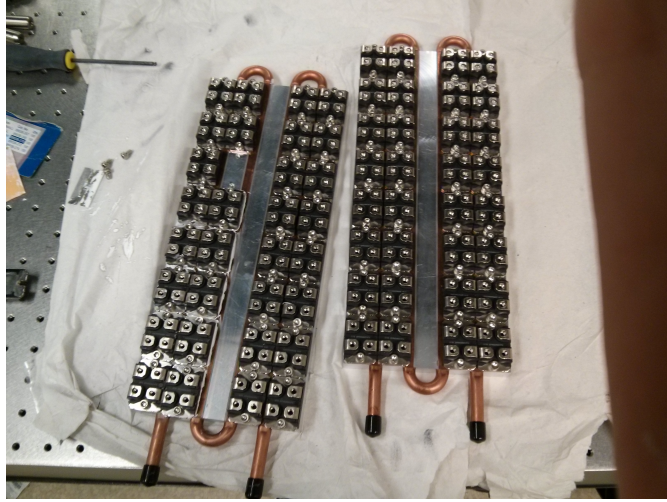
Figure A.2: Transistor bank assembly. Photograph showing the layout in 2 plates with 32 transistors each. An individual bank consists of 4 parallel elements. Contact slabs are not shown.

ples to 4 equidistant locations to monitor the global temperature of the transistor banks and prevent heat blowouts. We connect the thermistor outputs to a monitor, and using an Arduino with a temperature monitor shield, output a logic output to a temperature interlock such that if any one bank exceeds $T = 35\,°\mathrm{C}$, the power supplies are disabled.

Appendix B: New apparatus CAD documentation

B.1   A new apparatus for degenerate bosonic gases

I provide technical documentation for a newly designed quantum gas apparatus; which we call the new, or future apparatus. I try to summarize the new features, the motivation behind them, their implementation, and even some early characterization before the apparatus is even able to yield any scientific output.

B.1.1   New features

The new apparatus, in contrast to the current apparatus in RbChip has a series of novel features. Most of them have their origin on existing failure modes in the current apparatus. Even though these issues are not severe (i.e. they do not impede the normal operation of the experiment or the flow of science), the new apparatus provides an excellent opportunity for improvement and design optimization.

The *ab-initio* motivation for a new apparatus is the impending breaking of ultra-high vacuum (UHV) scheduled in the future of the current Rb–Chip machine. This will likely happen when/if the atom chip is updated/upgraded, a process that

Component	Related issue	Proposed update
Rb source	Temperature stability	New source design
Push coil	Reduced optical access	In plane shim pair
Coil tower	Temperature and field drifts	Monolithic mount
Line of sight	Blocked by the chip and source	New vacuum system
Magnetic field	Long term drifts	New coils layout
Transport	Long sequence and heating	Optimized coil design
Optical access	NA $\leq$ 0.4	NA $\leq$ 0.6

Table B.1: Existing issues and novel features in the old vs new apparatus.

will probably take months. The peripheral components (e.g. power supplies and lasers) may still be used in that case, so a plan is to have an independent UHV manifold along with a new coil assembly, breadboards and optics that can be rolled in on their own optical table as the Rb–Chip apparatus is rolled out for downtime. The new apparatus should be able to produce BECs sooner than an upgrade to our current apparatus is complete. This requires a stable, robust and optimized design, for which some improvements are incorporated.

The *ad-hoc* motivation for the new apparatus is the renovation of the RbLi mixtures lab located at the JQI. The Rb–chip apparatus is by far the most stable of the three experiments in the group, while the RbLi apparatus is usually on the other end. Since the RbLi apparatus will be rebuilt as a (bosonic) RbK experiment, duplicating the construction of a better, more stable new apparatus is a good idea.

Table B.1 briefly describes all the existing issues in the Rb–Chip machine and their proposed upgrades.

B.1.2   Coil tower

The transport coil pairs in the RbChip apparatus are mounted individually with interleaved aluminum frames forming a transport tower. Chilled water runs through a double straight line on each side of the transport towers. This possibly creates transient thermal gradients when the coils are active. Thermal gradients may give rise to thermal expansion and small background magnetization, which has the potential to affect the atoms. The new apparatus uses monolithic (single piece) transport coil holders. Additionally, we add optimized power dissipation elements in the cooling lines and coil mounting.

B.1.3   Line of sight

The RbChip apparatus (see Figure 1.1) is vertically oriented so that the chip hangs down from the top flange, aligned with the transport axis. The atomic source and TEC (described above, and in Chapter 1) are located on the opposite end, and no direct line of sight along the transport axis exists. Furthermore, BECs have a direct line of sight to the atomic source, which may reduce their lifetime. In the new apparatus, single ended glass cells on the MOT and science regions provide a direct line of sight for imaging the atoms before, during and after transport. Additionally, the atomic source is placed away from the line of transport.

B.1.4 Magnetic field control

Three bias coil pairs exist along each of the three main orthogonal directions $\mathbf{e}_x$, $\mathbf{e}_y$, $\mathbf{e}_z$ in the lab frame (see Figure 1.1). Two sets are mounted around the science cell region and the MOT cell region. An additional shim (offset) bias coil pair as well as the final quadrupole coil pair are oriented along $\mathbf{e}_z$ at the science cell region. Finally, an array of gradient cancellation coils in cloverleaf configuration are placed along $\mathbf{e}_x$, providing fixed gradient control in all three directions. In this configuration a lot of optical access is compromised by the coils and their supporting structures. For the new apparatus, we incorporate coplanar bias, transport and gradient cancellation coils, into a single pair of parallel planes along $\mathbf{e}_z$, freeing a significant portion of the available optical access.

B.1.5 Transport

The coils in the current apparatus dissipates up to $\sim 1\,\mathrm{kW}$ of total power at any given point during the sequence. As temperatures rise, the risk of melting insulating layers limits the experimental cycle time. Furthermore, the water cooling manifold dissipation rate is limited to prevent water condensation and electrical shock. The new apparatus improves heat dissipation and sequence timing by placing the coil pairs closer together such that they yield the same quadrupole field strength at a reduced current.

B.1.6 Optical access

The largest permitted numerical aperture (NA) along any direction in the current apparatus is $NA = 0.4$. Imaging with a wavelength of $\lambda = 780\,\text{nm}$ yields a diffraction-limited resolution of $\Delta_\perp = 1.18\,\mu\text{m}$. Repulsive (attractive) potentials may only present spatial features of order $\Delta_{532\text{nm}} = 0.81\,\mu\text{m}$ ($\Delta_{1064\text{nm}} = 1.62\,\mu\text{m}$). Together with the newly found optical access, the new apparatus will upgrade into a high NA compound objective lens to maximize light collection along the vertical direction. An example of the projected resonant imaging, repulsive and attractive potential resolutions are $\Delta_\perp = 0.68\,\mu\text{m}$, $\Delta_{532\text{nm}} = 0.46\,\mu\text{m}$ and $\Delta_{1064\text{nm}} = 0.93\,\mu\text{m}$ respectively.

B.2 CAD documentation

B.2.1 Coils

We produce homogeneous and linear gradient magnetic fields with homemade pairs of coils (electromagnets). To determine the number of control parameters needed to attain full control of the magnetic landscape to first order, we write the gradient of the magnetic field vector $\vec{B}$ in matrix representation

$$\nabla \vec{B} = B_{ij} = \begin{pmatrix} B_{xx} & B_{xy} & B_{xz} \\ B_{yx} & B_{yy} & B_{yz} \\ B_{zx} & B_{zy} & B_{zz} \end{pmatrix}, \tag{B.1}$$

with a total of nine components denoted B_{ij}. The field, denoted B_i, has three additional independent components which, along with the gradient components, add up to twelve components. This implies a total of twelve parameters. A reduction takes place by invoking Maxwell's equations. Off-diagonal elements of B_{ij} relate to each other through Ámpere's law $\mu_0 J_i = \epsilon_{ijk} B_{jk}$, where J_i is the current field and ϵ_{ijk} is the Levi–Civita symbol. Finally, the field must have zero divergence implying $\delta_{ij} B_{ij} = 0$, where δ_{ij} is a Kronecker delta and we follow Einstein's summation convention. These four equations eliminate four of the twelve independent parameters, hence full control over the field and its gradients lies within eight controllable degrees of freedom.
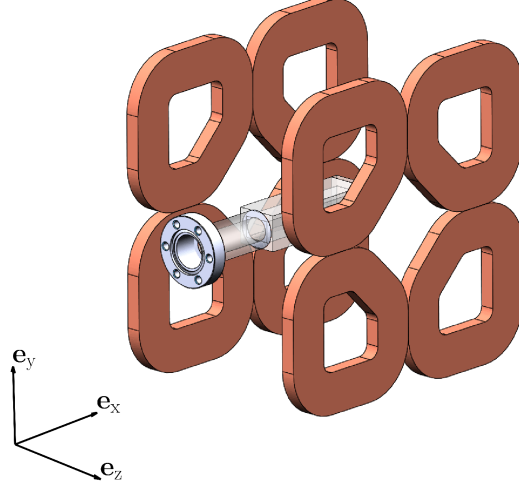
Figure B.1: Coplanar layout of bias coils surrounding science cell. The axes of the bias coil pairs are oriented along $\mathbf{e}_z$ while the mini CFF of the glass cell is aligned to $\mathbf{e}_x$.

All pairs of coils are confined to parallel planes perpendicular to $\mathbf{e}_z$, as shown

in Figure B.1. Coplanar coil pairs can be connected in series along $\mathbf{e}_{x-y}$ or $\mathbf{e}_{x+y}$ and then run together with their matching opposing pair along $\mathbf{e}_z$ to generate different bias fields B_i. Each of the coils in Figure B.1 is based on an optimized design by Chris Billington. The design computes values of B_i at the center of the glass cell (i.e. where the atoms will be) and generates electric and geometric constraints. Figure B.2 and Table B.2 present the optimized form and design constraints for a single bias coil respectively.
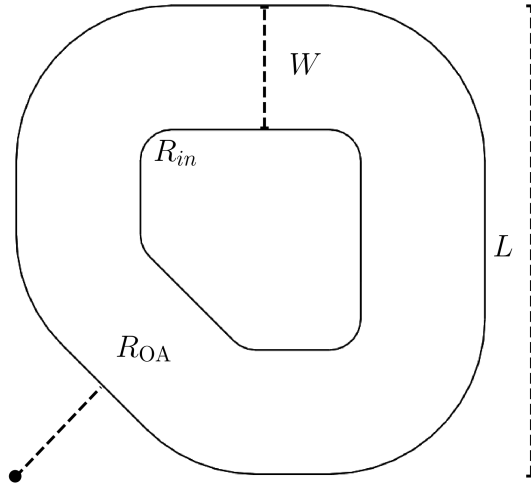
Figure B.2: Bias coil form. R_{OA} denotes the optical access radius taken from the bottom left corner to the edge of the form, R_{in} is the inner turn radius of curvature, L is the side length and W is the width taken to be constant around the loop.

When the bias coils carry the same amount of current I_0 around the science

Parameter	Description	Value
z_0	Placement distance along $\mathbf{e_z}$	$\pm 1.805\,\text{in}$
L	Side length	$2.969\,\text{in}$
W	Coil width (constant)	$0.780\,\text{in}$
R_{in}	Inner loops radius of curvature	$0.200\,\text{in}$
R_{OA}	Optical access radius	$0.800\,\text{in}$
H	Coil thickness (constant)	$0.250\,\text{in}$
R	Coil resistance	$122\,\text{m}\Omega$

Table B.2: Optimal bias coil form characteristics.

cell region, this design ought to reach field strength per unit current

$$\mathbf{B}/I_0 = [3.1981(\mathbf{e}_x + \mathbf{e}_y) + 1.5531\mathbf{e}_z]\,\text{G/A},$$

with a maximum current specification limited by the final power dissipation rate, implying not all coils operate simultaneously.

Only the science cell region needs full control of the eight parameters (a MOT may only use bias field control) in practice. The topology of the gradient cancellation coil layout [99] remains the same as in the Rb–Chip apparatus, but the optimized design changes the coil forms as well as their relative placement. The new layout is shown in Fig. B.3 The single form sketch is in Figure B.4 and the optimized form characteristics are in Table B.3.

When all the gradient cancellation coils carry the same amount of current
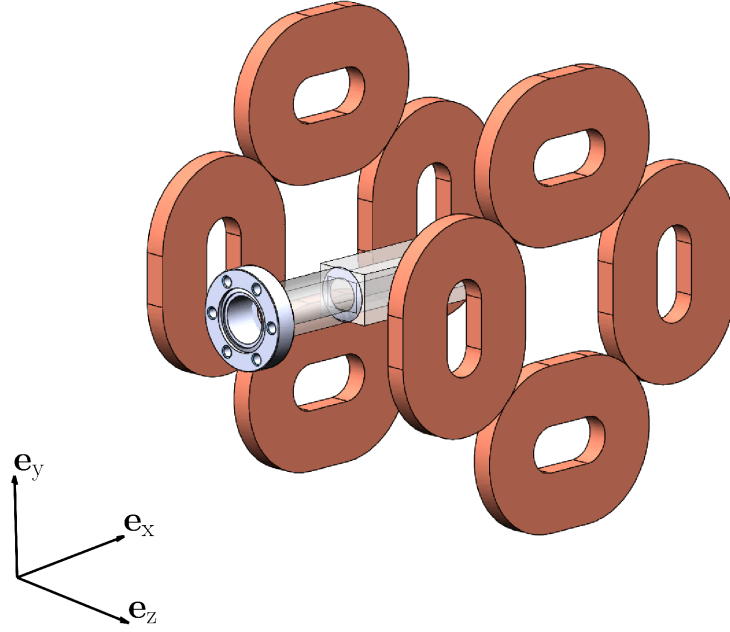
Figure B.3: Coplanar layout of gradient cancellation coils around the science cell. The axes of the gradient cancellation coil pairs are oriented along $\mathbf{e}_z$ while the mini CFF of the glass cell is aligned to $\mathbf{e}_x$.

.

Parameter	Description	Value
z_0	Position along $\mathbf{e}_z$	$\pm 2.075\,\text{in}$
L	Side length	$2.969\,\text{in}$
W	Coil width (constant)	$0.780\,\text{in}$
R_{in}	Inner loops radius of curvature	$(L - R_{\text{OA}})/2 - W$
R_{OA}	Optical access radius	$0.800\,\text{in}$
H	Coil thickness (constant)	$0.250\,\text{in}$
R	Coil resistance	$95\,\text{m}\Omega$

Table B.3: Optimal gradient coil form characteristics.

I_0 around the science cell region, the design may at most reach field gradient

202
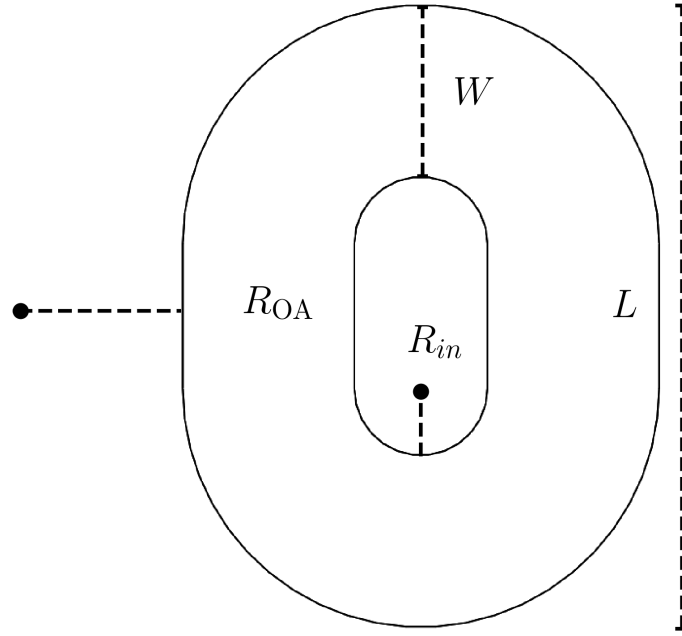
Figure B.4: Gradient coil form. R_{OA} denotes the optical access radius, measured from left side to the edge of the form, R_{in} is the inner turn radius of curvature, L is the side length and W is the width taken to be constant around the loop.

components per unit current

$$B_{xy}/I_0 = B_{yx}/I_0 = 0.9230\,\mathrm{G/A\,cm},$$

$$B_{xz}/I_0 = B_{zx}/I_0 = 0.9372\,\mathrm{G/A\,cm},$$

$$B_{yz}/I_0 = B_{zy}/I_0 = 0.9372\,\mathrm{G/A\,cm},$$

$$B_{zz}/I_0 = -2B_{yy}/I_0 = -2B_{xx}/I_0 = 0.3665\,\mathrm{G/A\,cm}.$$

The gradient coils provide independent field gradient components for full control

$$B_{xx}/I_0 = -B_{yy}/I_0 = 0.4924\,\mathrm{G/A\,cm}.$$
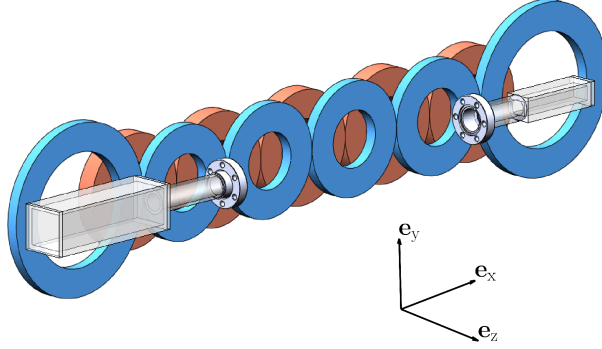
Figure B.5: "Left" side of the transport coil layout (coil pairs not shown) connecting the two glass cell regions. Highlighted in blue are the inner layer coils.

Connecting the science cell region with the MOT region are the transport coils, shown in Figure B.5. The transport coil layout is divided into an inner and outer layer, together containing a total of 11 coils (each coil pair is formed by a left and a right coil, where "left" and "right" are defined to be along $\mp\mathbf{e}_z$ respectively). These pairs produce quadrupole fields whose centers lie along the transport axis, coincident with $\mathbf{e}_x$. The inner layer, closer to the transport axis along $\mathbf{e}_z$, is formed by 4 small coils and two large coils located at the start and finish of the transport segment. The outer layer, farther away from the transport axis along $\mathbf{e}_z$, consists of slightly thicker small coils whose centers are interleaved with those from the coils in the inner layer. In this layout, three different coil forms exist. Chris Billington ran extensive numerical simulations of the transport sequence and provided the final design for each of the three different transport coils in this layout. Figure B.6 shows the sketch of a transport coil form, common to all three types of transport

coils. Table B.4 summarizes the final form characteristics of each of the coils.
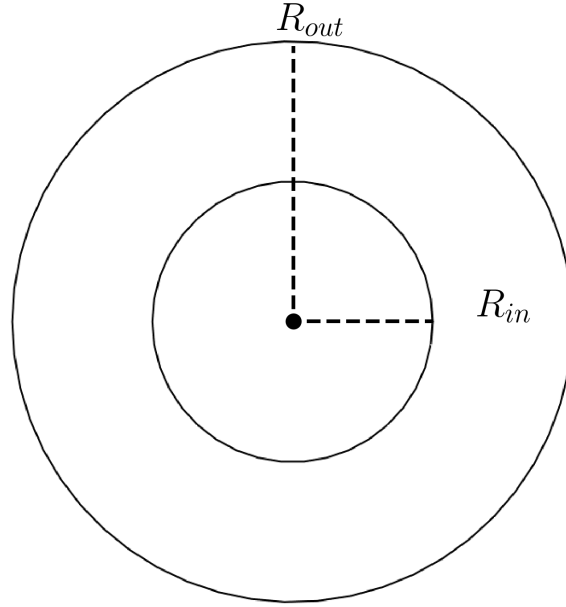
Figure B.6: Small inner layer transport coil form sketch.

Parameter	Description	Inner Small	Outer Small	Inner Large
z_0	Position along $\mathbf{e_z}$	$\pm 0.840\,\text{in}$	$\pm 1.160\,\text{in}$	$\pm 0.840\,\text{in}$
R_{in}	Inner radius	$0.780\,\text{in}$	$0.780\,\text{in}$	$0.780\,\text{in}$
R_{out}	Outer radius	$1.575\,\text{in}$	$1.575\,\text{in}$	$2.375\,\text{in}$
H	Coil thickness	$0.300\,\text{in}$	$0.500\,\text{in}$	$0.300\,\text{in}$
R	Coil resistance	$122\,\text{m}\Omega$	$61\,\text{m}\Omega$	$47\,\text{m}\Omega$

Table B.4: Optimal characteristics for the three transport coil forms.

The MOT cell region has the exact same bias field coil layout as the science cell region, so all the previously listed properties apply. For the MOT, no gradient

cancellation coils are installed. Instead, there is an additional bias coil pair along $\mathbf{e}_z$ which we call MOT z-bias. This pair replaces the push coil present in the original Rb–Chip apparatus, meant to help launch the atoms into transport. Figure B.7 shows the final coil layout around the MOT cell region. Table B.5 summarizes
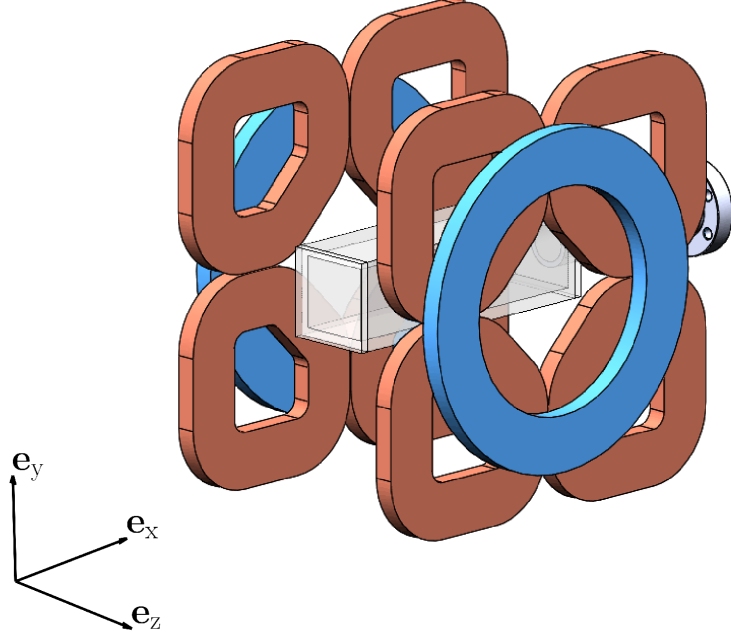
Figure B.7: Coil layout around MOT cell region. The same layout is used to provide bias fields and gradients while an additional pair along $\mathbf{e}_z$ (highligthed in blue) replaces the push coil to help initiate transport.

the optimal characteristics for the MOT z-bias coil form. When a current I_0 runs through the MOT z-bias coil pair, it provides a field component along $\mathbf{e}_z$ with magnitude

$$B_z/I_0 = 4.4203 \, \text{G/A}.$$

Parameter	Description	Value
z_0	Position along $\mathbf{e_z}$	$\pm 2.075\,\mathrm{in}$
R_{in}	Inner radius	1.595
R_{out}	Outer radius	$2.375\,\mathrm{in}$
H	Coil thickness	$0.270\,\mathrm{in}$
R	Coil resistance	$205\,\mathrm{m\Omega}$

Table B.5: Optimal form characteristics for the MOT z-bias coils.

The full coil layout for the new apparatus is in Fig. B.8. A total of 48 coils are included in this design. Even though the number of transport coils can be reduced through an appropriate optimization of the forms, we replicate the number of transport coils used in the current Rb–Chip apparatus to simplify the transition of all the control electronics and power supply connections when swapping the setup.
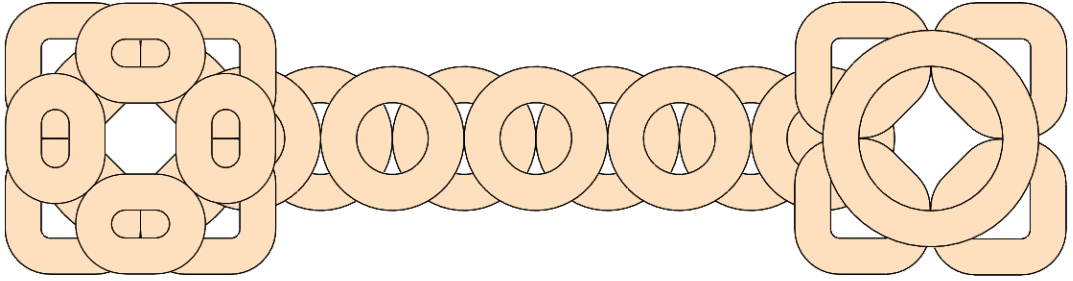
Figure B.8: Final coil layout as viewed from the "left" side. The science cell region would be at the left.

B.2.2   Bias, gradient cancellation, and MOT z-bias coil holders

We designed mounts for the bias, gradient cancellation, and MOT z-bias coils described in the preceding section. Two kinds of holders exist, one for the MOT cell region holding bias and MOT z-bias coils, and one for the science cell region, holding bias and gradient cancellation coils.

We start by sketching a single monolithic coil holder in the sketch labeled `Base_slab`. The shape is rectangular, 7.50 in wide and 7.00 in high. We then extrude the `Base_slab` by 0.75 in to create the `Slab` feature. On one face of the `Slab`, we sketch the four slots for a single set of coplanar bias coils, leaving a $\oslash = 1.50$ in circular gap in the center of the shape for optical access. This is depicted in Figure B.9.

We follow by making a 0.27 in deep cut on the designated gaps outlined by the sketched forms. Only for the MOT bias coil holder, we then sketch the form of the MOT z-bias coil nominally at the center of the `Slab`. We make a 0.54 in deep cut based on this contour to host the MOT z-bias coil, creating the `MOT_bias` feature, exclusive for this kind of bias coil holder.

Only for the science cell region, in contrast with the MOT z-bias sketch and cut, we sketch the four gradient cancellation coil forms. We then make a 0.54 in
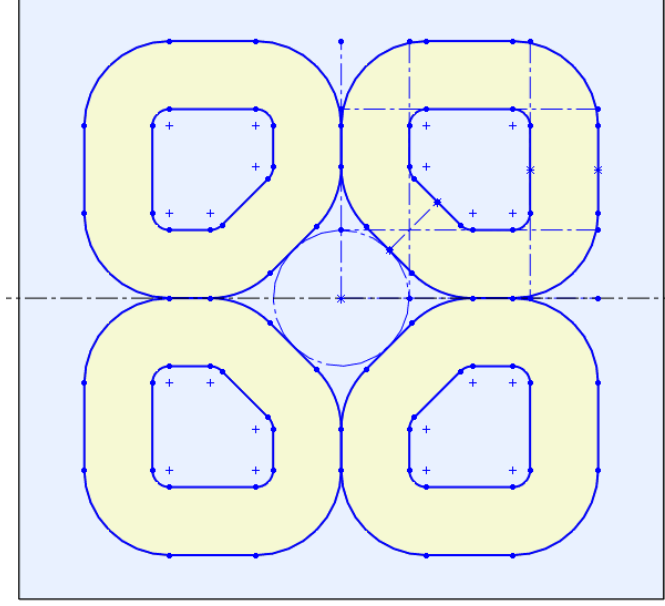
Figure B.9: Bias coil sketch on the `Slab` face.

deep cut based on the contours, creating the `Grad_cancellation_cut` feature, exclusive for this kind of bias coil holder.

As a next step for both kinds of holder we add counterbore holes on the other face as indicated in Figure B.10. These holes are for attachment, pressing the assembled pieces in place with the rest of the apparatus. Finally, we add a single set of threaded holes for $60\,\text{mm}$ cage mount rods for a quick and precise optical alignment along $\mathbf{e}_z$, as well as a set of anti-eddy current slit cuts. These features are all depicted in Figure B.10.

The final assembly, containing all the relevant coils placed at the relative separation along the transport axis between the MOT and science cell regions is

209
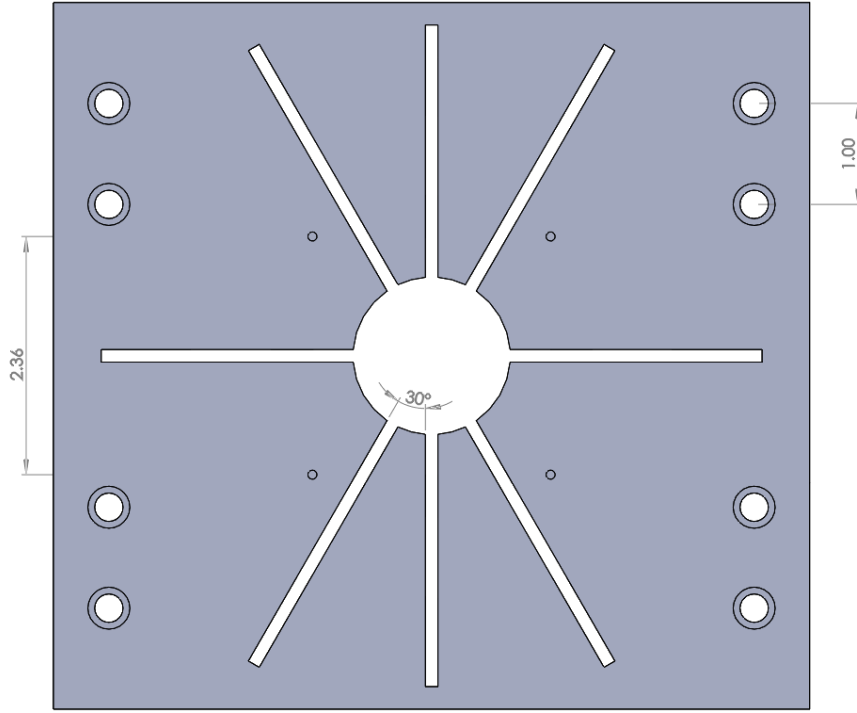
Figure B.10: Opposite face of the MOT bias coil holder showing the counterbore mounting holes as well as the 60 mm cage mount holes and anti-eddy current slits.

shown in Figure B.11. We design a complementary set with the same features,

Figure B.11: Single plane of the assembled bias and gradient cancellation coils, separated by the total transport distance. Highlighted in blue are the gradient cancellation coils (left) and the MOT z-bias coil (right).

related to the pair in Figure B.11 by a mirror reflection about the XY plane.

B.2.3 Monolithic transport coil holders

We designed a right-handed monolithic transport coil holder and a left-handed monolithic transport coil holder, but the general features are common to both and related by a mirror reflection about the XY plane. We begin by sketching the contour of a single monolithic coil holder in the `Main_slab` (B.12) sketch.
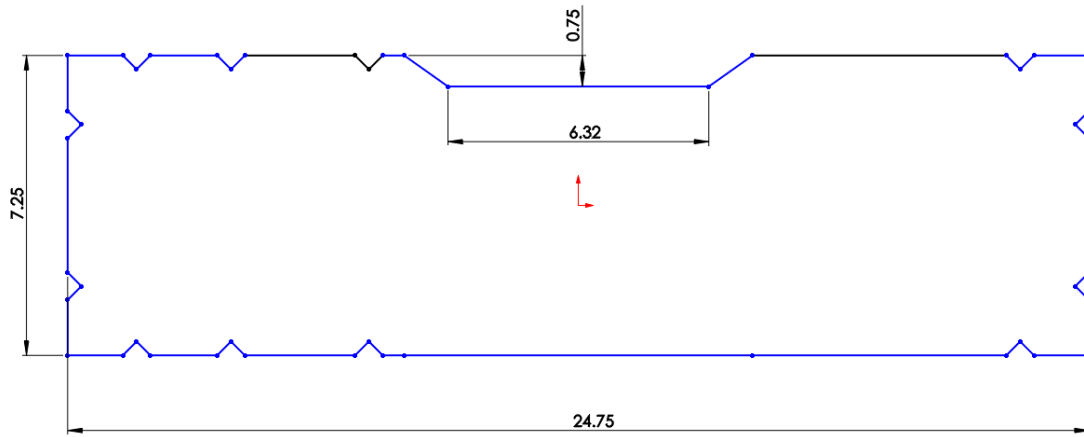
Figure B.12: `Main_slab` sketch

The overall shape is rectangular, with 24.75 in of width and 7.25 in of height. We outline a series of 45° triangular inlets in various locations as well as a waist close to the middle along the longer side. This waist provides a gap for returning coil wire while the inlets allow standard cage-hardware to attach into the slab at specific angles. The waist runs for 6.32 in and the gap is 0.75 in wide. We extrude the whole `Main_slab` sketch into the `Slab` feature by 1.00 in.

We sketch a pattern of circles labeled `Outer_Coil_Layer_Contour` (B.13) on

the top surface of the `Slab` that define the outer coil layer (outer here means away from the plane of the atoms).
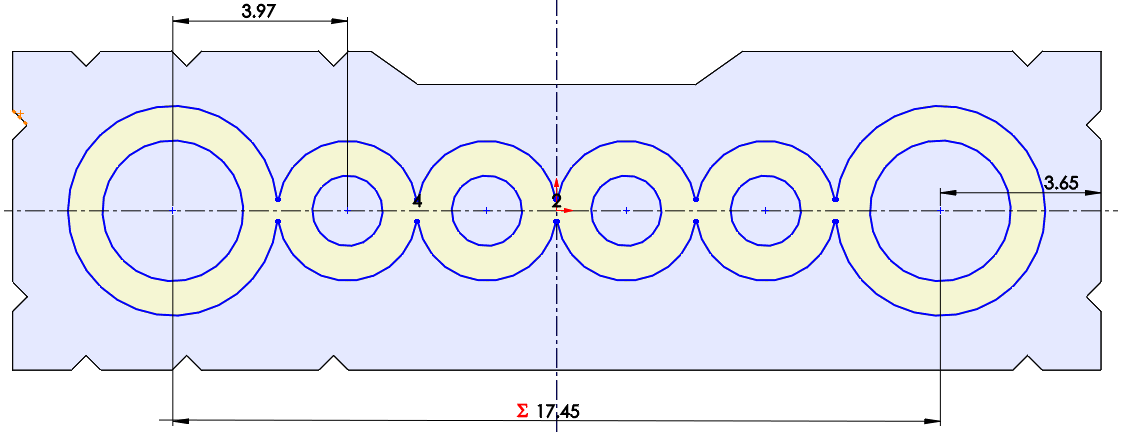
Figure B.13: `Outer_Coil_Layer_Contour` sketch

The `Outer_Coil_Layer_Contour` sketch contains two types of coil outlines. The bigger ones have an inner diameter of $\oslash_i = 1.60\,\text{in}$ and an outer diameter of $\oslash_o = 2.38\,\text{in}$ while the smaller ones have an inner diameter of $\oslash_i = 0.80\,\text{in}$ and an outer diameter of $\oslash_o = 1.60\,\text{in}$. The largest circles correspond to the larger quadrupole coils located about the glass cell areas while the smaller ones correspond to dedicated transport coils. The six coils are patterned along the transport axis with a total transport distance of $d_T = 17.46\,\text{in}$. The sketch turns into the `Outer_Coil_Layout` feature, which makes a $0.34\,\text{in}$ cut into the `Slab`.

Following this, we draw the `Inner_Coil_Layer_Contour` sketch (B.14) in the same surface to define the inner coil layer (inner here means closer to the atoms

212

plane).
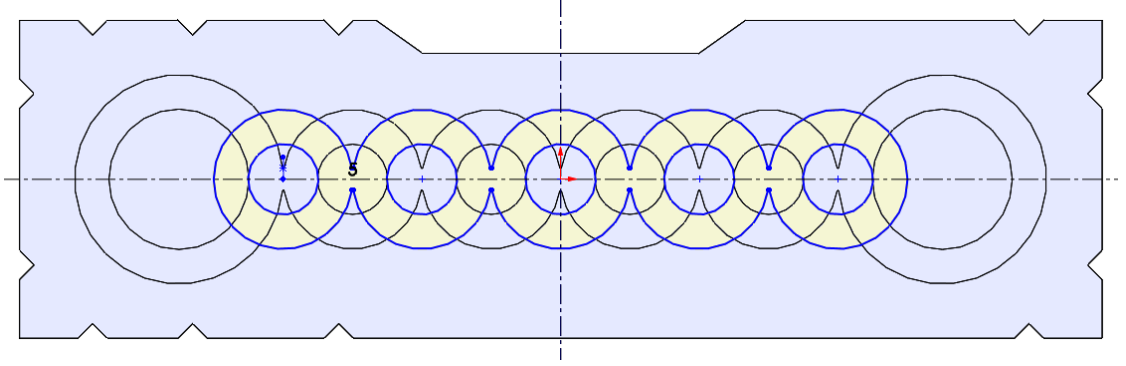
Figure B.14: `Inner_Coil_Layer_Contour` sketch

Here, the five coil contours have an outer diameter of $\oslash_o = 0.80\,\mathrm{in}$ and an inner diameter of $\oslash_i = 1.60\,\mathrm{in}$. The sketch turns into a cut feature labeled `Inner_Coil_Layer` which cuts $0.88\,\mathrm{in}$ into the slab. The depth of both cuts incorporate the width of the ribbon wire from which the coils are made as well as the insulating layers that separate the coils from each other.

We make another sketch labeled `Anti_eddy_current_slit` (B.15)to outline a grid of anti-eddy current cuts. In the `Anti_eddy_current_slit` sketch we outline
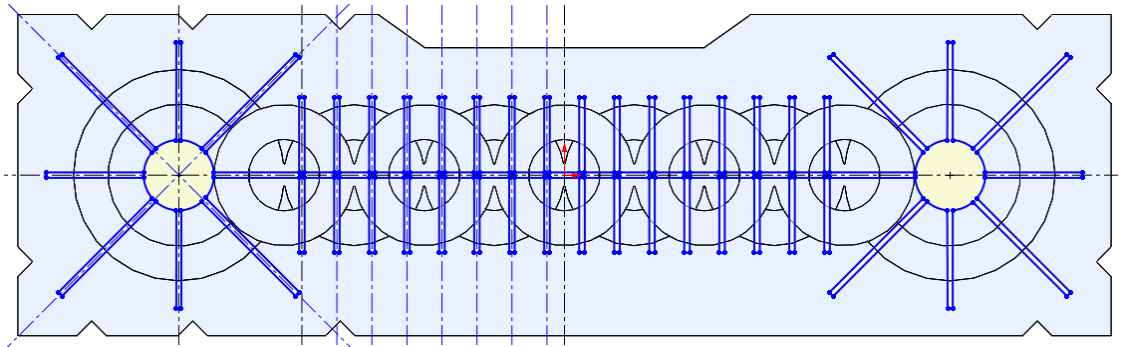
Figure B.15: `Anti_eddy_current_slit` sketch

213

two large optical access circles of diameter $\oslash = 1.5$ in which are concentric with the main quadrupole coils. We make a cut feature labeled `Optical_access_antieddy` that cuts through the piece (1.00 in).

On one side of the slab, we sketch the `Cooling_line_sketch` (B.16). This sketch consists of two features outlining the access and intended contact profile of the water cooling lines that provide a heat sink for the monolithic coil holders. The parts are offset from the line of transport by 2.00 in each and have a semi-circular profile of diameter $\oslash^3/\!{}_8$ in whose center is placed 0.16 in inside the slab from the opposing surface to the inner coil layers. We turn this into a cut through the full length of the piece which we label `Cooling_line`.
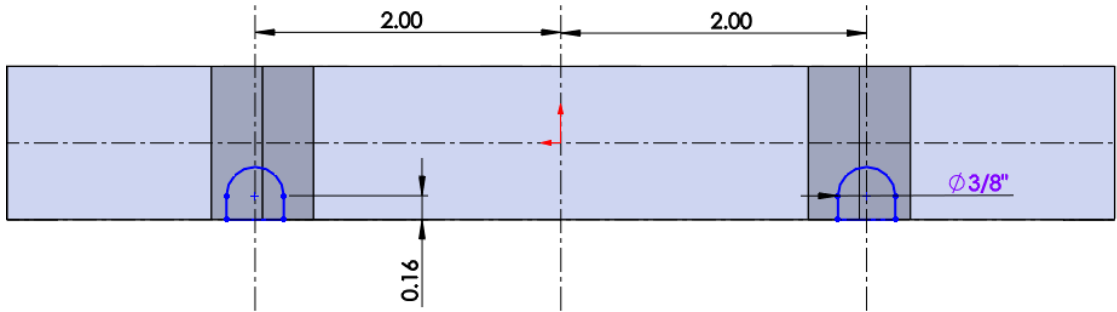
Figure B.16: `Cooling_line` sketch

In order to run the coil wire out of the coils into the power supplies, we sketch the `Wire_groove_sketch` (B.17) on the same surface as the coil layers. We provide eleven 0.31 in channels that turn into 0.10 in deep cuts in the `Wire_grooves` feature. The depth takes into account two units of ribbon wire thickness including insulation.
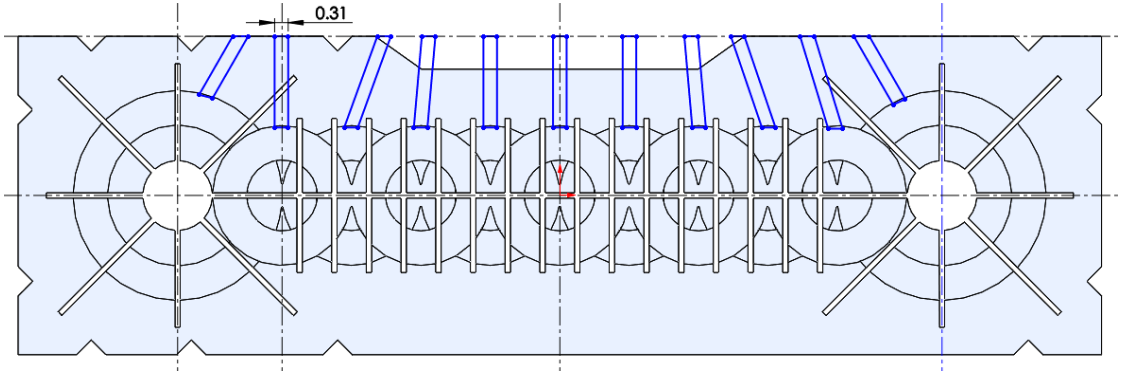
Figure B.17: `Wire_groove` sketch

We then sketch a grid of $\oslash\,{}^1\!/_4 - 20$ tapped holes in `Mounting_tap_holes` (see B.18) in the surface behind the inner coil layer for mounting a pressing piece to assist a better thermal contact between the cooling line and the aluminum in the `Cooling_line` cut. We set the positions of these holes in such a way as to avoid coils, wires and cooling lines (so not all of the holes laid out in B.18 are drilled). We use the cut feature to set a depth of 0.225 in and turn this into the `1/4_20_tap` feature.
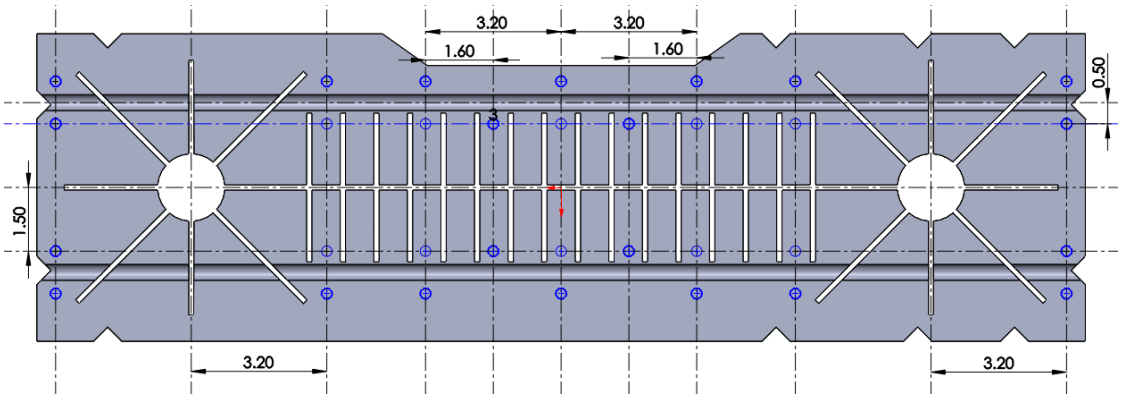
Figure B.18: `Mounting_tap_holes`

We sketch pilot lines that define the distance from the transport line to 30 mm

away in the direction of the monolithic coil holders in the surface defined by the triangular inlets first sketched in B.12. We then use the hole wizard tool to sketch two $\oslash 4 - 40$ separated by $60\,\mathrm{mm}$ (B.19). These holes are tapped and $0.20\,\mathrm{in}$ deep.
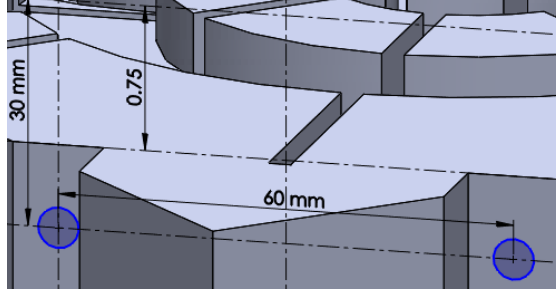
Figure B.19: `Corner_cage__4-40-pilot` sketch

We replicate the $60\,\mathrm{mm}$ cage attachment $\oslash 4 - 40$ hole constructions all around the monolithic coil holder by using mirror and patterning tools.

The MOT is designed to have three pairs of counterpropagating beams. One pair should propagate along $\mathbf{e}_z$, while the other two should propagate along the $\mathbf{e}_{x+y}$ and $\mathbf{e}_{x-y}$ axes (Figure B.20). In order to deflect the beams such that they meet at $90\,°$ in the MOT cell, we add thin cuts (in deep) to register a rectangular mirror normal to the transport axis $\mathbf{e}_x$. A single $45\,°$angled $\oslash 8 - 32$ tapped hole intersects this cut to allow fixing the mirror in place (with a nylon tip setscrew inserted from the top), visible in Figure B.20. The dimensions and positioning of the rectangular mirror slots are in Figure B.21

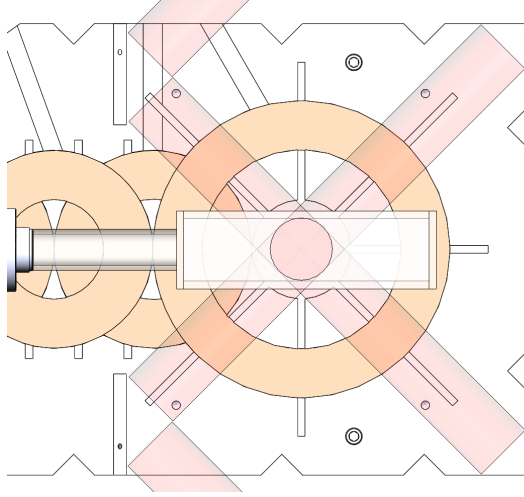The next features in the design of the monolithic transport coil holder are a

216

Figure B.20: MOT beam layout. Three pairs of beams that form the MOT region inside the glass cell. A pair is along $\mathbf{e}_z$ while the other two are along $\mathbf{e}_{x+y}$ and $\mathbf{e}_{x-y}$. Thin slots host a rectangular mirror that deflect the beams so that two pairs in the XY plane intersect at $90\,°$ in the MOT region.
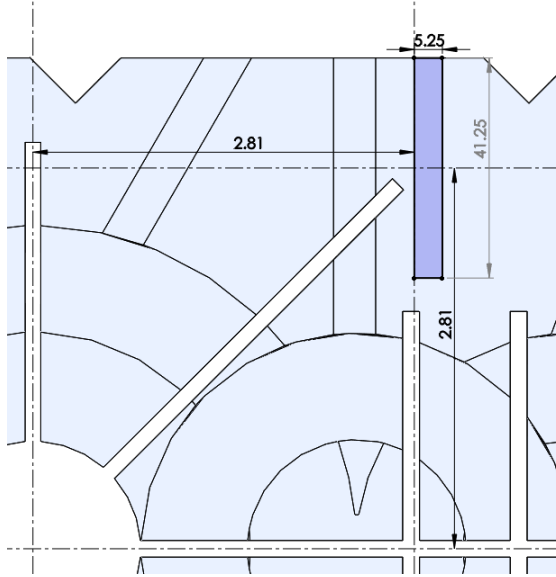

Figure B.21: Single rectangular mirror slot. Thinly cut into the monolithic coil holder slab, it registers a rectangular mirror into place.

series of holes and cuts that allow the piece to firmly mount and precisely register

its position into a stainless steel holder (documented in the next section below).

We use stainless steel for its mechanical properties (solid, and robust mounting),

as well as for a lower electrical conductivity relative to aluminum that mitigates the parasitic induced eddy currents from the coil pairs. Where possible, we sketch rectangular shapes that we turn into cuts. These cuts jointly define all three different planes to match a relative positioning of the same accuracy as the machining tolerance. This is done to make sure that when all the coils are assembled into the monolithic transport coil holder, the mounting of the left and right pieces already fixes the different coil pairs at nominally the right separations. The first of these features is a side grabber, depicted in Figure B.22. We draw a rectangular shape near the science cell end, and turn it into the Grab_groove feature by making a 0.375 in deep cut. This side grabber registers the monolithic coil holders in place. For attachment, we add a $\oslash\,1/4 - 20$ through hole from the back plane.
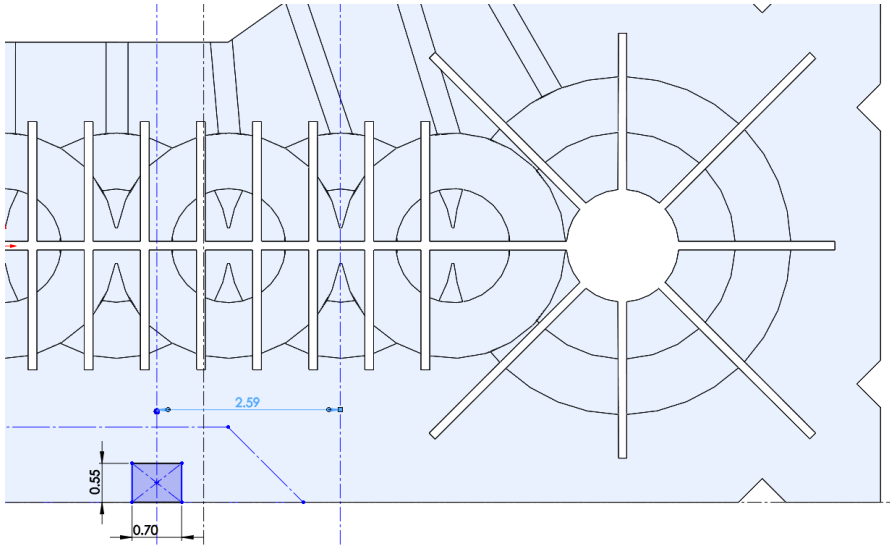
Figure B.22: Sketch for the side groove on the monolthic transport coil holder. A single rectangular shape that leads to a cut for registering the parts together.

Another feature for the stainless steel holder are a set of frontal holes, all

$\oslash 1/4 - 20$, through holes. These are attachment holes as well, fixing the left and right parts relative to the XY plane and to each other. Finally, there is a series of bottom holes to register the monolithic transport coil holders in place relative to the YZ plane. The frontal holes are shown in Figure B.23, while the bottom holes are shown in Figure B.24.
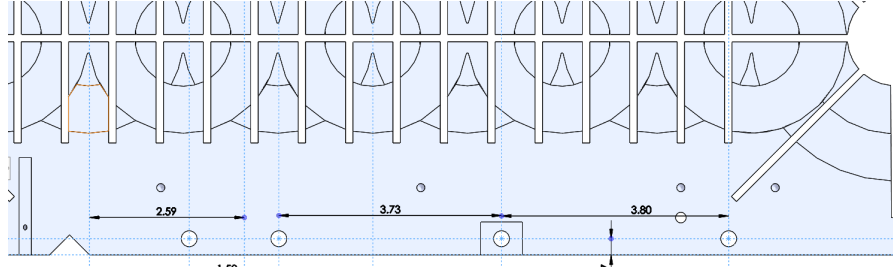

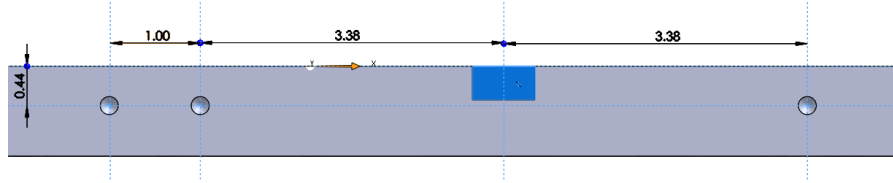Figure B.23: Frontal holes for mechanical registration.

Figure B.24: Bottom holes for mechanical registration.

A printed circuit board (PCB) based radiofrequency (RF) antenna is incorporated into the design of the new apparatus. We add a series of attachment holes for this PCB antenna in our monolithic transport coil holder. These threaded $\oslash 8 - 32$ holes and an additional set of convenience holes are highlighted in Figure B.25. Finally, anti splay holes are added in the Anti_splay_hole_sketch sketch. These holes have will host long anti splay screws to prevent relative shearing of the left and right monolithic transport coil holders, adding to the overall robust
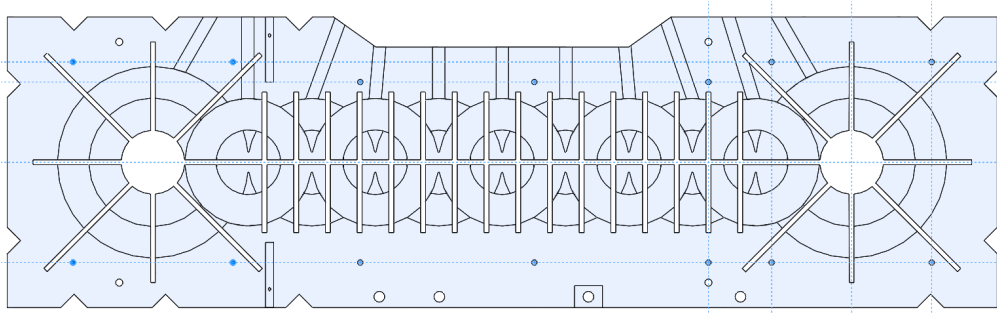
Figure B.25: Attachment holes for radiofrequency PCB antenna.

mechanical registration. The sketch for the hole locations is shown in Figure B.26.
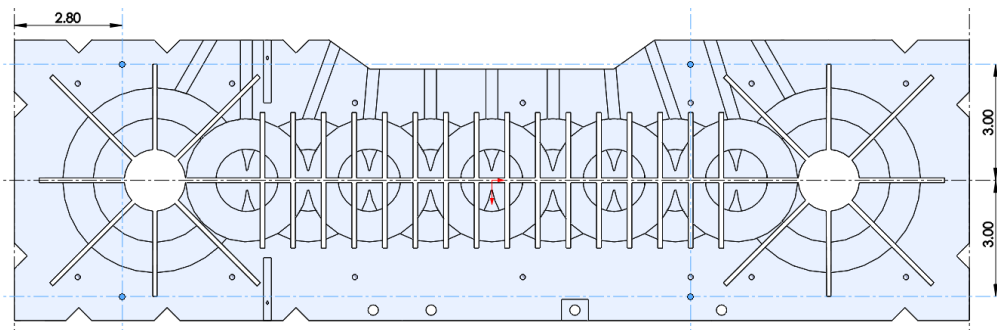

Figure B.26: Antisplay holes sketch.

B.2.4   Stainless steel holder

We design a single piece to support the weight of all the coils and vacuum components. We denominate this piece the stainless steel holder, since we opt to use a harder, heavier material such as stainless steel. We begin the design of the stainless steel holder by drawing a 10 in by 8 in rectangular shape. We then extrude the shape by 0.47 in to a Base_slab feature. On a face of the Base_slab, we add four counterbore $\oslash 5 - 16$ through holes to enable attachment to further

supporting structures. We then add two sets of 6 $\oslash 1/4 - 20$ holes in a circular pattern, to acommodate 2.75 in CF flange vacuum components. The four support holes and CFF attachment holes are shown in B.27.
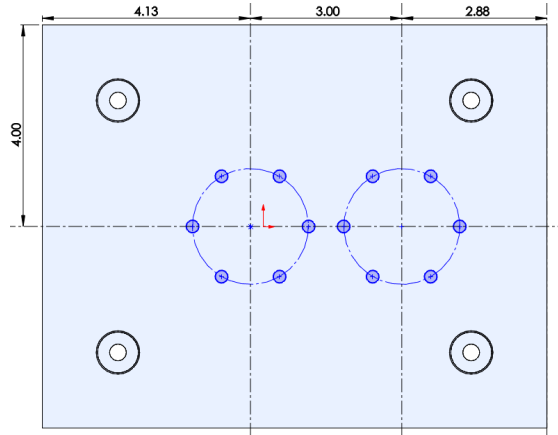

Figure B.27: Stainless steel holder with support and 2.75 in CFF pattern sketch.

We then add clearance cuts to the Base_slab, by first sketching two circular holes 1.60 in in diameter and an extended semicircular opening on one of the sides. These cuts clear two 1.33 in to 2.75 in CFF conical expanders and a single mini-CFF (1.33 in) nipple. These cuts are illustrated in Figure B.28.

Working on the same face, we extrude the Rail_step feature. This feature consists of separate "islands" that together provide side attachment and registration to the attaching monolithic transport coil holders. The extrusion is 0.53 in high, such that the whole piece can be started from a 1" slab. The Rail_step is shown in Figure B.29.
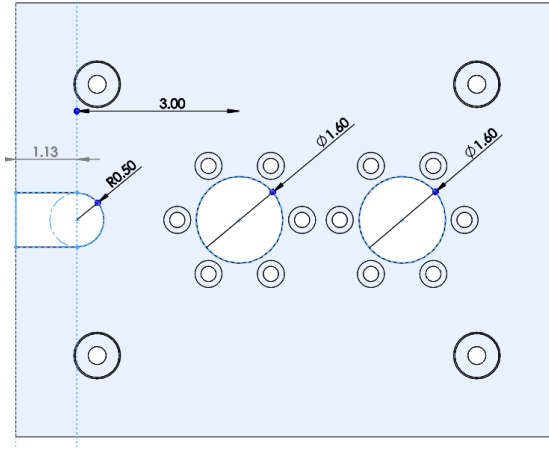
221

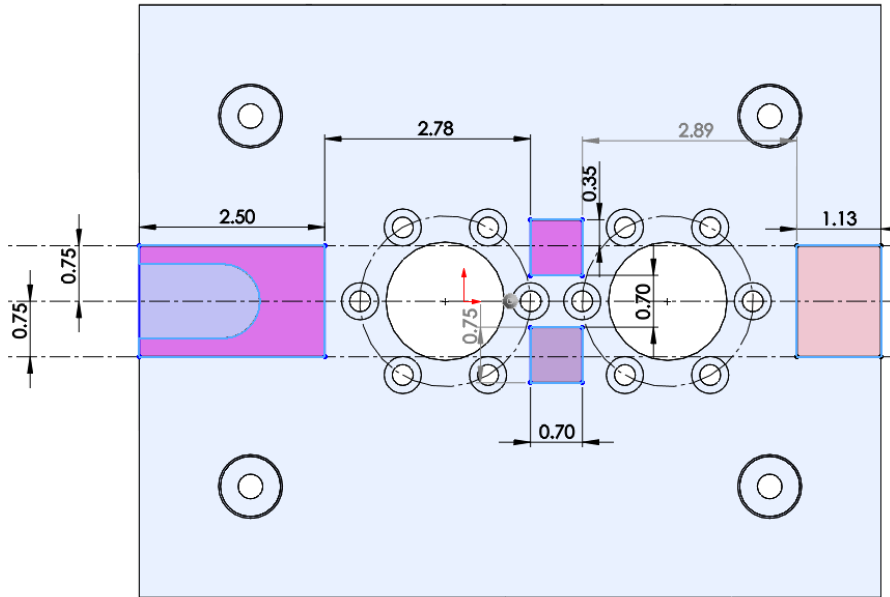Figure B.28: UHV clearance cuts through stainless steel holder.

Figure B.29: Rail step islands with relevant dimensions, highlighted in pink shading. The rail step islands are extruded to help attach and register the monolithic transport coil holders.

A set of 4 side $\oslash 1/4 - 20$ threaded holes are added on each side of the left and right planes of the Rail_step islands. An additional set of three counterbore $\oslash 1/4$ – 20 through holes appear from the opposite face of the Base_slab to grab the monolithic transport coil holders from below, registering them to the Base_slab

face. Finally, we add a lattice of interleaved $\oslash 1/4 - 20$ threaded through holes for convenience. All of the aforementioned features are depicted in Figure B.30.

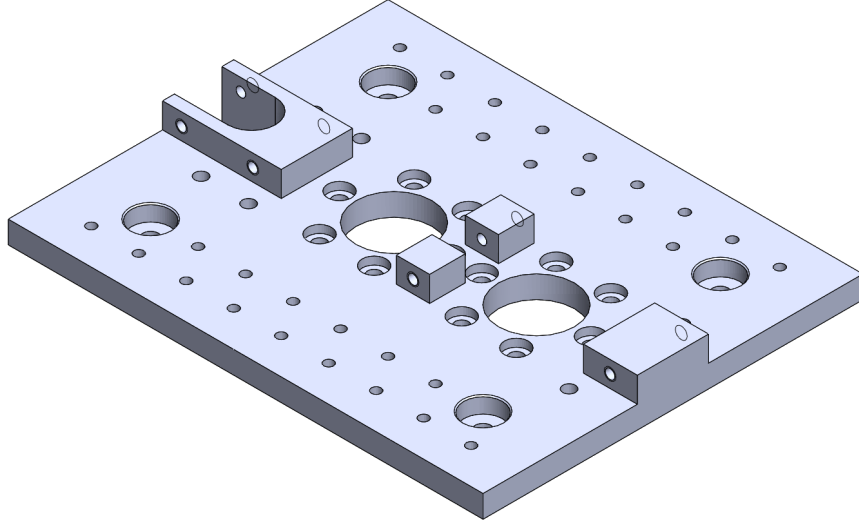

Figure B.30: Isometric view of the stainless steel holder. Side and bottom grabbing holes are seen as well as the convenience $\oslash 1/4 - 20$ screw hole lattice.

B.2.5   Vacuum system

The first major component of the vacuum system is the `MOT_cell`, shown in Figure B.31. The `MOT_cell` is square in its cross section, with a $1.00\,\mathrm{in}^2$ area profile, over an inner length of $3.94\,\mathrm{in}$. The glass to metal seal is at the end of a $0.50\,\mathrm{in}$ glass tube extending just over $2.35\,\mathrm{in}$ and finished off in a mini-CFF end. The `MOT_cell` was custom made by Precision Glassblowing and does not have any anti-reflection (AR) coated surfaces.

In a similar level of importance is the `Science_cell`, shown in Figure B.32. The `Science_cell` is rectangular in its cross section, with a $10\,\mathrm{mm}$ by $13\,\mathrm{mm}$ face
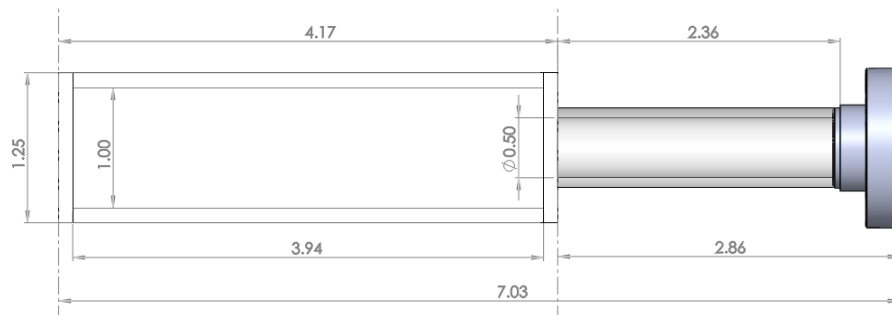
Figure B.31: Side view of the MOT_cell. The glass to metal seal connects to a mini-CF flange (1.33 in).

(Figure B.33, extending over an inner length of 60 mm. The glass to metal seal is at the end of a 33.10 mm long tube of diameter 11 mm. The end is adapted to a mini-CF Flange connection.

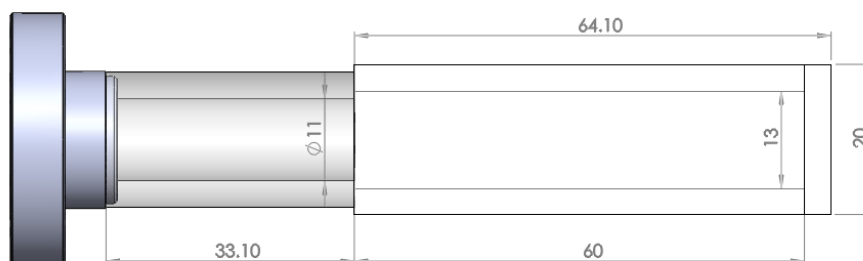The two glass cells are connected through three mini-CFF tees (3.00 in in length

Figure B.32: Top view of the Science_cell. The glass to metal seal connects to a mini-CF flange (1.33 in). All the annotated dimensions in this Figure are in mm.

each). The three tees connect to the atomic source vacuum subassembly (documented below), a dedicated MOT and source 25 L/s ion pump (Gamma Vacuum 25S) and a dedicated science 25 L/s ion pump (Gamma Vacuum 25S) respectively.

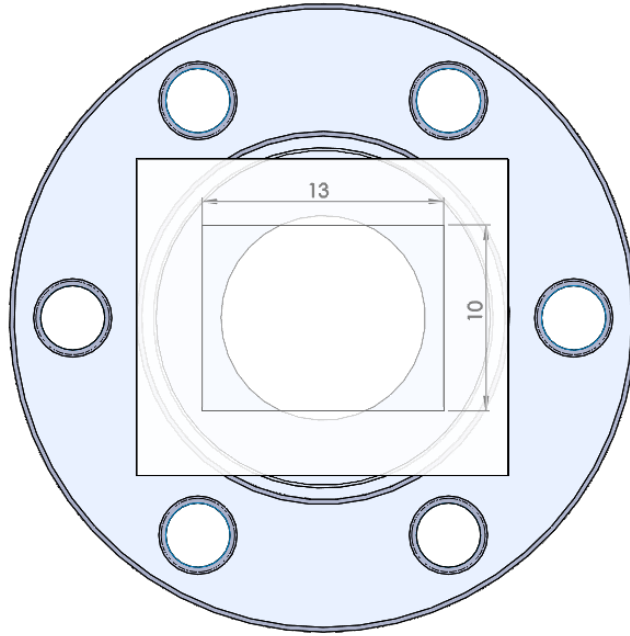A first mini-CFF (1.33 in) nipple runs down for 3.00 in to the source sub-

Figure B.33: Front view of the `Science_cell`. The UHV region has a rectangular cross section of the illustrated dimensions. All the annotated dimensions in this Figure are in mm.

assembly. Then, the ion pump subassemblies are almost symmetric. They both first expand the UHV cross section (to improve the pressure conductance) from 1.33 in to 2.75 in through straight conical expanders (`MDC-402030`), then run down two straight 2.75 in nipples (`MDC-402002`), and bend into the 2.75 in ion pump inlets through two $90°$ rounded elbows (`MDC-403042`). Due to the dimensions of the ion pumps, the two elbows bend away from the transport axis along $\mathbf{e}_z$ in opposite directions. The ion pumps are dual 2.75 in port. For the MOT and source ion pump we add an all-metal-valve (`VAT-54132-GE02`) that then can be pumped out first with a roughing pump followed by a turbomolecular pump before the ion pumps are fired. All the aforementioned UHV components are assembled in CAD and the resulting main vacuum assembly is shown in Figure B.35.
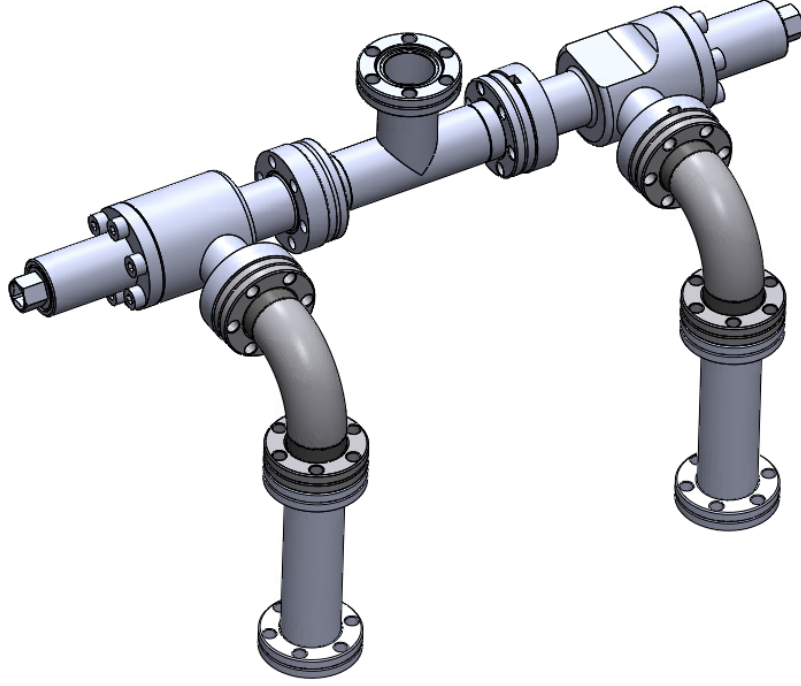
Figure B.34: View of the dual (^{87}Rb and K) species source subassembly. Two mini-CFF all-metal-valves control the flow of atomic vapor to the MOT cell region lying above (not shown).

There are two versions of the UHV subassembly for the atomic source continuing from the straight mini-CFF nipple described in the preceding section. The first one is for a single species ^{87}Rb experiment, consisting of a single mini-CF flange bellows terminating on a mini-CFF blank. The alternative version is a dual species assembly with either ^{87}Rb or bosonic (^{39,41}K) with the relative freedom to have a mixture or use a single atom. This subassembly starts with a mini-CFF tee (`Lesker-0133`), 3.00 in long, from which two mini-CFF all-metal-valves (`VAT`) connect along $\mathbf{e}_z$. The valves go through a pair of 90° mini-CFF elbows that drop down to a pair of straight mini-CFF nipples and finally connect to the hosting
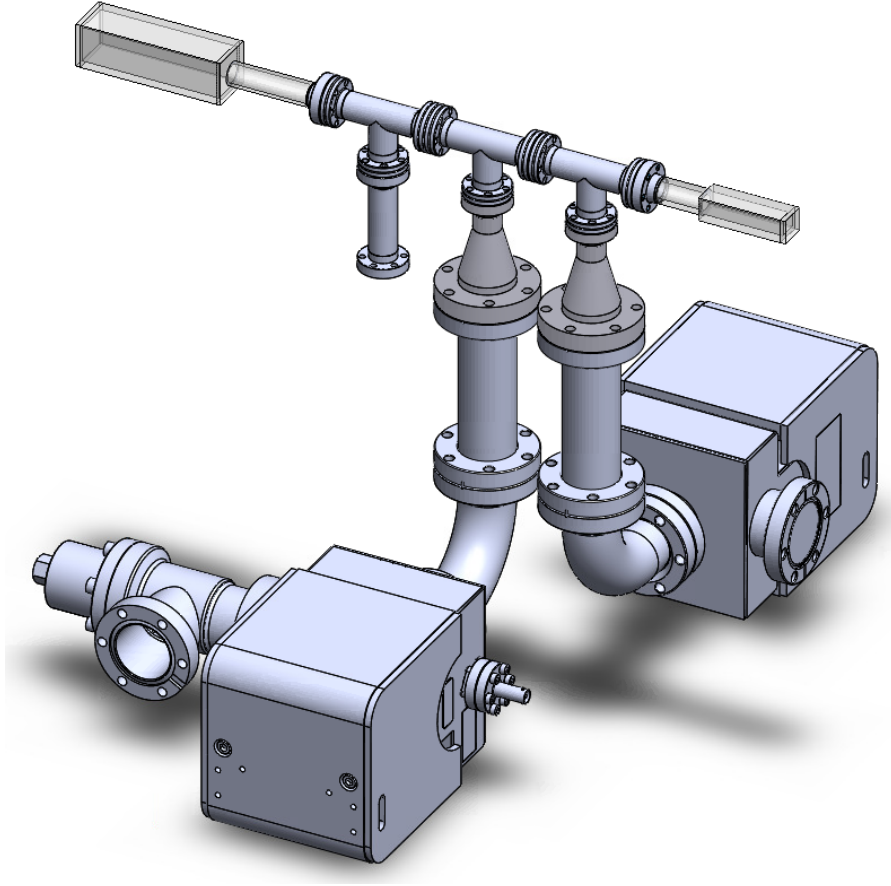
Figure B.35: Trimetric view of the main vacuum assembly. The two cells are connected by three mini-CFF tees, two of which then go through conical expanders, nipples and elbows connect to two ion pumps.

flexible mini-CFF bellows, where the ampoules are to be placed. This dual species version is depicted in Figure B.34.

B.2.6 MOT optics

The design of the monolithic transport coil holders (documented in a preceding section) incorporates various $\oslash 8 - 32$ threaded holes for $30\,\mathrm{mm}$ and $60\,\mathrm{mm}$ cage rods. The cage system provides robust optical alignment and fixed mechanical mounting for the optical elements through which our cooling, optical pumping,
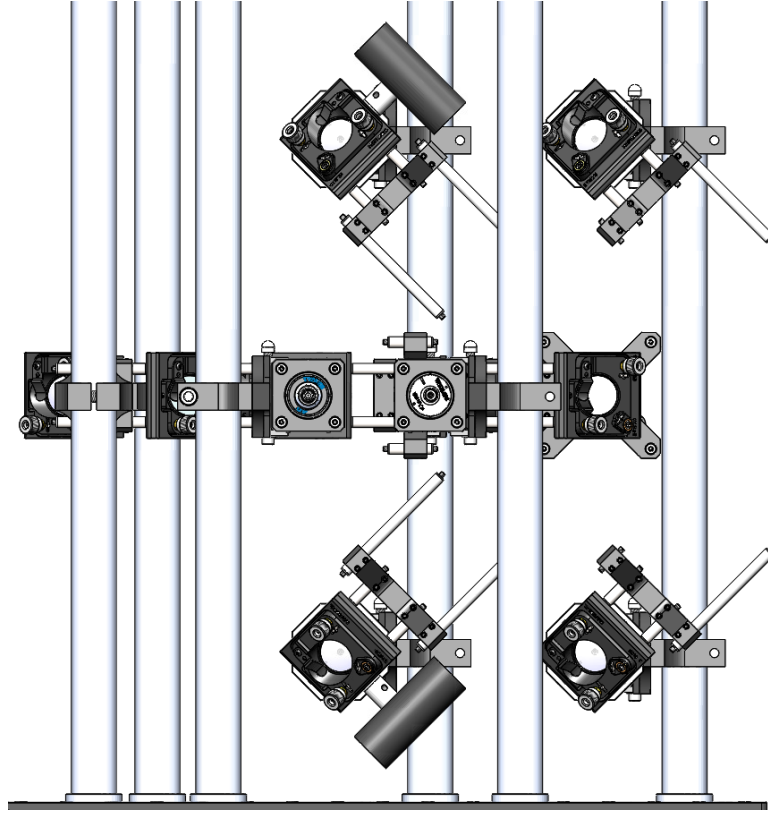
and imaging beams may propagate.

Figure B.36: Right side view of the MOT optics. 30 mm cage mount components include fiber collimating packages, corner 1.00 in elliptical mirror mounts, square threaded mounts and polarizing beam splitter (PBS) mounts. In this view the two pairs of 45° incident beam lines may be inferred. UV LEDs are visible as well, parallel to two of the angled beam launches. In addition to the attachment provided by the bias coil holders, tall 1.00 in pedestals support the MOT optics subassembly atop a breadboard.

Chris Billington was in charge of designing the layout presented in Figures B.39 and B.40. The MOT optics uses fiber injected beams which first go through Thorlabs collimating packages to make ~ 1.00 in diameter beams (for an optimal capture volume). Half and quarter waveplates follow in order to generate the appropriate polarizations along the three MOT axes. Achromat lenses may be
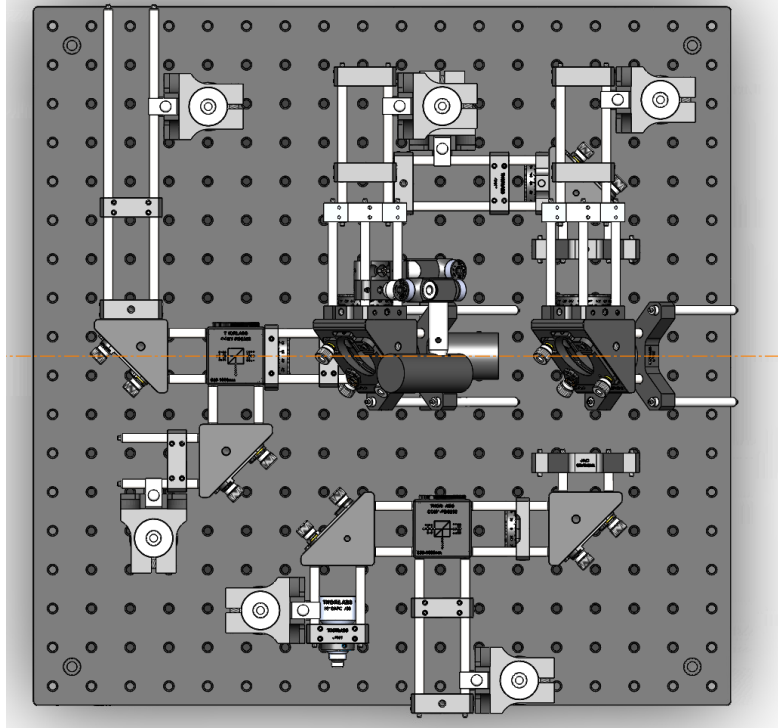
Figure B.37: Top view of the MOT optics. 30 mm cage mount components include fiber collimating packages, corner 1.00 in elliptical mirror mounts, square threaded mounts and polarizing beam splitter (PBS) mounts. The orange line indicates the transport axis. In this view,

added in positions with relative motional freedom to make the cooling beams slightly diverging as they go through the MOT glass cell. This relative tunability might optimize the MOT number and temperatures which profoundly affect the rest of the experiment. In contrast with the Rb–Chip apparatus, we explicitly add imaging paths that point along the direction of magnetic transport. This represents a significant opportunity for improvement in the magnetic transport optimization.

B.2.7 Full transport, MOT optics and UHV assembly

Placing all of the preceding coil, holders, UHV subassemblies and MOT optics components together, we form the assembly shown in Figure B.38. This comprises the majority of the new apparatus.
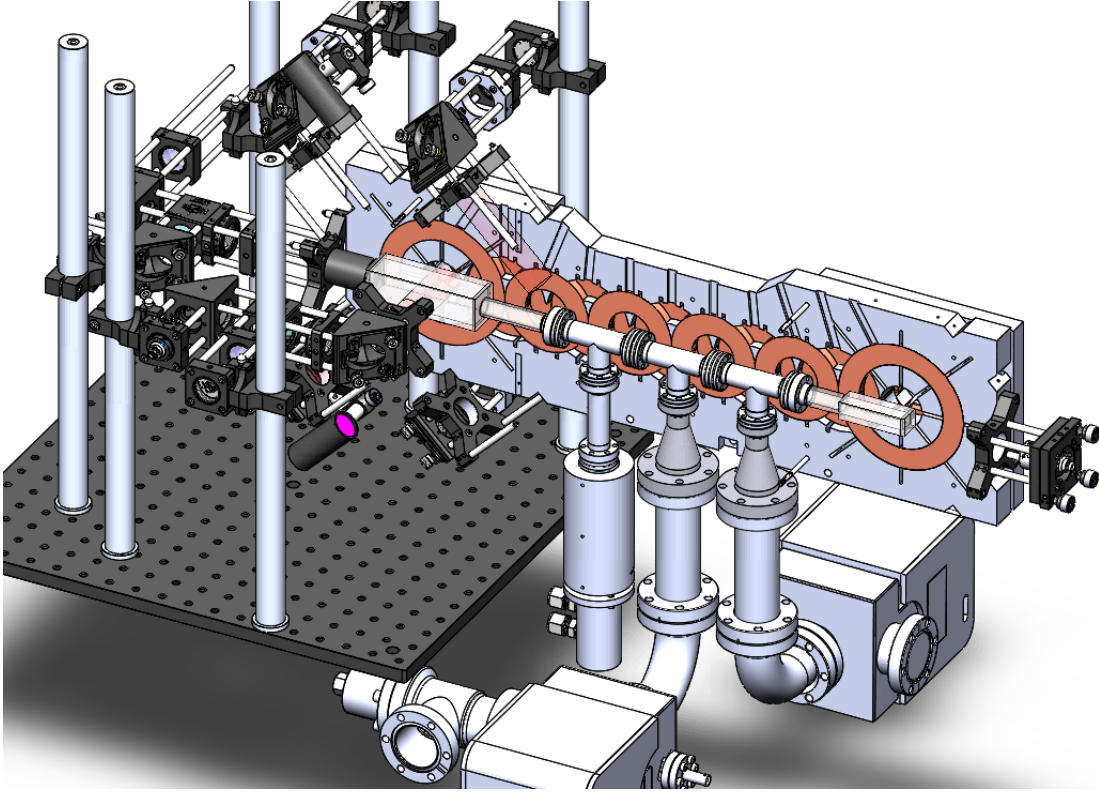
Figure B.38: View of the ^{87}Rb version of the new apparatus, including the coils, holders, UHV and MOT optics components. The right side coil holders and coils are hidden for an enhanced level of detail of the UHV system. An additional cage mounted beam launch for a transport imaging probe is shown on the science cell end of the transport axis.

The new apparatus is designed to be independent of free space laser alignment as well as power supply friendly; truly a plug-and-play machine. When fully

assembled, this modular design may fit within a cubic meter of volume, making it a highly compact quantum gas apparatus. Time will tell if it lived up to its awesome design specifications.

B.2.8   Optical table

The main portion of the new apparatus assembly (B.38) sits in an optical table of its own. We add legs and a 19 in rack mount subassembly to the 72 in by 30 in (TMC) optical table. We design and fabricate hollow aluminum cylinders for the legs, one of which is depicted in Figure B.39. The legs have a set of 1.00 in spaced holes for mounting 19 in rack mount frames. Four legs are connected to each other to form a rectangular frame support through 80/20 components. The full assembled frame is shown in Figure B.40.

B.2.9   Breadboards

Surrounding the main portion of the UHV and coil holders assembly are optical breadboards. Optical components may be mounted in three different height levels. First the level defined by the optical table itself, which we refer to as level 1. Then, the level defined by the height of the magnetic transport trajectory (and coils), which we call level 2. Finally, any optics hovering above may be mounted in a third level, or level 3. For levels 2 and 3 we design and fabricate thick (2.00 in) aluminum breadboards populated with $\oslash 1/4 - 20$ tapped holes in a square lattice pattern.
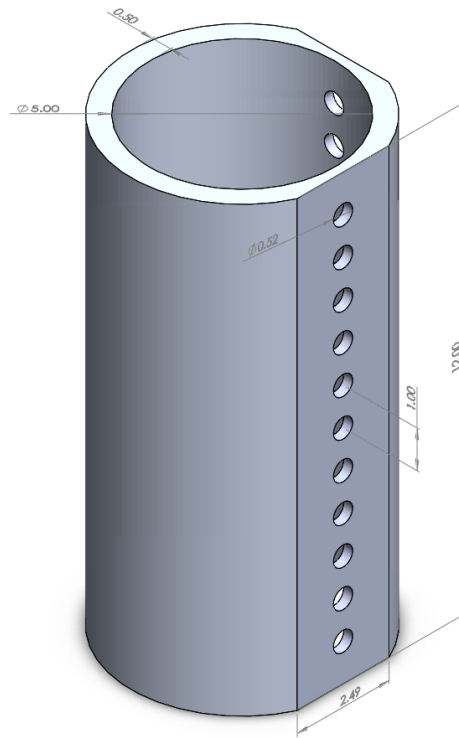
Figure B.39: Optical table leg with annotated dimensions (in inches). Two sides are faced down and populated with 1.00 in holes for rack attachment. The legs are 1 ft tall and 0.50 in thick.
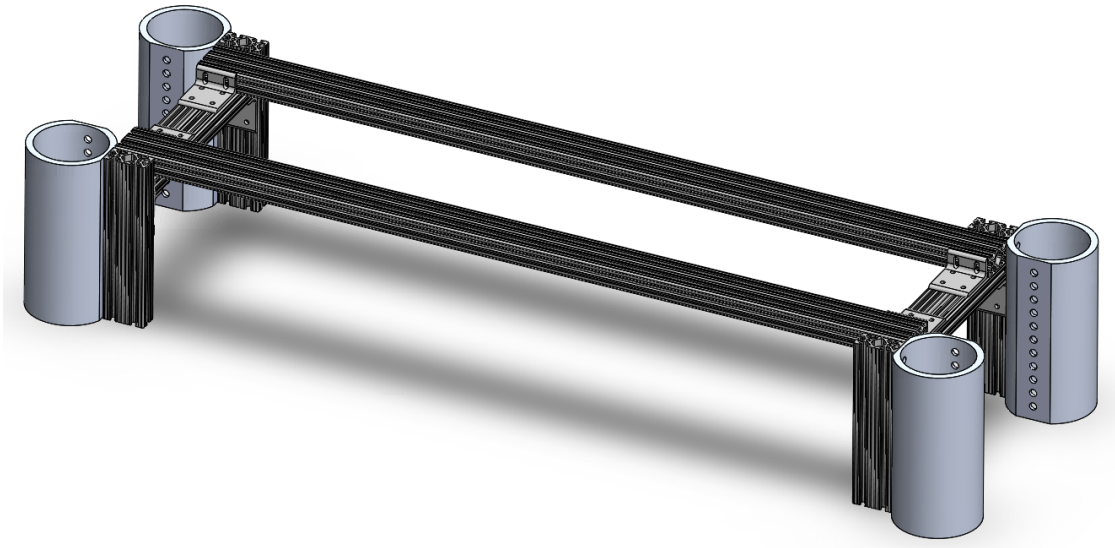
Figure B.40: Optical table base formed by 80/20 components and legs.

Figure B.41: Level 2 breadboard sketch. The general C-shape includes an C-slot through which vertical optical access and mounting of the stainless steel holder is possible.

Figure B.42: Level 2 breadboard with $\oslash 1/4 - 20$ hole lattice. Rounded corners on the C-slot are included for easy machining. The `Vacuum_support_niche` is present at the C-slot.

We start with the level 2 breadboard with a rectangular C-shape depicted in Figure B.41. The dimensions are 51 in by 26 in and the C-slot is 20 in by 3 in towards one end. After extruding by 2.00 in, we make a rectangular 22 in by 8 in cut around the C-slot that goes 1.585 in deep. This cut creates the `Vacuum_support_niche`

233

feature to slide and register the stainless steel holder. Additionally, we incorporate a $1.00\,\mathrm{in}$ spaced lattice of $\oslash\,1/4 - 20$ tapped holes on the top and side breadboard faces and a single set of four $\oslash\,5/16 - 18$ counterbore holes that facing from the bottom grab the stainless steel holder, as shown in Figure B.42.
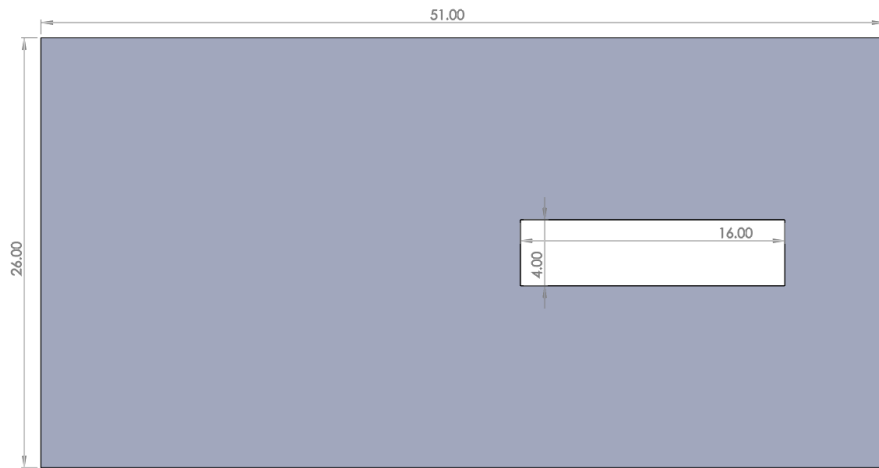
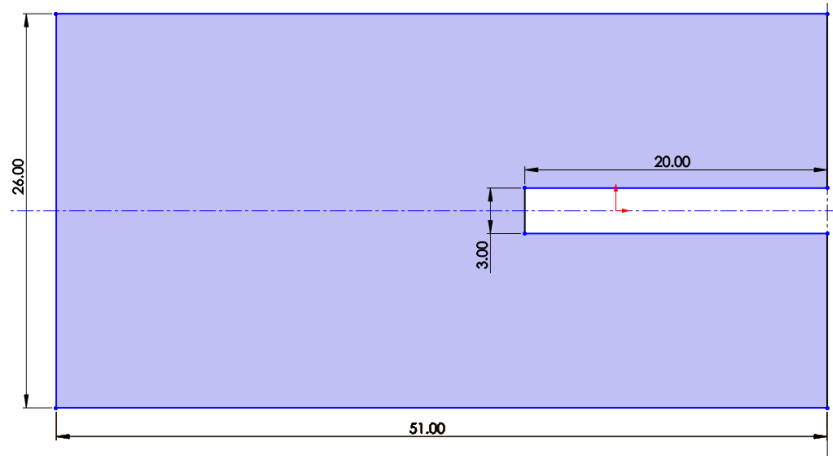Figure B.43: Level 3 breadboard sketch. The general O-shape includes an O-slot through which vertical optical access is possible.
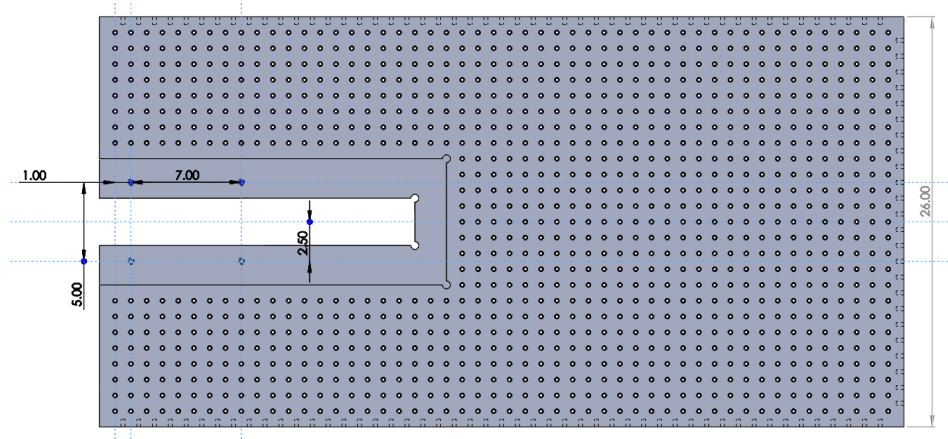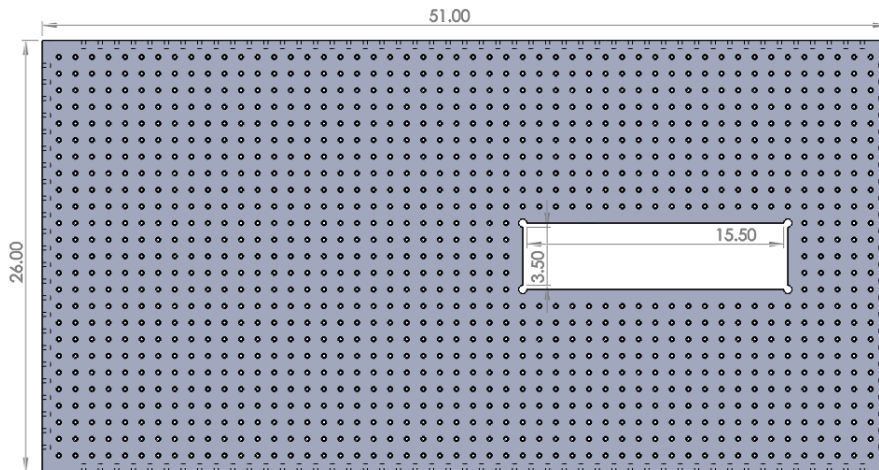

Figure B.44: Level 3 breadboard with $\oslash\,1/4 - 20$ hole lattice. Rounded corners at the O-slot are included for easy machining.

We follow with the level 3 breadboard for which we draw a rectangular O-shape depicted in Figure B.43. The dimensions are 51 in by 26 in and the O-slot is 16 in by 4 in, slightly off-centered in one direction. After extruding by 2.00 in, we incorporate a 1.00 in spaced lattice of $\oslash 1/4 - 20$ tapped holes on the top and side breadboard faces as shown in Figure B.44. The primary function of the
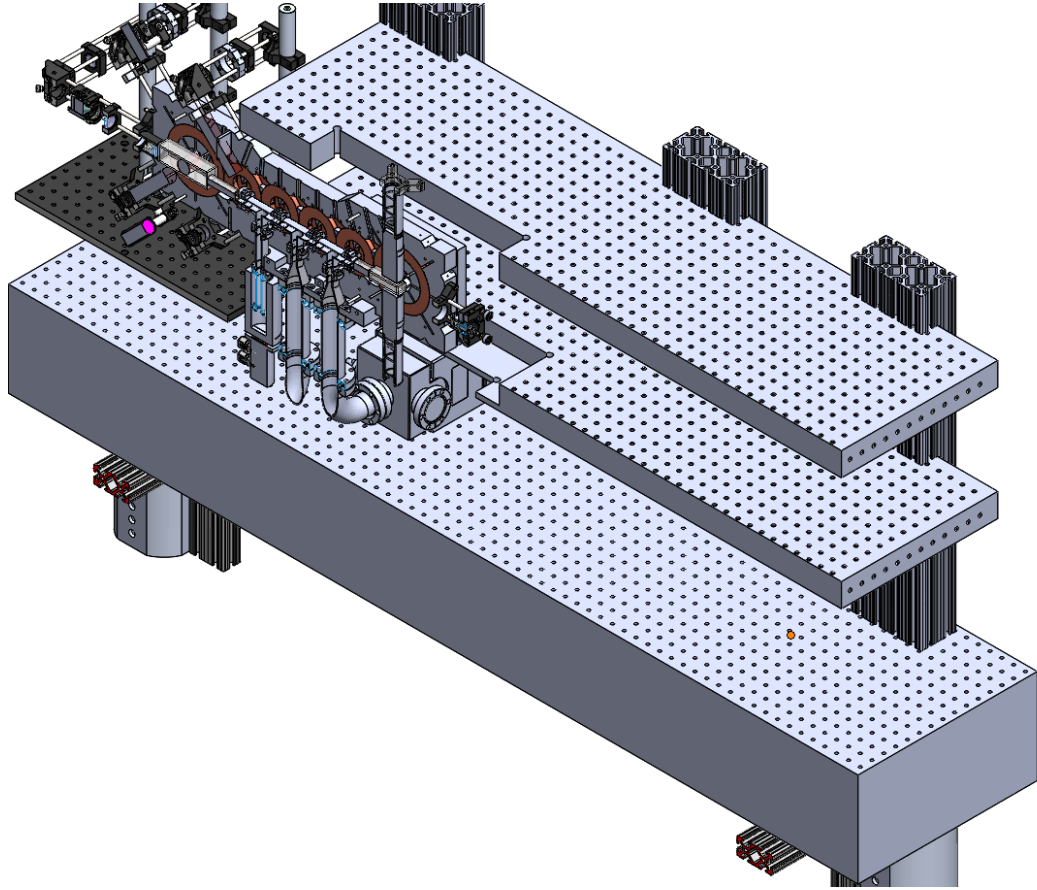
Figure B.45: Three-level optical breadboard assembly in a section view (only half of the assembly is shown for clarity).

level 1 breadboard is to hold the full weight of the machine and the MOT optics whose own breadboard is directly mounted to it. The main function of the level 2 breadboard is to support the full weight of the new apparatus UHV and coils

235

subassembly through the stainless steel holder. The main function of the level 3 breadboard is to provide optical access along $\mathbf{e}_y$. Level 2 and level 3 breadboards are held in place by 80/20 beams that in turn are mounted onto the level 1 surface. The three level structure is assembled and depicted in Figure B.45.

B.2.10 Coil winding forms

We wind coils to the right shapes with coil winding forms. We reuse the circular coil winding forms designed for the Rb–chip transport coils and design new ones for the bias and gradient cancellation coils, sketched in Figures B.46 and B.47 respectively.
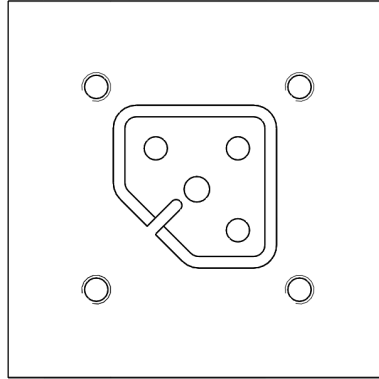
Figure B.46: Sketch of a single bias coil winding form.

All coil winding forms incorporate a two step extruded island whose height is equal to the (fixed) width of the coil wire. At the bottom of the island, separate thin plate masks provide a movable, flat frame to help remove the coils out of the form. Several holes (typically four) around the center island help push the flat frames with the help of $\oslash 1/4 - 20$ screws. Finally, a square plate pushes down on
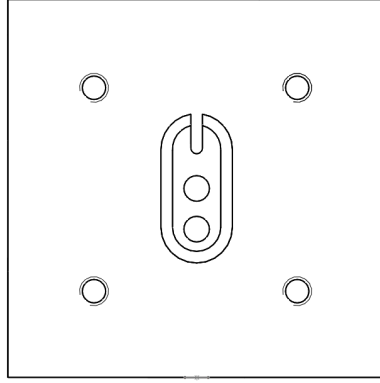
Figure B.47: Sketch of a single gradient cancellation coil winding form.

the coil to flatten it from the top of the winding form. Central holes on the islands mount these square plates tightly in place, while the tiny u-shaped slots mark the starting point for the winding process.

Appendix C: Yang–Yang thermodynamic methods

C.1 Dimensional reduction

The first-order, coupled integral equations

$$\epsilon(k) = \frac{\hbar^2 k^2}{2m} - \mu - \frac{k_{\mathrm{B}}T}{2\pi} \int_{-\infty}^{\infty} \frac{2c}{c^2 + (k-q)^2} \ln(1 + e^{-\epsilon(q)/k_{\mathrm{B}}T}) \, \mathrm{d}q \,, \qquad (\text{C.1})$$

$$2\pi f(k)(1 + e^{\epsilon(k)/k_{\mathrm{B}}T}) = 1 + \int_{-\infty}^{\infty} \frac{2c}{c^2 + (k-q)^2} \, f(q) \, \mathrm{d}q \,, \qquad (\text{C.2})$$

$$n = \int_{-\infty}^{\infty} f(q) \, \mathrm{d}q \,, \qquad (\text{C.3})$$

comprise the Yang–Yang (YY) thermodynamics from Chapter 5. Here m is the bosonic mass, k_{B} is the Boltzmann constant, T is the temperature, μ the chemical potential, and $c = mg/\hbar^2$ is the interaction wavenumber. The one-dimensional coupling constant $g = 2\hbar\omega_{\perp}a/(1 - Ca/l_{\perp})$, is written in terms of the three-dimensional s-wave scattering length a, and scattering regularization constant C. For the specific case of a three-dimensional harmonic potential, C is of order unity [100], and

$l_\perp = \sqrt{\hbar/m\omega_\perp}$ is the transverse oscillator length. Both k and q label longitudinal momenta.

In order to work with the natural energy, momentum and length scales of the problem, we transform all the momentum and energy quantities

$$\tilde{k} = \frac{k}{\sqrt{2mk_\mathrm{B}T/\hbar^2}}, \tag{C.4}$$

$$\tilde{E} = \frac{E}{k_\mathrm{B}T}, \tag{C.5}$$

so that the first two YY equations read

$$\tilde{\epsilon}(\tilde{k}) = \tilde{k}^2 - \tilde{\mu} - \int_{-\infty}^{\infty} \frac{1}{\pi} \frac{\tilde{c}}{\tilde{c}^2 + (\tilde{k} - \tilde{q})^2} \, \ln(1 + e^{-\tilde{\epsilon}(\tilde{q})}) \, \mathrm{d}\tilde{q}, \tag{C.6}$$

$$2\pi f(\tilde{k})(1 + e^{\tilde{\epsilon}(\tilde{k})}) = 1 + \int_{-\infty}^{\infty} \frac{1}{\pi} \frac{\tilde{c}}{\tilde{c}^2 + (\tilde{k} - \tilde{q})^2} \, f(\tilde{q}) \, \mathrm{d}\tilde{q}. \tag{C.7}$$

Here and what follows, I drop the tilde notation but keep the dimensionally reduced quantities.

C.2   Numerical integration

Here I describe the numerical methods to solve the YY equations. Together with the local density approximation (LDA), a numerical integrator takes as pa-

rameters the chemical potential μ, and temperature T as primary input, and the transverse harmonic frequency $f_\perp$, three-dimensional scattering length a, and mass m as secondary input. It then computes c and g with $l_\perp$, a and m, and recursively solves for $\epsilon(k)$ first, and then for $f(k)$. Finally, it computes the density n, entropy S, and pressure P equations of state.

We denote the Lieb–Liniger kernel (a normalized Lorentzian) as $\mathcal{L}(c, q)$. Our numerical solver performs a k-space convolution using the `fftconvolve` method from the `scipy.signal` library to evaluate the integrals in a $N_k = 1024$ points grid that covers the range $k = [-10\, k_{\mathrm{th}}, 10\, k_{\mathrm{th}}]$. Here, $k_{\mathrm{th}} = \sqrt{2mk_{\mathrm{B}}T/\hbar^2}$ is the thermal wavenumber, and we explicitly span over an order of magnitude above the thermal scale to avoid introducing artifical momentum cutoffs. Using convolution operations speeds up the numerical integration significantly. We nevertheless verify that for the parameters relevant to the experiment, using different grid sizes leaves the predicted equations of state the same, as demonstrated in figure C.1.

We begin with the ideal Bose gas dispersion $\epsilon_0(k) = k^2 - \mu$ to integrate the YY equations, and iterate over the recursive relation

$$\epsilon_{j+1}(k) = \epsilon_0(k) - \mathcal{L}(c_0, q) \circledast \ln(1 + e^{-\epsilon_j(q)}), \tag{C.8}$$

where $\circledast$ denotes the Fourier convolution operator. Once the convergence condition
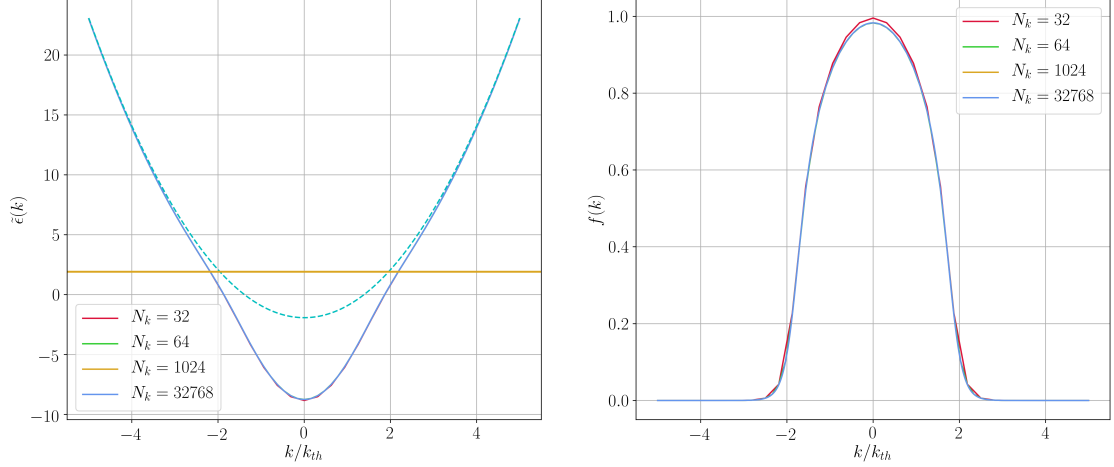
Figure C.1: YY dispersion and momentum distribution. Numerically integrated dispersion $\tilde{\epsilon}(\tilde{k})$ and momentum distribution for a $f_\perp = 16\,\text{kHz}$ trap holding a homogeneous 1D ^{87}Rb gas at $T = 50\,\text{nK}$. On the left, the convergent dispersion with $\epsilon_{\text{tol}} = 0.01$ for different grid sizes differs from the ideal Bose gas dispersion $\epsilon_0(k)$ at low momenta $|k/k_{th}| \leq 4$. A horizontal golden line indicates the value of the reduced chemical potential $\tilde{\mu} = 1.92$ used in this calculation. To the left, the momentum distribution evaluated for four different grid sizes.

$$\frac{1}{N_k}\sqrt{\sum_{i=0}(\epsilon_{i,j+1} - \epsilon_{i,j})^2} < \epsilon_{\text{tol}} \tag{C.9}$$

is satisfied, where N_k is the number of atoms in a certain momentum state k,

we turn to finding a solution $f(k)$ for the second equation with an initial guess

$f_0(k) = [2\pi\,(1 + e^{\epsilon(k)})]^{-1}$. There, we iterate over the recursive relation

$$f_{j+1}(k) = f_0(k) + \mathcal{L}(c_0, q) \circledast f_j(q), \tag{C.10}$$

using a similar convergence criterion. There is no appreciable difference in the

integrated quantities after $N_k \approx 100$, so we use $N_k = 1024$ everywhere. In the

range of experimentally accessible parameters, $|k/k_{th}| \leq 10$ accounts for all the

states of momentum distribution. With the convergent quasimomenta distribution $f(k)$, we evaluate (C.3), the linear density. After watching all the unit conversions we get the linear density in particles per meter.

C.3   Code

Here is the numerical implementation of the YY integrator written in Python.

```python
import numpy as np
from scipy import constants, signal
from numba import vectorize

hbar = constants.codata.value('Planck constant over 2 pi')
kB = constants.codata.value('Boltzmann constant')
pi = np.pi
nm, um, mm = 1e-9, 1e-6, 1e-3
Hz, kHz, MHz = 1, 1e3, 1e6

class harmonic_trap(object):
    """ Simple 1D harmonic oscillator methods """

    def __init__(self, frequency, mass):
        self.omega = 2 * pi * frequency
        self.frequency = frequency
        self.mass = mass
        self.oscillator_length = np.sqrt(hbar / (self.mass * self.omega))

    def sho_potential(self, x):
        return 0.5 * self.mass * self.omega**2 * x**2

    def sho_levels(self, number_of_levels):
        levels = []
        for i in range(number_of_levels):
            levels.append(hbar * self.omega * (i + 0.5))
        return np.array(levels)

class homogeneous_1DBG(harmonic_trap):
    """ Homogeneous one-dimensional Bose gas constants.
    The 3D scattering reduces to an effective 1D
    scattering assuming transverse harmonic
    confinement and s-wave contact interactions"""

    def __init__(self, trans_freq, mass, scatt_length):
        harmonic_trap.__init__(self, trans_freq, mass)
        self.trans_freq = self.frequency
        self.l_perp = self.oscillator_length
        self.a3D = scatt_length
        # Transverse scattering effects
        C = 1.4603 / np.sqrt(2)
        transverse_scatt_correction = (1 - C * self.a3D / self.l_perp)
        self.a1D = - transverse_scatt_correction * self.l_perp**2 / self.a3D
        self.g1D = - 2 * hbar**2 / (self.mass*self.a1D)
        self.c1D = self.mass * self.g1D / (hbar**2)

@vectorize('float64(float64)')
def log_factor(eps_q):
    """ Efficient computation of the logarithmic factor
    in the YY integrals. Whenever the dispersion drops
    below or equals zero, we use a stable approximation"""
```

```python
        if eps_q > 0:
            return np.log(1 + np.exp(-eps_q))
        else:
            return np.log(1 + np.exp(eps_q)) - eps_q

class bethe_integrator(homogeneous_1DBG):
    """ Methods to ingegrate YY equations, derived from the
    thermodynamic Bethe ansatz (TBA). Take as parameters,
    the transverse trapping frequency, the mass, the 3D
    s-wave scattering length, as well as the temperature
    and chemical potential. An additional parameter Nk
    defines the integration grid size. """

    def __init__(self, trans_freq, mass, scatt_length,
                       temperature, chemical_potential, Nk):
        # Start with SI units, then rescale
        homogeneous_1DBG.__init__(self, trans_freq, mass, scatt_length)
        self.mu = 2*pi*chemical_potential*hbar
        self.E_thermal = kB*temperature
        self.k_thermal = np.sqrt(2*self.mass*self.E_thermal)/hbar
        self.k_lim = 5 * self.k_thermal
        self.Nk = Nk
        self.k_space = np.linspace(-self.k_lim, self.k_lim, self.Nk)

        # Rescaled quantities
        self.mutilde = self.mu/self.E_thermal
        self.ctilde = self.c1D/self.k_thermal
        self.kappa = self.k_space/self.k_thermal
        self.dkappa = self.kappa[1] - self.kappa[0]

        # Zero temperature dispersion
        self.eps0 = self.kappa**2 - self.mutilde

        # Initial k-distribution
        self.epsk = self.eps_solver(eps_tol=1e-10)
        self.bose_factor = np.exp(log_factor(-self.epsk))
        self.f0=1/(2*pi*self.bose_factor)

    def lieb_kernel(self, k0):
        return 1/(pi*self.ctilde)/(1+((k0-self.kappa)/self.ctilde)**2)

    def epsilon_update(self, eps_q, method='convolution'):
        g_tilde = log_factor(eps_q)*self.dkappa
        if method == 'integral':
            return np.array([np.sum(g_tilde*self.lieb_kernel(k0=ki))
                for ki in self.kappa])
        elif method == 'convolution':
            return signal.fftconvolve(g_tilde, self.lieb_kernel(k0=0), "same")

    def f_update(self, f_q, method='convolution'):
        if method == 'integral':
            return np.array([np.sum(f_q*self.dkappa*self.lieb_kernel(k0=ki))
                for ki in self.kappa])
        elif method == 'convolution':
            return signal.fftconvolve(f_q*self.dkappa,
]self.lieb_kernel(k0=0), "same")

    def eps_solver(self, eps_tol=1e-3):
        def iterator(eps_it):
            eps_next = self.eps0 - self.epsilon_update(eps_it)
            eps_error = np.sqrt(np.mean((eps_it-eps_next)**2))
            return eps_error, eps_next
        min_iteration, eps_err = 500, 1.0
        eps_i = self.eps0
        for i in range(min_iteration):
            _, eps_f = iterator(eps_i)
            eps_i = eps_f
        while (eps_err > eps_tol) and (min_iteration < 1000):
            min_iteration += 1
```

```python
            eps_err, eps_f = iterator(eps_i)
            eps_i = eps_f
        return eps_f

    def f_solver(self, f_tol=1e-3):
        def iterator(f_it):
            f_next = self.f0 + self.f_update(f_it)/self.bose_factor
            f_error = np.sqrt(np.mean((f_it-f_next)**2))
            return f_error, f_next
        min_iteration, f_err = 500, 1.0
        f_i = self.f0
        for i in range(min_iteration):
            f_err, f_f = iterator(f_i)
            f_i = f_f
        while (f_err > f_tol) and (min_iteration < 1000):
            min_iteration += 1
            f_err, f_f = iterator(f_i)
            f_i = f_f
        return f_f

    def density(self):
        dk = self.dkappa*self.k_thermal()
        return np.trapz(self.f_solver(f_tol=1e-10), dx=dk)

    def entropy_per_particle(self):
        eps = self.eps_solver(eps_tol=1e-3)
        fp = self.f_solver(f_tol=1e-3)
        fh = fp*np.exp(eps)
        f = fp + fh
        n = self.density()
        dk = self.dkappa*self.k_thermal
        S0 = np.sum(dk*f*np.log(1+np.exp(-eps)))
        S1 = np.sum(dk*fp*eps)
        return (S0 + S1)/n

    def pressure(self):
        T = self.E_thermal/kB
        dk = self.dkappa*self.k_thermal
        eps = self.eps_solver(eps_tol=1e-3)
        P0 = np.sum(dk*np.log(1+np.exp(-eps)))
        n = self.density()
        return T*P0/(2*pi*n)
```

Appendix D: Objective lens

We adapt the compound objective [16] originally by Wolfgang Alt for the current apparatus in RbChip. A remarkable aspect of this design is that it works the minimum set of surfaces that account for the dominating spherical aberrations of the vacuum window. A few previous adaptations of the same design appear in the literature [101, 102], forming cold atom microscopes for absorption and fluorescence imaging.
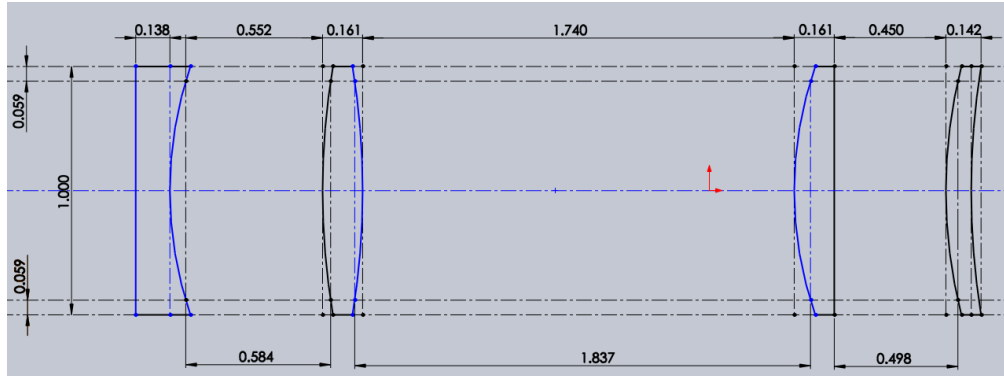

Figure D.1: CAD drawing of lens-stack. The compound objective faces the UHV system (not shown) on the right. The distances are all in millimeters.

The optimized design is summarized in Figure D.1, following the parameter optimization in `Zemax`. Our lens uses off the shelf components, with a `Thorlabs LC1582-B`, $f = -75\,\mathrm{mm}$ plano-concave lens, followed by a `Thorlabs LB1901-B`,

$f = 75\,\text{mm}$ bi-convex, a `Thorlabs LA1608-B`, $f = 75\,\text{mm}$ plano-convex, and finally a `Thorlabs LE1234-B`, $f = 100\,\text{mm}$ meniscus facing the UHV glass cell. The compound objective is designed to work at $\lambda = 780\,\text{nm}$ only, and therefore the tolerances do not heavily constrain its performance.

We assemble the objective into a 40 mm long, 1" diameter lens tube. We replicate the spacers from [101], for which Figure shows the final measurements. We machine the spacers out of Brass, for its compromise in maleability and reduced inductive response. Incidentally, brass is a widely used material in optical engineering. The design specifications give a diffraction limited spot with radius $\Delta = 1.55\,\mu\text{m}$, working distance of 31 mm, object space numerical-aperture of 0.30, field of view of 270 mm, and an effective focal length $f = 39.03\,\text{mm}$. Finally, the tolerance analysis reveals that the plano-concave lens is most sensitive to lateral displacements. For example, when it shifts its position by $\pm150\,\mu\text{m}$, the working distance changes by $\pm45\,\mu\text{m}$. We characterize the objective lens on the test bench, using a $1\,\mu\text{m}$ pinhole as a point source, giving a measured Airy disk radius of $1.61(4)\,\mu\text{m}$.
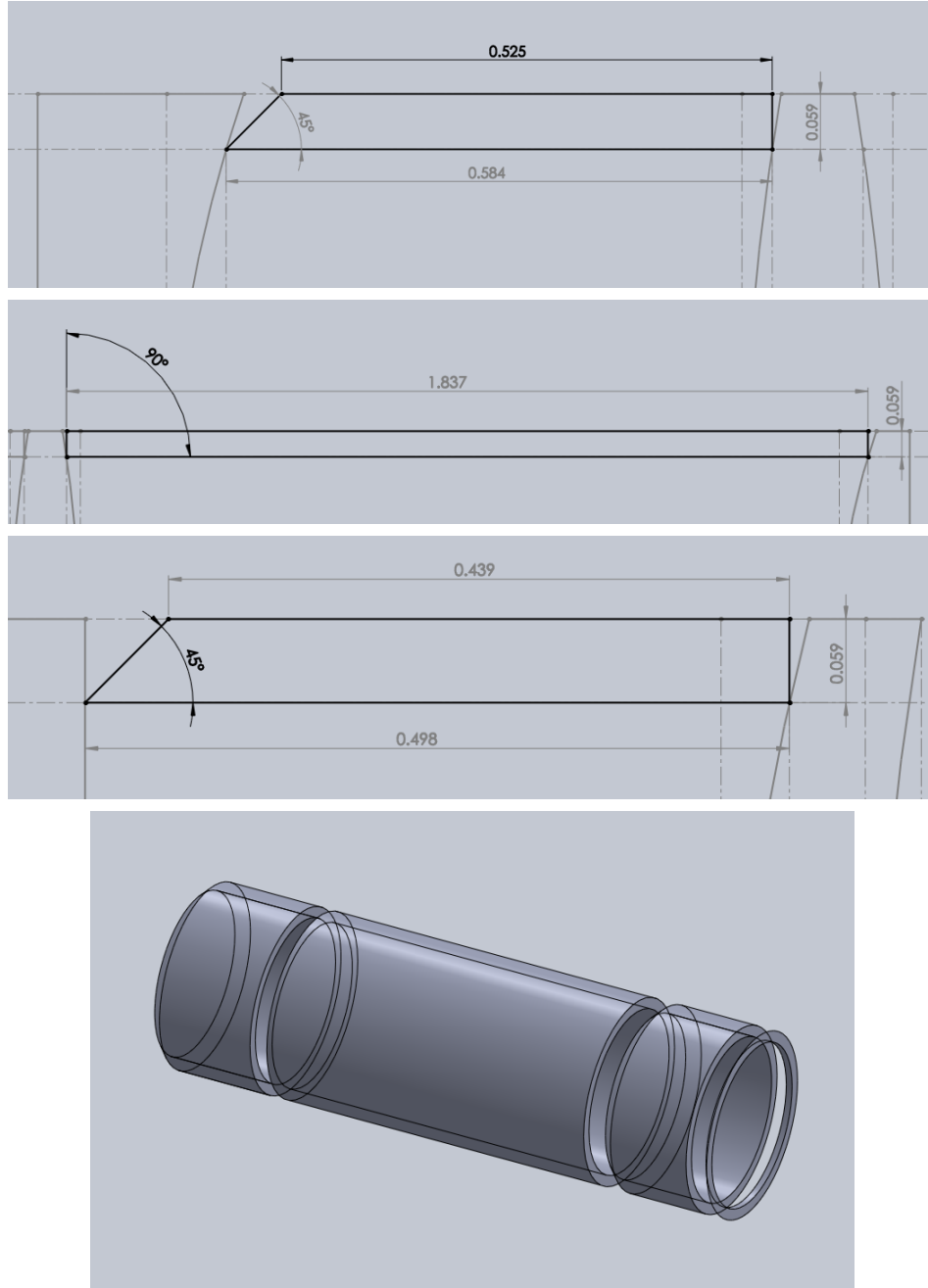
Figure D.2: CAD drawings of lens-stack ring spacers. We adapt the original design from [101], and machine them out of brass. Each figure shows the cross section of the annular piece. The annotated dimensions are in millimeters. We use a conventional threaded ring at the end to hold the meniscus in place.

Bibliography

[1] Jan Klaers, Julian Schmitt, Frank Vewinger, and Martin Weitz. Bose-einstein condensation of photons in an optical microcavity. *Nature*, 468:545 EP –, 2010.

[2] J. Kasprzak, M. Richard, S. Kundermann, A. Baas, P. Jeambrun, J. M. J. Keeling, F. M. Marchetti, M. H. Szymanska, R. André, J. L. Staehli, V. Savona, P. B. Littlewood, B. Deveaud, and Le Si Dang. Bose-einstein condensation of exciton polaritons. *Nature*, 443(7110):409–414, 2006.

[3] M. H. Anderson, J. R. Ensher, M. R. Matthews, C. E. Wieman, and E. A. Cornell. Observation of bose-einstein condensation in a dilute atomic vapor. *Science*, 269(5221):198–201, 1995.

[4] K. B. Davis, M. O. Mewes, M. R. Andrews, N. J. van Druten, D. S. Durfee, D. M. Kurn, and W. Ketterle. Bose-einstein condensation in a gas of sodium atoms. *Phys. Rev. Lett.*, 75:3969–3973, 1995.

[5] S. Jochim, M. Bartenstein, A. Altmeyer, G. Hendl, S. Riedl, C. Chin, J. Hecker Denschlag, and R. Grimm. Bose-einstein condensation of molecules. *Science*, 302(5653):2101–2103, 2003.

[6] Laszlo Tisza. The theory of liquid helium. *Phys. Rev.*, 72:838–854, Nov 1947.

[7] J. Bardeen, L. N. Cooper, and J. R. Schrieffer. Theory of superconductivity. *Phys. Rev.*, 108:1175–1204, 1957.

[8] A. A. Penzias and R. W. Wilson. A measurement of excess antenna temperature at 4080 mc/s. *apj*, 142:419–421, 1965.

[9] Cheng Chin, Rudolf Grimm, Paul Julienne, and Eite Tiesinga. Feshbach resonances in ultracold gases. *Reviews of Modern Physics*, 82(2):1225, 2010.

[10] Sarang Gopalakrishnan, Benjamin L. Lev, and Paul M. Goldbart. Frustration and glassiness in spin models with cavity-mediated interactions. *Phys. Rev. Lett.*, 107:277201, 2011.

[11] Thierry Lahaye, C Menotti, L Santos, M Lewenstein, and T Pfau. The physics of dipolar bosonic quantum gases. *Reports on Progress in Physics*, 72(12):126401, 2009.

[12] R. A. Williams, L. J. LeBlanc, K. Jiménez-García, M. C. Beeler, A. R. Perry, W. D. Phillips, and I. B. Spielman. Synthetic partial waves in ultracold atomic collisions. *Science*, 335(6066):314–317, 2012.

[13] Markus Greiner, Olaf Mandel, Tilman Esslinger, Theodor W. Hänsch, and Immanuel Bloch. Quantum phase transition from a superfluid to a mott insulator in a gas of ultracold atoms. *Nature*, 415(6867):39–44, 2002.

[14] Thibault Peyronel, Ofer Firstenberg, Qi-Yu Liang, Sebastian Hofferberth, Alexey V. Gorshkov, Thomas Pohl, Mikhail D. Lukin, and Vladan Vuletic. Quantum nonlinear optics with single photons enabled by strongly interacting atoms. *Nature*, 488(7409):57–60, 2012.

[15] Belén Paredes, Artur Widera, Valentin Murg, Olaf Mandel, Simon Fölling, Ignacio Cirac, Gora V Shlyapnikov, Theodor W Hänsch, and Immanuel Bloch. Tonks–girardeau gas of ultracold atoms in an optical lattice. *Nature*, 429(6989):277–281, 2004.

[16] Wolfgang Alt. An objective lens for efficient fluorescence detection of single atoms. *Optik*, 113(3):142 – 144, 2002.

[17] A. R. Perry. *An apparatus for light-less artificial gauge fields and new imaging techniques.* PhD thesis, Joint Quantum Institute, National Institute of Standards and Technology and University of Maryland Department of Physics, 2015.

[18] P. T. Starkey, C. J. Billington, S. P. Johnstone, M. Jasperse, K. Helmerson, L. D. Turner, and R. P. Anderson. A scripted control system for autonomous hardware-timed experiments. *Review of Scientific Instruments*, 84(8):085111, 2013.

[19] A. Putra. *Magnetized plane wave and stripe-ordered phases in spin-orbit-coupled Bose Gases.* PhD thesis, National Institute of Standards and Technology and Joint Quantum Institute, Department of Physics at the University of Maryland, 2018.

[20] D. Genkina. *Measuring topology of BECs in a synthetic dimensional optical lattice.* PhD thesis, National Institute of Standards and Technology and Joint Quantum Institute, Department of Physics at the University of Maryland, 2019.

[21] A. Valdes. *Topological dispersion relations in spin-orbit coupled Bose gases*. PhD thesis, National Institute of Standards and Technology and Joint Quantum Institute, Department of Physics at the University of Maryland, 2019.

[22] C. J. Billington. *State-dependent forces in cold quantum gases*. PhD thesis, Monash University, 2018.

[23] A. Gozzini, F. Mango, J. H. Xu, G. Alzetta, F. Maccarrone, and R. A. Bernheim. Light-induced ejection of alkali atoms in polysiloxane coated cells. *Il Nuovo Cimento D*, 15(5):709–722, 1993.

[24] Daniel A. Steck. Rubidium 87 d line data. *available online at http://steck.us/alkalidata*, 2019.

[25] Y.-J. Lin, A. R. Perry, R. L. Compton, I. B. Spielman, and J. V. Porto. Rapid production of ^{87}Rb bose-einstein condensates in a combined magnetic and optical potential. *Phys. Rev. A*, 79:063631, 2009.

[26] J. Dalibard and C. Cohen-Tannoudji. Laser cooling below the doppler limit by polarization gradients: simple theoretical models. *J. Opt. Soc. Am. B*, 6(11):2023–2045, 1989.

[27] C. Salomon, J. Dalibard, W. D Phillips, A. Clairon, and S. Guellati. Laser cooling of cesium atoms below 3 μk. *Europhysics Letters (EPL)*, 12(8):683–688, 1990.

[28] Markus Greiner, Immanuel Bloch, Theodor W. Hänsch, and Tilman Esslinger. Magnetic transport of trapped cold atoms over a large distance. *Phys. Rev. A*, 63:031401, 2001.

[29] P. B. Wigley, P. J. Everitt, A. van den Hengel, J. W. Bastian, M. A. Sooriyabandara, G. D. McDonald, K. S. Hardman, C. D. Quinlivan, P. Manju, C. C. N. Kuhn, I. R. Petersen, A. N. Luiten, J. J. Hope, N. P. Robins, and M. R. Hush. Fast machine-learning online optimization of ultra-cold-atom experiments. *Scientific Reports*, 6(1):25890, 2016.

[30] Wolfgang Petrich, Michael H. Anderson, Jason R. Ensher, and Eric A. Cornell. Stable, tightly confining magnetic trap for evaporative cooling of neutral atoms. *Phys. Rev. Lett.*, 74:3352–3355, 1995.

[31] Rudolf Grimm, Matthias Weidemüller, and Yurii B. Ovchinnikov. Optical dipole traps for neutral atoms. volume 42 of *Advances In Atomic, Molecular, and Optical Physics*, pages 95 – 170. Academic Press, 2000.

[32] Gordon Baym and C. J. Pethick. Ground-state properties of magnetically trapped bose-condensed rubidium gas. *Phys. Rev. Lett.*, 76:6–9, 1996.

[33] Seiji Sugawa, Francisco Salces-Carcoba, Abigail R. Perry, Yuchen Yue, and I. B. Spielman. Second chern number of a quantum-simulated non-abelian yang monopole. *Science*, 360(6396):1429–1434, 2018.

[34] Xiao-Gang Wen. Colloquium: Zoo of quantum-topological phases of matter. *Rev. Mod. Phys.*, 89:041004, 2017.

[35] Tomoki Ozawa, Hannah M. Price, Alberto Amo, Nathan Goldman, Mohammad Hafezi, Ling Lu, Mikael C. Rechtsman, David Schuster, Jonathan Simon, Oded Zilberberg, and Iacopo Carusotto. Topological photonics. *Rev. Mod. Phys.*, 91:015006, 2019.

[36] Zhaoju Yang, Fei Gao, Xihang Shi, Xiao Lin, Zhen Gao, Yidong Chong, and Baile Zhang. Topological acoustics. *Phys. Rev. Lett.*, 114:114301, 2015.

[37] Roman Süsstrunk and Sebastian D. Huber. Observation of phononic helical edge states in a mechanical topological insulator. *Science*, 349(6243):47–50, 2015.

[38] Jia Ningyuan, Clai Owens, Ariel Sommer, David Schuster, and Jonathan Simon. Time- and site-resolved dynamics in a topological circuit. *Phys. Rev. X*, 5:021031, 2015.

[39] S. Pancharatnam. Generalized theory of interference, and its applications. *Proceedings of the Indian Academy of Sciences - Section A*, 44(5):247–262, 1956.

[40] Y. Aharonov and D. Bohm. Significance of electromagnetic potentials in the quantum theory. *Phys. Rev.*, 115:485–491, 1959.

[41] Michael Victor Berry. Quantal phase factors accompanying adiabatic changes. *Proceedings of the Royal Society of London. A. Mathematical and Physical Sciences*, 392(1802):45–57, 1984.

[42] J. Zak. Berry's phase for energy bands in solids. *Phys. Rev. Lett.*, 62:2747–2750, 1989.

[43] Frank Wilczek and A. Zee. Appearance of gauge structure in simple dynamical systems. *Phys. Rev. Lett.*, 52:2111–2114, 1984.

[44] R. B. Laughlin. Quantized hall conductivity in two dimensions. *Phys. Rev. B*, 23:5632–5633, 1981.

[45] M. D. Schroer, M. H. Kolodrubetz, W. F. Kindel, M. Sandberg, J. Gao, M. R. Vissers, D. P. Pappas, Anatoli Polkovnikov, and K. W. Lehnert. Measuring a topological transition in an artificial spin-1/2 system. *Phys. Rev. Lett.*, 113:050402, 2014.

[46] P. J. Leek, J. M. Fink, A. Blais, R. Bianchetti, M. Göppl, J. M. Gambetta, D. I. Schuster, L. Frunzio, R. J. Schoelkopf, and A. Wallraff. Observation of berry's phase in a solid-state qubit. *Science*, 318(5858):1889–1892, 2007.

[47] Zhenxing Zhang, Tenghui Wang, Liang Xiang, Jiadong Yao, Jianlan Wu, and Yi Yin. Measuring the berry phase in a superconducting phase qubit by a shortcut to adiabaticity. *Phys. Rev. A*, 95:042345, 2017.

[48] V. Gritsev and A. Polkovnikov. Dynamical quantum hall effect in the parameter space. *Proceedings of the National Academy of Sciences*, 109(17):6457–6462, 2012.

[49] M. Lohse, C. Schweizer, O. Zilberberg, M. Aidelsburger, and I. Bloch. A thouless quantum pump with ultracold bosonic atoms in an optical superlattice. *Nature Physics*, 12(4):350–354, 2016.

[50] H.-I Lu, M. Schemmer, L. M. Aycock, D. Genkina, S. Sugawa, and I. B. Spielman. Geometrical pumping with a bose-einstein condensate. *Phys. Rev. Lett.*, 116:200402, 2016.

[51] H. M. Price, O. Zilberberg, T. Ozawa, I. Carusotto, and N. Goldman. Four-dimensional quantum hall effect with ultracold atoms. *Phys. Rev. Lett.*, 115:195303, 2015.

[52] B. K. Stuhl, H.-I. Lu, L. M. Aycock, D. Genkina, and I. B. Spielman. Visualizing edge states with an atomic bose gas in the quantum hall regime. *Science*, 349(6255):1514–1518, 2015.

[53] T. T. Wu and Chen-Ning Yang. Some solutions of the classical isotopic gauge field equations. 1967.

[54] Seiji Sugawa, Francisco Salces-Carcoba, Yuchen Yue, Andika Putra, and I. B. Spielman. Observation and characterization of a non-abelian gauge field's wilczek-zee phase by the wilson loop, 2019.

[55] Ariel Lipson, Stephen G. Lipson, and Henry Lipson. *Optical Physics*. Cambridge University Press, 4 edition, 2010.

[56] Leslie Allen and Joseph H Eberly. *Optical resonance and two-level atoms*, volume 28. Courier Corporation, 1987.

[57] D Genkina, L M Aycock, B K Stuhl, H-I Lu, R A Williams, and I B Spielman. Feshbach enhanceds-wave scattering of fermions: direct observation with optimized absorption imaging. *New Journal of Physics*, 18(1):013001, 2015.

[58] Klaus Hueck, Niclas Luick, Lennart Sobirey, Jonas Siegl, Thomas Lompe, Henning Moritz, Logan W. Clark, and Cheng Chin. Calibrating high intensity absorption imaging of ultracold atoms. *Opt. Express*, 25(8):8670–8679, 2017.

[59] M. L. Citron, H. R. Gray, C. W. Gabel, and C. R. Stroud. Experimental study of power broadening in a two-level atom. *Phys. Rev. A*, 16:1507–1512, 1977.

[60] F. Salces-Carcoba, C. J. Billington, A. Putra, Y. Yue, S. Sugawa, and I. B. Spielman. Equations of state from individual one-dimensional bose gases. *New Journal of Physics*, 20:113032, 2018.

[61] C. F. Ockeloen, A. F. Tauschinsky, R. J. C. Spreeuw, and S. Whitlock. Detection of small atom numbers through image processing. *Phys. Rev. A*, 82:061606, 2010.

[62] Xiaolin Li, Min Ke, Bo Yan, and Yuzhu Wang. Reduction of interference fringes in absorption imaging of cold atom cloud using eigenface method. *Chin. Opt. Lett.*, 5(3):128–130, 2007.

[63] Jorge Cadima and Ian Jolliffe. On relationships between uncentred and column-centred principal component analysis. *Pakistan Journal of Statistics*, 25(4), 2009.

[64] K. V. Kheruntsyan, D. M. Gangardt, P. D. Drummond, and G. V. Shlyapnikov. Finite-temperature correlations and density profiles of an inhomogeneous interacting one-dimensional bose gas. *Phys. Rev. A*, 71:053615, 2005.

[65] Elliott H. Lieb and Werner Liniger. Exact analysis of an interacting bose gas. i. the general solution and the ground state. *Phys. Rev.*, 130:1605–1616, 1963.

[66] C. N. Yang and C. P. Yang. Thermodynamics of a one-dimensional system of bosons with repulsive delta-function interaction. *Journal of Mathematical Physics*, 10(7):1115–1122, 1969.

[67] W. Kohn and L. J. Sham. Self-consistent equations including exchange and correlation effects. *Phys. Rev.*, 140:A1133–A1138, 1965.

[68] Zur theorie der metalle. *Zeitschrift für Physik*, 71(3):205–226, 1931.

[69] M. Girardeau. Relationship between systems of impenetrable bosons and fermions in one dimension. *Journal of Mathematical Physics*, 1(6):516–523, 1960.

[70] C. P. Yang. One-dimensional system of bosons with repulsive δ-function interactions at a finite temperature t. *Phys. Rev. A*, 2:154–157, 1970.

[71] E. P. Gross. Structure of a quantized vortex in boson systems. *Il Nuovo Cimento (1955-1965)*, 20(3):454–477, 1961.

[72] Lev P Pitaevskii. Vortex lines in an imperfect bose gas. *Sov. Phys. JETP*, 13(2):451–454, 1961.

[73] J. Denschlag, J. E. Simsarian, D. L. Feder, Charles W. Clark, L. A. Collins, J. Cubizolles, L. Deng, E. W. Hagley, K. Helmerson, W. P. Reinhardt, S. L. Rolston, B. I. Schneider, and W. D. Phillips. Generating solitons by phase engineering of a bose-einstein condensate. *Science*, 287(5450):97–101, 2000.

[74] Simone Donadello, Simone Serafini, Marek Tylutki, Lev P. Pitaevskii, Franco Dalfovo, Giacomo Lamporesi, and Gabriele Ferrari. Observation of solitonic vortices in bose-einstein condensates. *Phys. Rev. Lett.*, 113:065302, 2014.

[75] J. Stenger, S. Inouye, D. M. Stamper-Kurn, H.-J. Miesner, A. P. Chikkatur, and W. Ketterle. Spin domains in ground-state bose-einstein condensates. *Nature*, 396(6709):345–348, 1998.

[76] D. S. Petrov, G. V. Shlyapnikov, and J. T. M. Walraven. Regimes of quantum degeneracy in trapped 1d gases. *Phys. Rev. Lett.*, 85:3745–3749, 2000.

[77] M. Olshanii. Atomic scattering in the presence of an external confinement and a gas of impenetrable bosons. *Phys. Rev. Lett.*, 81:938–941, 1998.

[78] Y-J Lin, K Jiménez-García, and Ian B Spielman. Spin–orbit-coupled bose–einstein condensates. *Nature*, 471(7336):83–86, 2011.

[79] Siddhartha Saha, E. J. König, Junhyun Lee, and J. H. Pixley. Strongly interacting spin-orbit coupled bose-einstein condensates in one dimension. *Phys. Rev. Research*, 2:013252, Mar 2020.

[80] B Laburthe Tolra, KM O'hara, JH Huckans, William D Phillips, SL Rolston, and James V Porto. Observation of reduced three-body recombination in a correlated 1d degenerate bose gas. *Physical review letters*, 92(19):190401, 2004.

[81] Toshiya Kinoshita, Trevor Wenger, and David S Weiss. Observation of a one-dimensional tonks-girardeau gas. *Science*, 305(5687):1125–1128, 2004.

[82] Bernhard Rauer, Pjotrs Grišins, Igor E Mazets, Thomas Schweigler, Wolfgang Rohringer, Remi Geiger, Tim Langen, and Jörg Schmiedmayer. Cooling of a one-dimensional bose gas. *Physical review letters*, 116(3):030402, 2016.

[83] AH Van Amerongen, JJP Van Es, P Wicke, KV Kheruntsyan, and NJ Van Druten. Yang-yang thermodynamics on an atom chip. *Physical review letters*, 100(9):090402, 2008.

[84] L. Allen, M. W. Beijersbergen, R. J. C. Spreeuw, and J. P. Woerdman. Orbital angular momentum of light and the transformation of laguerre-gaussian laser modes. *Phys. Rev. A*, 45:8185–8189, 1992.

[85] S Kulin, S Aubin, S Christe, B Peker, S L Rolston, and L A Orozco. A single hollow-beam optical trap for cold atoms. *Journal of Optics B: Quantum and Semiclassical Optics*, 3(6):353–357, 2001.

[86] K. Bongs, S. Burger, S. Dettmer, D. Hellweg, J. Arlt, W. Ertmer, and K. Sengstock. Waveguide for bose-einstein condensates. *Phys. Rev. A*, 63:031602, 2001.

[87] Matthew S Walhout. Studies of laser-cooled and magneto-optically trapped xenon. 1995.

[88] S. Kadlecek, J. Sebby, R. Newell, and T. G. Walker. Nondestructive spatial heterodyne imaging of cold atoms. *Opt. Lett.*, 26(3):137–139, 2001.

[89] Lincoln David Turner. *Holographic imaging of cold atoms*. PhD thesis, 2004.

[90] Xiao Yu, Jisoo Hong, Changgeng Liu, and Myung K. Kim. Review of digital holographic microscopy for three-dimensional profiling and tracking. *Optical Engineering*, 53(11):1 – 22, 2014.

[91] Philipp M. Holl and Friedemann Reinhard. Holography of wi-fi radiation. *Phys. Rev. Lett.*, 118:183901, May 2017.

[92] Ian McNulty, Janos Kirz, Chris Jacobsen, Erik H. Anderson, Malcolm R. Howells, and Dieter P. Kern. High-resolution imaging by fourier transform x-ray holography. *Science*, 256(5059):1009–1012, 1992.

[93] Peng Gao, Baoli Yao, Irina Harder, Norbert Lindlein, and Francisco Jose Torcal-Milla. Phase-shifting zernike phase contrast microscopy for quantitative phase measurement. *Opt. Lett.*, 36(21):4305–4307, 2011.

[94] von F. Zernike. Beugungstheorie des schneidenver-fahrens und seiner verbesserten form, der phasenkontrastmethode. *Physica*, 1(7):689 – 704, 1934.

[95] Tong Yang, Guo-Fan Jin, and Jun Zhu. Automated design of freeform imaging systems. *Light: Science & Applications*, 6(10):e17081–e17081, 2017.

[96] Andika Putra, Daniel L. Campbell, Ryan M. Price, Subhadeep De, and I. B. Spielman. Optimally focused cold atom systems obtained using density-density correlations. *Review of Scientific Instruments*, 85(1):013110, 2014.

[97] Chen-Lung Hung, Xibo Zhang, Li-Chung Ha, Shih-Kuang Tung, Nathan Gemelke, and Cheng Chin. Extracting density–density correlations fromin situimages of atomic quantum gases. *New Journal of Physics*, 13(7):075019, 2011.

[98] François Orieux, Jean-François Giovannelli, and Thomas Rodet. Bayesian estimation of regularization and point spread function parameters for wiener–hunt deconvolution. *J. Opt. Soc. Am. A*, 27(7):1593–1607, 2010.

[99] M.-O. Mewes, M. R. Andrews, N. J. van Druten, D. M. Kurn, D. S. Durfee, and W. Ketterle. Bose-einstein condensation in a tightly confining dc magnetic trap. *Phys. Rev. Lett.*, 77:416–419, 1996.

[100] V. Dunjko, V. Lorent, and M. Olshanii. Bosons in cigar-shaped traps: Thomas-fermi regime, tonks-girardeau regime, and in between. *Phys. Rev. Lett.*, 86:5413–5416, 2001.

[101] L. M. Bennie, P. T. Starkey, M. Jasperse, C. J. Billington, R. P. Anderson, and L. D. Turner. A versatile high resolution objective for imaging quantum gases. *Opt. Express*, 21(7):9011–9016, 2013.

[102] J. D. Pritchard, J. A. Isaacs, and M. Saffman. Long working distance objective lenses for single atom trapping and imaging. *Review of Scientific Instruments*, 87(7):073107, 2016.